High resolution RCS imaging in anechoic chamber by introducing a random medium

Stefania Bucuci

ANNÉE 2017

UNIVERSITÉ DE RENNES 1

UNIVERSITE BRETAGNE LOIRE

THÈSE / UNIVERSITÉ DE RENNES 1
sous le sceau de l'Université Bretagne Loire

pour le grade de

DOCTEUR DE L'UNIVERSITÉ DE RENNES 1

Mention : Traitement de Signal et Télécommunications

Ecole doctorale MathSTIC

présentée par

Ștefania Bucuci

Préparée à l'unité de recherche IETR (UMR CNRS 6164)
Institut d'Electronique et de Télécommunications de Rennes
Université de Rennes 1

Imagerie Haute Résolution SER en Chambre Anéchoïque grâce à l'introduction d'un Milieu Diffusant

Thèse soutenue vue à Rennes le 21/12/2017

devant le jury composé de :

Elodie RICHALOT
Professeure à l'Université Paris-Est Marne-la-Vallée / *rapporteur*

Cyril DECROZE
Maître de Conférences à l'Institute de recherche XLIM / *rapporteur*

Joseph SAILLARD
Professeur à l'Université de Nantes / *examinateur*

Philippe POULIGUEN
Responsable du Domaine Scientifique de la MRIS « Ondes Acoustiques et Radioélectriques » / *examinateur*

Patrick POTIER
Docteur DGA/MI à Bruz / *examinateur*

Ala SHARAIHA
Professeur à l'Université de Rennes 1 / *directeur de thèse*

Matthieu DAVY
Maître de Conférences à l'Université de Rennes 1 / *co-directeur de thèse*

Quote

"Science is made up of mistakes, but they are mistakes which it is useful to make, because they lead little by little to the truth."

Jules Verne

Acknowledgements

This manuscript presents the work carried out at Institute of Electronics and Telecommunications of Rennes with the financial support of the Direction Générale de l‟Armement (DGA).

Foremost, I would like to express my sincere gratitude to Prof. Elodie Richalot and Dr. Cyril Decroze for doing me the honor to be the reviewers of my PhD thesis. I am grateful for their detailed review of the manuscript that helped me improve and complete my thesis. As well, I would like to thank Prof. Joseph Saillard who has agreed to be the president of my thesis jury and I am deeply appreciative to all jury members, namely Dr. Philippe Pouliguen and Dr. Patrick Potier for consenting to read the manuscript.

Moreover, I would like to present my profound gratitude to my supervisor Prof. Ala Sharaiha for his continuous support of my PhD study and research, for his motivation and his vast knowledge.

Besides, I would like to convey my great appreciation for my co-supervisor Dr. Matthieu Davy for his patience and guidance which helped me in all the time of research.

Besides my advisors, I would like to express my gratitude to Dr. Philippe Pouliguen for his encouragement and insightful comments during my study.

I am also grateful for all the support I received from all the members from the lab: the IETR director, the secretaries and mechanics. Their help has facilitated my work throughout my thesis.

I was fortunate to have kind colleagues especially Mr. Jerome Sol from National institute of Applied Sciences of Rennes (INSA) and Mr. Frédéric Boutet from IETR, who helped me and provided me all the apparatus I needed for measurements.

I also want to thank my fellow lab mates for the pleasant time we had in the last three years and for their support. Special thanks go to Laura Pometcu, a wonderful colleague who always helped me and to Dr. Mohsen Koohestani, an awesome colleague who had been always there to support and encourage me.

Last but not least, I would like to thank my family and friends for all their encouragement, support and motivation. Here, another special thanks goes to Prof. Răzvan Tamaş from Constanţa Maritime University.

Rennes, 2017

Contents

Quote i

Acknowledgments iii

Contents v

Acronyms ix

List of Tables xi

List of Figures xiii

Résumé xix

Introduction 1

CHAPTER 1 Radar cross section principles

1.1 Introduction 5

1.2 Radar basic definitions 5

1.2.1 History of radar 5

1.2.2 Introduction to radar systems 6

1.2.3 Radar equation 9

1.3 Radar cross section fundamentals 10

1.3.1 Radar cross section determination 10

1.4 Scattering regimes 13

1.4.1 Low-frequency scattering region 13

1.4.2 Mie resonant scattering region 14

1.4.3 High-frequency optical scattering region 15

1.5 Calibration targets 16

1.5.1 Flat plate 16

1.5.1.1 Rectangular flat plate 16

1.5.1.2 Circular flat plate 17

1.5.2 Dihedral reflector 18

1.5.3 Trihedral reflector 20

1.5.3.1 Rectangular trihedral reflector 20

1.5.3.2 Circular trihedral reflector 21

1.5.3.3 Triangular trihedral reflector 22

1.6 Polarization scattering matrix 23
1.7 Radar cross section measurements 25
1.7.1 Measurement facilities 26
1.7.1.1 Indoor facilities and anechoic chamber – far field range 26
1.7.2 Radar cross section imagery 29
1.7.2.1 One-dimensional range profile 29
1.7.2.2 One-dimensional cross-range profile 31
1.7.2.3 Two-Dimensional ISAR image 33
1.8 Conclusion 36

CHAPTER 2 Time reversal technique

2.1 Introduction 39
2.2 Time reversal in acoustics 40
2.2.1 Wave equation 40
2.2.2 Time reversal cavity 41
2.2.3 Time reversal mirror 45
2.2.4 Time reversal in random media 46
2.2.5 Time Reversal in a waveguide 49
2.2.6 Time Reversal in a chaotic cavity 51
2.3 Time reversal in electromagnetics 52
2.3.1 Time-symmetry of electromagnetic waves 53
2.3.2 Reciprocity of electromagnetic waves 54
2.3.3 Electromagnetic time reversal cavity 55
2.3.4 Time Reversal within a reverberation chamber 57
2.3.5 Radar imaging using a time reversal beamformer 60
2.4 Time reversal focusing through a random medium 63
2.4.1 Basics of the finite-difference time-domain method 64
2.4.1.1 FDTD grid 64
2.4.1.2 Boundary conditions 65
2.4.2 The finite-difference time-domain simulations 65
2.4.2.1 Focusing on a position 65
2.4.2.2 Focusing on multiple positions 73
2.5 Conclusion 75

CHAPTER 3 Modeling of a microwave imaging system using a random medium

3.1 Introduction 77
3.2 Microwave imaging 77
3.3 Conception and design of the medium 79
3.3.1 First trial - rod diameter: 10 mm 79
3.3.2 Second trial - rod diameter: 15 mm 81
3.3.3 Third trial - rod diameter: 20 mm 83
3.4 Target detection through a random medium 2D simulations 85
3.4.1 Random medium characteristics 85
3.4.2 First simulation setup: Setup A 90
3.4.2.1 Time reversal method 92
3.4.2.2 Matrix inversion method 93
3.4.3 Second simulation setup: Setup B 97
3.4.3.1 Time reversal method 98
3.4.3.2 Matrix inversion method 99
3.4.4 Comparison of different metallic boundaries on simulation setup A 100
3.4.4.1 Time reversal method 103
3.4.4.2 Matrix inversion method 105
3.5 Conclusion 109

CHAPTER 4 Imaging through a random medium using two antennas

4.1 Introduction 111
4.2 Random medium fabrication 111
4.3 Experimental results 113
4.3.1 Measurement setup 113
4.3.2 Multiple antennas measurement setup 121
4.3.2.1 Case 1 – one antenna emitting through the medium 124
4.3.2.2 Case 2 – two antennas emitting through the medium 129
4.3.2.3 Case 3 – three antennas emitting through the medium 133
4.4 Conclusion 136

General conclusion and future work 139

Communication and publication 143

Bibliography 145

Acronyms

1D	One-Dimensional
2D	Two-Dimensional
3D	Three Dimensional
ABC	Absorbing Boundary Conditions
CW	Continuous Waveform
FFT	Fast Fourier Transform
FM	Frequency modulation
FDTD	Finite-Difference Time-Domain
HF	High Frequency
HH	Horizontal-Horizontal
HV	Horizontal-Vertical
IETR	Institute of Electronics and Telecommunications of Rennes
IFT	Inverse Fourier Transform
ISAR	Inverse Synthetic Aperture Radar
LL	Left-Left
LR	Left-Right
MI	Matrix Inversion
NTF	Near-to-Far-field Transformation
PEC	Perfect Electrical Conductor
PML	Perfectly Matched Layers
RADAR	RAdio Detection and Ranging
RCS	Radar Cross Section
RF	Radio Frequency
RL	Right-Left

RR	Right-Right
SNR	Signal-to-Noise Ratio
TE	Transverse Electric
TM	Transverse Magnetic
TR	Time Reversal
TRM	Time Reversal Mirror
UHF	Ultra High Frequency
U.K.	United Kingdom
U.S.	United States
UWB	Ultra Wide Band
VH	Vertical-Horizontal
VHF	Very High Frequency
VV	Vertical-Vertical

List of Tables

Table 1.1 Radar frequency bands [6] 9

Table 1.2 Polarization cases 25

Table 2.1 Random medium - focal spot dimensions for different apertures of TRM 71

Table 2.2 Free space - focal spot dimensions for different apertures of TRM 72

Table 3.1 First trial - The number of rods and the distances between them 79

Table 3.2 Second trial - The number of rods and the distances between them 81

Table 3.3 Third trial - The number of rods and the distances between them 83

List of Figures

Figure 1 La configuration de simulation: a) le premières deux étapes; b) la troisième étape xxi
Figure 2 La reconstruction de la surface scannée – Retournement temporel xxi
Figure 3 Les lobes secondaires – Retournement temporel xxii
Figure 4 La reconstruction de la surface scannée – Inversion matricielle xxiii
Figure 5 Les lobes secondaires – Inversion matricielle xxiii
Figure 6 La configuration de mesure : a) la première étape ; b) la deuxième étape xxv
Figure 7 Detection de la position du triedre : a) $x3{\sim}300\ mm$; b) $x5{\sim}500\ mm$; c) $x6{\sim}600\ mm$; d) $x7{\sim}700\ mm$; e) $x9{\sim}900\ mm$; xxvii
Figure 1.1 Radar working principle 7
Figure 1.2 Monostatic radar: 11
Figure 1.3 Bistatic radar 12
Figure 1.4 Forward scatter radar 12
Figure 1.5 Normalized RSC of a metallic sphere over the three scattering regimes 13
Figure 1.6 Square plate 17
Figure 1.7 Simulated monostatic RCS of a flat square plate 17
Figure 1.8 Circular plate 18
Figure 1.9 Simulated monostatic RCS of a flat circular plate 18
Figure 1.10 Dihedral reflector 19
Figure 1.11 Simulated monostatic RCS of a dihedral reflector 19
Figure 1.12 Rectangular trihedral reflector 20
Figure 1.13 Simulated monostatic RCS of a rectangular trihedral reflector 20
Figure 1.14 Circular trihedral reflector 21
Figure 1.15 Simulated monostatic RCS of a circular trihedral reflector 21
Figure 1.16 Triangular trihedral reflector 22
Figure 1.17 Simulated monostatic RCS of a triangular trihedral reflector 23
Figure 1.18 SOLANGE indoor RCS range [19] 26
Figure 1.19 CHEOPS anechoic chamber 26
Figure 1.20 Anechoic room schematic – top view 27
Figure 1.21 Tapered anechoic room schematic – top view 28
Figure 1.22 Range profile [24] 30

Figure 1.23 Range profile of a model airplane [24] 31
Figure 1.24 Cross-range profile [24] 32
Figure 1.25 Cross range profile of a model airplane [24] 33
Figure 1.26 Geometry for monostatic ISAR imaging [24] 34
Figure 2.1 Time reversal process using time reversal cavity: - first step 43
Figure 2.2 Time reversal process using time reversal cavity: - second step 44
Figure 2.3 Time reversal process using time reversal mirror: - first step 45
Figure 2.4 Time reversal process using time reversal mirror: - second step 45
Figure 2.5 Time reversal process using a random medium: - first step 46
Figure 2.6 Time reversal process using a random medium: - second step 47
Figure 2.7 The aperture of TRM in homogeneous medium 47
Figure 2.8 The virtual aperture of TRM using a random medium 48
Figure 2.9 Example of time signal registered on TRM 48
Figure 2.10 Waveguide experiment schematic 49
Figure 2.11 Waveguide - temporal signals [45]: 50
Figure 2.12 Directivity pattern [45] 50
Figure 2.13 The principle of mirrors 50
Figure 2.14 Chaotic cavity experimental setup 51
Figure 2.15 Chaotic cavity - time signals [41]: 52
Figure 2.16 Time reversal process using electromagnetic time reversal cavity: first step . 56
Figure 2.17 Time reversal process using electromagnetic time reversal cavity: second step 57
Figure 2.18 Reverberation chamber at IETR research laboratory 58
Figure 2.19 Time signals corresponding to measurement steps [55] 59
Figure 2.20 Total efficiency [55] 60
Figure 2.21 Principle of a $1 \times N$ passive beamformer [61] 61
Figure 2.22 Experimental 1×4 beamformer [61] 62
Figure 2.23 Radiation pattern [61] 63
Figure 2.24 a) Radar imaging setup; b) radar imaging using TR beamformer [61] 63
Figure 2.25 FDTD simulation setup: a) first step; b) second step 66
Figure 2.26 Emitted pulse 66
Figure 2.27 First step of time reversal FDTD simulation: a) emitting source; 67
Figure 2.28 Time signal recorded on TRM 67
Figure 2.29 Second step of time reversal FDTD simulation: 68

Figure 2.30 Time signal recorded on source location 69
Figure 2.31 3D focal spot 70
Figure 2.32 2D focal spot 70
Figure 2.33 Focal spot dimensions – 61 elements TRM: 70
Figure 2.34 Focal spot dimensions – 1 element TRM in free space 72
Figure 2.35 Focal spot dimensions – 11 elements TRM 72
Figure 2.36 FDTD simulation setup: a) first step; b) second step 73
Figure 2.37 Multiple foci 73
Figure 2.38 Merged foci: a) one wide focus; b) three wide foci; c) three merged foci in different planes 74
Figure 3.1 Microwave imaging hardware system schematic 78
Figure 3.2 Test configuration 80
Figure 3.3 First trial - Electric field surface for distances: a) 10 mm; b) 25 mm; c) 50 mm; d) 100 mm; e) 125 mm; f) 150 mm; 80
Figure 3.4 First trial - Electric field transmitted and backscattered for distances: a) 10 mm; b) 25 mm; c) 50 mm; d) 100 mm; e) 125 mm; f) 150 mm; 81
Figure 3.5 Second trial - Electric field surface for distances: a) 10 mm; b) 25 mm; c) 50 mm; d) 100 mm; e) 125 mm; f) 150 mm; 82
Figure 3.6 Second trial - Electric field transmitted and backscattered for distances: a) 10 mm; b) 25 mm; c) 50 mm; d) 100 mm; e) 125 mm; f) 150 mm; 83
Figure 3.7 Third trial - Electric field surface for distances: a) 10 mm; b) 25 mm; c) 50 mm; d) 100 mm; e) 125 mm; f) 150 mm; 84
Figure 3.8 Third trial - Electric field transmitted and backscattered for distances: a) 10 mm; b) 25 mm; c) 50 mm; d) 100 mm; e) 125 mm; f) 150 mm; 85
Figure 3.9 2D Time reversal configuration 86
Figure 3.10 Surface electric field plot 86
Figure 3.11 Electric field amplitude versus frequency 87
Figure 3.12 Time signal on TRM 87
Figure 3.13 Spatial correlation function 88
Figure 3.14 Spectral correlation function 90
Figure 3.15 First 2D simulation setup: 91
Figure 3.16 Reconstruction of scanned area using TR method – Setup A 92
Figure 3.17 Sidelobes amplitude using TR method – Setup A 93

Figure 3.18 Distribution of singular values of matrix H 94
Figure 3.19 SNR 95
Figure 3.20 Reconstruction of scanned area using MI method – Setup A 96
Figure 3.21 Sidelobes amplitude using MI method – Setup A 96
Figure 3.22 Second 2D simulation setup: 97
Figure 3.23 Reconstruction of scanned area using TR method – Setup B 98
Figure 3.24 Sidelobes amplitude using TR method – Setup B 99
Figure 3.25 Reconstruction of scanned area using MI method – Setup B 99
Figure 3.26 Sidelobes amplitude using MI method – Setup B 99
Figure 3.27 Scanning configuration: a) version 1; b) version 2; c) version 3 100
Figure 3.28 DUT configuration: a) version 1; b) version 2; c) version 3 100
Figure 3.29 Electric field amplitude versus frequency: a) version 1; b) version 2; c) version 3 101
Figure 3.30 Spectral correlation function: a) version 1; b) version 2; c) version 3 102
Figure 3.31 Reconstruction of scanned area using TR method: 104
Figure 3.32 Sidelobes amplitude using TR method: 105
Figure 3.33 Distribution of singular values of matrix H 106
Figure 3.34 Reconstruction of scanned area using MI method: 107
Figure 3.35 Sidelobes amplitude using MI method: 108
Figure 4.1 Fabricated medium parts schematic 111
Figure 4.2 Fabricated random medium schematic 112
Figure 4.3 Fabricated random medium: a) top view; b) side view 113
Figure 4.4 Measurement setup: 114
Figure 4.5 S parameters at central frequency: a) $S31r$; b) $S32r$ 115
Figure 4.6 Schematic setup: 116
Figure 4.7 Reconstructed area: 117
Figure 4.8 Reconstruction of area F using MI method – Measurement setup: 119
Figure 4.9 Sidelobes amplitude MI vs TR method: 121
Figure 4.10 Multiple antennas measurement setup: 122
Figure 4.11 Multiple antennas schematic setup: 123
Figure 4.12 Reconstructed area: 124
Figure 4.13 Multiple antennas schematic - case 1: 125
Figure 4.14 Reconstruction of area F using TR method – Multiple antennas measurement setup: a) case 1.1; b) case 1.2; c) case 1.3 126

Figure 4.15 Reconstruction of area F using MI method – Multiple antennas measurement setup: a) case 1.1; b) case 1.2; c) case 1.3 127
Figure 4.16 Sidelobes amplitude MI vs TR method – Multiple antennas measurement setup: a) case 1.1; b) case 1.2; c) case 1.3 128
Figure 4.17 Multiple antennas schematic - case 2: 129
Figure 4.18 Reconstruction of area F using TR method – Multiple antennas measurement setup: a) case 2.1; b) case 2.2; c) case 2.3 130
Figure 4.19 Reconstruction of area F using MI method – Multiple antennas measurement setup: a) case 2.1; b) case 2.2; c) case 2.3 131
Figure 4.20 Sidelobes amplitude MI vs. TR method – Multiple antennas measurement setup: a) case 2.1; b) case 2.2; c) case 2.3 132
Figure 4.21 Multiple antennas schematic: Case 3 133
Figure 4.22 Reconstruction of area F using TR method – Multiple antennas measurement setup: Case 3 133
Figure 4.23 Reconstruction of area F using MI method – Multiple antennas measurement setup: Case 3 134
Figure 4.24 Sidelobes amplitude MI vs. TR method – Multiple antennas measurement setup: Case 3 134
Figure 4.25 Comparison for the three cases - TR method: a) amplitude; b) sidelobes 135
Figure 4.26 Comparison for the three cases - MI method: a) amplitude; b) sidelobes..... 135
Figure 4.27 Comparison between coherent and incoherent sum of images - TR method: a) TR method; b) MI method 136

Résumé

Les mesures utilisées actuellement en chambres anéchoïque, pour la caractérisation de la surface équivalente radar (SER) des antennes ou des objets sont généralement perturbées, en particulier en basse fréquence lorsque les longueurs d'onde sont supérieures au mètre. L'épaisseur des matériaux absorbants devient faible devant la longueur d'onde et ceux-ci ne peuvent plus être considérés comme parfaitement absorbants. Les parois de la chambre (murs, plafond, sol) qui sont illuminées génèrent des trajets multiples. Dans ce cas, le champ total incident sur la cible sous test est la somme du champ incident direct et des champs réfléchis par les parois.

Ce résume de la thèse présente une nouvelle technique d'illumination permettant de focaliser le champ incident sur la zone utile occupée par la cible. Nous présentons la méthodologie utilisée et la configuration proposée en simulations. L'analyse des résultats expérimentaux est aussi réalisée.

La méthode se base sur le principe de retournement temporel (RT) qui permet de focaliser spatialement et temporellement une onde électromagnétique. Dans une première phase d'enregistrement, une source émet un signal très bref qui est diffusé à travers un milieu dispersif. Le signal est enregistré sur un réseau d'antennes, le miroir à retournement temporel (MRT). Puis, les signaux inversés temporellement sont réémis afin de focaliser l'onde à la position de la source initiale.

Un signal à large bande transmis à travers un milieu complexe s'étale sur un temps beaucoup plus long que la durée du signal incident du fait de la propagation multi-trajets dans le milieu. Du fait de la diffusion multiple des ondes, le signal aux temps longs semble complètement aléatoire. Néanmoins, l'onde ne perd pas sa cohérence. L'information spatiale donnée par les temps longs fournit une grande diversité spatiale qui est exploitée pour focaliser les ondes avec une résolution fine dans la deuxième phase du retournement temporel. L'intensité focalisée est la somme de l'intensité directe et l'intensité diffuse qui décroit en fonction de la distance parcourue à travers le milieu diffusant.

La performance de focalisation du RT à travers un milieu complexe peut être caractérisée par le rapport entre l'amplitude du signal focalisé et l'amplitude des lobes secondaires. Ce rapport est égal au nombre de degrés de liberté spatio-temporels.

Considérons la transmission à travers un milieu aléatoire de longueur L qui peut être caractérisé par le libre parcours moyen ℓ. Le libre parcours moyen est lié au coefficient de

diffusion du milieu par $D = V_E \ell / d$, où V_E est la vitesse de transport des ondes et d la dimension du milieu. La transformée de Fourier de la réponse impulsionnelle de la source à un élément du MRT peut s'écrire comme :

$$H(\omega) = \langle H(\omega) \rangle + N(\omega) \tag{1}$$

où $\langle H(\omega) \rangle$ correspond à la réponse impulsionnelle cohérente et $N(\omega)$ donne l'apport de la partie incohérente. Les contributions de ces termes sont alors donnés par:

$$|\langle H(\omega) \rangle|^2 = e^{-\frac{L}{\ell}} \tag{2}$$

$$\langle |N(\omega)|^2 \rangle \cong \frac{\ell}{L} \tag{3}$$

Si $L \gg \ell$, le signal est dominé par la contribution incohérente et la taille de la tache focale ne dépend plus de l'ouverture du réseau d'antennes émettrices mais de l'ouverture du milieu diffusant. Pour des signaux large-bande, il est ainsi possible de focaliser les ondes en utilisant un unique élément du MRT.

Le milieu complexe à deux dimensions proposé en simulations est une forêt de tiges métalliques de diamètre $d = 10\ mm$. La bande de fréquence considérée est comprise entre 5 et 7 GHz. La largeur du milieu est de 20λ et la longueur est de 10λ pour la fréquence centrale de 6 GHz. La distance minimale entre les tiges est de 0.5 λ.

La configuration du milieu est présentée sur la Figure 1. Deux port en émission/réception (P_1 et P_2) sont considérées. La simulation se déroule en trois étapes. Dans les deux premières étapes les champs électriques correspondant à une émission par P_1 puis P_2, notés $E_1(r, \omega)$ et $E_2(r, \omega)$ sont enregistrés sur une surface de $1000\ mm$ par $300\ mm$ devant le milieu. De plus, la transmission entre les deux ports, $S_{21}^{wo}(\omega)$ sans cible est enregistrée.

Dans la troisième étape de simulation, une sphère métallique, est ajoutée à l'intérieur de la surface scannée précédemment et nous enregistrons la transmission entre les deux ports, $S_{21}^{w}(\omega)$ avec la cible. La différence entre les deux paramètres enregistrés $S_{21}^{wo}(\omega)$ et $S_{21}^{w}(\omega)$ donne le paramètre contenant la rétrodiffusion de la cible, en présence du milieu.

En supposant que le coefficient de diffusion de la cible est indépendant de la fréquence $\sigma(\omega, r) = \sigma(r)$, le paramètre $S_{21} = S_{21}^{w}(\omega)$ -$S_{21}^{wo}(\omega)$ peut être écrit sous l'approximation de Born comme :

$$S_{21}(\omega) = \int_{\Omega} E_1(r, \omega) \cdot E_2(r, \omega) \cdot \sigma(r)\, d^2 r \tag{4}$$

La configuration pour les trois étapes de simulation est présentée sur la Figure 1.

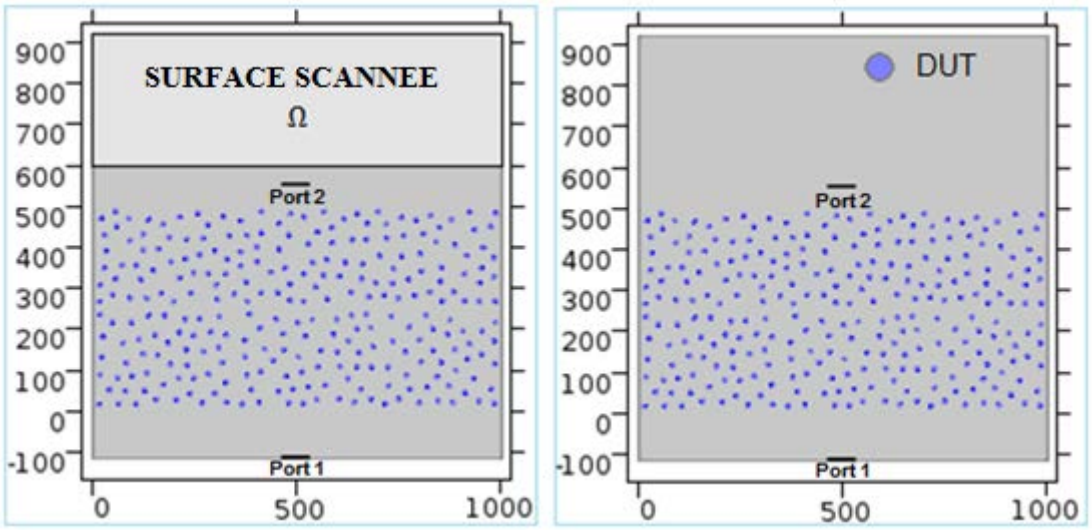

a) b)

Figure 1 La configuration de simulation: a) le premières deux étapes; b) la troisième étape

Nous utilisons d'abord une méthode de RT pour imager la cible. Le signal focalisé est obtenu par convolution dans le domaine temporel, qui devient dans le domaine fréquentiel une multiplication de $S_{12}^{*}(\omega)$ par le produit des deux champs électriques enregistrés sur la surface scannées pour chaque port. Pour chaque position scannée dans les deux premières étapes, on exprime l'‟image par:

$$I(r) = \left| \int S_{21}^{*}(\omega) E_1(r,\omega) E_2(r,\omega)\, d\omega \right|^2 \qquad (5)$$

Les équations (4) et (5) montrent que pour une cible ponctuelle située à la position r_0, les interférences constructives des fréquences dans la bande passante donnent une forte intensité à cette position. Au contraire, pour les positions $r \neq r_0$, les interférences doivent être destructives. La reconstruction de la surface scannée pour la troisième étape de simulation est présentée sur la Figure 2.

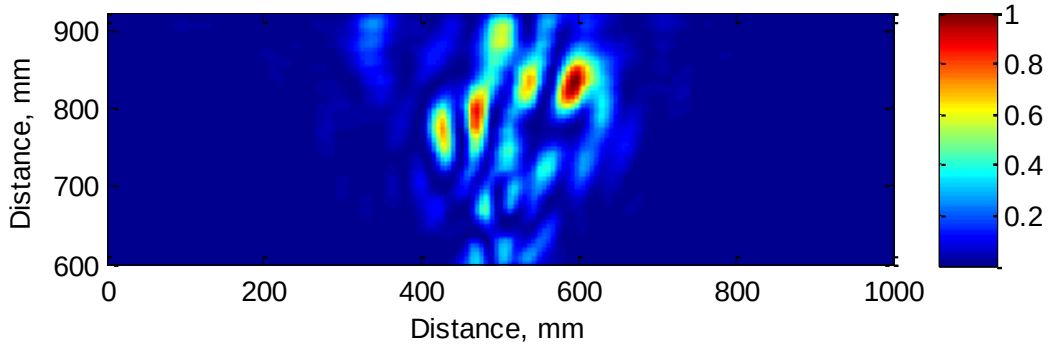

Figure 2 La reconstruction de la surface scannée – Retournement temporel

La cible, une sphère métallique ajoutée à l'intérieur de la surface scannée est détectée et localisée à la position ($x = 600\ mm,\ y = 830\ mm$). Des lobes latéraux sont observés dans cette configuration lors de la focalisation du signal sur la position de la cible. La Figure 3 montre l'amplitude des lobes secondaires.

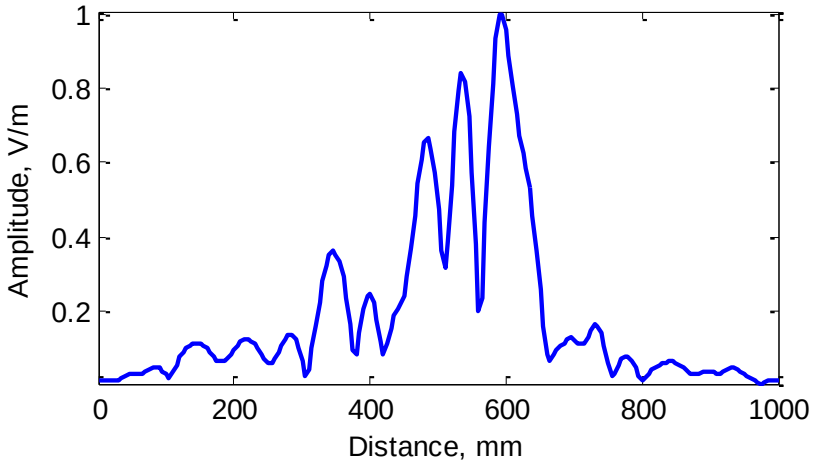

Figure 3 Les lobes secondaires – Retournement temporel

La présence de la cible est détectée à la position $x = 600\ mm$. Les lobs secondaires peuvent être observés sur les positions adjacentes sur l'abscisse.

Puisque les lobes latéraux sont inhérents à la méthode de retournement temporel, nous utilisons une méthode basée sur une inversion matricielle qui fournit des lobes secondaires plus faible.

En supposant que le coefficient de rétrodiffusion de la cible dépend à peine de la fréquence sur la gamme de fréquences utilisés et afin d'améliorer la détection, nous écrivons l'équation (4) sous une forme matricielle :

$$S_{21} = H\sigma \tag{6}$$

La matrice H est le produit des deux champs électriques enregistrés : $H_{ij} = E_1(r_j, \omega_i)E_2(r_j, \omega_i)$. Dans cette équation, pour trouver l'inconnue, σ, il est nécessaire d'inverser la matrice H :

$$\sigma = H^{-1}S_{21} \tag{7}$$

L'inversion de la matrice H necesite une décomposition en valeur singulières (SVD), $H = USV^{\dagger}$. U et $V^{\dagger}$ sont les matrices des valeurs singulières orthonormées. S est une matrice diagonale contenant les valeurs singulières de la matrice H. L'expression de la matrice inverse est donnée par :

$$H^{-1} = VS^{-1}U^{\dagger} \tag{8}$$

Néanmoins dans ce cas, un poids significatif est donné aux valeurs singulières faibles et la procédure d'inversion peut devenir instable en présence de bruit.

Une méthode de régularisation doit ainsi être appliquée. Nous appliquons la méthode de la SVD tronquée en rejetant les plus petites valeurs singulières. Une autre méthode de régularisation est la régularisation de Tikhonov. Dans ce cas, l'image est estimée par :

$$\tilde{\sigma} = (H^{\dagger}H + \mu I)^{-1}H^{\dagger}S_{21} \tag{9}$$

où $\mu \geq 0$, est le paramètre de régularisation et I est la matrice identité.

La Figure 4 présente la reconstruction de la surface scannée pour la troisième étape de simulation.

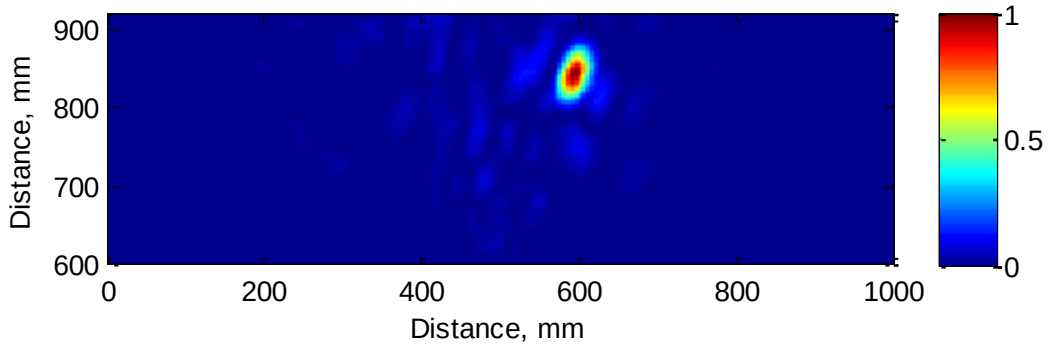

Figure 4 La reconstruction de la surface scannée – Inversion matricielle

La cible est détectée et localisée et les lobes secondaires ont été fortement atténués par rapport à la méthode du retournement temporel. La Figure 5 montre l'amplitude des lobes secondaires.

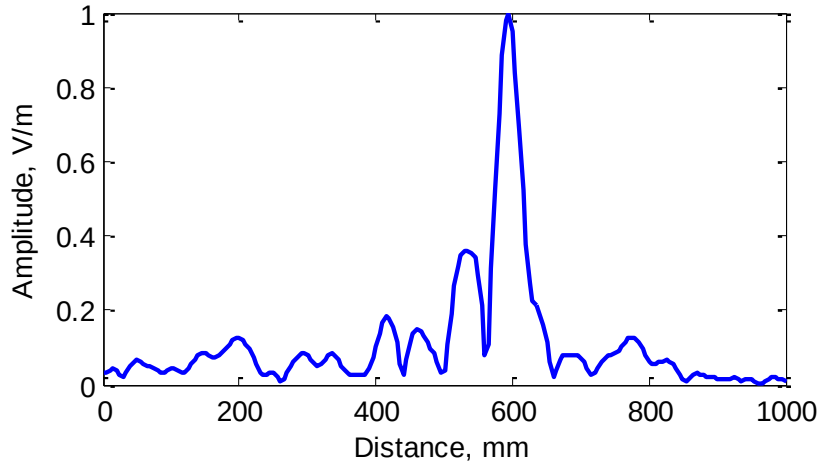

Figure 5 Les lobes secondaires – Inversion matricielle

La présence de la cible est détectée à la position $x = 600\ mm$. Une nette amélioration des lobes secondaires peut être observée.

La configuration de mesure est similaire à la configuration de simulation. Le milieu est encadré par deux antennes cornet A_1 et A_2 derrière et devant le milieu. Une troisième antenne omnidirectionnelle et large bande est utilisée pour scanner le champ sur une ligne. La longueur de la ligne scannée est d'un mètre et les paramètres S sont enregistrés sur 100 positions de 10 à 10 mm.

Les caractéristiques physiques de milieu sont les mêmes. Les tiges d'acier ont un diamètre d = 10 mm. La largeur du milieu est de 20λ et la longueur est de 10λ pour la fréquence centrale de 6 GHz. La distance minimale entre les tiges est de 0.5 λ. La hauteur des tiges $H = 400\ mm$ est bien supérieure à λ afin de se positionner dans une configuration quasi-2D.

Les mesures seront effectuées en deux étapes. Dans la première étape, l'antenne A_3 scanne le champ devant le milieu diffusant sur une ligne, tandis que les antennes A_1 et A_2 sont en émission. Pour chaque position de A_3, tous les paramètres S sont enregistrés. La transmission entre les deux antennes A_1 et A_2, le paramètre $S_{12}^{wo}(\omega)$ sans cible est aussi enregistrée. Dans la deuxième étape de la configuration de mesures, la troisième antenne est remplacée par la cible, dans ce cas, un trièdre. La cible est déplacée sur 10 positions de 100 à 100 mm afin de vérifier la concordance des positions estimées et des positions réelles. La transmission entre les deux antennes A_1 et A_2, le paramètre $S_{12}^{w}(\omega)$ avec la cible est enregistrée. La différence entre les deux paramètres enregistrés donne le paramètre contenant la rétrodiffusion de la cible.

La configuration pour les deux étapes de mesures est présentée sur la Figure 6.

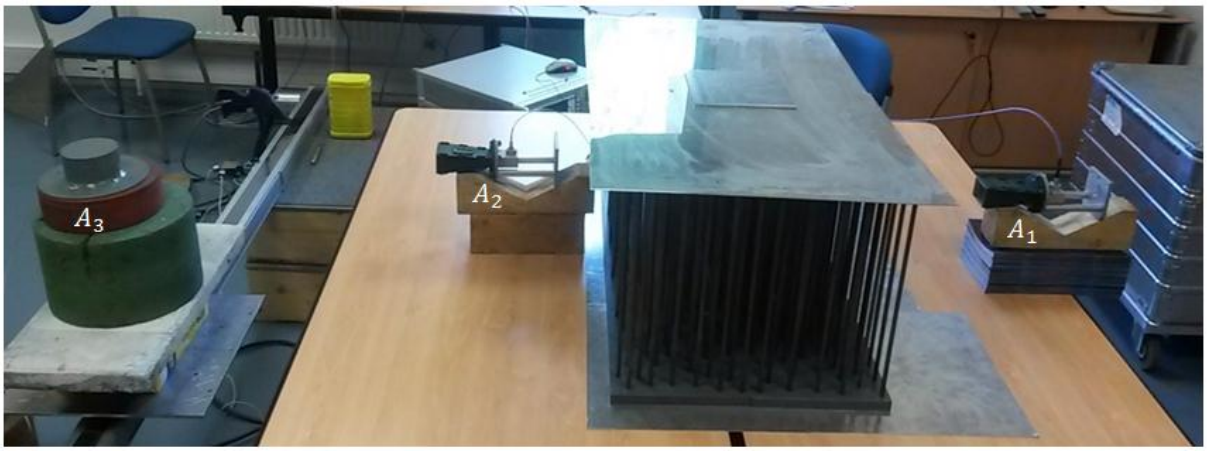

a)

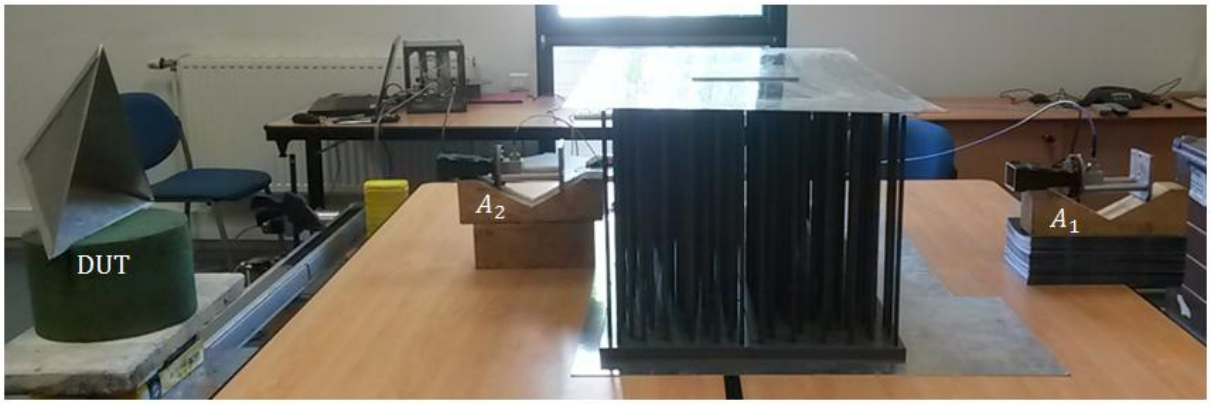

b)

Figure 6 La configuration de mesure : a) la première étape ; b) la deuxième étape

A partir du scan du champ le long d'une ligne, nous pouvons reconstruire le champ émis par les antennes devant et derrière cette ligne afin d'obtenir le champ en toute position de l'espace. La re-propagation du champ scanne sur la ligne est réalisée grâce à la somme cohérente des signaux multiplies par les fonctions de Green 3D :

$$G_{3D}(\mathrm{r},\mathrm{r}') = \frac{\exp(-\mathrm{j}\mathrm{k}|\mathrm{r}-\mathrm{r}'|)}{4\pi|\mathrm{r}-\mathrm{r}'|} \tag{10}$$

où k est le nombre d'onde et $|\mathrm{r}-\mathrm{r}'|$ est la distance de propagation entre la position de l'antenne et la position du champ à reconstruire. La propagation en arrière est obtenue en appliquant les fonctions Green conjuguées.

La détection de la position du trièdre en quelques positions est présentée dans la figure 7. En raison de la directivité limitée de la seconde antenne A_2, la detection de la position de la cible est plus precise pour la partie située à droite du milieu. Néanmoins toutes les positions du trièdre sont reconstruites de façon précise, validant la méthode utilisée.

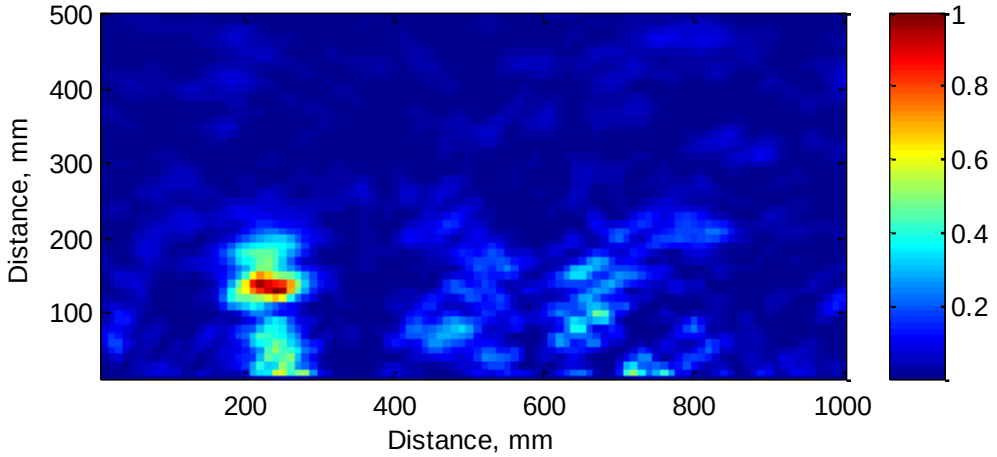

a)

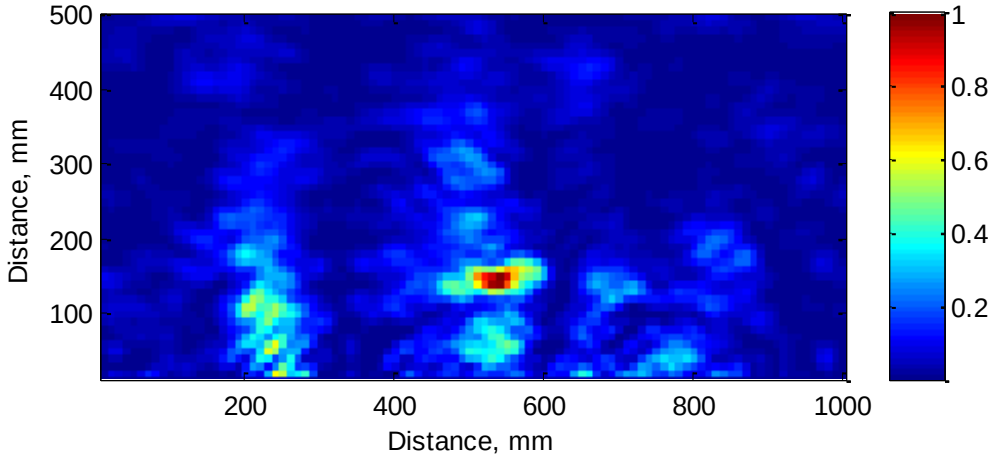
500
400
300
200
100
Distance, mm
200
400
600
800
1000
Distance, mm
1
0.8
0.6
0.4
0.2

b)

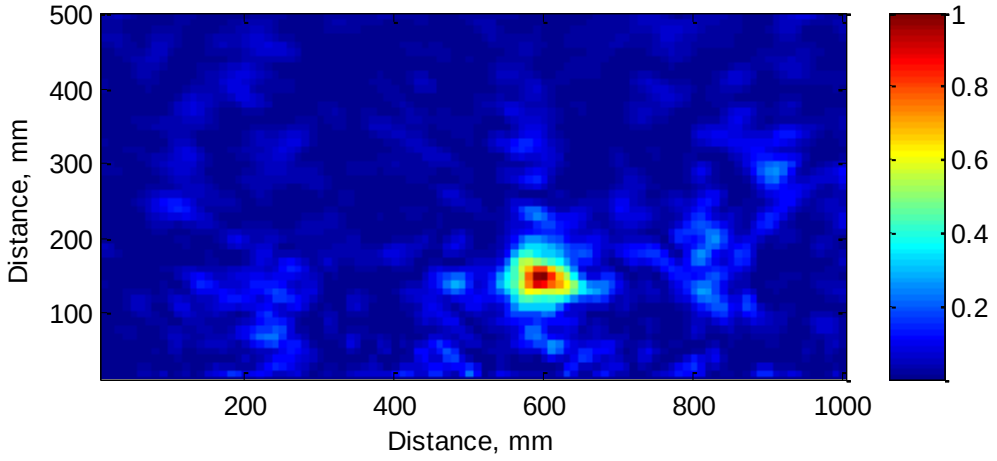
500
400
300
200
100
Distance, mm
200
400
600
800
1000
Distance, mm
1
0.8
0.6
0.4
0.2

c)

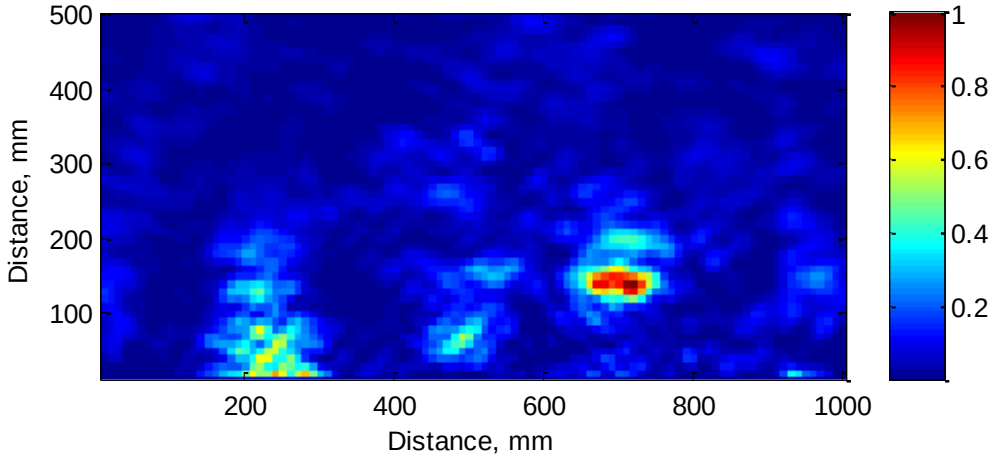
500
400
300
200
100
Distance, mm
200
400
600
800
1000
Distance, mm
1
0.8
0.6
0.4
0.2

d)

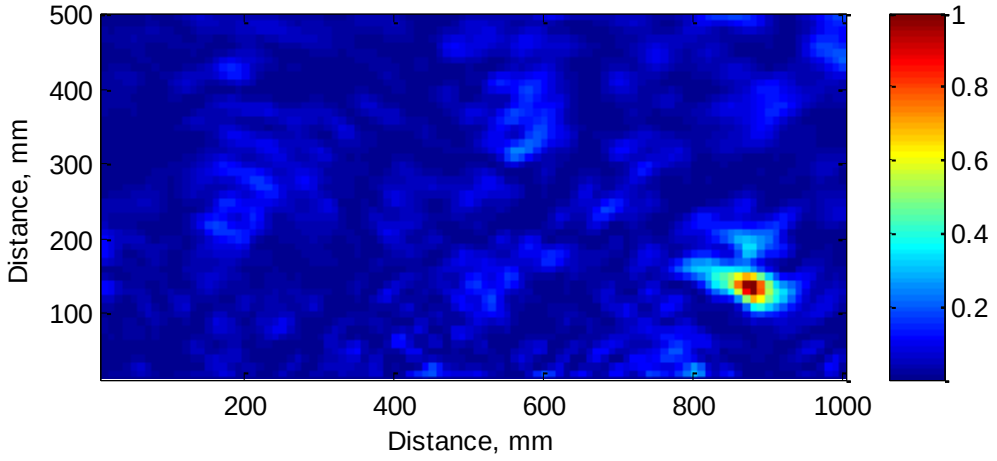

e)

Figure 7 Detection de la position du triedre : a) x_3~300 mm; b) x_5~500 mm; c) x_6~600 mm; d) x_7~700 mm; e) x_9~900 mm;

Cette étude présente une première étape pour une nouvelle méthode de mesure de la SER des objets en appliquant le RT ainsi que la méthode d'inversion matricielle à travers un milieu fortement désordonné. En introduisant un milieu fortement désordonné en chambre anéchoïque, il n'est ainsi plus nécessaire de rendre les parois entièrement absorbantes, principalement aux basses fréquences. Nous profitons ici des degrés de liberté spatio-temporels de la propagation au sein d'un milieu diffusant afin de détecter une cible avec une haute résolution.

Introduction

Radar cross section (RCS) measures the visibility of a target on radars described by the ratio of scattered power density towards the radar to the power density that is intercepted by the target. RCS of a target is influenced by different factors such as the geometry or the material of the target, or the frequency and the polarizations of the transmitter and the receiver. In the measurement process of the RCS, the most important step is the RCS calibration in which metrological reference targets such as flat plates, discs or cylinders may be used. A preferred RSC reference is the trihedral corner reflector which produces a high radar cross section which remains constant over a wide angle. Another important aspect of the RCS measurement process is the requirement of an illuminating radar wave of acceptably uniform amplitude and phase.

As for the measurement facilities, indoor test ranges offer more productive testing. Anechoic chambers are indoor facilities used for testing with an electromagnetic field absorbing wall, creating an electromagnetic-field-free environment. The walls, the floor and ceiling must be covered with high-quality absorbing material and the lower the working frequency, the more expensive the absorber becomes.

At low frequencies, the wavelength becomes greater than the size of the absorbent materials and their ability to absorb the wave without any reflection decreases and the illuminated boundaries generate multipath propagation. Therefore, the incident field on the object under test becomes the sum of the incident wave and the reflected waves from the walls of the chamber, causing perturbations in the measurements results.

One solution to overcome these inconveniences for RCS characterization at low frequencies, may be introducing a random medium within the anechoic chamber to focus the incident wave on the target using the time reversal (TR) method, in order to avoid the reflections from the walls and possibly eliminating the need of providing walls fully absorbent for the anechoic room.

Time reversal is a process which allows spatial and temporal focusing of an electromagnetic wave, taking the multipath propagation to its own advantage. Based on the invariance of the wave equation under a time reversal operation and the spatial reciprocity of the propagation channel, this process can be applied to every phenomenon described by

equations which contain only second-order derivatives with respect to time, such as wave equation. Therefore, for each solution $\Psi(r,t)$, there exist a second solution of the form $\Psi(r,-t)$, because their second derivative are identical.

Time reversal experiments typically consist of two steps. First, a wave field is generated either by a source or by the scattering of an obstacle. This wave field $\Psi_s(r,t)$ propagates through a random medium and is measured at different fixed positions on a time reversal mirror (TRM) as a function of time and stored. Next, the measurements at each position are reversed in time. In the second step, the elements of the TRM are used as sources where the time reversed signals $\Psi_s(r,-t)$ are applied simultaneously. The resulting waves propagate back through the medium and interfere constructively at the position of the original source.

Compared to classical focusing devices, such as lenses, the time reversal mirror presents a major interest which is the relation between the medium complexity and the size of the focal spot which is given by the aperture of the medium. Using complex environments to appear wider than it is, the TRM aperture does not control the quality of the focus. The resolution being independent of the number of elements of the mirror, even with only one element TRM, the quality of focusing should be quite good.

From acoustics to electromagnetics or optics, the applications of time reversal method are various, ranging from telecommunications, biomedical engineering or optical tomography to microwave imaging or radar applications.

Detection and localization of unknown targets is achieved by placing the object under test in an investigation domain confined by measurement probes which receive parts of the scattered field. Using a classic configuration of a time reversal process, by taking advantage of the spectral degrees of freedom provided by the propagation through a random medium, a microwave imaging method is attained.

The subject of the present thesis is to propose an imaging method in the microwave range by taking advantage of the spectral degrees of freedom provided by the propagation through a random medium. Experimentally, the location of a scatterer can be extracted with a high resolution even though only two antennas are used. The ability to image the target is shown using a synthetic time reversal technique and a matrix inversion method.

This work, supported by the *Direction Générale de l'Armement* (DGA) was conducted at the *Institute d'Electronique et de Télécommunication de Rennes* (IETR), with

the *Compact and Ultra small anTEnnas* (CUTE) team of the *Antennes et Dispositifs Hyperfréquences* department (ADH).

The thesis manuscript is organized in four chapters. The first chapter gives a general description of radar systems and radar cross section basic principles presenting RCS behavior for three types of calibration target, a brief description of the target support structures influence on measurements and the measurement facilities, as well as basic ideas on RCS imagery: one-dimensional range profile/cross-range profile and two-dimensional ISAR image.

The second chapter introduces theoretical aspects on time reversal technique, followed by simulations results in FDTD showing the properties of a random medium used in a time reversal process which yields a focus quality that is not dependent on the aperture of the TRM. Using a FDTD method with a PML function to treat the boundaries, 2D simulations are carried out showing also that with multiple sources in a TR process, multiple foci can be obtained on different positions at the same time, or by controlling the distance between the point-like sources a wide focus can be achieved.

The third chapter presents the modeling of a microwave imaging system using a random medium. Conception details regarding the design of the random medium and a few theoretical aspects regarding the characteristics of a random medium used for target detection are given in the beginning. Further it is presented the simulation setup for an imaging method in the microwave range using a random medium. The results are presented for two methods: one based on time reversal technique and another method based on matrix inversion which provides lower sidelobes. As well, inspired from the use of a cavity for microwave imaging, the results of a comparison between simulation setups are presented. Three versions of a chosen simulated setup with different PEC boundaries are compared in order to determine the best results for an imaging method that takes advantage of the spectral degrees of freedom provided by the propagation through a random medium.

The final chapter of the thesis presents the experimental validation of the imaging system using a setup similar with the ones previously presented in simulation, applying both methods based on TR and matrix inversion. Moreover, it is presented a comparison between layouts with an increased number of antennas used to improve the image quality. Comparing the results for the cases of one, two or three antennas used simultaneously, the constructive interferences of their individual contributions, give the best results for the last case.

At the end of the manuscript, are given a general conclusion of the thesis summarizing the obtained results and future work.

CHAPTER 1 Radar cross section principles

1.1 Introduction

Radar cross section (RCS) is the measure of an object‟s ability to reflect radar signals in the direction of the radar. It is a measure of the ratio of scattered power density towards the radar to the power density that is intercepted by the target. There are different factors that influence the RCS: the geometry of the target, the materials, the working frequency, the transmitter and receiver polarizations and the directions of the radar transmitter and receiver.

The purpose of this chapter is to present a short overview of radar basic definitions and radar cross section fundamentals, measurement facilities, instrumentation and RCS imagery.

1.2 Radar basic definitions

1.2.1 History of radar

The origins of the basic idea of radar are found in the classical experiments on electromagnetic radiation conducted by the physicist Heinrich Hertz during the late 1880s, when he set out to experimentally verify the earlier theoretical work of the physicist James Clerk Maxwell. By developing the general equations of the electromagnetic field, Maxwell‟s work led to the conclusion that radio waves can be reflected from metallic objects and refracted by a dielectric medium, just as light waves.

Based on the theory demonstrated by Hertz, a first prototype named “Telemobiloskop” was patented in 1904 by Christian Hülsmeyer [1]. The working principle of the device was based on the concept of reflected waves by metallic surfaces. The wave emitted by an antenna, hits a metallic object and is partly reflected back, towards several antennas which were serving as receivers. Hülsmeyer‟s invention did not draw attention since there was no need for the radar until the 1930s when long-range military bombers were developed and brought the interest of detecting the approach of hostile aircrafts.

Radar was developed in the period before and during World War II by several nations: United Kingdom, France, Germany, Italy, Japan, Netherlands, the Soviet Union and the United States. In 1934, following systematics studies, France began developing an obstacle-locating radio apparatus. By the end of the year, the first full radar evolved as a pulsed

system, was demonstrated in U.S. The next year, Germany and U.K demonstrated such elementary apparatus.

After the war, the progress in radar technology slowed considerably. The last half of the 1940s was dedicated to developments initiated during the war. Two of these were the monopulse tracking radar and the moving-target indication radar. Many years of development were necessary to bring these radar techniques to full capability.

New and better radar systems emerged during the 1950s, like the high-powered radars designed to operate at 220 MHz and 450 MHz. Being equipped with large mechanically rotating antennas, it could reliably detect aircraft at very long ranges. Synthetic aperture radar first appeared in this decade, but it took almost 30 more years to reach a high state of development.

Furthermore, serious applications of the Doppler principle to radar started to advance becoming vital in the operation of many radar systems. The Doppler frequency shift of the reflected signal resulted from the relative motion between the target and the radar is indispensable in continuous wave and pulse radar, used to detect moving targets in the presence of large clutter echoes.

As the digital age arose in the 1970s, the signal and data processing required for modern radars was made practical. Radar methods evolved over the next decade, to a point where radars were able to distinguish one type of target to another. In the 1990s, due to continued advances in computer technology, increased information about the nature of targets was available [2].

The 21st century brought advances in digital technology which sparked further improvement in signal and data processing with the goal of developing nearly all-digital phased-array radars.

1.2.2 Introduction to radar systems

The term RADAR was conceived in 1940 as an acronym for RAdio Detection and Ranging [3], but later on the term has entered English and other languages as a common noun and lost the capitalization.

As the name implies, radar is an electromagnetic system used for the detection and location of objects such as aircrafts, ships, vehicles or terrain. By transmitting a particular type of wave form, for example a pulse-modulated sine wave, the radar detects a target and

from the nature of the echo signal, identifies the distance, range, altitude, direction or speed of the target.

An elementary form of radar consists of a transmitting antenna emitting electromagnetic radiation, a receiving antenna and an energy-detecting device. The target intercepts a part of the transmitted signal and reradiates it in all directions.

The prime interest to the monostatic radar is the energy radiated backwards in the direction of the radar. The receiving antenna collects the returned energy and delivered it to a receiver, where it is processed to detect the presence of the target and to extract its location and relative velocity.

Figure 1.1 presents the working principle of a radar system.

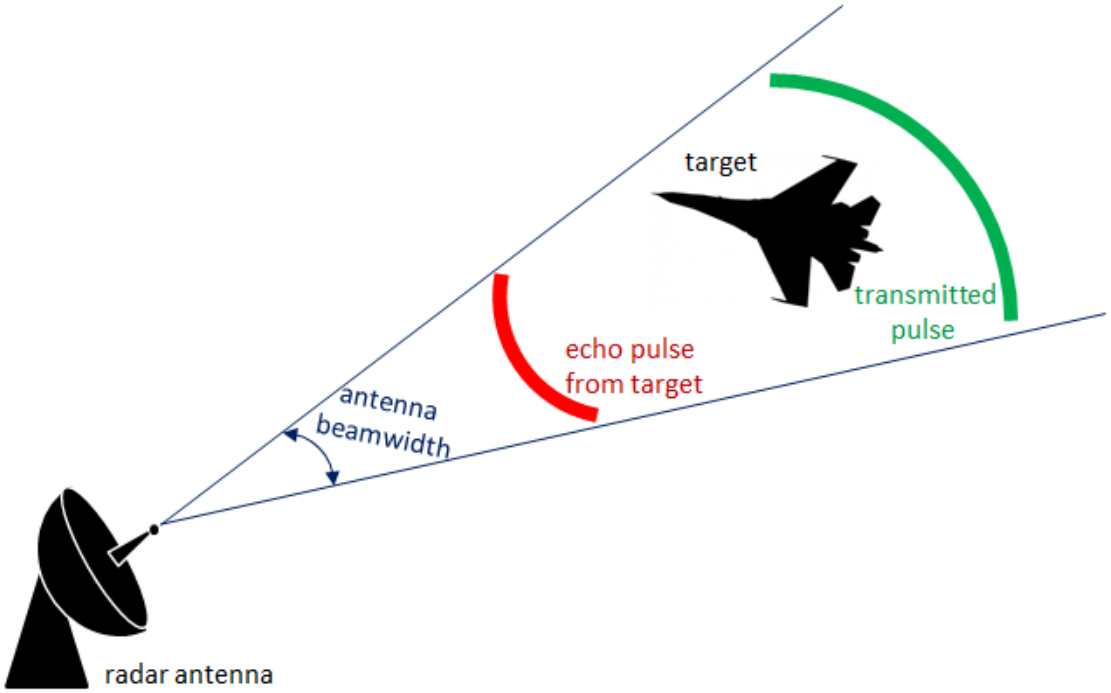

Figure 1.1 Radar working principle

The distance to the target is determined by measuring the time T_R, taken by the signal to travel from the emitting antenna to the target and back. Since electromagnetic waves propagate at the speed of light $c = 3e8\ m/s$, the range R is expressed:

$$R = \frac{cT_R}{2} \tag{1.1}$$

The direction of the target may be determined from the direction of arrival of the reflected wave-front. The usual method of measuring the direction of arrival is by using narrow beam antennas. To distinguish moving targets from stationary objects, the relative

motion between the target and the radar, which is represented in a shift in the carrier frequency of the reflected wave known as Doppler effect, is used as a measure of target‟s relative velocity.

A sufficient length of time must elapse after the transmitted pulse is emitted by the radar, to allow any echo signals to return and be detected before the next pulse may be transmitted. Otherwise, ambiguities in range measurements might result, if echo signals from some targets might arrive after the transmission of the next pulse. Echoes that arrive after the transmission of the next pulse are called second-time-around echoes. Such an echo would appear to be at a much shorter range and could be misleading if it were not known as a second-time-around echo [4].

There are different suitable modulations that can be used. However, the typical radar transmits a simple pulse-modulated waveform. The pulse carrier might be frequency or phase modulated to permit echo signals to be compressed in time after reception, achieving the benefits of high-range resolution without the need to resort to a short pulse. By taking advantage of the Doppler frequency shift to separate the received echo from the transmitted signal and the echoes from the clutter, continuous waveforms (CW) can also be used.

CW radars typically use separate transmit and receive antennas because it is not usually possible to receive with full sensitivity through an antenna while it is transmitting a high power signal [5].

Radars operate in the RF band of the electromagnetic spectrum between 5 MHz and 300 GHz. Table 1.1 lists the radar frequency bands and applications:

Band Designation	Frequency range	Wavelength	Typical application
HF	3 – 30 MHz	100 – 10 m	Observation: over the horizon radar
VHF	30 – 300 MHz	10 – 1 m	Very long range surveillance Ground penetration radar
UHF	300 – 1000 MHz	100 – 30 cm	Very long range surveillance Foliage penetration
L	1 – 2 GHz	30 – 15 cm	Long range surveillance
S	2 – 4 GHz	15 – 7.5 cm	Medium range surveillance Air traffic control
C	4 – 8 GHz	7.5 – 3.75 cm	Long range tracking Shooting and missile guidance Air traffic control Airborne altimeter

X	8 – 12 GHz	3.75 – 2.5 cm	Combat aircraft radar Short range tracking Long range ground surveillance Airborne weather radar Marine radar police radar
Ku	12 – 18 GHz	2.5 – 1.67 cm	Guidance High resolution mapping Airborne altimeter Medium range ground surveillance
K	18 – 27 GHz	1.67 – 1.11 cm	Police radar
Ka	27 – 40 GHz	1.11 – 0.75 cm	Short range ground surveillance Targeting Imaging
V	40 – 75 GHz	75 – 40 mm	Automotive anti-collision
W	75 – 110 GHz	40 – 27 mm	Imaging Automotive anti-collision Airborne wire detection
mm	110 – 300 GHz	27 – 1 mm	Imaging

Table 1.1 Radar frequency bands [6]

Low-frequency radars require large antennas and have limitations on resolution because fine resolution implies large instantaneous bandwidth of the transmit signal. The bandwidth could represent a significant percentage of transmit frequency and may cause problems with the transmitter and receiver design.

1.2.3 Radar equation

The radar equation relates the range of a radar target to the characteristics of the transmitter, receiver, antenna, target and environment, representing a basis for radar design. In monostatic, the received power can be expressed as:

$$P_r = \frac{P_t G^2 \lambda^2 \sigma}{(4\pi)^3 R^4} \tag{1.2}$$

where, σ is the radar cross section which is a measure of the equivalent or radio-electric size of the target, as seen by the radar, having units of area; P_t is the power radiated by the transmitter; G is the gain of the transmitting and receiving antennas; λ is the wavelength and R is the distance between the radar and the target.

An important use of the radar range equation is the determination of detection range, or the maximum range at which a target has a given probability of being detected by radar.

The radar equation can be written under the following form which gives the maximum radar range:

$$R_{max} = \sqrt[4]{\frac{P_t\, G^2\, \lambda^2\, \sigma}{(4\pi)^3 P_{min}}} \tag{1.3}$$

where, P_{min} is the minimum detectable power.

One other form of the basic radar equation takes into account the noise. Considering the bandwidth, B of the receiver, the ambient temperature expressed in degrees Kelvin, T_0, and the noise contribution of the receiver, F, the noise power at the output can be written as:

$$P_N = kT_0BF \tag{1.4}$$

where k is Boltzman‟s constant.

In this case, the minimum detectable power is expressed as a function of the noise level:

$$P_{min} = kT_0BF\frac{S}{N} \tag{1.5}$$

where $\frac{S}{N}$ represents the signal to noise ratio.

Taking into consideration a factor, L, representing all the losses, for example from the transmission lines or feeders, the radar range equation becomes:

$$R_{max} = \sqrt[4]{\frac{P_t G^2 \lambda^2\, \sigma}{(4\pi)^3 kT_0BF\frac{S}{N}L}} \tag{1.6}$$

A multitude of factors can degrade radar performance. These factors include those related to radar itself, the environment in which the radar operates the operator of the radar and often, the inexperience of the radar analyst.

1.3 Radar cross section fundamentals

1.3.1 Radar cross section determination

Radar cross section is a measure of the power scattered in a given direction when a target is illuminated by a plane wave. According to IEEE dictionary of standards terms [7], RCS is defined as 4π times the ratio of the power per unit solid angle scattered toward the radar receiver with the power density of the plane wave incident on the scatterer. More

precisely, it is the limit of that ratio as the distance from the scatterer to the point where the scattered power is measured, R, approaches infinity.

Considering E_{inc} the field incident on the target and E_{scat}, the field scattered by the target, the radar cross section, σ is expressed:

$$\sigma = \lim_{R\to\infty} 4\pi R^2 \frac{|E_{scat}|^2}{|E_{inc}|^2} \tag{1.7}$$

RCS is a function of multiple parameters, such as: the positions of transmitter and receiver relative to the target, the angular orientation of the target relative to transmitter and receiver, the polarization of transmitter and receiver, the target geometry and material composition and the frequency or wavelength [8].

Three types of RCS are distinguished: a) Monostatic or backscatter RCS when the incident and the scattering directions are coincident but opposite in sense. b) Bistatic RCS when the two directions are different: c) Forward-scatter RCS when the two directions and senses are the same.

Monostatic or backscatter RCS, is the usual case of interest for most radar systems where the receiver and transmitter are colocated, often using the same antenna for transmitting and receiving. Figure 1.2 shows the configuration for monostatic RCS presenting two cases: one with the same antenna used for emission/reception and the second one using two different antennas close enough to be in a monostatic configuration.

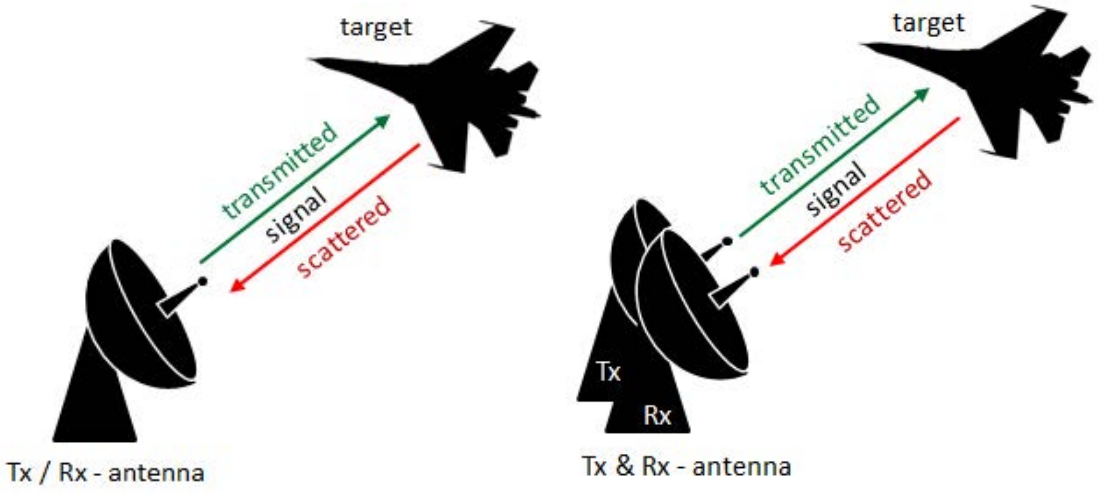

a) b)

Figure 1.2 Monostatic radar:
a) one emission/reception antenna; b) two antennas for emission and reception.

Bistatic RCS is the case when the transmitter and the receiver are separated in angle. This configuration is used to express the RCS when the target is illuminated and observed by spatially separated radar stations. Figure 1.3 shows the configuration for bistatic RCS.

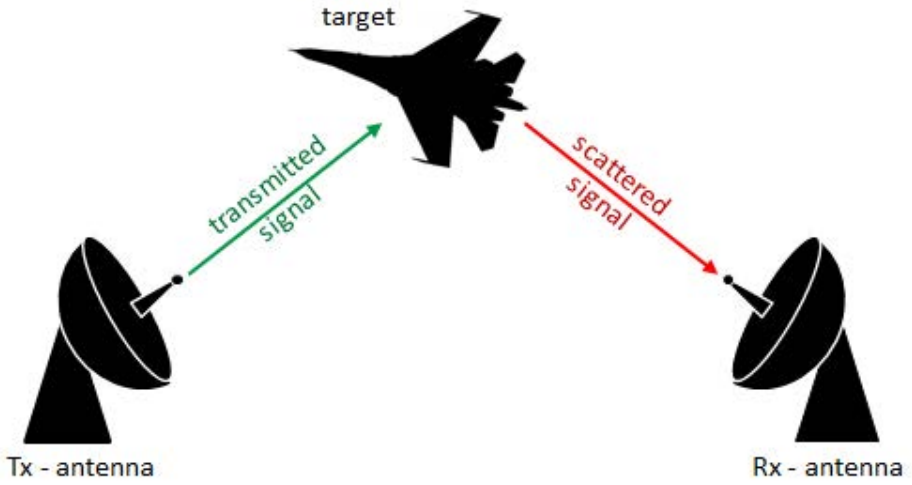

Figure 1.3 Bistatic radar

A special case of bistatic radar is the forward scatter radar. Forward RCS is the measure of scattered power in the forward direction, in the same direction as the incident field, as shown in Figure 1.4. This forward scattered power is usually 180° out of phase with the incident field so that when added to the incident field a shadow region is formed behind the scattering object.

Figure 1.4 Forward scatter radar

Modeling software can be used to obtain estimates of target cross sections, but the most accurate method is by measurement, because in this case no approximation is done on the target. However, even this method encounters great difficulty, particularly if the target is large, the far field criteria is not always respected and it is often impractical to measure the cross section over all aspect angles in azimuth and elevation.

The targets are complex and consist of many scattering surfaces. The effective surface roughness of a target, as a function of λ, plays an important role in determining its RCS.

1.4 Scattering regimes

There are three regimes that characterize the RCS scattering, depending on the ratio of wavelength, λ to the size L of the target, λ/L. In the Rayleigh region, the wavelength is greater than the size of the target, $\lambda \gg L$. If the size of the target is comparable with the wavelength $\lambda \propto L$, the scattering is in the resonant (Mie) region. The optics region corresponds to wavelengths very small compared to the size of the target, $\lambda \ll L$.

Figure 1.5 shows the classic illustration of cross section of a sphere over these three regions. The radar cross section has been normalized to the projected area of the sphere, πa^2, plotted as a function of sphere circumference normalized to the wavelength, $2\pi a/\lambda$.

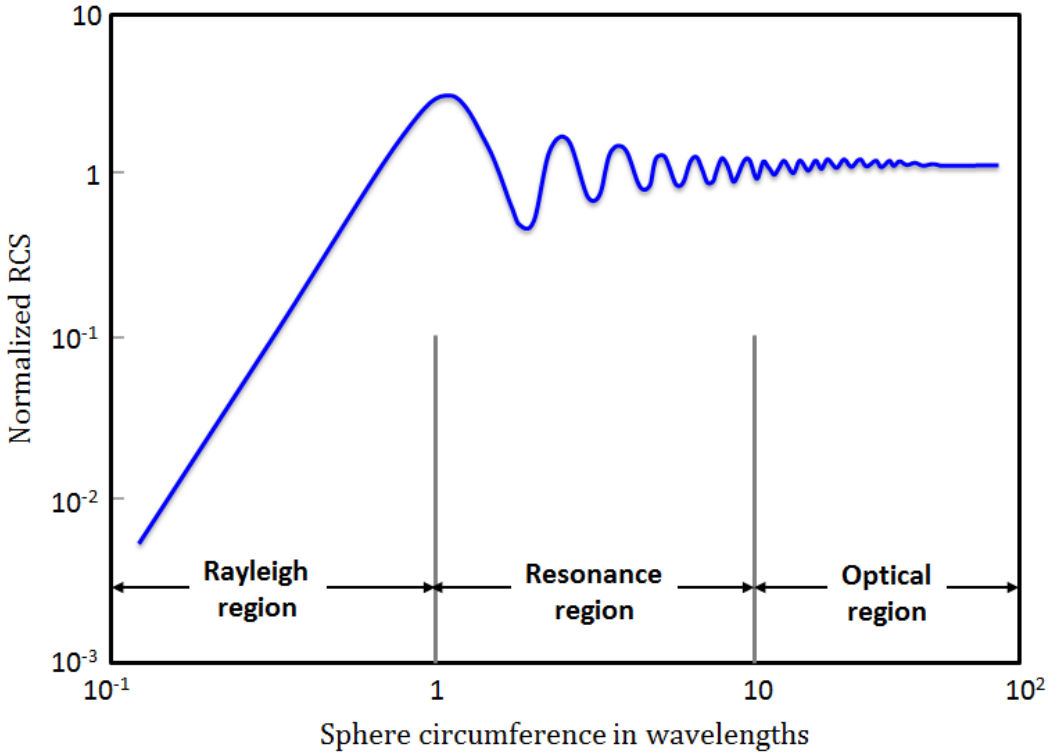

Figure 1.5 Normalized RSC of a metallic sphere over the three scattering regimes

1.4.1 Low-frequency scattering region

Lower frequencies imply greater wavelengths compared with the target‟s body size and the scattering is in the Rayleigh region which is named after Lord Rayleigh. He stated the sky is blue due to the longer blue wavelengths which reach earthbound observers, as opposed to the shorter wavelengths which suffer greater scattering by atmosphere particles.

In the low-frequency case, there is little phase variation of the incident wave over the spatial extent of the scattering body, so each part of the target encounter the same incident

field at each moment of time. The situation is similar to a static field problem, with the exception that the incident field is changing in time. This quasi-static field builds up opposite charges at the ends of the body of the target.

When the wavelength is much greater than the sphere circumference, in Rayleigh region, its cross section is proportional to $a^2(ka)^4$, where $k = 2\pi/\lambda$ is the wavenumber. Consequently, although the radar cross section is small, it increases as the fourth power of frequency and sixth power of radius. The most notable characteristic of Rayleigh scattering is that cross section is proportional to the fourth power of the frequency: $\sigma \propto \omega^4$.

The strong wavelength dependence means that shorter wavelengths are scattered more efficiently than longer wavelengths [9]. Since Rayleigh scattering is essentially a static field problem, analytical procedures as the integral equation approach or the dipole and multidipole expansions can be invoked.

For low-frequency scattering, the entire body of the target participates in the scattering process. Thus, the details of the shape are not important and only a basic geometric description is required because the overall shape is more significant than detailed shape information.

As the target size increases and becomes comparable to the wavelength, the Rayleigh theory breaks down and Mie theory describes the scattering process.

1.4.2 Mie resonant scattering region

When the incident wave length is on the order of the size of target the phase of the incident field changes significantly over the length of the scattering body. Conventionally, if the size of the target falls between 1 and 10 wavelengths, the scattering is considered to be in the resonant region.

Mie scattering is different from Rayleigh theory by the point of view of the intensity of radiation. Mie-scattered radiation is larger in forward direction than in backward direction and slightly not dependent on the wavelength, while Rayleigh-scattered radiation is identical in forward and backward direction. A distinctive property of Mie scattering, are the Mie resonances, where the scattering is particularly strong or particularly weak [10].

In this region there are two classes of scattering mechanisms, surface wave effects that are unique to only resonant region and the optical mechanism. Surface wave types are traveling waves, creeping waves and edge traveling waves. These waves occur when the

surface energy is reflected from some aft body discontinuity, or as in the case for creeping waves, the energy flows completely around the body of the target.

Surface wave scattering is independent of target size. Cross section magnitudes are proportional to λ^2; therefore these effects are important for resonant region target size. Surface wave effects are present in optical region, but the scattering magnitudes are much smaller than optical scattering magnitudes.

In this scattering regime body-body interaction is important as the field at any part of the body is the sum of the incident field and the field scattered by other regions of the target. This collective interaction determines the resultant current density. Overall geometry is important, yet small scale details, compared with the wavelength are not. In this regime an exact solution of Maxwell‟s equations is required. Typically the method of moments is used to solve the integral form of Maxwell‟s equations to obtain the induced currents from which the scattered field is obtained.

1.4.3 High-frequency optical scattering region

When the wavelength becomes much smaller than the size of the target, usually at least ten times smaller, a localized scattering center approach is used. In this region, collective interactions are very weak and the target is treated as a collection of independent scattering centers. In the scattering process, detailed geometries now become important. The net scattering from the target is the complex phasor sum of all the individual scattering centers.

There are several types of scattering mechanism in the optical regime. Specular scattering is the ray optical case of angle of reflection equal to angle of incidence. The scattering is the optical mirror reflection and it is the mechanism responsible for bright spike-like scattering.

The end-region scattering is the scattering from the end regions of finite objects, which produces sidelobe scattering in directions away from specular. Diffraction is end-region scattering in the specular direction due to edge induced currents at leading or trailing edges, tips or object regions of rapid curvature change.

Multiple-bounce is the separate case of mutual body interaction in the sense that one object‟s surface scatters energy to another object surface that is oriented to reflect this energy back to the observer, like corner reflectors or cavities.

1.5 Calibration targets

The RCS calibration is the most important part of measurements and a variety of metrological reference targets are considered, such as flat plates, discs, cylinders and corner reflectors in addition to spheres. The flat plate offers the highest RCS for a given size, but it gives a specular reflection which makes it difficult to align.

Another used shape is the trihedral corner-reflector which also produces a high radar cross section which remains constant over a wide angle, being a preferred RCS reference.

The sphere is also often used as a reference for moving targets since its radar cross section is invariant with observed angle. The inconvenient is that the RCS is very small for its size and also large conductive perfect spheres are difficult to manufacture.

It is generally advisable to choose the reference in the upper dynamic range of the measured target. The radar cross section of a sphere is often taken as reference value as the radar return reflected from a target is compared to the one reflected from a sphere. Generally, the accepted size of the sphere circumference has to be 10 times greater than the operating wavelength.

Yet if calibrated, other objects like cylinders, flat plates, dihedral and trihedral corner reflectors or Luneburg lens can also be used for comparative radar cross section measurements [11].

In the next sections, the monostatic RCS of all presented calibration targets have been simulated using CST Microwave Studio 3D EM software. Simulations are carried at central frequency of 6 GHz using a plane wave configuration.

1.5.1 Flat plate

1.5.1.1 Rectangular flat plate

The flat plate is the target which presents the largest peak RCS for its size [12]. Its echo near normal incidence is known with a high degree of confidence.

Generally, the flat plate is used as reference target when it is observed at normal incidence, where the monostatic RCS of a rectangular plate becomes:

$$\sigma_{max} = \frac{4\pi A^2}{\lambda^2} \tag{1.8}$$

where, A^2 is the physical area of the plate.

As an example, a square plate is modeled in CST MWS 3D EM using a perfect electrical conductor (PEC) as the material. The sides of the plate have the dimension equal to five wavelengths, $w = h = 300\ mm$, for the central frequency of 6 GHz. Figure 1.6 presents the square plate.

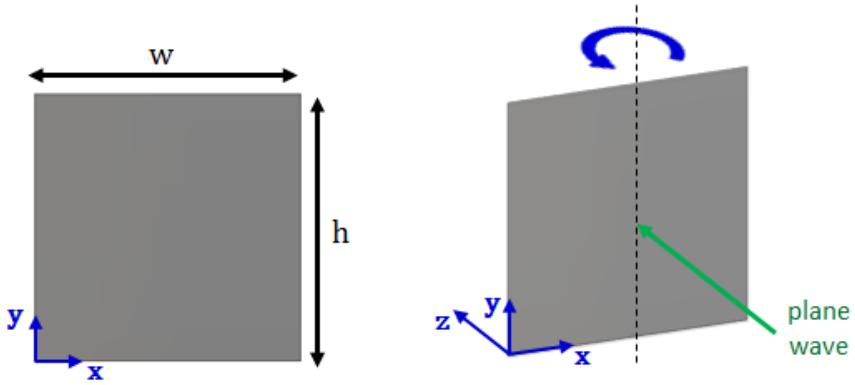

Figure 1.6 Square plate

The monostatic RCS as a function of aspect angles of a PEC plate, shown in Figure 1.7, is simulated facing a plane wave.

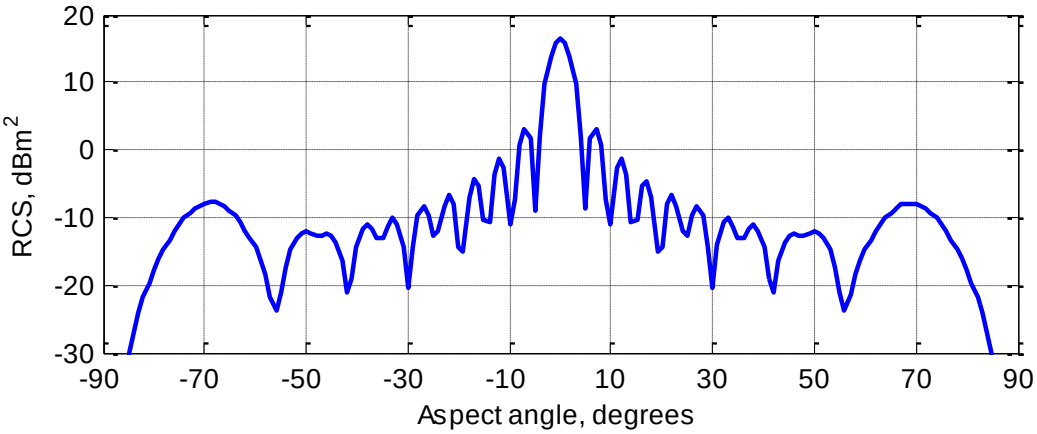

Figure 1.7 Simulated monostatic RCS of a flat square plate

Because the sidelobes of this pattern are governed by a *sinc* function, the first sidelobes are 13.3 dB lower from the normal-incidence echo of the square plate.

1.5.1.2 Circular flat plate

For a circular flat plate, the normal-incidence RCS is also high, but its sidelobes decay faster away from normal incidence in comparison with the square flat plate. For normal incidence, the monostatic RCS of a circular plate is expressed as:

$$\sigma_{max} = \frac{4\pi^3 r^4}{\lambda^2} \tag{1.9}$$

where, r is the radius of the plate.

For instance, a PEC modeled circular plate with a diameter equal to five wavelengths, $d = 300\ mm$, shown in Figure 1.8, has the simulated monostatic RCS at 6 GHz presented in Figure 1.9.

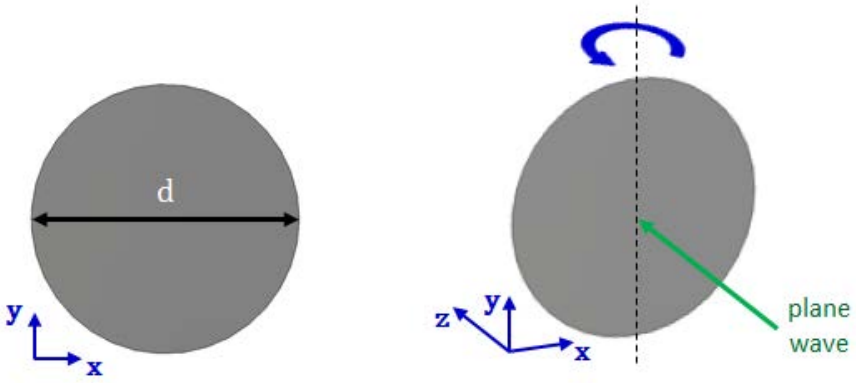

Figure 1.8 Circular plate

The normal-incidence value for the circular flat plate is 2.1 dB lower than that of the circumscribing square plate due to the area reduction from the square shape to the circular one, especially near the sides of the disc.

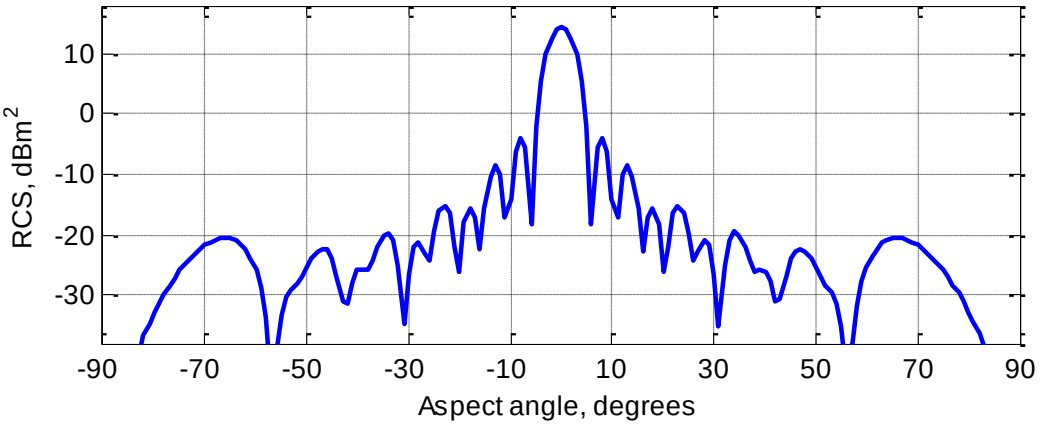

Figure 1.9 Simulated monostatic RCS of a flat circular plate

In this case the first sidelobe level is 18.5 dB below the normal incidence echo, while the first sidelobe level for the square plate is 13.3 dB below the normal incidence echo.

1.5.2 Dihedral reflector

The dihedral corner reflector consists of two faces joined at right angles. Even if the faces may have different shapes, the dihedrals used for calibration have rectangular faces. Among the passive reflectors, the dihedral corner reflector is most suitable for polarimetric calibration measurements [13].

The studied reflector is a PEC modeled rectangular dihedral reflector whose square faces have the dimension of 5λ. Figure 1.10 presents a rectangular dihedral reflector with $w = h = 300\ mm$.

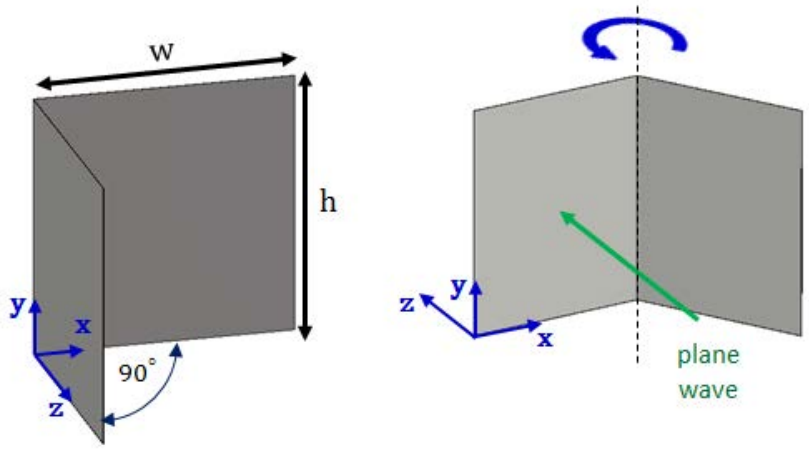

Figure 1.10 Dihedral reflector

Figure 1.11 shows the monostatic RCS of the square-faced dihedral corner reflector presented in Figure 1.10, illuminated by a plane wave at the frequency of 6 GHz.

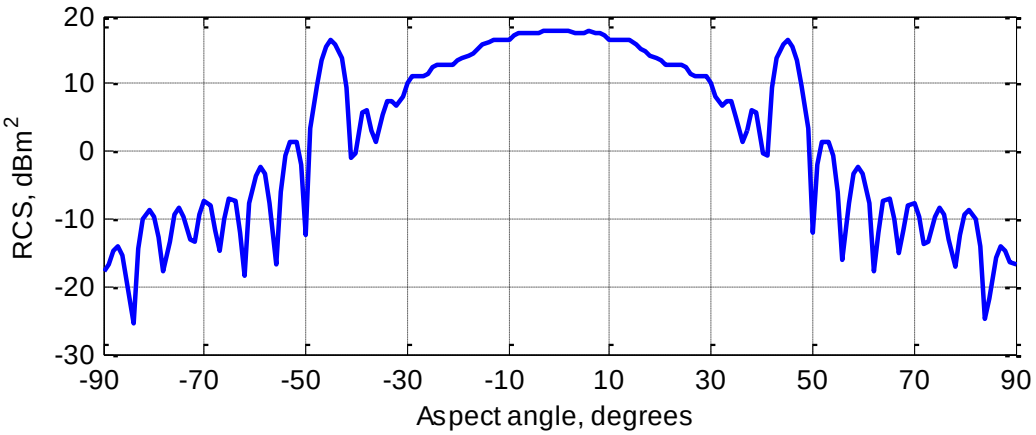

Figure 1.11 Simulated monostatic RCS of a dihedral reflector

The dihedral reflector has a similar scattering mechanism as the metal plate [14]. The dominant echo mechanism is a double bounce, one per face. The echo reaches its peak when the corner is seen from a direction along the bisector of the corner angle and in a plane perpendicular to the dihedral axis.

The ripples in the pattern are due to sidelobes of the single bounce flat-plate returns, combined with the double-bounce interaction between two faces [15]. The first bigger sidelobes are the main lobes of the single-bounce patterns.

1.5.3 Trihedral reflector

The typical trihedral reflector consists of three flat plates mutually orthogonal joined in a corner where the dominant scattering mechanism is a triple bounce in which all three faces of the trihedral participate. The common shapes of the plates are squares, quarter-discs or right triangles.

1.5.3.1 Rectangular trihedral reflector

One type of trihedral corner is the rectangular three-face reflector. As an example, a PEC modeled reflector consisting of three square plates is considered. The sides equal to five wavelengths, $w = 300\ mm$. Figure 1.12 presents the trihedral rectangular reflector.

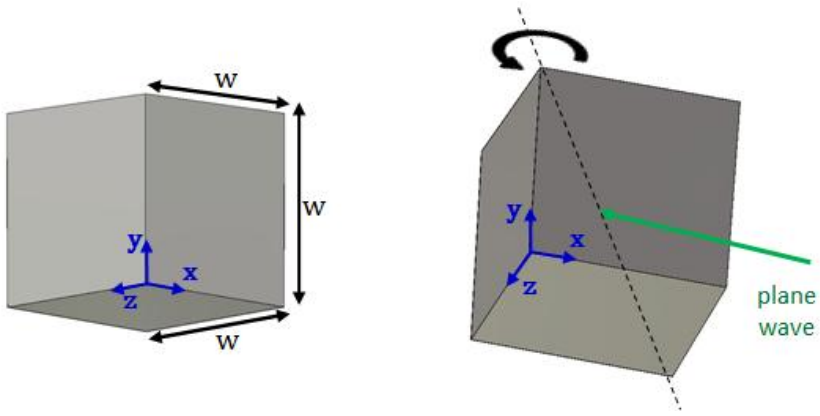

Figure 1.12 Rectangular trihedral reflector

The RCS for normal incidence to the corner aperture is expressed as [16]:

$$\sigma = \frac{12\pi w^4}{\lambda^2} \tag{1.10}$$

Figure 1.13 shows the monostatic RCS of the three-faced rectangular trihedral reflector, illuminated by a plane wave at the frequency of 6 GHz.

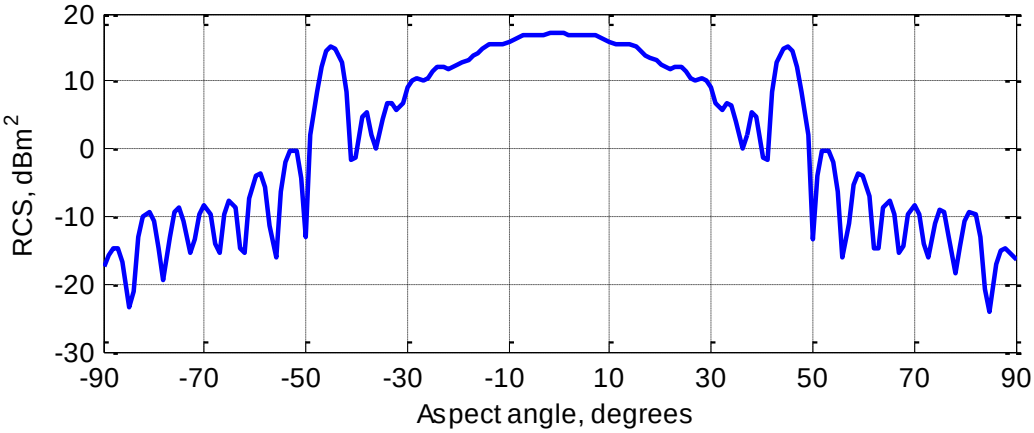

Figure 1.13 Simulated monostatic RCS of a rectangular trihedral reflector

The mutual orthogonality assures that most of the rays entering the corner will suffer three internal reflections, one from each face. The rays that are indeed reflected three times will be sent back in the direction from which they came. This retrodirective property is responsible for the broad aspect angle pattern of the trihedral reflector. The first sidelobes at the sides of the pattern are echoes from double-bounces from two of the trihedral faces, when the angle of incidence swings far enough.

1.5.3.2 Circular trihedral reflector

One other type of corner reflector is the three orthogonal faces shaped as a quarter-disc. In the considered example, one face of the reflector is one quarter of a PEC modeled disc with the radius $a = 300\ mm$. Figure 1.14 presents the quarter-disc faced trihedral reflector.

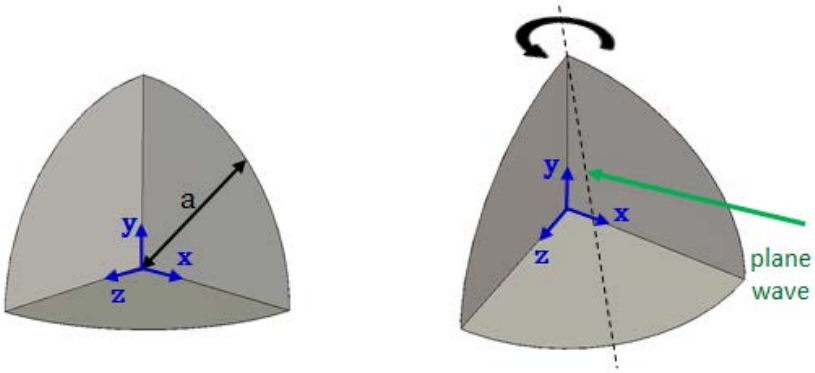

Figure 1.14 Circular trihedral reflector

The maximum RCS for normal incidence to the corner aperture is calculated as [16]:

$$\sigma = \frac{15.6a^4}{\lambda^2} \tag{1.11}$$

Figure 1.15 shows the monostatic RCS of the quarter-disc-faced trihedral reflector, illuminated by a plane wave at the frequency of 6 GHz.

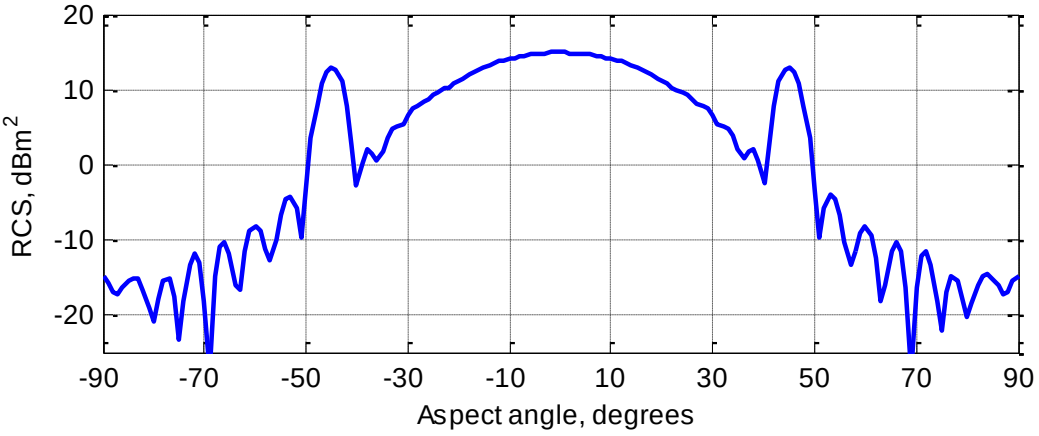

Figure 1.15 Simulated monostatic RCS of a circular trihedral reflector

Compared to the rectangular trihedral reflector, the circular one has the normal incidence value 2 dB lower, as the surface of one face is reduced from a square with the side $w = 300\ mm$ to a quarter of a disc with the same radius $a = 300\ mm$, the equivalent of five wavelengths. The difference between the normal incidence level and the level of the first two greater sidelobes remains of 2 dB, for the both cases.

1.5.3.3 Triangular trihedral reflector

The trihedral reflector usually used on RCS test ranges is the trihedral reflector with three identical faces that are isosceles triangles joined along their short sides.

As an example, a PEC modeled trihedral triangular reflector has the length of the perpendicular sides of the triangles $l_1 = l_2 = 300\ mm$, the equivalent of 5λ and the length of the hypotenuse is $l_3 = l\sqrt{2} = 424\ mm$. Figure 1.16 shows a triangular corner reflector.

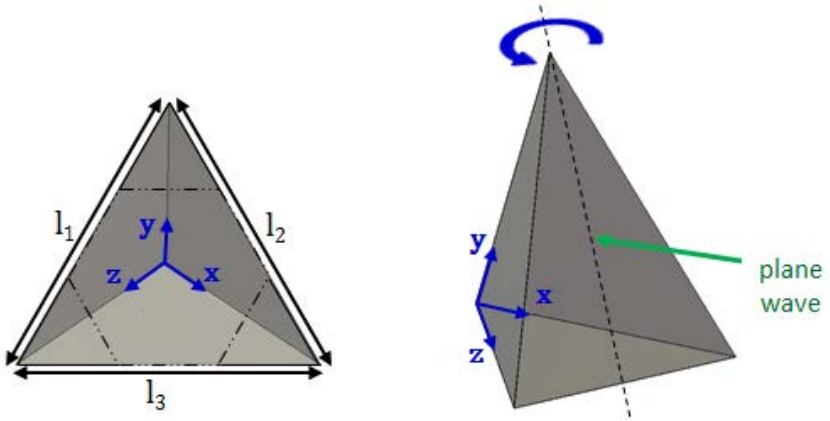

Figure 1.16 Triangular trihedral reflector

Not all rays entering the corner are bounced three times before they exit the reflector aperture. Depending on the orientation of the aperture, formed by the long sides of the faces, with respect to the line of sight, some rays miss the third face after a double reflection off the other two and some even miss the second and third faces after a single reflection off the first.

The tips of the reflector do not participate in the triple bounce mechanism. These areas constitute one-third of the aperture and the remaining effective region is a hexagon whose sides are $l = l_1/3$ long, but the size and shape of active region changes with aspect angle.

The radar cross section for normal incidence to the corner aperture using the hexagonal area $A = 3l^2\sqrt{3}/2$ is expressed as [16]:

$$\sigma = \frac{4\pi l^4}{3\lambda^2} \tag{1.12}$$

Figure 1.17 shows the simulated monostatic RCS of a three-faced triangular trihedral reflector, illuminated by a plane wave at the frequency of 6 GHz.

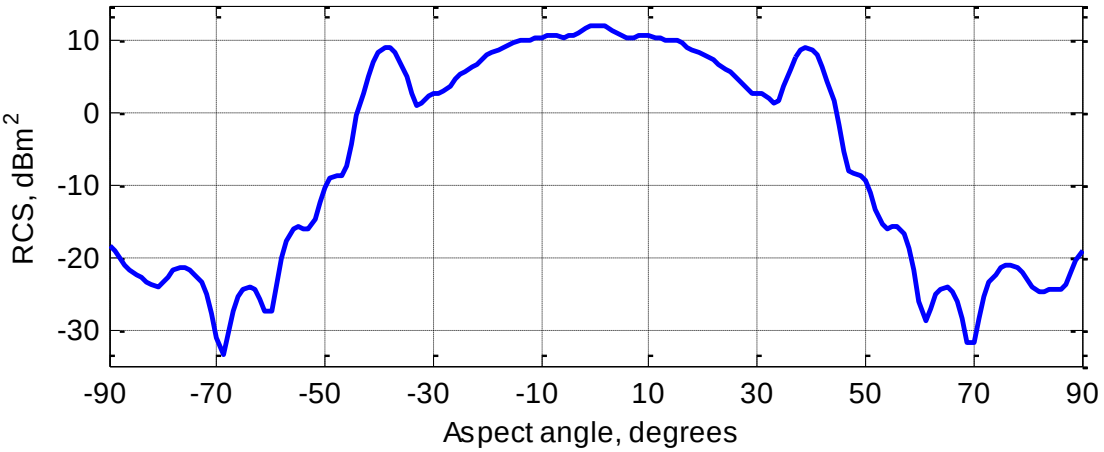

Figure 1.17 Simulated monostatic RCS of a triangular trihedral reflector

In comparison with the rectangular and the round trihedral reflectors, the surface participating in the scattering process has decreased, giving a value with 4.85 dB, respective 2.15 dB lower, for normal incidence.

As for the first bigger sidelobes corresponding to double bounce echoes, their level is lower with 3.2 dB than the normal incidence level. Compared to the other two presented trihedral reflectors, there is an increased difference between the normal incidence level value and the level value of the first sidelobes.

Due to its characteristics and the wide RCS pattern, a trihedral triangular reflector is used as a target for the experimental validation in a following section.

1.6 Polarization scattering matrix

Radar cross section is a function of the polarization of the incident and received waves. Target backscattered cross section is described by the polarization scattering matrix which gives the complete description of the interaction of the incident wave and the target. It relates component by component, the scattered electric field vector E^s to the incident field vector E^i:

$$\begin{bmatrix} E_1^s \\ E_2^s \end{bmatrix} = [S] \begin{bmatrix} E_1^i \\ E_2^i \end{bmatrix} = \begin{bmatrix} S_{11} & S_{12} \\ S_{21} & S_{22} \end{bmatrix} \begin{bmatrix} E_1^i \\ E_2^i \end{bmatrix} \tag{1.13}$$

where, each of the scattered and incident fields have independent vector components E_1 and E_2. The components of matrix S are related to the square root of the cross section:

$$S_{ij} = \frac{\sqrt{\sigma_{ij}}}{4\pi r^2} \tag{1.14}$$

The polarization scattering matrix can be defined for linear or circular polarization. Usually, the linear polarization directions are horizontal and vertical, noted with H, respective V subscripts. Circular polarization is defined by left circular or right circular noted L and R, respectively. Linear polarization is the most common one used in radar cross section measurements. Considering the different possible orthogonal polarizations, equation (1.13) can be written as the following for linear polarization:

$$\begin{bmatrix} E_H^s \\ E_V^s \end{bmatrix} = \begin{bmatrix} S_{HH} & S_{HV} \\ S_{VH} & S_{VV} \end{bmatrix} \begin{bmatrix} E_H^i \\ E_V^i \end{bmatrix} \tag{1.15}$$

In circular polarization, the electric field vector rotates in the plane perpendicular to propagation. In this case, equation (1.13) becomes:

$$\begin{bmatrix} E_R^s \\ E_L^s \end{bmatrix} = \begin{bmatrix} S_{RR} & S_{RL} \\ S_{LR} & S_{LL} \end{bmatrix} \begin{bmatrix} E_R^i \\ E_L^i \end{bmatrix} \tag{1.16}$$

The matrix which links the two polarizations basis, linear and circular, is the transformation matrix, $[T]$:

$$[T] = \frac{1}{\sqrt{2}} \begin{bmatrix} 1 & -j \\ 1 & j \end{bmatrix} \tag{1.17}$$

Using the transformation matrix [17], the circular scattering elements can be expressed from the linear scattering elements:

$$\begin{bmatrix} S_{RR} & S_{RL} \\ S_{LR} & S_{LL} \end{bmatrix} = [T] \begin{bmatrix} S_{HH} & S_{HV} \\ S_{VH} & S_{VV} \end{bmatrix} \begin{bmatrix} 1 & 0 \\ 0 & -1 \end{bmatrix} [T]^{-1} \tag{1.18}$$

In a similar manner, the linear scattering elements can be expressed from the circular scattering elements:

$$\begin{bmatrix} S_{HH} & S_{HV} \\ S_{VH} & S_{VV} \end{bmatrix} = [T]^{-1} \begin{bmatrix} S_{RR} & S_{RL} \\ S_{LR} & S_{LL} \end{bmatrix} \begin{bmatrix} 1 & 0 \\ 0 & -1 \end{bmatrix} [T] \tag{1.19}$$

The combinations of incident and scattered polarizations are distinguished in two cases for both polarizations, as parallel-polarized or cross-polarized. Table 1.2 presents the two cases for linear and circular polarizations.

Polarization	Co-polarized	Cross-polarized
Linear	VV	VH
	HH	HV

Polarization	Co-polarized	Cross-polarized
Circular	RL	RR
	LR	LL

Table 1.2 Polarization cases

A characteristic feature of circular polarization is that single-bounce scattering changes the polarization from left circular to right circular or right circular to left circular. In the case of linear polarization, the scattered energy has the same polarization as the incident polarization for single-bounce specular scattering.

1.7 Radar cross section measurements

Radar cross section measurements may be required for several reasons from scientific inquiry to verification of compliance with product specifications. Depending on the size of the test object, the frequency range or other test requirements, measurements can be made in indoor test facilities or on outdoor test ranges. Since the interest in radar cross section of a device under test is rarely for only one aspect angle, all static tests ranges use turntables or rotators to vary the target aspect angle.

For radar cross section measurements, the most important aspect requires the target to be illuminated by a radar wave of acceptably uniform amplitude and phase. In general, the amplitude of the incident wave does not deviate more than $0.5\,dB$ over the transverse and longitudinal extent of the target and phase deviation should be less than $22.5°$. The phase requirement is the basis of the far-field range criterion: $R > 2D^2/\lambda$, where R is the distance between the instrumentation radar and the target and D is the maximum target dimension transverse to the line of sight. All error sources within far-field requirements should generally yield data with an accuracy of $1\,dB$ or better [18].

Measurements should be calibrated by substitution method, in which the device under test is substituted by a metrological standard (or reference) target presented in the previous section.

Since residual background reflections alter the desired target echo signal, interior walls in indoor test chambers must be covered in high-quality radar-absorbing material, and in outdoor ranges, the surface should be smooth and without vegetation.

1.7.1 Measurement facilities

1.7.1.1 Indoor facilities and anechoic chamber – far field range

Indoor test ranges offer protection from weather and more productive testing, but the maximum target size is limited to a few meters, unless very large facilities are available to accommodate bigger targets. For example, the DGA defense agency‟s DGA/IS (DGA Information Superiority) laboratory constructed the SOLANGE indoor RCS range which is one of the biggest in the world, capable of measuring real fighter RCS [19]. Figure 1.18 presents a photograph of SOLANGE range.

Figure 1.18 SOLANGE indoor RCS range [19]

An anechoic chamber is an indoor facility used for testing with an electromagnetic field absorbing wall, creating an electromagnetic-field-free environment. Figure 1.19 shows a photograph of CHEOPS anechoic chamber of CELAR (DGA).

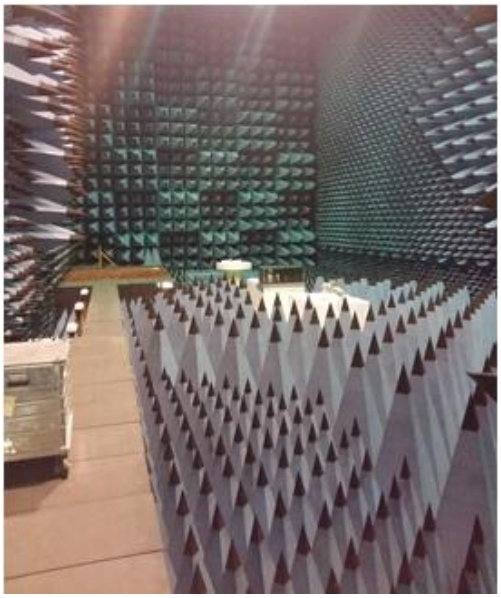

Figure 1.19 CHEOPS anechoic chamber

The outer structure is a Faraday cage, keeping the interior of the room quiet regarding the RF radiation. Any radiation created inside the chamber cannot escape outside. Full anechoic chamber has the floor absorbing the radiation, while the semianechoic chamber has a conducting floor [20].

The walls of indoor test rangers, the floor and ceiling must be covered with high-quality absorbing material. Aside from the ferrite tiles, pyramidal absorbers impregnated with carbon are used for the attenuation of waves. The lower the working frequency, the more expensive the absorber becomes.

In an anechoic chamber, the goal is to obtain a volume in the chamber where any reflected energy from the walls is much lower than any of the features of interest on the radiation pattern. This volume is known as the quiet zone [21]. A primary criterion is the uniformity of the field strength that illuminates the target, obtained by satisfying the far field criterion when conducting the tests.

Usually, indoor chambers have a rectangular shape, but despite the good quality of the installed absorbers materials on the walls, radar cross section measurements could be contaminated by wall reflection. Figure 1.20 shows a schematic representation of a rectangular anechoic chamber.

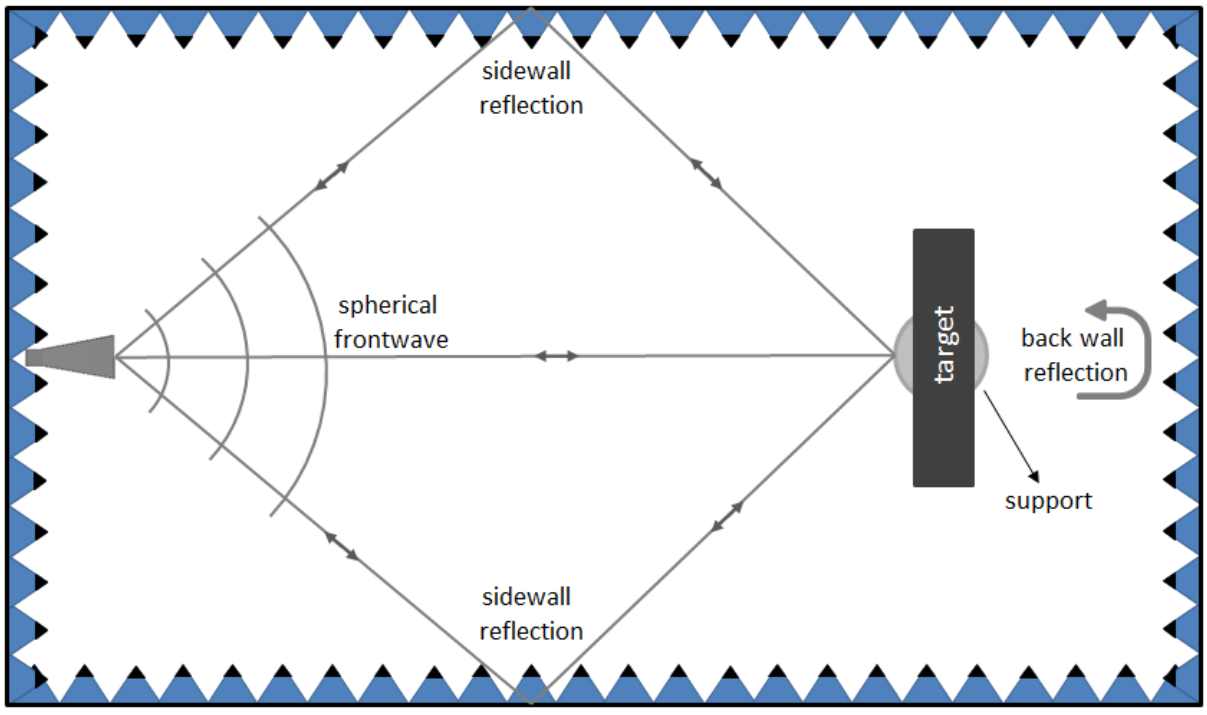

Figure 1.20 Anechoic room schematic – top view

The most sensitive part of the anechoic chamber is the rear wall, which receives 95 to 99 percent of the power radiated by the radar, yet the sidewalls, the floor and the ceiling also contribute errors to measurement results. The compensation for the back wall reflections is done using substitution method involving precalibrating the empty chamber. Anechoic chambers are not effective at lower frequencies because the absorbers are less efficient, while at high frequencies an anechoic chamber provides a well-controlled, isolated, reflectionless environment. Depending upon chamber size and the size and composition of the used absorbers, the deterioration in performance typically occurs between $50\ MHz$ and $500\ MHz$ [22].

A solution for low frequency test is using the tapered anechoic chamber, which eliminates most of the sidewall reflections by tapering one end of the chamber. This design usually permits lower frequency operation at a given reflectivity level than for a similar sized rectangular design. The source antenna is mounted at the apex of the taper section and for taper angles of 30° or less, the specularly reflected waves from the sides of the taper are at grazing incidence to walls resulting in little reflected radiation. Therefore, an almost unperturbed wavefront propagates down the taper to the cubical working volume where the target is placed [23]. Figure 1.21 shows a schematic representation of a tapered anechoic room.

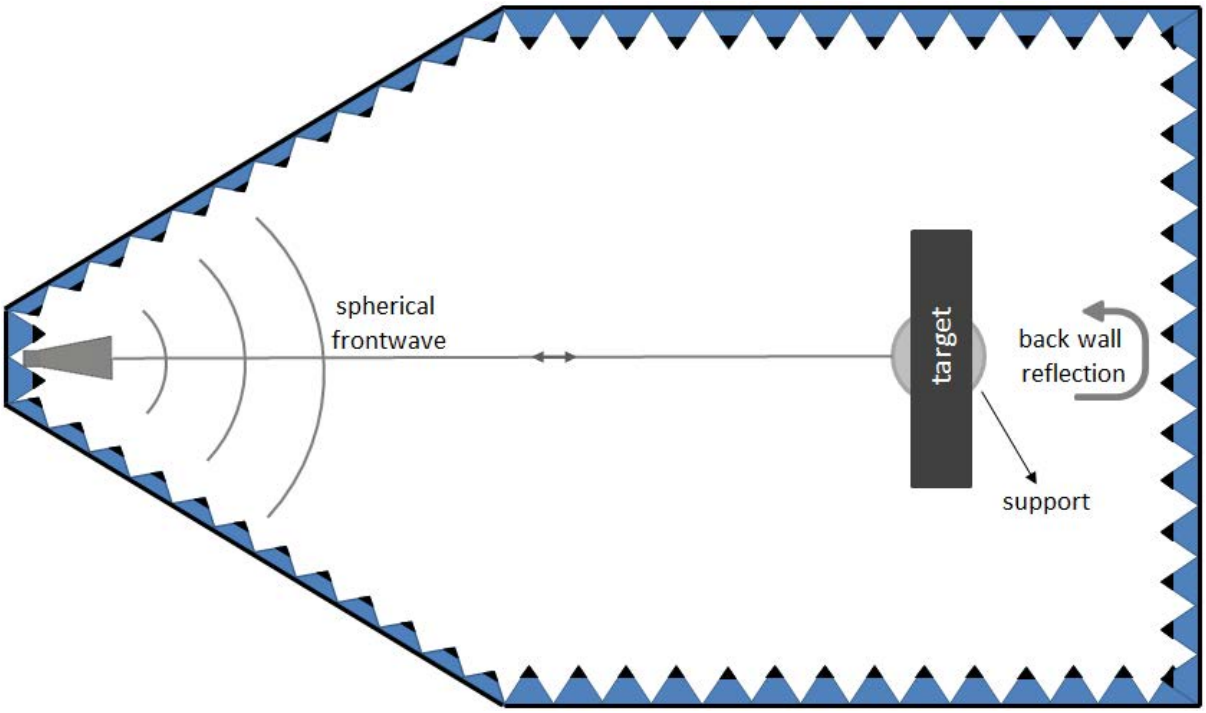

Figure 1.21 Tapered anechoic room schematic – top view

For the targets exceeding the far field requirement due to their size, it is possible to provide the necessary uniformity of illumination by inserting a lens between the radar and the target or by reflecting the radar beam off a collimating reflector. This concept is known as the compact range because a beam of parallel rays can be generated in a much shorter distance than what would be possible without the collimating device.

1.7.2 Radar cross section imagery

In radar imaging, RCS has an important role, as ISAR (inverse synthetic aperture radar) images of a target are constructed from backscattered field measurements. By transforming all data measured at different frequencies and aspect angles to the location where the scattering phenomena originated, it is basically obtained an ISAR image of the target.

An ISAR image is the display of range profile and cross-range profiles of the target in the 2D range/cross-range plane.

1.7.2.1 One-dimensional range profile

The range profile is the returned waveform shape from a target which was illuminated by the radar with a sufficiently large bandwidth. The physical meaning of the range profile shown in Figure 1.22, is Figure 1.22 Range profile illustrating a range profile of an airplane. As the incident waveforms pass along with the target, some of the energy will reflect back toward the radar from so - called scattering centers on the target. If these scattering centers are located at different range distances from the radar, they will return at different time instants to the radar receiver so that they can be distinguished in the corresponding 1D range profile.

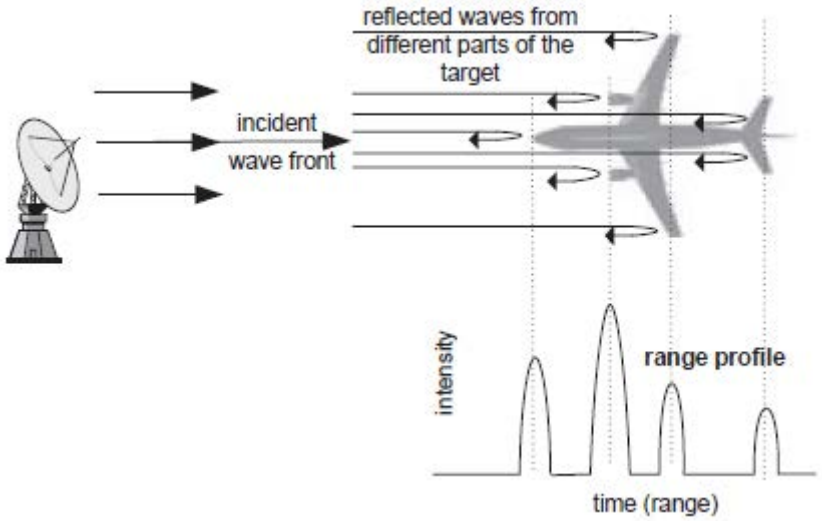

Figure 1.22 Range profile [24]

In time domain, the reflected signal which is collected by the receiver will have 1D characteristics as field intensity or RCS, while in frequency domain, for an illuminating signal with stepped frequency waveform, the inverse Fourier transform of the received signal will present the target"s 1D profile.

When the target is illuminated, the energy reflected toward the radar arises from target scattering centers. As long as, the scattering centers are located at different range distances from the radar, their respective return will arrive at different time instants on the radar receiver and each one will be distinguishable in the 1D range profile.

Since the returned waveform shape of a target is unique, the range profile is also named in the radar literature as the radar signature.

Considering N point scatterers located at different (x_i) points, the backscattered electric field in far-field can be approximated as [24]:

$$E^s(f) = \sum_{i=1}^{N} A_i \cdot e^{-j2k \cdot x_i} \tag{1.20}$$

where, A_i is the backscattered field amplitude for each point scatterer at x_i and $k = 2\pi f/c$ is the wavenumber.

Considering the backscattered field data collected within the bandwidth $[f_L, f_H]$, the range profile can be constructed by inverse Fourier transforming as:

$$E^s(x) = \sum_{i=1}^{N} A_i \cdot \int_{f_L}^{f_H} e^{2j\pi\left(\frac{2f}{c}\right)(x-x_i)} df \tag{1.21}$$

Taking the definite integral in the above equation, it can be simplified as:

$$E^s(x) = \frac{2B}{c} \cdot \sum_{i=1}^{N} A_i \cdot e^{2jk_c(x-x_i)} \cdot \mathrm{sinc}\left[\frac{2B}{c}(x - x_i)\right] \tag{1.22}$$

where, B is the bandwidth, k_c is the wavenumber corresponding to the center frequency.

The exponential from equation (1.22) is the phase term and has the unitary amplitude. The second term, the sinc, is the amplitude term that specifies the shape function of the point scatterer at x_i. Therefore, the scattering centers on the range are centered at the true locations x_i with their corresponding field amplitudes A_i.

An example of range profile of a simulated commercial airplane, whose backscattered electric field is collected in far field from the nose of the airplane between $3.97 - 4.03\ GHz$ for a total of 32 discrete frequencies, is shown in Figure 1.23.

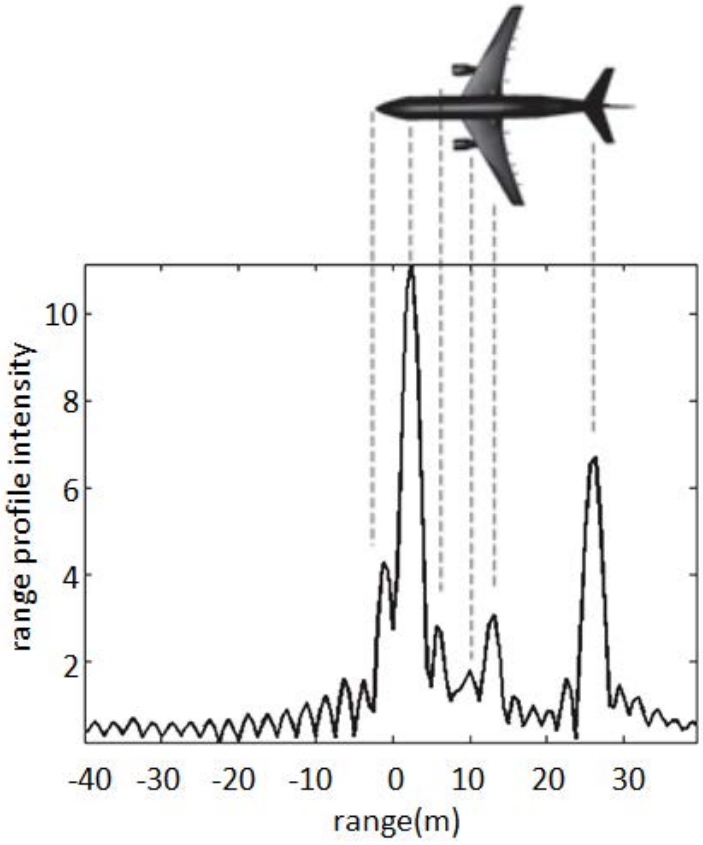

Figure 1.23 Range profile of a model airplane [24]

In radar imaging, the concept of range profile, has an important role, due to the fact that it can be used determine the length of a target or to extract the scattering centers.

1.7.2.2 One-dimensional cross-range profile

The cross-range profile can be obtained from collecting data return from a target at different angles. As opposed to range profile which is acquired from backscattered field at a single look and different frequencies, the cross-range profile, shown in Figure 1.24, needs a width aspect of the look angles in order to gather the necessary cross-range point to form the 1D cross-range profile.

Considering M point scatterers located at different (x_i, y_i) points, the backscattered electric field at the far field for different aspect angles can be approximated as:

$$E^s(\theta) = \sum_{i=1}^{M} A_i \cdot e^{-2j\vec{k}\cdot\vec{r_i}} \tag{1.23}$$

where, A_i is the backscattered field amplitude for each point scatterer and $\vec{r_i}$ is the vector from the origin to the point scatterer at (x_i, y_i). Also, the argument$\vec{k} \cdot \vec{r_i}$ can be written as:

$$\vec{k} \cdot \vec{r_i} = k \cos\theta \cdot x_i + k \sin\theta \cdot y_i \tag{1.24}$$

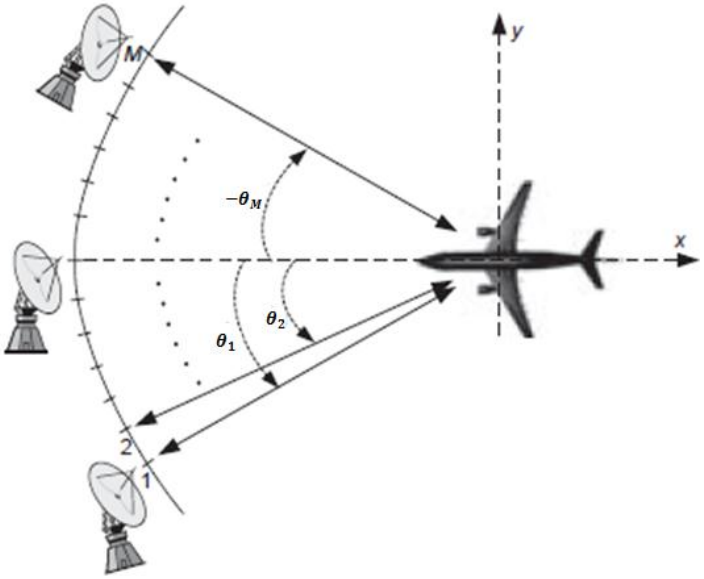

Figure 1.24 Cross-range profile [24]

Considering that the small values of the aspect angle allow the approximation of $\cos\theta$ to 1 and the approximation of $\sin\theta$ to θ, equation (1.23) can be reduced to:

$$E^s(\theta) = \sum_{i=1}^{N} B_i \cdot e^{-2j\pi\left(\frac{2f}{c}\right)\theta y_i} \tag{1.25}$$

where, B_i is a constant equal to $A_i \cdot exp(-j2k \cdot x_i)$.

Considering the backscattered field data collected at a total number of angular width Ω, by taking the 1D IFT, the cross-range profile can be expressed as:

$$E^s(y) = \sum_{i=1}^{M} B_i \cdot \int_{-\Omega/2}^{\Omega/2} e^{2j\pi\left(\frac{2f}{c}\right)\theta(y-y_i)} d\theta \tag{1.26}$$

Taking the definite integral in the above equation, it can be simplified as:

$$E^s(y) = \frac{2f}{c}\Omega \cdot \sum_{i=1}^{N} B_i \cdot \mathrm{sinc}\left[\frac{2f}{c}\Omega(y - y_i)\right] \tag{1.27}$$

An example of 1D cross-range profile imaging is illustrated in Figure 1.25. The variation of the aspect angle is in the azimuth plane in the range $[-1.04^{\circ}, 1.01^{\circ}]$, for a total number of 64 discrete frequencies. Similarly with the previous presented case, the backscattered electric field is collected in far field around the nose of the airplane.

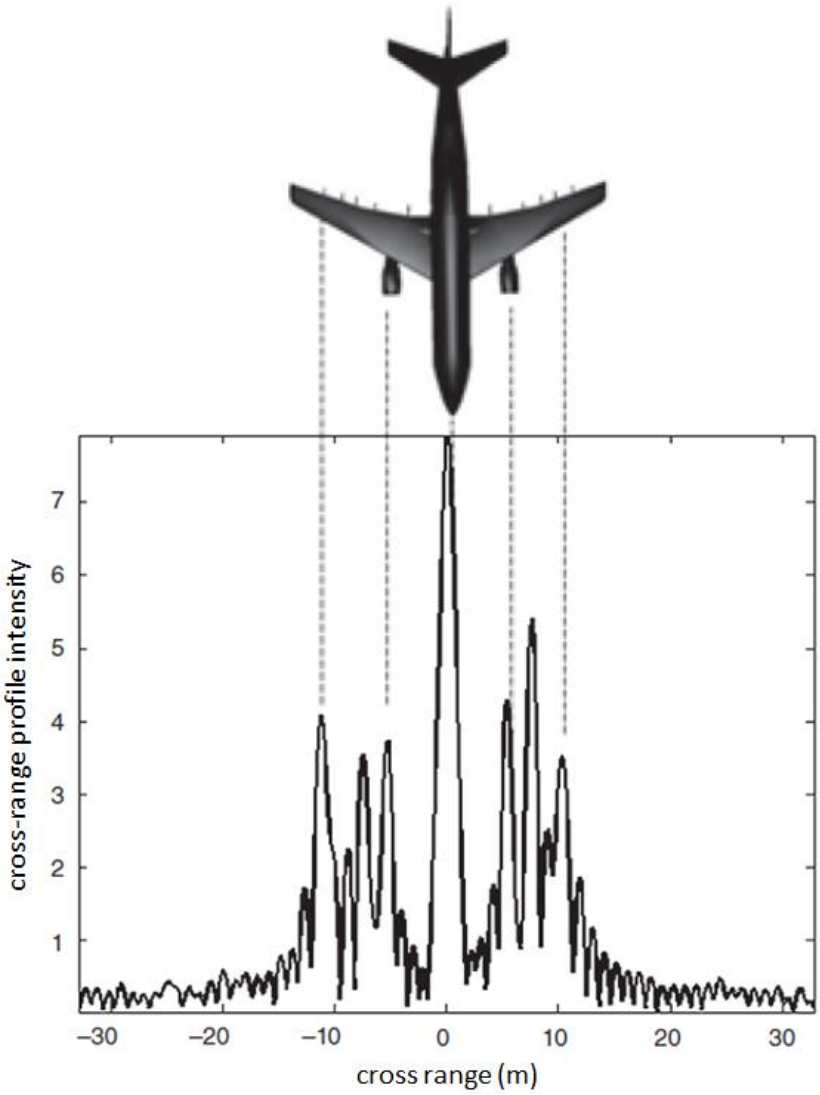

Figure 1.25 Cross range profile of a model airplane [24]

The cross-range profile from the above figure shows the scattering centers of the plane, the nose, the engine ducts and the wings.

1.7.2.3 Two-Dimensional ISAR image

A 2D ISAR image is formed by displaying the range profile in one axis and the cross-range profile in the other axis, so that the scattered field should be collected for various frequencies and aspects.

The availability of low-cost, phase-locked, frequency-synthesized sources makes it attractive to collect wideband RCS data, which contain far more target-scattering information than CW measurements made at single frequencies. If coherent radar cross section scattering data are suitably processed, it is possible to generate ISAR imagery or two-dimensional maps of the echo sources of test objects.

One way to gather high-range and cross-range resolution image data on instrumentation ranges is to employ a wideband step chirp for high range resolution and ISAR processing for high cross-range resolution. A complete set of frequency samples is gathered at each angle position to be processed. The raw data are a two-dimensional array of complex numbers whose columns represent frequency samples over the radar bandwidth at a given angle and the rows represent samples at single frequency over the angular window.

When selecting the frequency and angle step size, the samples should be close enough together in both domains in order to avoid range and Doppler ambiguities. Range ambiguities would cause aliasing in range and Doppler ambiguities would produce cross range aliasing.

A 2D FFT is applied to the data to produce a high-resolution image in both range and cross-range.

Considering the point scatterer (x_0, y_0) , shown in Figure 1.26, is situated on a target.

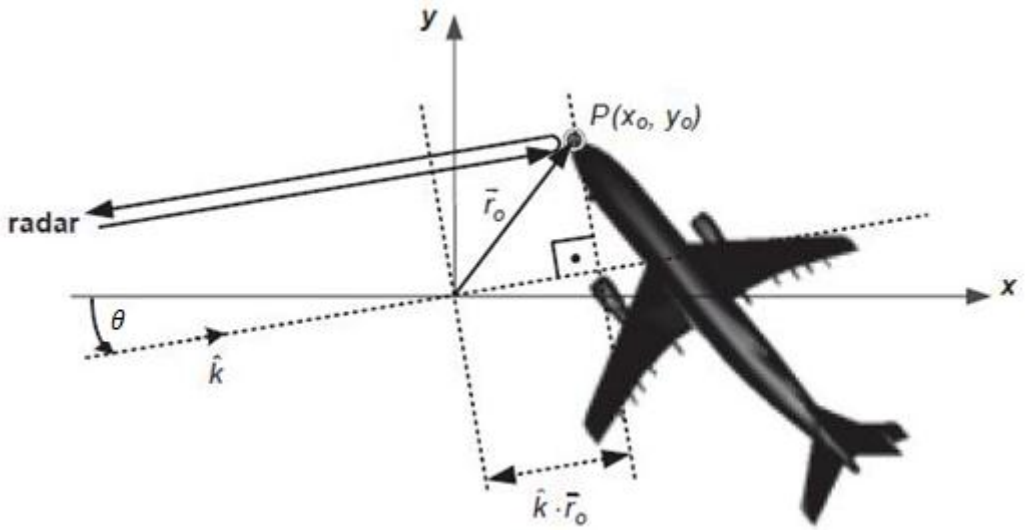

Figure 1.26 Geometry for monostatic ISAR imaging [24]

If the origin is assumed to be the phase center of the geometry, the far-field backscattered field from the point scatterer at an azimuth angle θ, can be approximated as:

$$E^s(k,\theta) \cong A_0 \cdot e^{-2j\vec{k}\cdot\vec{r_0}} \tag{1.28}$$

where, A_0 is the amplitude of the backscattered electric field intensity, $\vec{k}$ is the vector wavenumber in the propagation direction and $\vec{r_0}$ is the vector from origin to point P.

By rewriting the vector $\vec{k}$ in terms of wavenumbers in x and y directions, the above equation can be expressed as:

$$E^s(k,\theta) \cong A_0 \cdot e^{-2jk\cos\theta\cdot x_0} \cdot e^{-2jk\sin\theta\cdot y_0} \tag{1.29}$$

Equation (1.29) offers two separate phase terms as a function of both the spatial frequency variable, k and the aspect angle variable, θ. By using the 2D IFT, the ISAR image can be generated in range and cross-range domains.

Supposing a small bandwidth and a small aspect width, then the frequency bandwidth is small compared to center frequency and the wave number can be approximated as: $k \cong k_c$. Similarly, a small value of the aspect angle allows the approximation of $\cos\theta$ to 1 and the approximation of $\sin\theta$ to θ. Therefore, the backscattered field becomes:

$$E^s(k,\theta) \cong A_0 \cdot e^{-2j\pi\left(\frac{2f}{c}\right)\cdot x_0} \cdot e^{-2j\pi\left(\frac{k_c\theta}{\pi}\right)\cdot y_0} \tag{1.30}$$

By applying 2D IFT, the above equation can be written as:

$$\begin{aligned} E^s(x,y) = A_0 \cdot &\left[\int_{-\infty}^{\infty} e^{-2j\pi\left(\frac{2f}{c}\right)\cdot x_0} \cdot e^{2j\pi\left(\frac{2f}{c}\right)\cdot x} d\left(\frac{2f}{c}\right)\right] \\ &\cdot \left[\int_{-\infty}^{\infty} e^{-2j\pi\left(\frac{k_c\theta}{\pi}\right)\cdot y_0} \cdot e^{2j\pi\left(\frac{k_c\theta}{\pi}\right)\cdot y} d\left(\frac{k_c\theta}{\pi}\right)\right] \end{aligned} \tag{1.31}$$

$$E^s(x,y) = A_0 \cdot \delta(x - x_0, y - y_0) \tag{1.32}$$

In equation (1.32), $\delta(x,y)$ represents the 2D impulse function on the $x-y$ plane.

Approximating the backscattered field from the target as the sum of scattering from a finite number of single point scatterers, it can be expressed as:

$$E^s(k,\theta) \cong \sum_{i=1}^{N} A_i \cdot e^{-2j\vec{k}\cdot\vec{r_i}} \tag{1.33}$$

The backscattered electric field from a target is approximated as the sum of backscattered field from N different scattering centers on the target. While A_i represents the complex backscattered field amplitude for the ith scattering center, $\vec{r_i}$ is the displacement vector from origin to the location of the ith scattering center.

Taking the 2D inverse Fourier integral of the 2D backscattered field data, gives the ISAR image of the target:

$$ISAR(x,y) = \iint_{-\infty}^{\infty} \{E^s(k,\theta)\} \cdot e^{2j\pi\left(\frac{2f}{c}\right)\cdot x} \cdot e^{2j\pi\left(\frac{k_c\theta}{\pi}\right)\cdot y} d\left(\frac{2f}{c}\right)\, d\left(\frac{k_c\theta}{\pi}\right) \tag{1.34}$$

The small-bandwidth, small-angle ISAR image, assuming that the backscattered signal can be represented by a total of scattering centers, can then be expressed as:

$$ISAR(x,y) = \sum_{i=1}^{M} A_i \cdot \delta(x - x_i, y - y_i) \tag{1.35}$$

Therefore, the resultant ISAR image is composed of the sum of N scattering centers with their electromagnetic reflectivity coefficients.

For a better display of 2D ISAR imagery, windowing and zero-padding processing are very useful for suppressing sidelobes [25]. The reconstructed ISAR image would have high sidelobes next to the main peaks, without windowing the motion compensated data. Thus, the windowing function should be applied to reduce the sidelobes at the cost of a slightly reduced resolution. Hamming windows are commonly for this purpose.

1.8 Conclusion

From the general description of radar systems, followed by radar cross section basic principles, a brief description of the electromagnetic scattering regimes is given. The scattering process comprises three regimes: the low-frequency or Rayleigh region where the wavelength is much longer than the scattering target size; the Mie resonant region where the wavelength is on the same order as the scattering target size; and the high-frequency optical region where the wavelength much smaller than the scattering target size.

RCS behavior was presented for three types of calibration targets. Objects with a simple geometry and known radar cross section, as the flat plates of different shapes, square or circular, dihedral reflectors or trihedral square or triangular reflectors, are used for calibration before measuring a complex real target.

As for the target support structures, the influence on measurements results given by the foam columns, string suspension systems and metal pylons was described. Even if the foam column is considered to be invisible, the return echo rises with the frequency and as well, with the volume, due to the random internal scattering given by the millions of cells inside the foam column. The string structure provides a lower residual echo, with cost of being difficult to work with. The metal pylon offers greater strength compared with the foam column and string suspension method, being able to support heavier targets with the advantage of a small echo despite the amount of metal exposed to the radar.

For radar cross section measurements performed in indoor facilities, the absorbent material covering the walls, floor and ceiling provide an electromagnetic-field-free environment, proved to be very efficient at high frequency. However, at low frequency, the

efficacy of the absorbers decreases and the measurements results may be altered by wall reflections inside the anechoic room. One way to improve low-frequency measurements is the tapered anechoic room which has one end tapered and most of the sidewall reflections are eliminated.

The currently used methods for RCS measurements in anechoic chambers can be perturbed at low frequencies, due to multi-path propagation from the scattering on the boundaries which can no longer be neglected, causing the incident field on the target to be the superposition of the direct incident field and the fields reflected by the walls.

In this context, where the absorber materials prove to be less efficient as the wavelength becomes greater than the thickness of absorbents, this thesis presents a novel imaging method using a technique based on time reversal, by introducing a strongly disordered medium within the chamber. By taking advantage of this properly calibrated medium, the limitations of measurements in anechoic chamber, may be overcome. As well, the necessity of rendering fully absorbing walls, mainly at low frequencies, may be reduced.

CHAPTER 2 Time reversal technique

2.1 Introduction

Time reversal is an operation which describes the events of a physical process taking place in reverse sequence, similar to a movie that can be played back in reverse, creating the impression of going back in time.

One given example assumes to imagine filming the trajectory of a billiard ball. It receives an impulse, bounces a number of times on the edges of the pool table and then an operator stops it. If the film is rewound, the ball seems to reverse its trajectory and return to the same position where it has received the impulse. However, experimentally it is impossible for the operator to perfectly give the ball an impulse equal in speed and direction but in opposite sense of movement, in order to send the ball to its original position.

The beginning of time reversal can be traced back to 1957 when B.P. Bogert from Bell Telephone Laboratories published a paper on experiments related to methods of correcting the delay distortion occurred on picture and slow speed television transmissions over telephone lines, by time-reversal techniques [26]. Similar approaches are based on noncausal filtering for television signal deghosting, phase distortion compensation of linear systems or underwater communications [27], [28], [29].

In the later years, increased attention is centered on time reversal concept, time reversal mirror and time reversal cavities as new means of focusing ultrasonic fields, with the more recent work of M. Fink and others [30], [31], [32]. Thus, these highly appreciated papers become a lead for the future research works.

Nowadays, time reversal method is used in different fields from acoustics and ultrasonics to electromagnetics or optics in various applications as telecommunications [33], UWB communications [34], biomedical engineering (ultrasonic hyperthermia brain therapy [35], optical tomography [36]), seismic imaging [37], locating lightning discharges [38], nondestructive testing [39] or structural health monitoring [40].

Therefore, by its large number of application, time reversal proves that the complexity of a propagation environment can be exploited to its own advantage in order to focus the waves with greater quality than in simple media.

2.2 Time reversal in acoustics

2.2.1 Wave equation

Considering the example of the billiard ball trajectory, numerical simulations of this process could not play back the path of the ball due to minor truncation error made by the computer which will dramatically change the outcome.

The irreversibility of the experiment is based on the high sensitivity to initial conditions, which is a property of nonlinear chaotic systems [41]. In contrast, the wave propagation is a linear operation and the waves are correlated on a typical scale given by the wavelength. Thus, a minor change on the initial conditions will have a minor effect on the output.

Time reversal is a process based on the invariance of the wave equation under a time reversal operation and the spatial reciprocity of the propagation channel. Considering an acoustic wave expressed in terms of a scalar potential $\Psi(r,t)$, the wave equation in a non-dissipative heterogeneous medium is given by:

$$\Delta\Psi(r,t) = \frac{1}{c_0^2(r)}\frac{\partial^2\Psi(r,t)}{\partial t^2} \tag{2.1}$$

where $c_0(r)$ represents the spatial distribution of the velocity within the medium. The left term of the wave equation, the spatial part, is self-adjoint in space, satisfying the condition of spatial reciprocity. The right term of the equation contains only second-order derivatives with respect to time, therefore is self-adjoint in time, satisfying the condition of invariance under a time reversal operator.

Since the wave equation depends only on a second-order time-derivative operator, for each sound wave $\Psi(r,t)$ emitted by a source and propagating through a heterogeneous medium, there is a second set of waves $\Psi(r,-t)$ which satisfies the wave equation. This solution can be interpreted as a wave converging to the source, as if the time were going backwards [42].

The principle of time-reversal focusing is the following. First, an acoustic point-like source radiates a short pulse that propagates through a complex environment. The field is then measured in the volume and retransmitted in reversed chronology through the same medium. This creates a wave which will travel back, following the same paths and focusing on the initial source position.

Time reversal exploits the Helmholtz-Kirchhoff reciprocity theorem which describes the link between two pressure fields, $p_1(r,\omega)$ and $p_2(r,\omega)$ and their velocities, $v_1(r,\omega)$ and $v_2(r,\omega)$, to their sources is written:

$$\oiint_S [p_2(r,\omega)v_1(r,\omega) - p_1(r,\omega)v_2(r,\omega)]dS = \iiint_V [p_1(r,\omega)s_2 - p_2(r,\omega)s_1]\, dV \tag{2.2}$$

where, the surface S surrounds the volume V around the sources and ω is the angular frequency.

Considering each one of the two sources s_1 and s_2 is emitting a Dirac $\delta(r - r_1)$ and $\delta(r - r_2)$, the resulting pressure fields can be considered as the Green functions $G(r_1, r, \omega)$ and $G(r_2, r, \omega)$. The field can be expressed as:

$$\Psi(r) = \iiint_V p(r_0)G(r_0, r)dV \tag{2.3}$$

where, $p(r_0)$ represents the source term.

Assuming the integration volume V being of infinite radius, the left term of equation (2.2) tends to zero. Thus, the reciprocity of the medium is given by:

$$G(r_1, r_2, \omega) = G(r_2, r_1, \omega) \tag{2.4}$$

Therefore, the field produced at r_2 position, by a source s_1, situated in r_1 location is equal with the field produced at r_1 position by a source s_2 located at r_2. Using this reciprocity property, the roles of emitters and receivers can be interchanged.

2.2.2 Time reversal cavity

From the desire to know the field on each and every position on a closed surface surrounding the scattering medium, arises the concept of time reversal cavity developed in [32]. The authors demonstrated that there is not necessary to reverse in time the acoustic field at any given position in the considered volume, in order to achieve the time reversal process. By exploiting the Helmholtz-Kirchhoff principle, it is sufficient to reverse only the field and its derivative on the surface that encloses the volume. Therefore, by having an enclosed surface of acoustic transducers around the complex medium and a source emitting a divergent acoustic wave within the medium is possible to measure the field over the whole surface, in

order to have total knowledge of the field in the medium. This field $\Psi(r,t)$ in a volume V can be described by a surface integral:

$$\Psi(r,t) = \oint_S [G(r_S,r,t)\otimes\nabla\Psi(r_S,t) - \nabla G(r_S,r,t)\otimes\Psi(r_S,t)]dS \tag{2.5}$$

In the equation above, ∇ is the normal derivative operator at the point r_S on the surface S outward the volume V. The function $G(r_S,r,t)$ represents the Green function between the points r_S and r in the propagation medium. This Green function is defined as the solution of the propagation equation considering a point source in space and time as a Dirac function: $\delta(t)\delta(r_S - r)$. Considering the field in equation (2.5) is the solution of the acoustic wave equation, it is easy to compute the time reversed field $\Psi(r,-t)$ associated with the convergent waves that retraces the waves originally emitted. Thus, this cavity allows to the initial divergent waves emitted through the medium to return to their source.

Time reversal experiments typically consist of two steps. The first step is the recording step, in which an acoustic source is emitting a short pulse. The transducers forming the time reversal cavity record the outgoing field $\Psi(r_S,t)$ and its normal derivative $\nabla\Psi(r_S,t)$ on the surface S enclosing the heterogeneous medium.

The second step is called the time-reversed or reconstruction step. From equation (2.5), the field after time reversal $\Psi^{TR}(r,t)$, can be deducted from the reversed field $\Psi(r_S,t)$on the surface S as:

$$\Psi^{TR}(r,t) = \oint_S [G(r_S,r,t)\otimes\nabla\Psi(r_S,-t) - \nabla G(r_S,r,t)\otimes\Psi(r_S,-t)]dS \tag{2.6}$$

During this phase, each of the antennas of the cavity becomes a source which is emitting the field in the opposite direction and in reversed chronology.

Considering two point-like sources located at positions r_1 and r_2 inside the cavity which emit each a divergent wave with the field described by $\{G(r_1,r,\omega),\nabla G(r_1,r,\omega)\}$ and $\{G(r_2,r,\omega),\nabla G(r_2,r,\omega)\}$, previous mentioned Helmholtz-Kirchhoff theorem is expressed as:

$$\oiint_S [G(r_2,r,\omega)\nabla\, G^*(r_1,r,\omega) - \, G^*(r_1,r,\omega)\nabla G(r_2,r,\omega)]dS = j\omega \iiint_V [G^*(r_1,r,\omega)\delta(r-r_2) - G(r_2,r,\omega)\delta^*(r-r_1)]\, dV \tag{2.7}$$

Considering the sources are real: $\delta^*(r-r_1)=\delta(r-r_1)$ and by using the reciprocity of the medium: $G(r_1,r_2,\omega)=G(r_2,r_1,\omega)$, equation (2.7) becomes:

$$\oiint_S [G(r,r_2,\omega)\nabla\, G^*(r_1,r,\omega) - \, G^*(r_1,r,\omega)\nabla G(r,r_2,\omega)]dS \\ = -2i\omega\, \Im\{G(r_1,r_2,\omega)\} \tag{2.8}$$

where $\Im$ represents the imaginary part.

Therefore, the time-reversed focal spot is governed by the imaginary part of the Green‟s function. Returning in time domain, equation (2.7) becomes:

$$\oiint_S [G(r_2,r,t)\otimes\nabla\, G(r_1,r,-t) - \, G(r_1,r,-t)\otimes\nabla G(r_2,r,t)]dS \\ = \iiint_V [G(r_1,r,-t)\otimes\delta(r-r_2) - G(r_2,r,t)\otimes\delta(r-r_1)]\, dV \tag{2.9}$$

which gives the following proportionality:

$$\Psi^{TR}(r,t) \propto G(r_1,r_2,-t) - G(r_1,r_2,t) \tag{2.10}$$

where, $G(r_1,r_2,t)$ is the causal Green‟s function and $G(r_1,r_2,-t)$ is the anticausal Green‟s function creating the converging wave. Also, $-G(r_1,r_2,t)$ is the diverging wave that appears due to energy conservation at the focus position [43].

Figure 2.1 presents the first step of a time reversal process.

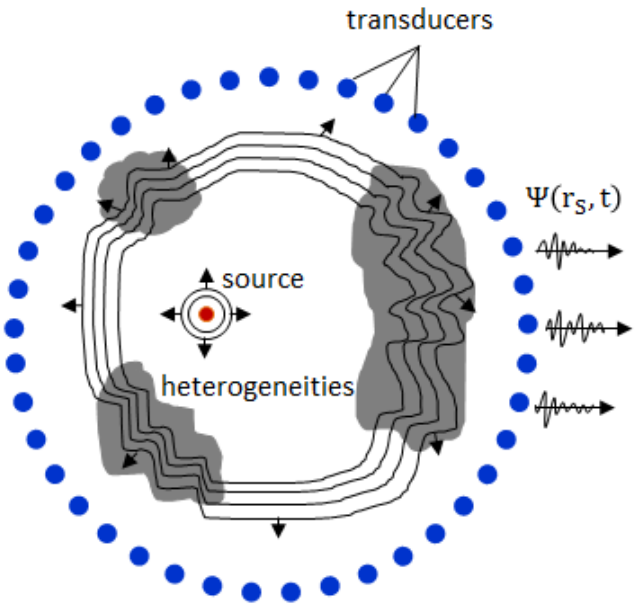

Figure 2.1 Time reversal process using time reversal cavity: - first step

In a first phase, a point-like source is placed inside a time reversal cavity consisting of acoustic transducers enclosing a heterogeneous environment where a spherical wave is emitted and it propagates through the medium towards the transducers. The scattered field $\Psi(r_S, t)$ and its normal derivative $\nabla\Psi(r_S, t)$ are recorded on each element on the surface S. In the second step, shown in Figure 2.2, each transducer on the surface contouring the medium becomes a source which emits the previously time reversed recorded field, $\Psi(r_S, -t)$.

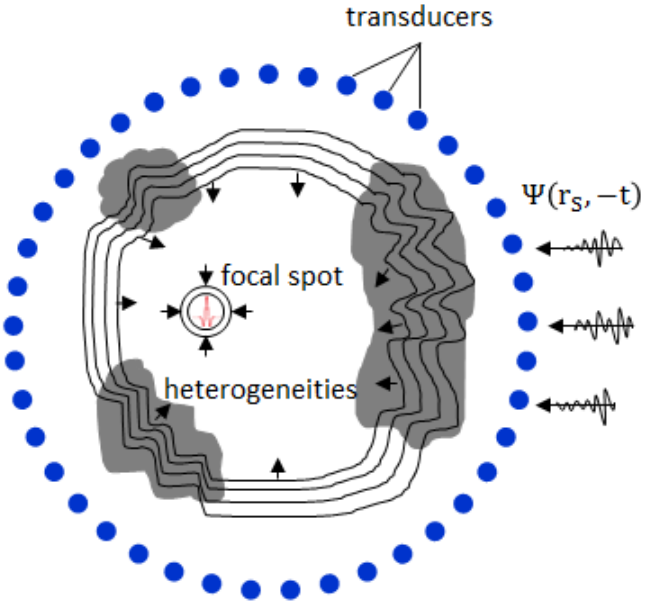

Figure 2.2 Time reversal process using time reversal cavity: - second step

This backward propagating field retraces all its paths and converges on the location of the source where a second diverging wave is created. Due to the reemission of the field and its normal derivative from the enclosing surface S, the time reversal process in the cavity reaches the classical limit of diffraction. Considering a homogeneous medium, the Green function between two points r_1 and r_2 can be written as:

$$G(r_1, r_2, \omega) = \frac{exp[ik(r_2 - r_1)]}{k(r_2 - r_1)} \tag{2.11}$$

From equation (2.8), the time-reversed field obtained at the focus is expressed as:

$$\Psi^{TR}(r, \omega) = -2i\omega \frac{sin[k(r_2 - r_1)]}{k(r_2 - r_1)} \tag{2.12}$$

Thus, the focal spot width, which is defined at the half of the height of the zone where the energy in concentrated, is given to tend to half-wavelength for the used frequency range.

The concept of time reversal cavity allows theoretically the acoustic waves to retrace their paths. According to Shannon‟s theorem, an ultrasonic field is correctly spatially sampled

if the distance between two transducers is inferior to half-wavelength. Therefore, practically it is difficult to realize such spherical cavity for ultrasonic waves.

2.2.3 Time reversal mirror

As opposed to the cavity concept, a time reversal mirror (TRM) uses arrays of transducers with a limited aperture, facilitating their fabrication. In the first step of the process, shown in Figure 2.3, the mirror records the divergent wave emitted from the source over the finite aperture of the transducers. Since the cavity records the acoustic wave in all the direction around the source, there is an obvious loss of information in case of the mirror, because in the second step, only a part of the emitted wave will be reversed in time and sent back, leading to a degradation of the focal spot.

Figure 2.3 presents the first phase of a time reversal process using a time reversal mirror consisting in an array of transducers as a cut of the time reversal cavity.

Figure 2.4 presents the second phase of a time reversal process using a time reversal mirror as cut-off part of the time reversal cavity.

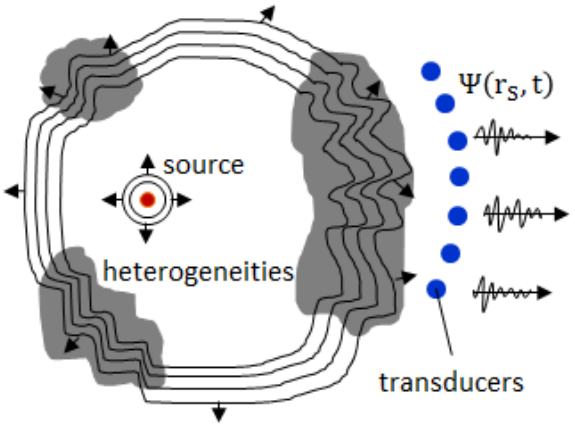

Figure 2.3 Time reversal process using time reversal mirror: - first step

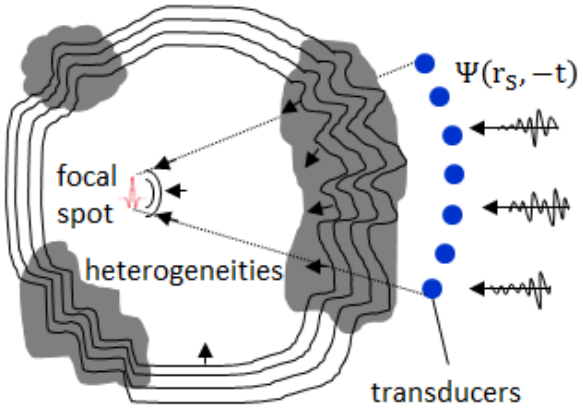

Figure 2.4 Time reversal process using time reversal mirror: - second step

The width, δ, of the focal spot is given by the ratio between the focal distance, F and the length, D of the mirror: $\delta \approx \frac{\lambda F}{D}$. Therefore, the use of TRM in homogeneous media has many limitations.

Nevertheless, even if the limited aperture of the time reversal mirror degrades the quality of the focal spot, it will be shown in the following paragraphs that in complex media, the aperture is virtually increased.

2.2.4 Time reversal in random media

First experiments showing the reversibility of transient acoustic waves through a random medium using an acoustic time reversal mirror are reported in [44]. In spite of propagating through a high-order scattering medium, the time reversed waves are found to converge to their source position and recover their original form. As opposed to an ideal time reversal experiment that implies an emitting acoustic source, an inhomogeneous environment, which requires measuring the Green functions over a closed surface surrounding the source, these experiments shown a surprising resolution, smaller than the theoretical limit for the mirror"s aperture in free space.

The experiment consists of the two steps of a time reversal process: the recording step and the reversing in time of the registered waves. The used random medium consists of a collection of identical steel rods immersed in water.

Figure 2.5 shows the first step of a time reversal process using a random medium placed between the acoustic source and the time reversal mirror.

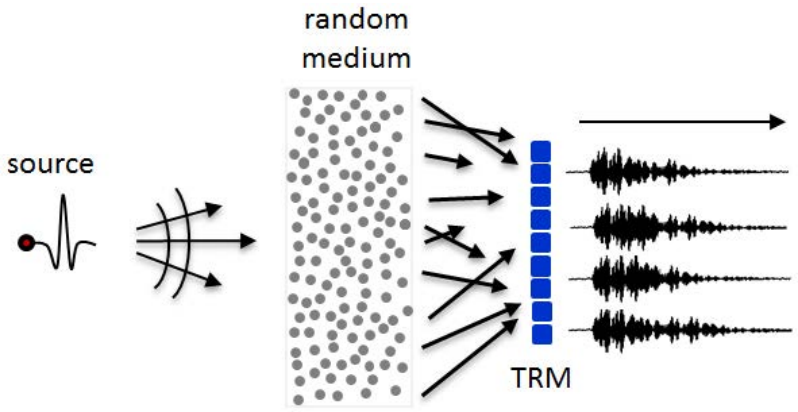

Figure 2.5 Time reversal process using a random medium: - first step

By emitting a large bandwidth wave through a high-order scattering medium, the wave will experience multiple scattering events before arriving at the TRM. The mirror, consisting of piezoelectric transducers, will record the variations of the ultrasonic scattered signal in

order transmit them reversed in time, in the second step. The recorded signals spread over a time much longer than the incident pulse, due to the propagation within the medium.

During the second step of the process, shown in Figure 2.6, after the time reversal mirror no longer receives energy from the medium, it switches from the recording state to the emitting state and the signals received on each of the transducers are reversed in time and transmitted back through the medium.

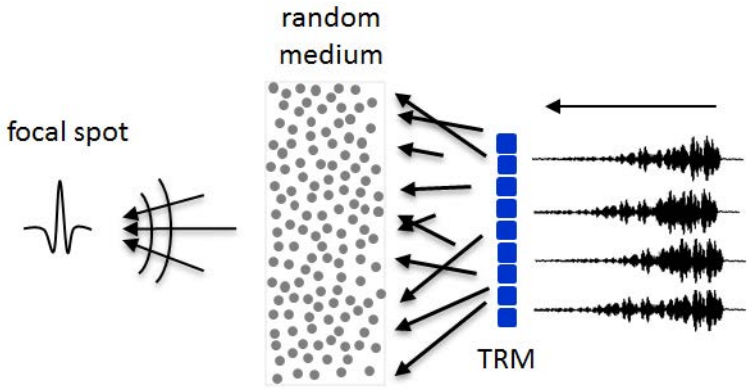

Figure 2.6 Time reversal process using a random medium: - second step

The waves experience the reversed scattering events before reaching the position of the initial source, causing them to retrace all of their paths and focus on the incident emitting location. Using the random medium allows the time reversal mirror to virtually increase its aperture, resulting in a better focusing quality. It may seem less obvious, since the TRM receives just a part of the emitted field and the recorded signals may have lost the information about their source.

Considering the absence of the medium, as shown in Figure 2.7, the dimension of the focal spot in homogeneous medium is given by: $\delta_{HM} = \frac{\lambda F_{HM}}{D_{HM}}$ where F_{HM} is the focal distance, D_{HM} is the length of the mirror and λ is the wavelength.

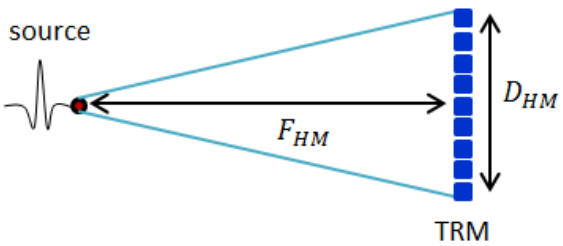

Figure 2.7 The aperture of TRM in homogeneous medium

However, when placing the random medium between the source and the TRM, as shown in Figure 2.8, the mirror receives the scattered wave coming from the whole length of the complex medium. The length of the medium being greater than the length of the time

reversal mirror, gives it a virtual increased aperture, due to the propagation of multiple scattered waves which otherwise would not be registered on the TRM.

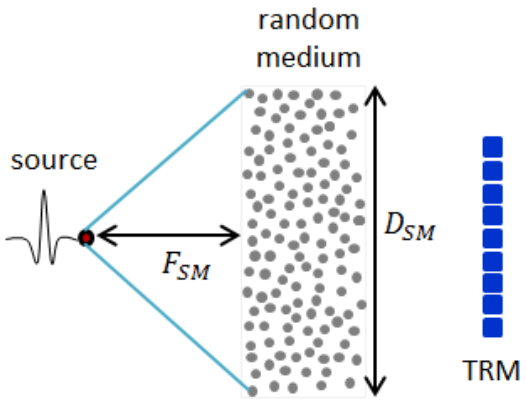

Figure 2.8 The virtual aperture of TRM using a random medium

Figure 2.9 shows an example of a time signal recorded on the TRM which can be divided in two parts: the ballistic wavefront corresponding to the direct path from the source to the TRM and the coda corresponding to the multipath scattering within the medium.

The spatial information corresponding to those long paths within the random media are encoded temporally within the coda of the impulse response between the source and the TRM. Those paths are re-excited in the second step of the TR experiment and are summed coherently both in space and time.

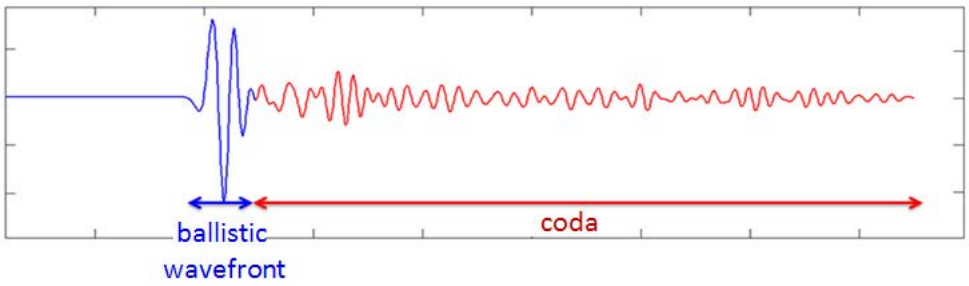

Figure 2.9 Example of time signal registered on TRM

The width δ_{SM} of the focal spot can therefore be estimated by: $\delta_{SM} = \frac{\lambda F_{SM}}{D_{SM}}$, where F_{SM} is the focal distance to the scattered medium, D_{SM} is the length of the scattered medium and λ is the wavelength.

In comparison, the width of the focal spot, δ_{RM} in complex media is smaller than the width of the focal spot, δ_{HM} in homogeneous media. Therefore, the time reversal mirror uses complex environments to appear wider than it is, resulting in a focusing quality that does not depend on the mirror aperture.

2.2.5 Time Reversal in a waveguide

Another way to virtually increase the limited aperture of the time reversal mirror is by using propagation in a waveguide. Due to the multiple reflections on the walls, the apparent aperture of the TRM is significantly enlarged. An important difference between random media and waveguides is the arrival time of each wavefront. As opposed to the multiple scattering medium, within the waveguide, the time of arrival is predictable, depending on a few characteristics as the length and the depth of the waveguide.

The spatial and temporal focusing using a small number of transducers in an ultrasonic waveguide is demonstrated in [45] with an experiment conducted in a waveguide whose interfaces are plane are parallel, as show in Figure 2.10.

A point-like ultrasonic source is located on one side of the waveguide and can be used either as a source or a hydrophone. At the other end of the waveguide, is placed a TRM made of a linear array of 96 transducers identical to the transducer source. The total length of the channel is $L = 740\ mm$, which is the order of 20 time the water depth $H = 40\ mm$.

The experiment is divided in three steps. In the first step, the source transmits a pulsed wave, during the second one, a temporal window selects one part of the transmitted wave which has been recorded by the TRM and these data are time reversed and retransmitted along the same channel.

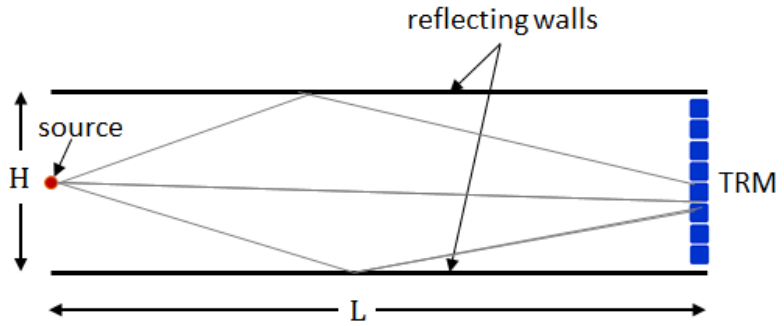

Figure 2.10 Waveguide experiment schematic

In the last step, the time-reversed field is measured in the source plane by the transducer source which is used as a hydrophone. Both the temporal compression and the spatial focusing of the time reversed field around the source were analyzed.

Figure 2.11.a) shows the signal received on one transducer of the time reversal mirror. After the time reversal experiment, the signal recorded at the location of the source shown in Figure 2.11.b) presents temporal compression.

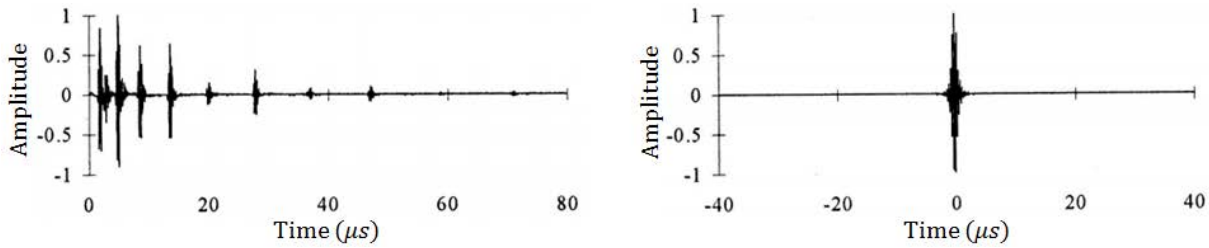

a) b)

Figure 2.11 Waveguide - temporal signals [45]:
a) temporal signal measured on TRM; b) time-reversed signal measured at source location;

Concerning the spatial focusing, Figure 2.12 presents the directivity pattern of the time-reversed field in the source plane, showing the focal spot much smaller for the waveguide compared with a free space experience.

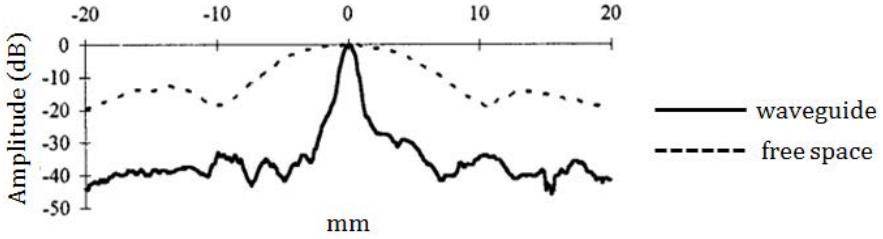

Figure 2.12 Directivity pattern [45]

The improvement in the quality of focusing is interpreted by the principles of mirror images in a medium bounded by two mirrors. For an observer located at the position of the source, the TRM appears to be a periodic vertical array of TRM images, as shown in Figure 2.13.

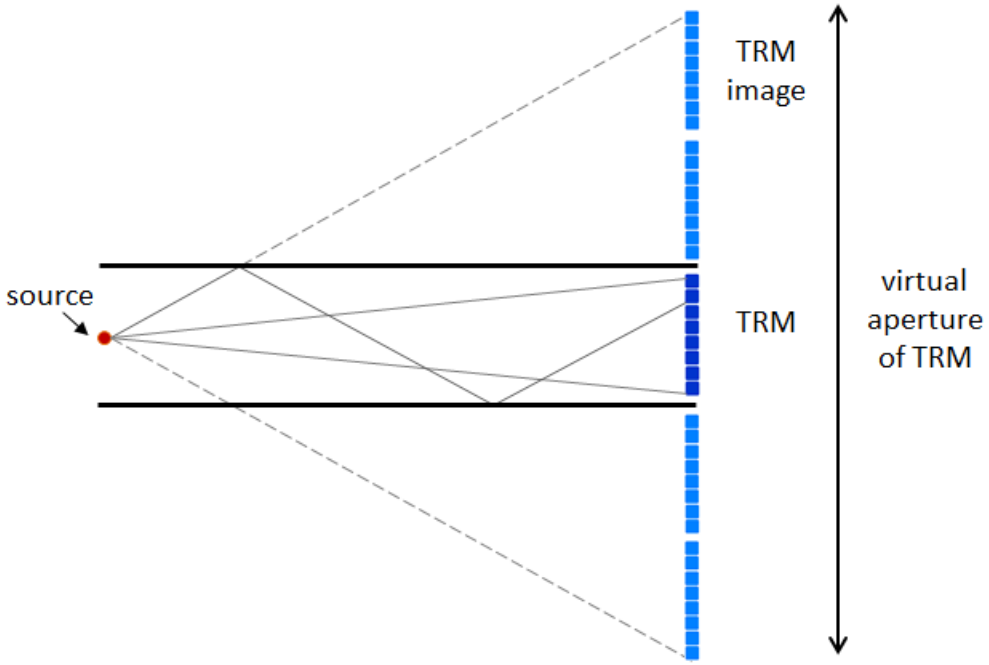

Figure 2.13 The principle of mirrors

If the first ten received echoes are considered, the virtual aperture of the TRM is approximately ten times larger than the real aperture. However, it was observed that the width of the focal spot increases linearly with the inverse of the number of echoes selected by the time-reversed window. When more than eight echoes are selected, the width of the focal spot no longer changes due to the apodization of the TRM images, showing that the effective aperture of the TRM is directly related to the duration of the time reversal window.

2.2.6 Time Reversal in a chaotic cavity

Closed cavities with reflecting walls provide such boundary condition that no information can escape from the system and a reverberant acoustic field is created. It has been shown theoretically and experimentally [46], [47], [48] that operating in a closed cavity, a time reversal experiment can be achieved using only one channel, by measuring the field at one point over a long time period and re-emitting the time-reversed signal from the same position. The experiment depicted in Figure 2.14, is a two-step process which presents the acoustic waves generated and detected by transverse transducers fixed on aluminum cones.

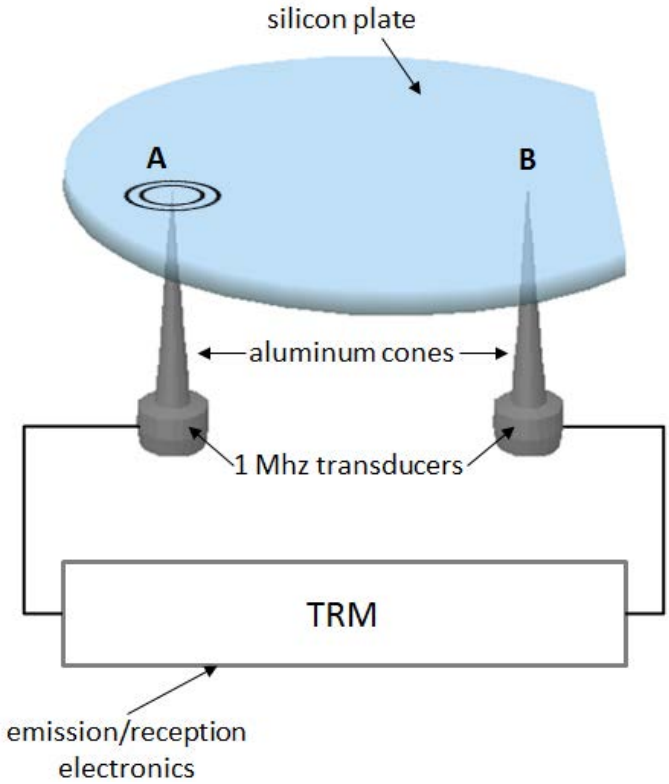

Figure 2.14 Chaotic cavity experimental setup

In the first step, the transducer located at point A emits a short ultrasonic pulse which propagates and is reflected on the walls of the cavity. The emitted omnidirectional signal has 1 μs duration. The other transducer located at point B, registers a very long chaotic signal

resulted from multiple reflection of the incident signal along the edges of the cavity. Corresponding to hundreds of reflections along the boundaries, the received signal continues for more than 50 ms [49].

In the second step of the experiment, a portion of 2 ms of the signal received on transducer B is reversed in time and re-emitted. Figure 2.15 shows the initial signal emitted by transducer A, the very long chaotic signal received by transducer B and the time-reversed signal received by transducer A after the second step of the experiment.

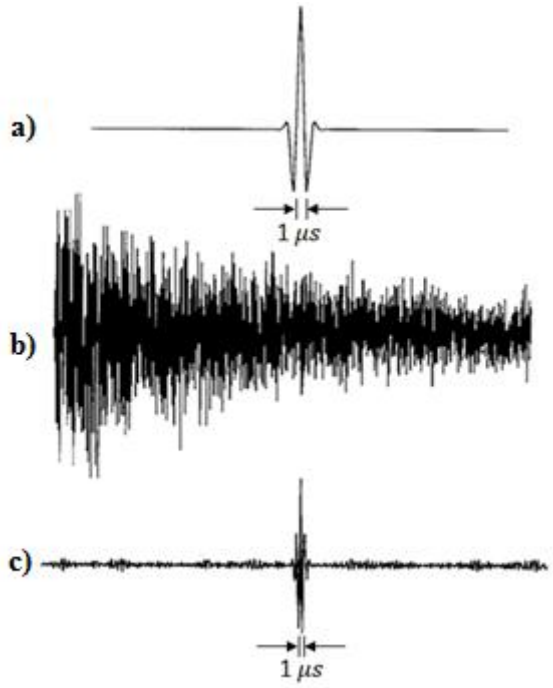

Figure 2.15 Chaotic cavity - time signals [41]:
a) initial pulse emitted by transducer A; b) signal received by transducer B;
c) time-reversed signal received by transducer A

A focus is obtained at the point of emission of the initial pulse. The boundaries reflect the time-reversed signal and the field converges towards the origin from all directions giving a circular spot, as one could be obtained with a closed time-reversal cavity covered with transducers.

2.3 Time reversal in electromagnetics

As opposed to acoustic waves, electromagnetic waves consists of magnetic and electric field vectors oscillating perpendicular to each other and perpendicular to the direction of propagation of the wave, given by the pointing vector, $\vec{S}$ [50]:

$$\vec{S} = \vec{E} \times \vec{H} \tag{2.13}$$

Transverse waves present polarization which is conventionally referred to the direction of the electric field. In linear polarization, the fields oscillate in a single direction, horizontally or vertically. In circular polarization, the fields rotate in a plane at a constant rate, as the wave travels. Depending on the direction of rotation, the polarization can be right hand circular polarization or left hand circular polarization [51].

Electromagnetic waves in free space are solutions to Maxwell‟s equations. There are two types of solutions, spherical waves and plane waves which can be considered as the limiting case of spherical wave.

The waveform of both types of waves can be an arbitrary time function which can be decomposed in individual sinusoidal components, called monochromatic, each containing a single frequency, amplitude and phase. A monochromatic wave can be characterized by its frequency, peak amplitude, direction of propagation and polarization.

2.3.1 Time-symmetry of electromagnetic waves

Considering Maxwell equations:

$$\nabla \cdot D(\vec{r},t) = \rho(\vec{r},t) \tag{2.14}$$

$$\nabla \cdot B(\vec{r},t) = 0 \tag{2.15}$$

$$\nabla \times E(\vec{r},t) = -\frac{\partial}{\partial t} B(\vec{r},t) \tag{2.16}$$

$$\nabla \times H(\vec{r},t) = \frac{\partial}{\partial t} D(\vec{r},t) + J(\vec{r},t) \tag{2.17}$$

where $D(\vec{r},t)$ is the electric displacement, $\rho(\vec{r},t)$ is the charge density, $B(\vec{r},t)$ is the magnetic induction, $E(\vec{r},t)$ is the electric field, $H(\vec{r},t)$ is the magnetic field and $\vec{J}(\vec{r},t)$ is the electric current density.

The electric displacement, D and the magnetic induction B, have the following expressions:

$$D(\vec{r},t) = \varepsilon(\vec{r},t) \otimes E(\vec{r},t) \tag{2.18}$$

$$B(\vec{r},t) = \mu(\vec{r},t) \otimes H(\vec{r},t) \tag{2.19}$$

where, $\varepsilon(\vec{r},t)$ is the electric permittivity and $\mu(\vec{r},t)$ is the magnetic permeability.

By applying the time reversal operator T, to the electric and magnetic fields, is obtained:

$$TE(\vec{r},t) = E(\vec{r},-t) \tag{2.20}$$

$$TH(\vec{r},t) = -H(\vec{r},-t) \tag{2.21}$$

$$TD(\vec{r},t) = D(\vec{r},-t) \tag{2.22}$$

$$TB(\vec{r},t) = -B(\vec{r},-t) \tag{2.23}$$

Similar to acoustic waves, these equations describing the electromagnetic waves are time-symmetric. Therefore, the propagation medium is reversible assuming that the permittivity and the permeability tensors are themselves time-symmetric.

Considering the wave propagation linear, the general relation between the electric displacement, D and the electric field, E as presented in equation (2.18), for time-symmetric fields, becomes $D(\vec{r},-t) = \varepsilon(\vec{r},-t) \otimes E(\vec{r},-t)$. However, the propagation medium being reversible, $D(\vec{r},-t) = \varepsilon(\vec{r},t) \otimes E(\vec{r},-t)$ is also a solution of the propagation equations. Hence, the electric permittivity is time-symmetric: $\varepsilon(\vec{r},t) = \varepsilon(\vec{r},-t)$. Similarly, starting from equation (2.19) describing the relation between the magnetic induction, B and the magnetic field, H the time-symmetry of the magnetic permeability is deduced: $\mu(\vec{r},t) = \mu(\vec{r},-t)$ [43].

2.3.2 Reciprocity of electromagnetic waves

Likewise acoustic time reversal experiments, in order to achieve a time reversal process in electromagnetics, it is necessary to prove that it is sufficient to measre the electric and magnetic fields on a closed surface S around the volume V, containing the source.

Two sources with the current densities J_1 and J_2 give the electric fields E_1, E_2 and the magnetic fields H_1, H_2. The reciprocity property is given by Lorenz theorem:

$$\oiint_S [E_1 \times H_2 - E_2 \times H_1] dS = \iiint_V [J_2 \cdot E_1 - J_1 \cdot E_2]\, dV \tag{2.24}$$

Using this property is possible to transpose the time reversal cavity in electromagnetics. Instead of observing the electric field and the currents at any point of space, it is sufficient to know the electric and magnetic fields on an enclosed surface surrounding the source.

In order to establish the reciprocity of electromagnetic waves in heterogeneous media, the volume of integration V, is considered a sphere of infinite radius. Hence, the left-hand term of equation (2.24) tends to zero, giving the principle of reciprocity:

$$\iiint_V J_1(\vec{r}) \cdot E_2(\vec{r},\omega)\, dV = \iiint_V J_2(\vec{r}) \cdot E_1(\vec{r},\omega) dV \tag{2.25}$$

Assuming the sources are elementary dipole antennas with the currents $J_1(\vec{r}) = -i\omega\, p_1\delta(\vec{r}-\vec{r}_1)$ and $J_2(\vec{r}) = -i\omega\, p_2\delta(\vec{r}-\vec{r}_2)$, where p_1 and p_2 are the polarization densities of the dipole antennas, equation (2.25) can be written as:

$$p_1 \cdot E_2(\vec{r}_1,\omega) = p_2 \cdot E_1(\vec{r}_2,\omega) \tag{2.26}$$

The roles of the emitting and receiving antennas can be interchanged. The electric field towards the source is unchanged when the position of the emitter and receiver are replaced with each other.

2.3.3 Electromagnetic time reversal cavity

Starting from the principle of reciprocity, the notion of electromagnetic time reversal cavity arises. Considering two sources as elementary dipole antennas, their current vectors are $J_1(\vec{r}) = i\omega\, p_1\delta(\vec{r}-\vec{r}_1)$, $J_2(\vec{r}) = i\omega\, p_2\delta(\vec{r}-\vec{r}_2)$, where p_1 and p_2 are the polarization densities of the dipole antennas. Their respective electric fields are $E_1(\vec{r},\omega)$, $E_2(\vec{r},\omega)$ and their magnetic fields are $H_1(\vec{r},\omega)$, $H_2(\vec{r},\omega)$. Assuming a paraxial plane-wave approximation:

$$H(\vec{r},\omega) = \frac{\vec{n}\times E(\vec{r},\omega)}{\eta} \tag{2.27}$$

where $\eta = \sqrt{\frac{\mu}{\varepsilon}}$ is the wave impedance and n is the normal to the cavity surface. Lorentz equation of reciprocity can be written as:

$$\frac{2}{\eta}\oiint_S E_1^*(\vec{r},\omega)\times E_2(\vec{r},\omega)dS = -\iiint_V \{J_2(\vec{r},\omega)E_1^*(\vec{r},\omega) - J_1^*(\vec{r},\omega)E_2(\vec{r},\omega)\}\, dV \tag{2.28}$$

Taking into consideration the expression of currents J_1 and J_2 and the theorem of reciprocity, equation (2.28) can be simplified as:

$$\frac{1}{\eta}\oiint_S E_1^*(\vec{r},\omega)\times E_2(\vec{r},\omega)dS = -i\omega\, p_2\vec{n}_2\Re\{E_1(\vec{r}_2,\omega)\} \tag{2.29}$$

Similarly to acoustics, the Green function has the analog dyadic Green function used to express the electric field as:

$$E(\vec{r},\omega) = i\omega\mu\iiint_V \vec{G}(\vec{R},\vec{r},\omega)J(\vec{r},\omega)dV \tag{2.30}$$

where, R is a point in the volume of integration.

Therefore, the electric fields E_1 and E_2 can be expressed as:

$$E_1(\vec{r},\omega) = -\omega^2 p_1 \mu \, \overleftrightarrow{G}(\vec{r}_1,\vec{r},\omega)\vec{n}_1 \tag{2.31}$$

$$E_2(\vec{r},\omega) = -\omega^2 p_2 \mu \, \overleftrightarrow{G}(\vec{r}_2,\vec{r},\omega)\vec{n}_2 \tag{2.32}$$

Considering the above expressions of the E field, equation (2.29) becomes:

$$k \oiint_S \overleftrightarrow{G}^*(\vec{r}_1,\vec{r},\omega)\vec{n}_1 \times \overleftrightarrow{G}(\vec{r}_2,\vec{r},\omega)\vec{n}_2 dS = \vec{n}_2 \Im\{\overleftrightarrow{G}(\vec{r}_1,\vec{r}_2,\omega)\}\vec{n}_1 \tag{2.33}$$

where, $k = \omega\mu/\eta$.

Due to the reciprocity of dyadic functions and considering the equation (2.27) is valid with any chosen vectors n, a similar expression as for acoustic theory, can be obtained:

$$k \oiint_S \overleftrightarrow{G}(\vec{r},\vec{r}_2,\omega) \, \overleftrightarrow{G}^*(\vec{r}_1,\vec{r},\omega) dS = \Im\{\overleftrightarrow{G}(\vec{r}_1,\vec{r}_2,\omega)\} \tag{2.34}$$

A source located at position r_1, is emitting while the field is registered on a closed surface by small electric dipoles which will re-emit the complex conjugate of the field with the same polarization. The field generated at any point r_2 is the imaginary part of the dyadic Green function which connects the points r_1 and r_2.

As in acoustics, the electromagnetic time reversal experiment consists of two steps. First of all, a source of current with the polarization along n_1 which is located inside the electromagnetic time reversal cavity emits a short electromagnetic pulse. Figure 2.16 shows the first step of time reversal process, while the second step is shown in Figure 2.17.

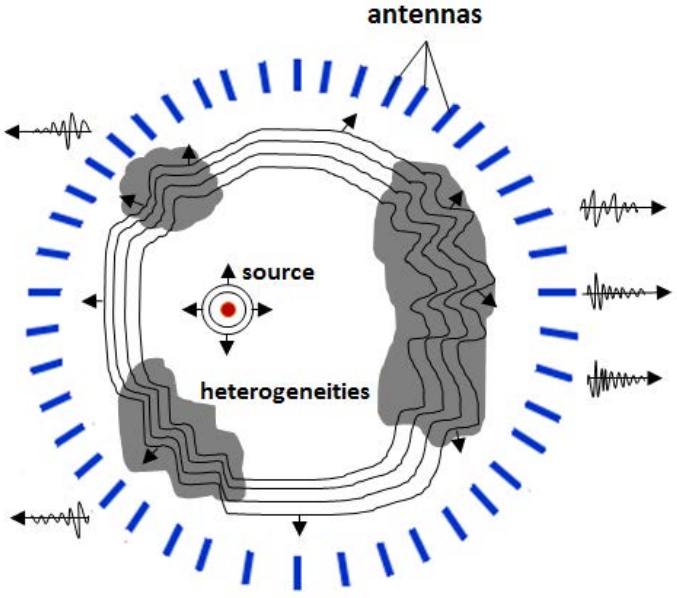

Figure 2.16 Time reversal process using electromagnetic time reversal cavity: first step

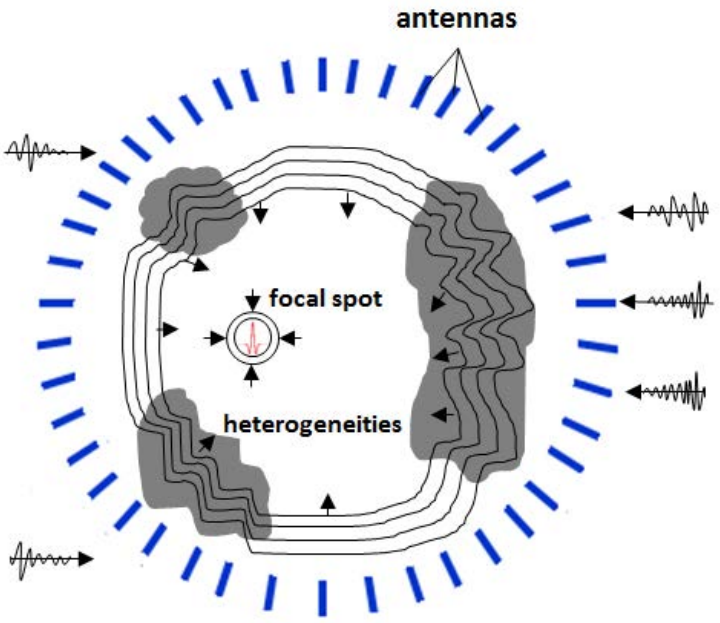

Figure 2.17 Time reversal process using electromagnetic time reversal cavity: second step

The generated spherical wave propagates through the heterogeneous medium being scattered multiple times. When the wave reaches the surface S contouring the source, the electric field $E(\vec{r},t)$ and the magnetic field $H(\vec{r},t)$ are recorded by antennas which are sensitive on different polarizations. The signals are digitized and stored in memory. The acquisition phase stops when there is no longer energy inside the cavity.

During the second step, the time-reversed versions of the electric field $E(\vec{r},-t)$ and the magnetic field $-H(\vec{r},-t)$ are transmitted by each antenna of the surface S. The time reversed waves are as well, solutions of the Maxwell equations.

The field emitted by the antennas on the surface S in all the volume of the cavity is equal to the field generated by the source, but reversed in time; therefore, those waves will converge towards their initial source location.

2.3.4 Time Reversal within a reverberation chamber

A reverberation chamber is a large, in terms of wavelength, high quality cavity whose boundary conditions are continuously and randomly perturbed by means of a rotating conductive tuner or stirrer which is an assembly of large metallic reflectors moved to different orientations in order to achieve different boundaries conditions. If this Faraday cage is overmoded enough, the field can be described as a combination of numerous modes. The real and imaginary parts of the field follow identical Gaussian distributions [52] and the time averaged field is formed by uniformly distributed plane waves coming from all directions. Figure 2.18 shows a reverberation chamber photograph.

Figure 2.18 Reverberation chamber at IETR research laboratory

There are two analytical approaches that can be used prior the design step in order to provide basic knowledge. A formal solution, rather difficult to obtain, involves the direct solution of Maxwell‟s equations with time varying boundary conditions. A second approach implies linear combinations of basic eigenmodes of the unperturbed cavity. Time-dependent expansion coefficients are taken to represent the field and to satisfy approximately the boundary condition on the surface of the rotating mode stirrer. A necessary condition for the validity of this method is that the total number of eigenmodes with eigenfrequencies less than, or equal to the operating frequency be large enough for the chamber sizes [53]. The overlap in the frequency domain of an infinite number of modes can be summed up to the frequency response of a single mode [54].

The reverberation chamber can be set for two mode of testing. One of them is „Mode Stirred‟, when the paddle is continually turned with RF energy applied for a full paddle revolution and the speed is varied to meet specific requirements of the device under test. The second one is „Mode Tuned‟ when the paddle is stepped to a position and FR is applied for a dwell time sufficient to exercise the equipment.

An electromagnetic time-reversal experiment in a reverberation chamber is reported in [55]. The time reversal technique is applied in a reverberation chamber to perform analysis of antenna efficiency. It was shown how an overmoded cavity can be used in combination with TR technique to measure UWB antenna efficiency. The resonant cavity (RC) favors TR since

it offers a very dense multipath environment. Moreover the SNR of the focusing signal is proportional to the bandwidth of the input signal.

The method requires an arbitrary waveform generator and a digital storage oscilloscope and the two antennas are placed in the reverberant chamber in a way which minimizes the direct coupling.

The experiment consists of four steps. In a first step, antenna 1 connected to the waveform generator transmits a pulse to antenna 2 connected to the oscilloscope. During the second step, the signal received on antenna 2 is sampled and recorded while in the third step the signal is time reversed, amplified and then transmitted via the waveform generator to antenna 1. In the last step of the measurement procedure, the signal is focused at antenna 2 due to the high level of multipath propagation inside the chamber and the large bandwidth of the signal. The receiving antenna behaves as a time reversal mirror and the signal travels backwards. Figure 2.19 show the corresponding signal to each described step.

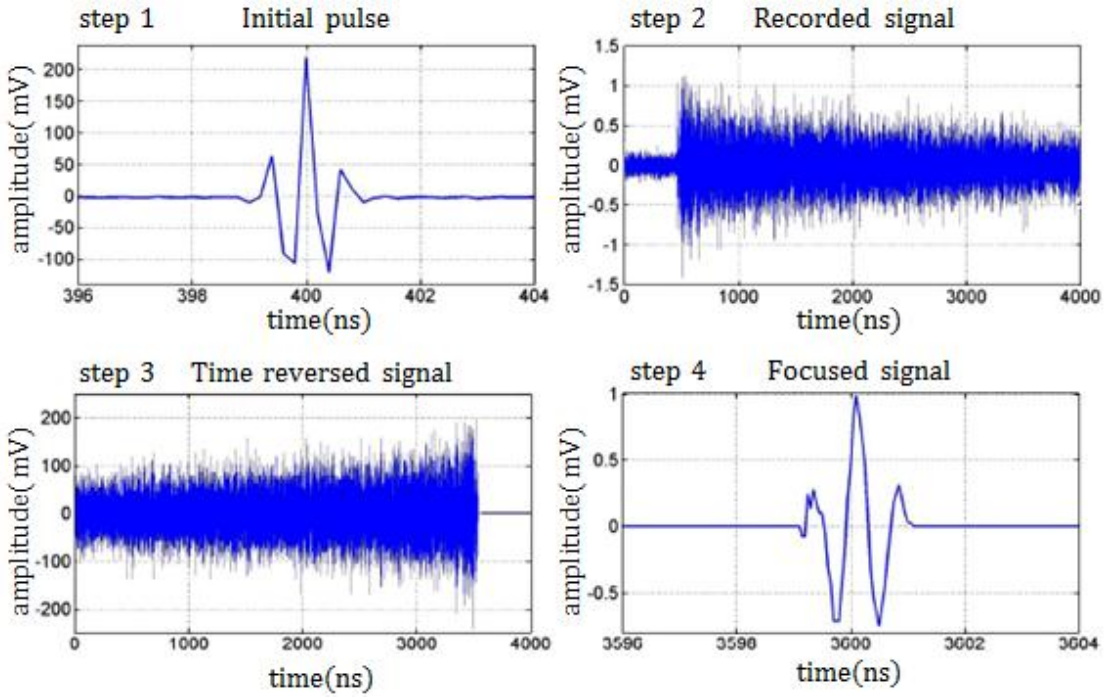

Figure 2.19 Time signals corresponding to measurement steps [55]

The time reversal efficiency measurement protocol consists of performing the above described procedure for antenna 1, the efficiency of which could be unknown and for antenna 2, considered as the reference antenna. Then, the same procedure is performed using the same transmitted pulse and antenna 1 but the antenna under test is substituted for antenna 2. The UWB efficiency of the unknown antenna is a function of the energy ratio of signals from step 1 and step 4 in Figure 2.19. A good agreement between simulation and time reversal

efficiency measurement results for an excitation pulse centered at 1.8 GHz, on the bandwidth of interest is shown in figure Figure 2.20

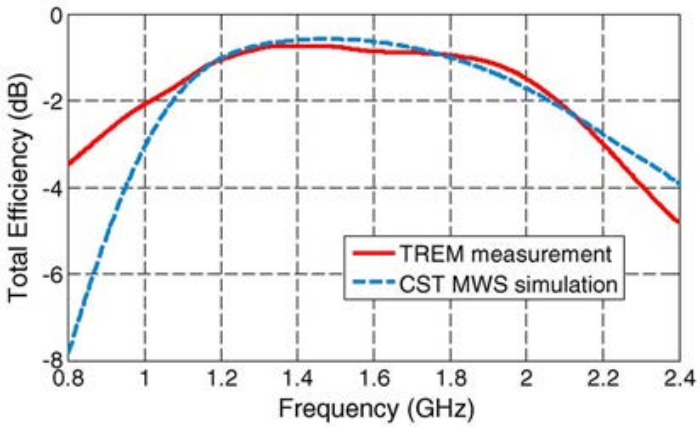

Figure 2.20 Total efficiency [55]

Time reversal is used as a tool to improve the accuracy of results due to temporal and spatial focus. Using TR process yields a fast measurement and the determination of efficiencies with respect to frequency is enhanced through the spectral analysis of simple pulses with higher SNR.

2.3.5 Radar imaging using a time reversal beamformer

There is a wide domain of time reversal applications in electromagnetics from UWB communications [56], microwave imaging [57], imaging of a target in cluttered environment for radar applications [58], or beamforming [59], [60].

A new concept of passive antenna beamformer applied to realize a passive UWB phased array radar for target imaging is proposed in [61]. It is developed a $(1 \times N)$-ports device in which the weightings on output ports are applied by time reversal operation. The approach is validated experimentally by radiation pattern measurement of an array with four Vivaldi antennas, associated to a small reverberation cell beamformer. The aim of the study is to provide an optimized focalization by generating the channels impulses responses well fitted to time reversal, focusing a signal to the desired output port.

Figure 2.21 shows the principle used to study the feasibility the $1 \times N$ passive demultiplexer in order to achieve antenna beamforming. By independently controlling the signal sent to each element of the array, a passive beamformer can be obtained having the control signal contained in the input signal. The chosen input waveform will focus the signal on each output port simultaneously by using the appropriate control signals.

The received signal $p_k(t)$ on the output port k is expressed as:

$$p_k(t) = x(t) \otimes h_k(t) \tag{2.35}$$

where, $h_k(t)$ is the impulse response between the output port k and the input port and $x(t)$ is the input signal.

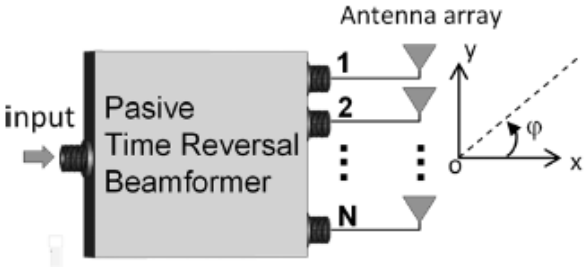

Figure 2.21 Principle of a $1 \times N$ passive beamformer [61]

Considering the impulses responses as known, than the input signal can be written as:

$$x(t) = \sum_{k=1}^{N} h_k^*(-t)\, x(t) \otimes a_k(t) \tag{2.36}$$

where, $h_k^*(-t)$ is the time-reversed complex conjugate of the kth channel impulse response and $a_k(t)$ is a magnitude and delay operator used to apply weightings on each output port.

The radiated field $s(t, \varphi)$ of the overall array is expressed as:

$$s(t, \varphi) = \sum_{k=1}^{N} x(t) \otimes h_k(t) \otimes e_k(t, \varphi) \tag{2.37}$$

where, $e_k(t, \varphi)$ is the radiated field of antenna k in the plane of the antennas array.

Furthermore, considering $\beta_k \cdot R_{kk}(t) + b_k(t)$ being the result of the impulse response autocorrelation which is formed by a short pulse at focalization time $t = 0\, s$, with a maximum amplitude β_k and the resulting deterministic noise $b_k(t)$ and assuming that the coupling between antennas can be neglected, the radiated field is expressed as:

$$s(t, \varphi) = \sum_{k=1}^{N} [\beta_k \cdot R_{kk}(t) \otimes a_k(t) \otimes e_k(t, \varphi)] \tag{2.38}$$

where:

$$e_k(t, \varphi) = g_k(t, \varphi) \otimes \delta\left(t - (k-1)\frac{d \cdot \sin(\varphi)}{c}\right) \tag{2.39}$$

where, $g_k(t, \varphi)$ is the radiation pattern of the kth antenna, d is the separation distance between each antenna and c is the speed of light.

To realize a beam-steering operation, $a_k(t)$ is expressed as:

$$a_k(t) = a_k \cdot \delta(t - \tau_k) \tag{2.40}$$

where, $\tau_k = -(k-1)\frac{d \cdot \sin(\varphi_0)}{c}$

The desired steering angle is denoted by φ_0 and a_k corresponds to the magnitude weighting. In case of impulse responses imbalance, a_k can be used to equalize the magnitude β_k of the pulses. Therefore, all the pulses generated on each port will be coherently summed in φ_0 direction at the focalization time. The appropriate choice of the input signal leads to passive beamforming operation.

The experimental validation of the feasibility of passive beamforming by the use of time reversal operation is performed using a 1×4 beamformer constituted by a small reverberation cell, as shown in Figure 2.22.

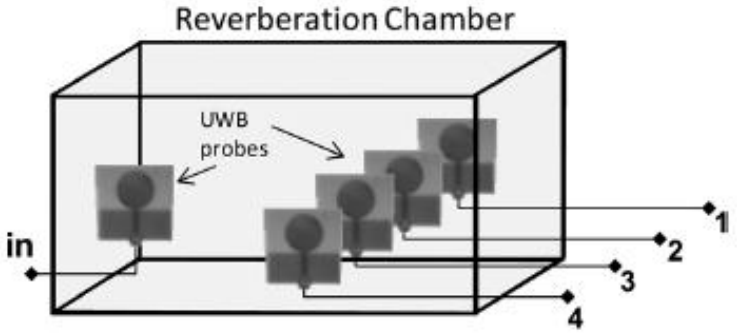

Figure 2.22 Experimental 1×4 beamformer [61]

Using a network vector analyzer (VNA), each transfer function $H_k(f)$ was measured in the range $2 - 5\ GHz$. Equation (2.37) is computed in frequency domain:

$$S(f,\varphi) = X(f) \cdot \sum_{k=1}^{N} H_k(f) \cdot G_k(f,\varphi) \cdot e^{\frac{j \cdot (k-1) \cdot 2\pi \cdot f \cdot d \cdot \sin(\varphi)}{c}} \tag{2.41}$$

where $X(f) = (\sum_{k=1}^{N} H_l^*(f) \cdot A_l(f))$.

In order to fit the appropriate delay, the weighting operator $A_l(f)$ is calculated as a phase ramp for each frequency. The signal $s(t,\varphi)$ is obtained by performing the inverse Fourier transform. Figure 2.23.a) shows the normalized signal $s(t,\varphi)$ for $\varphi_0 = 0°$ presenting the radiated field focused into a narrow time instant. Figure 2.23.b) presents the radiation patterns at focalization time for different steering angles, shoeing that the radiation pattern reaches its maximum at the specified angle.

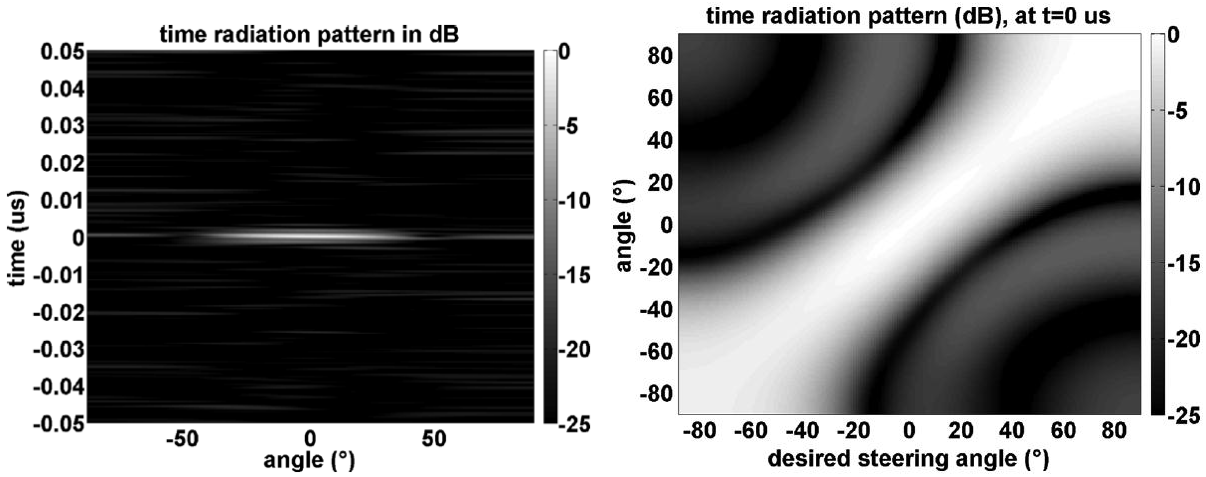

a) b)

Figure 2.23 Radiation pattern [61]

Beam-steering operation with time reversal is realized by using a small reverberation cell as beamformer to provide efficient impulse channel responses.

Moreover, the principle is applied to UWB radar imaging using four Vivaldi antennas as the transmitter array, a UWB omnidirectional monopole as the receiver and two cylindrical metal posts as targets. Figure 2.24.a) presents the setup.

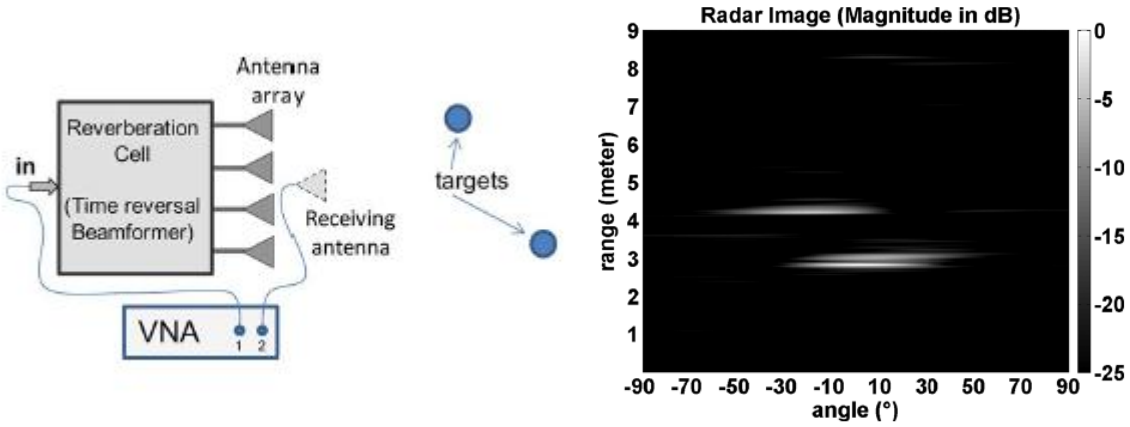

a) b)

Figure 2.24 a) Radar imaging setup; b) radar imaging using TR beamformer [61]

Figure 2.24.b) presents the obtained results. The targets localization is precise and consistent with the time and angular resolution of the system. The second signature around the closest target corresponds to the target support.

2.4 Time reversal focusing through a random medium

Focusing through a random medium in a time reversal process, takes advantage of the multipath propagation within the multiple scattering medium, in order to generate a focal spot of width given only by the medium, which acts as a lens.

The next section presents the effect of different apertures of the time reversal mirror on the focus, using a finite-difference time-domain (FDTD) simulation of a time reversal process focusing through a random medium. Moreover, by controlling the number and the positions of multiple sources, the experience provides multiple foci at the same time.

2.4.1 Basics of the finite-difference time-domain method

2.4.1.1 FDTD grid

The FDTD method is a numerical technique based on the finite-difference concept used to solve Maxwell‟s equations for electric and magnetic field distributions in the time and spatial domains [62]. This numerical analysis technique uses approximate solutions to the associated system of differential equations for modeling computational electrodynamics. With the cost of being generally computationally expensive, the FDTD method can solve complicated problems. A large amount of memory and computation time is required to find the solutions [63]. Being a time-domain method, the solutions cover a wide frequency range.

Considering the following Maxwell‟s equations

$$\nabla \times \vec{E} = -\mu \times \frac{\partial \vec{H}}{\partial t} \tag{2.42}$$

$$\nabla \times \vec{H} = \vec{J} \times \varepsilon \frac{\partial \vec{E}}{\partial t} \tag{2.43}$$

where, $\vec{H}$ and $\vec{E}$ are the magnetic and electric field vectors, μ is the magnetic permeability, ε is the electric permittivity and $\vec{J}$ is the density of the electric current. The FDTD method is based on the approximations of the spatiotemporal partial derivatives of arbitrary functions by the following finite differences:

$$\frac{\partial f(x_j)}{\partial t} \approx \frac{f\left(x_j + \frac{\Delta x_j}{2}\right) - f\left(x_j - \frac{\Delta x_j}{2}\right)}{\Delta x_j} \tag{2.44}$$

$$\frac{\partial g(t)}{\partial t} \approx \frac{d\left(t + \frac{\Delta t}{2}\right) - g\left(t - \frac{\Delta t}{2}\right)}{\Delta t} \tag{2.45}$$

where $x_j = x, y, z$ and the central differences, Δx_j and Δt are discretized steps in space and time, respectively. A spatiotemporal lattice in three dimensions is expressed by: $(x, y, z, t) = (i\Delta x, j\Delta y, k\Delta z, n\Delta t)$ where, i, j, k, n are integer indices.

The principle in the FDTD approach is to model the propagation of an incident electromagnetic wave into a volume of space which contains the studied structure. Space is

sliced up into box-shaped cells which are small compared to the wavelength.

The FDTD method requires the discretization of time and space. Therefore, samples in time and space must be specified in order to perform a simulation. Usually, at least ten cells per wavelength are desired to ensure an adequate representation.

2.4.1.2 Boundary conditions

Wave propagation phenomena extending to infinity needs the truncation of the computational domain to a finite domain, in order to numerically model it. To reduce the undesired reflections, the boundaries must be treated [64]. The most commonly used grid truncation techniques are differential type ABC (Absorbing Boundary Conditions) obtained by factoring the wave equation and allowing a solution which permits only outgoing waves and PML (Perfectly Matched Layers) a material-based boundary condition which are defined so that fields are dampened as they propagate into an absorbing medium.

Although the FDTD grid was commonly terminated by local ABCs, due to relatively high reflections errors experienced with local ABCs, the truncation boundary had to be extended sufficiently far off such that evanescent near-fields were amply decayed and waves would not impinge on the boundary near grazing incidence [65]. The change to PML introduced by Berenger in [66] brought an effective mean to terminate a FDTD grid in a similar manner to an anechoic chamber covered with absorbing materials. The perfectly matched layer allows an arbitrarily polarized broad-band electromagnetic wave impinging on a PML to penetrate into the medium with a rapidly decay and without reflection. As opposed to local ABCs, the PML can absorb both propagating and evanescent waves. The PML can also be perfectly matched to complex media, like lossy, dispersive, inhomogeneous or non-linear media.

2.4.2 The finite-difference time-domain simulations

2.4.2.1 Focusing on a position

Time reversal 2D simulations are carried out using a FDTD method with a PML function implemented in Matlab software, in order to show the properties of a time reversal process. Figure 2.25 shows a schematic representation of the FDTD computational domain.

The computational domain consists of 500×500 grid points where the wavelength is considered to be $\lambda = 10$ grid points. The medium which consists of a random collection of 0.2 index scatterers spread over a surface of 100×300 grid points with a density of 5%, is placed between the source and the time reversal mirror.

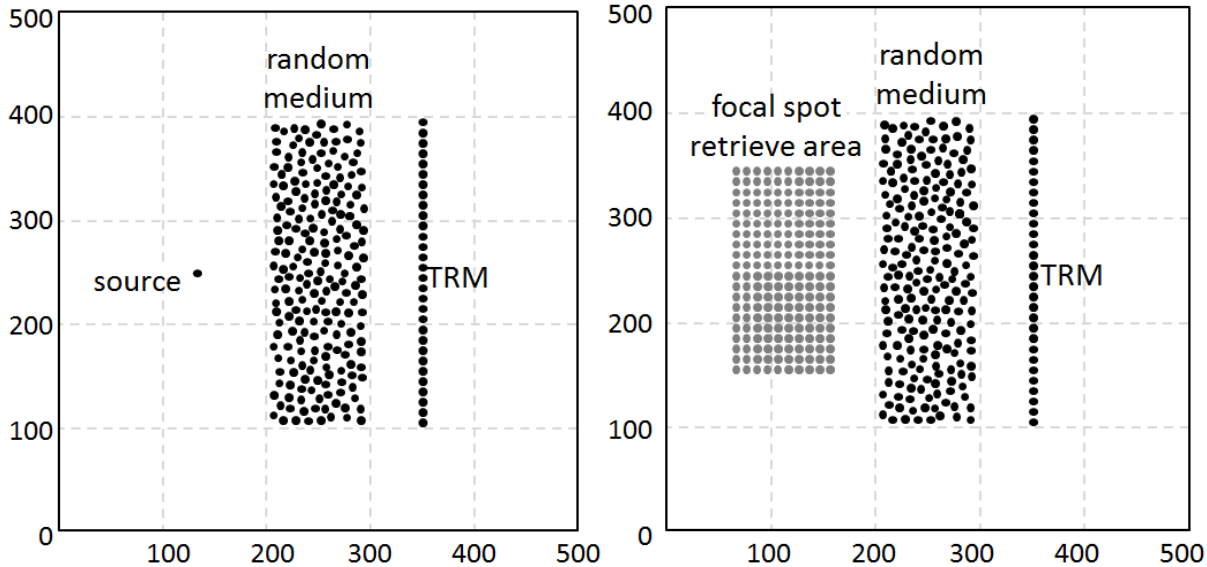

Figure 2.25 FDTD simulation setup: a) first step; b) second step

The simulation comprises the two steps of a time reversal process. In the first step, a point-like source is emitting a Gaussian pulse $s(r_0, t)$, on the frequency $f = 3\,MHz$ with 25% bandwidth, which is shown in Figure 2.26. The pulse propagates through the random medium, towards the TRM where the scattered signals are recorded.

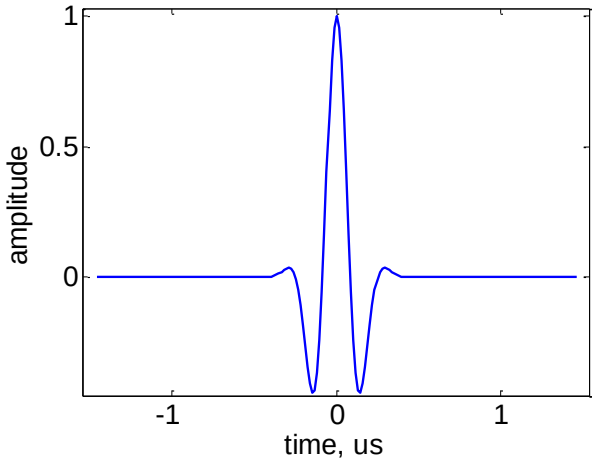

Figure 2.26 Emitted pulse

The time reversal mirror is an array formed by 61 elements with a distance of half of wavelength between them. Figure 2.27 shows captures from the first step of the process: Figure 2.27.a) shows the emission of the point-like source, Figure 2.27.b) shows the wave scattering through the random medium placed in front of the source and in Figure 2.27.c) is shown the scattered wave front while reaching the TRM.

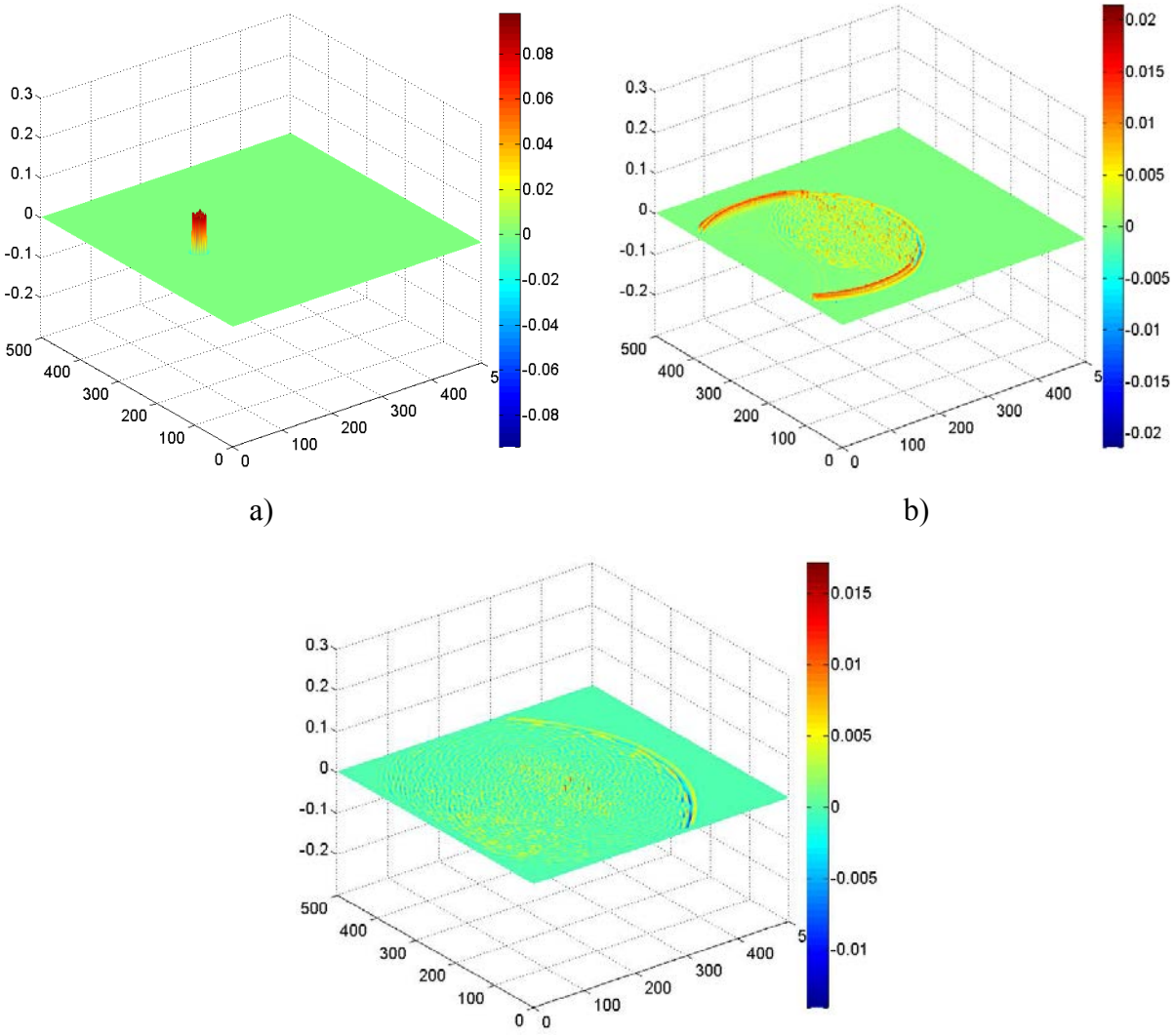

a) b)

c)

Figure 2.27 First step of time reversal FDTD simulation: a) emitting source; b) the wave scattered through the medium; c) scattered wave front reaching the TRM

Figure 2.28 shows the signal, $h(r_i, t)$, registered on the ith element of the TRM.

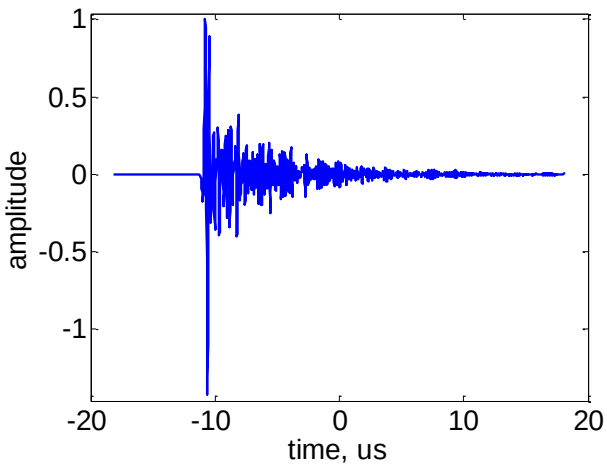

Figure 2.28 Time signal recorded on TRM

The scattered signal spreads over a time more than thirty times longer compared to the length of the initial pulse. Observing the waveform, it is distinguished between the long-wavelength coherent waves and the short-wavelength waves scattered by the medium [67]. The first arrival of the coherent ballistic wave is followed by the coda resulted from the scattering within the medium.

The impulse response registered on the TRM is the convolution between its corresponding Green function and the source signal [68] and can be expressed as:

$$h(r_i, t) = G(r_0, r_i, t) \otimes s(r_0, t) \tag{2.46}$$

where, r_0 represent the source position and r_i is the position of the ith element from the TRM.

Figure 2.29 shows captures from the second step of the process.

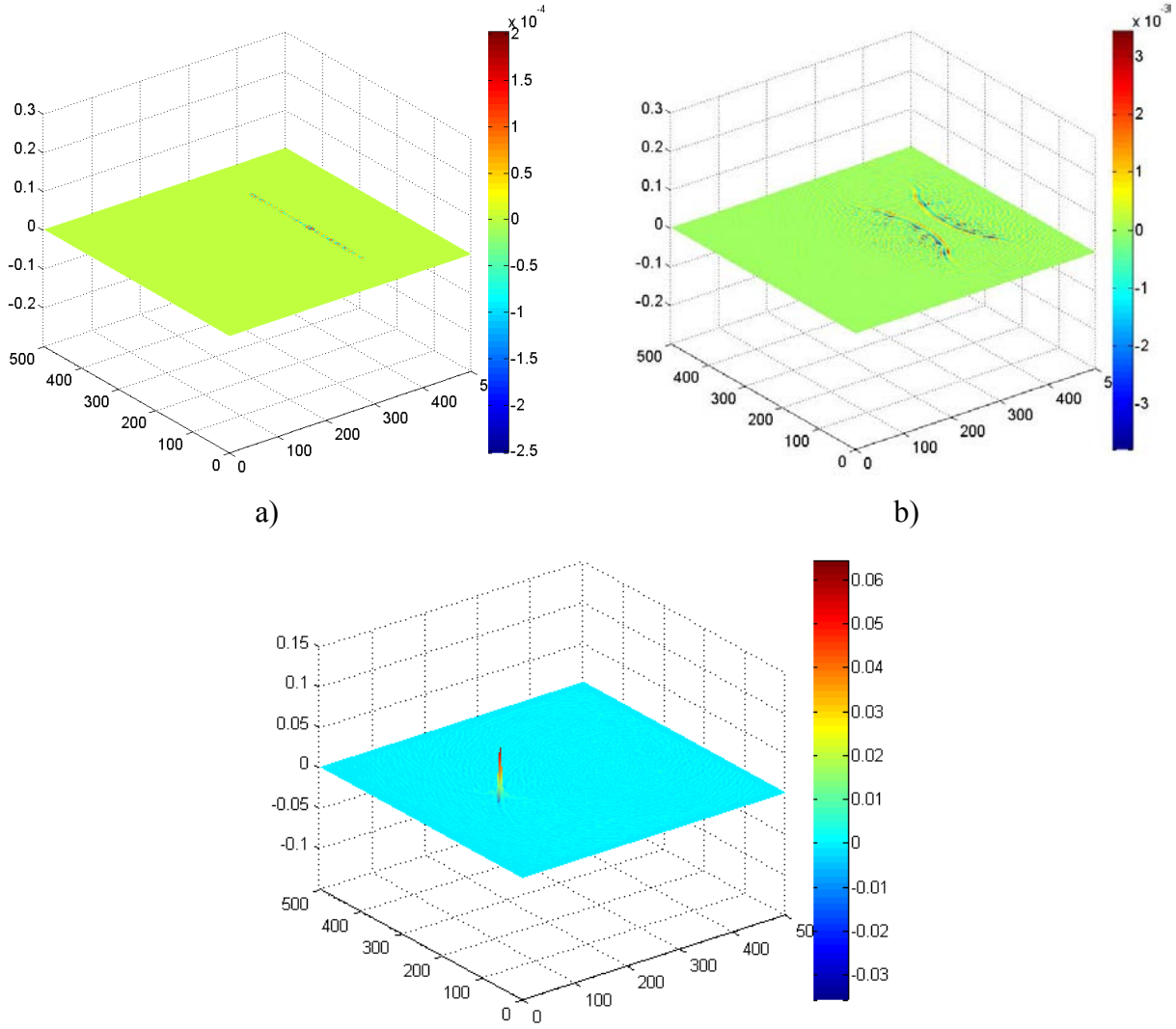

Figure 2.29 Second step of time reversal FDTD simulation:
a) emitting TRM; b) backward traveling wavefront; c) focusing on source position

Figure 2.29.a) shows the TRM elements emitting the time-reversed signals, Figure 2.29.b) shows the scattered wave front emitted by the time reversal mirror"s elements, which are omnidirectional, resulting in two mirrored wave fronts and in Figure 2.29.c) is shown the focused wave, when reaching the position of the initial source.

During the second step, the TRM emits the time reversed signals, $h(-t)$, which retrace their path backwards in order to focus on the position of the source.

One time reversed signal emitted from the TRM is expressed as:

$$h(r_i, -t) = G(r_0, r_i, -t) \otimes s(r_0, -t) \tag{2.47}$$

The signal registered on the position of the initial source, $s_F(r_0, t)$, is shown in Figure 2.30.

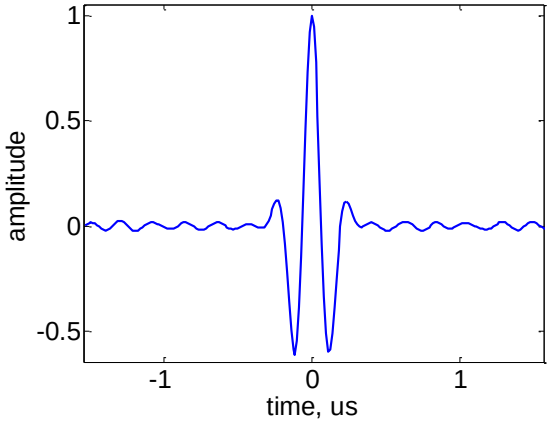

Figure 2.30 Time signal recorded on source location

The focused signal, $s_F(r_0, t)$, is expressed as the convolution between its corresponding Green function and the TRM emitted signal:

$$s_F(r_0, t) = G(r_i, r_0, t) \otimes h(-t) \tag{2.48}$$

Moreover, by expanding the expression of $h(-t)$, equation (2.48) becomes:

$$s_F(r_0, t) = G(r_i, r_0, t) \otimes G(r_0, r_i, -t) \otimes s(r_0, -t) \tag{2.49}$$

Figure 2.31 shows a 3D capture of the focal spot retrieve area.

Considering the 2D image of the focal spot, shown in Figure 2.32, transversal width is set along the abscissa and the longitudinal width is set along the ordinate of the figure.

Figure 2.33 shows the dimensions of focal spot for the case where the time reversal mirror has the same aperture as the medium, being spread over 300 grid points with 61 elements half-wavelength spaced. The longitudinal width is found $W_L = 0.75\,\lambda$ and the transversal width of the focal spot is $W_T = 0.34\,\lambda$.

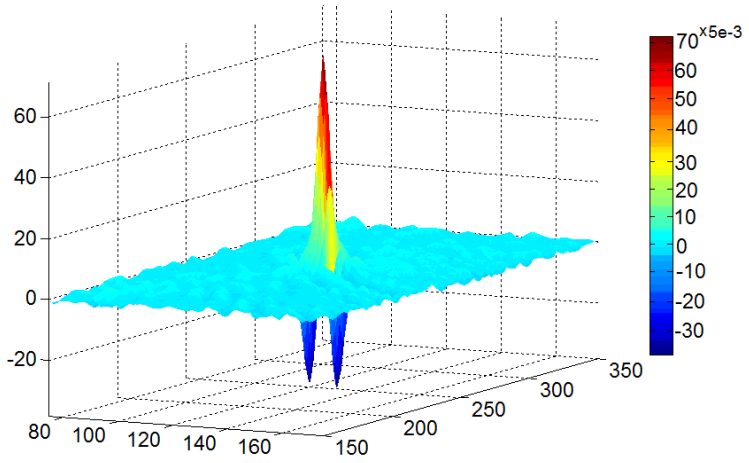

Figure 2.31 3D focal spot

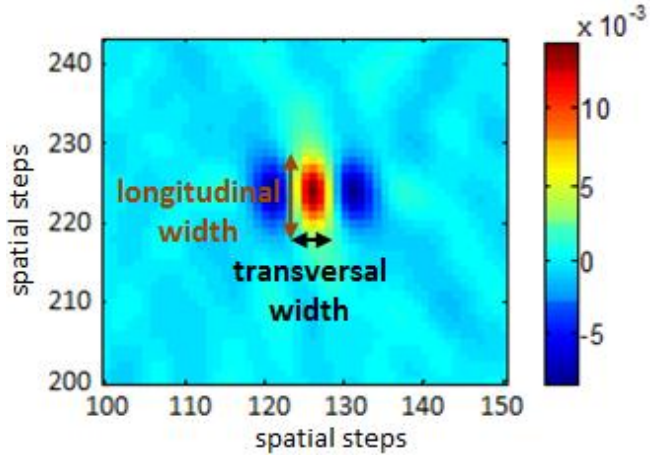

Figure 2.32 2D focal spot

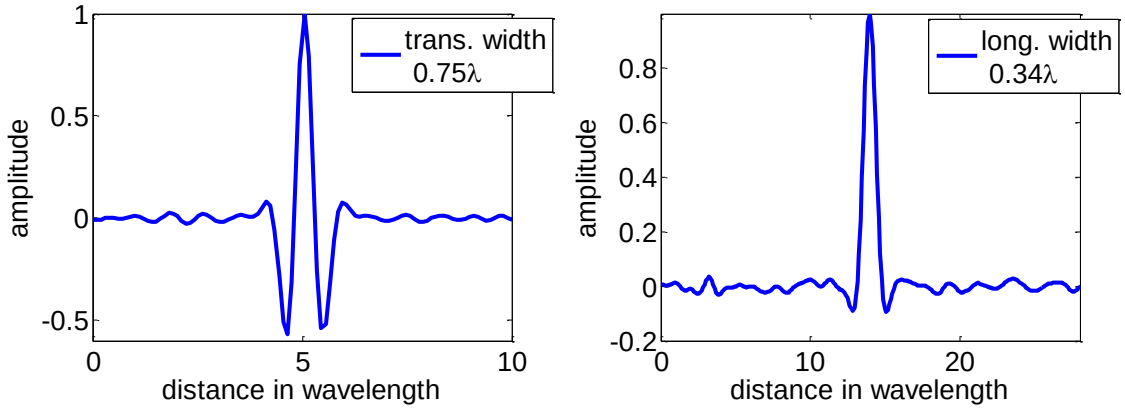

a) b)

Figure 2.33 Focal spot dimensions – 61 elements TRM:
a) longitudinal width; b) transversal width

Table 2.1 shows the dimensions, expressed in wavelengths, of the focal spot for different apertures of the time reversal mirror. In the first case, the aperture of the TRM is

equal to the length of the medium and has 61 elements. In each next case, the number of elements is decreased with ten and the aperture is decreased with 5 wavelengths until the case of one element TRM. Along with the focus dimensions: longitudinal and transversal width, the signal to noise ratio of the focused signal, defined as the ratio between the peak amplitude at the focal time and the standard deviation (RMS) of the symmetrically surrounding side-lobes [69], is also studied.

No.	Number of elements on TRM	TRM aperture (λ)	Longitudinal width (λ)	Transversal width (λ)	SNR
1.	61	30	0.75	0.34	127
2.	51	25	0.79	0.33	112
3.	41	20	0.80	0.33	118
4.	31	15	0.80	0.33	101
5.	21	10	0.80	0.32	72
6.	11	5	0.92	0.32	57
7.	1	0.1	2.13	0.33	19

Table 2.1 Random medium - focal spot dimensions for different apertures of TRM

For the first six situations, the dimensions of the focal spot do not have a significant variation. The last case, where the TRM is constituted by only one element, presents a bigger variation in longitudinal width, due to the low density of scatterers which allows the wave to reach the TRM in a direct path.

It is therefore verified that the focal spot does not depend on the width of the TRM but on the aperture of the medium. While, the focal spot does not have a remarkably variation when the number of elements of the TRM decreases, the signal to noise ratio shows an increased amplitude of the secondary lobes of the time signal for each case.

As a comparison, the same configurations of the TRM were simulated in the absence of the scattering medium. Table 2.2 shows the dimensions, expressed in wavelengths, of the focal spot for different apertures of the time reversal mirror.

No.	Number of elements on TRM	TRM aperture (λ)	Longitudinal width (λ)	Transversal width (λ)
1.	61	30	0,84	0.34
2.	51	25	1	0.33
3.	41	20	1.22	0.33

4.	31	15	1.61	0.33
5.	21	10	2.33	0.32
6.	11	5	3.96	0.32
7.	1	0.1	N/A	N/A

Table 2.2 Free space - focal spot dimensions for different apertures of TRM

For free space propagation, it can be clearly seen the dependence of the focal spot dimension on the aperture of the TRM. As the number of elements of TRM decreases, the longitudinal width increases progressively. The size of the focal spot is then given by $\delta = \lambda F/D$, where F is the focal distance and D is the aperture of the medium. In the last case, where the TRM has only one element, there is no focusing occurring, as shown in the 2D capture of the focal spot retrieve area, presented in Figure 2.34.

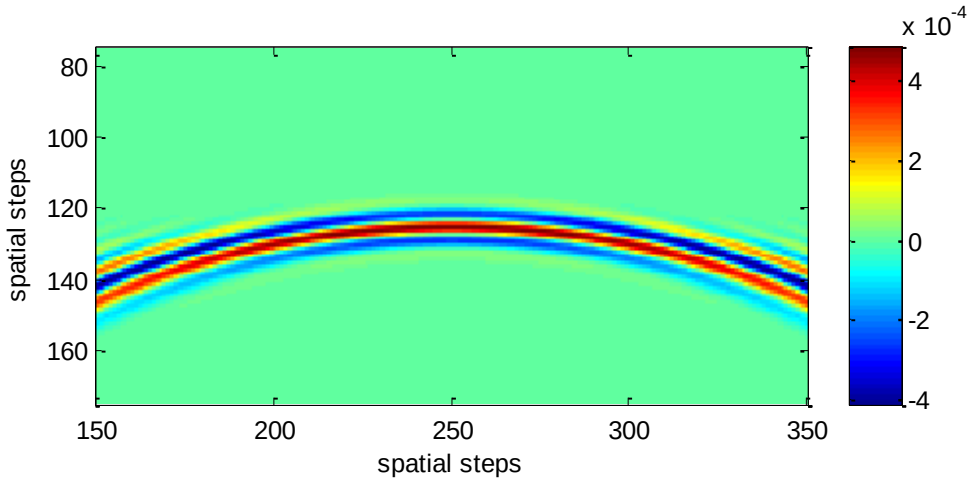

Figure 2.34 Focal spot dimensions – 1 element TRM in free space

As an example, Figure 2.35 shows the comparison between the longitudinal width of the focal spot for a TR process through a random and a TR process in free space.

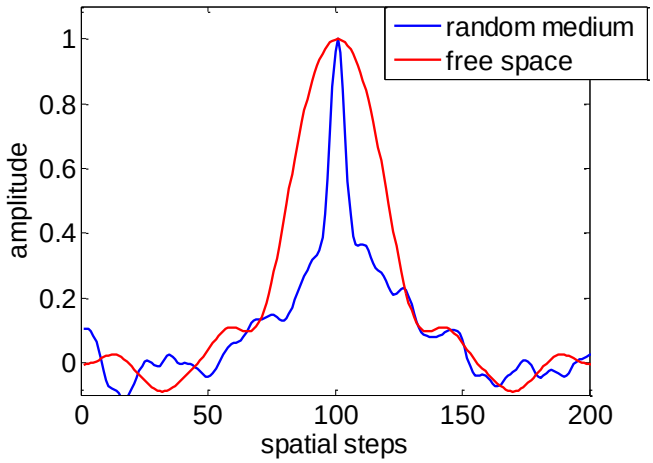

Figure 2.35 Focal spot dimensions – 11 elements TRM

In free space, while the TRM has a reduced aperture comprising 11 elements, the focal width is four times greater than in the presence of the medium. The effect of the medium is to act as a lens that focuses the signal on the source position, due to spatial frequencies that are redirected towards the mirror by the multiple scattering inside the medium, whereas in a free space environment, the spatial frequencies are lost.

2.4.2.2 Focusing on multiple positions

Considering the previous presented configuration, a multiple number of sources can be configured in order to focus on different positions. Figure 2.36 shows a schematic representation of the FDTD computational domain with multiple sources.

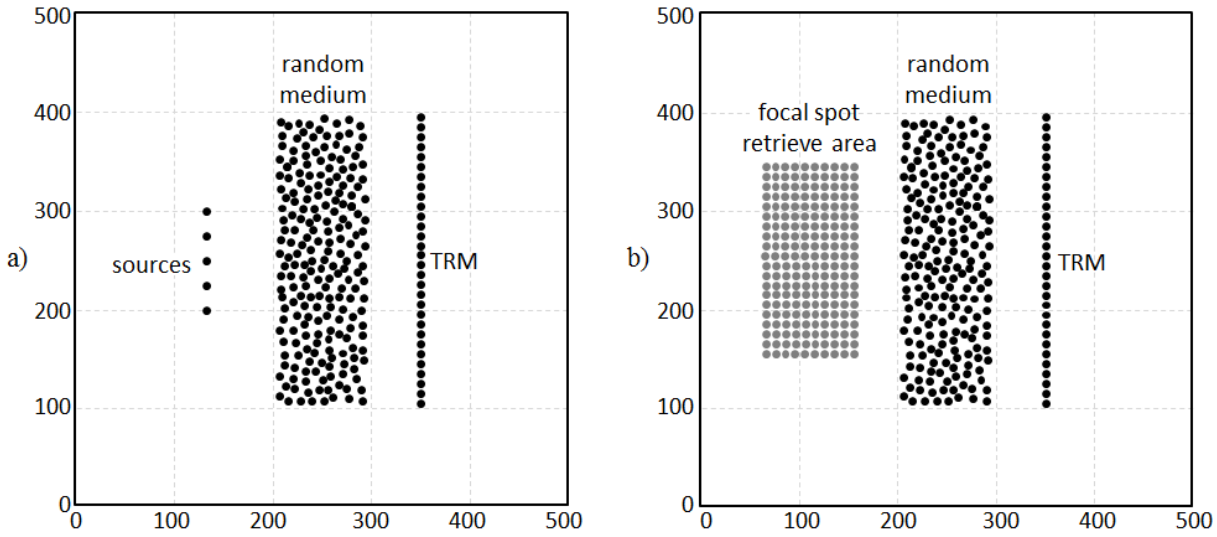

Figure 2.36 FDTD simulation setup: a) first step; b) second step

Depending on the number of point-like sources and the distance between them, the foci can be on multiple separated positions or can be combined in a larger focus. Figure 2.37 shows an example of distanced multiple foci with $3{,}5\lambda$ distance between the sources.

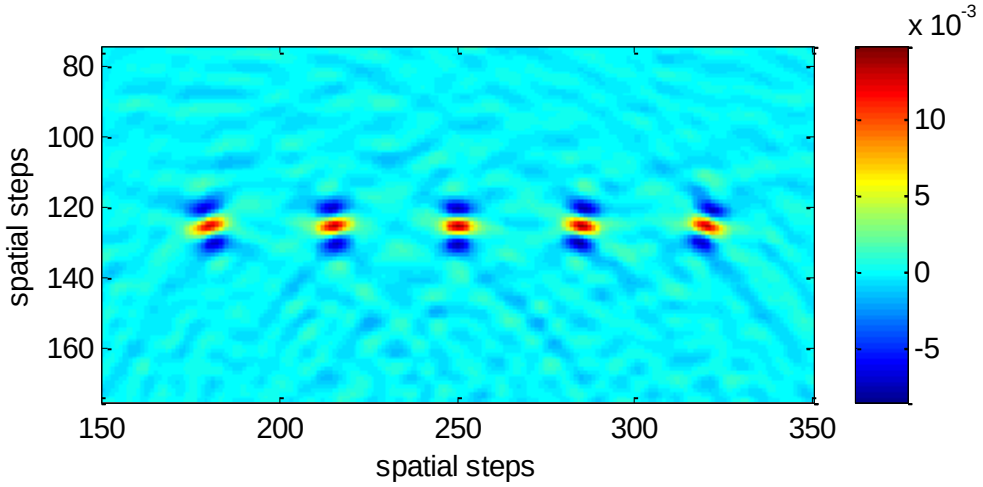

Figure 2.37 Multiple foci

When the distance between sources is half of wavelength, the longitudinal widths of all foci merges into one wide focal spot. Figure 2.38 shows examples of merged foci: a) one merged focus with $0{,}5\lambda$ distance between the sources, b) three coplanar merged foci and c) three merged foci in different planes.

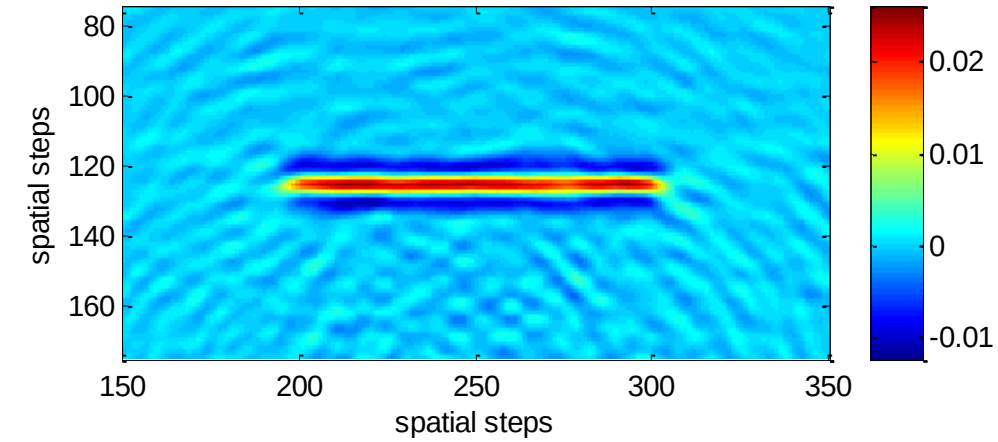

a)

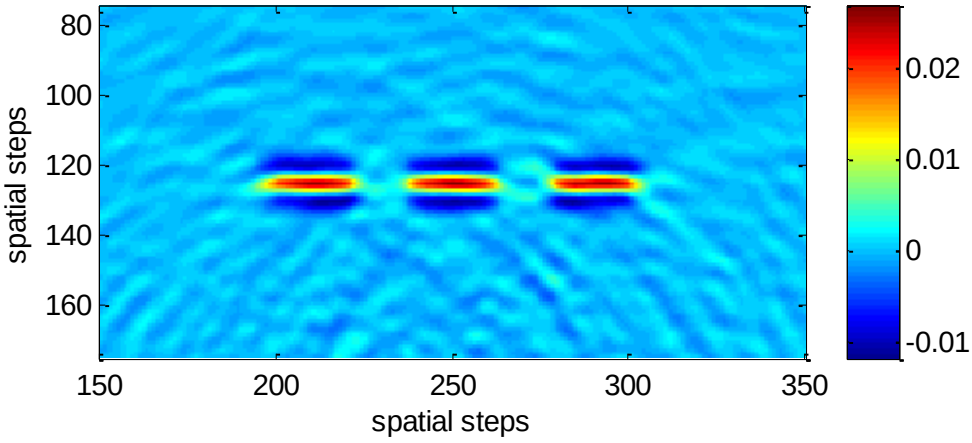

b)

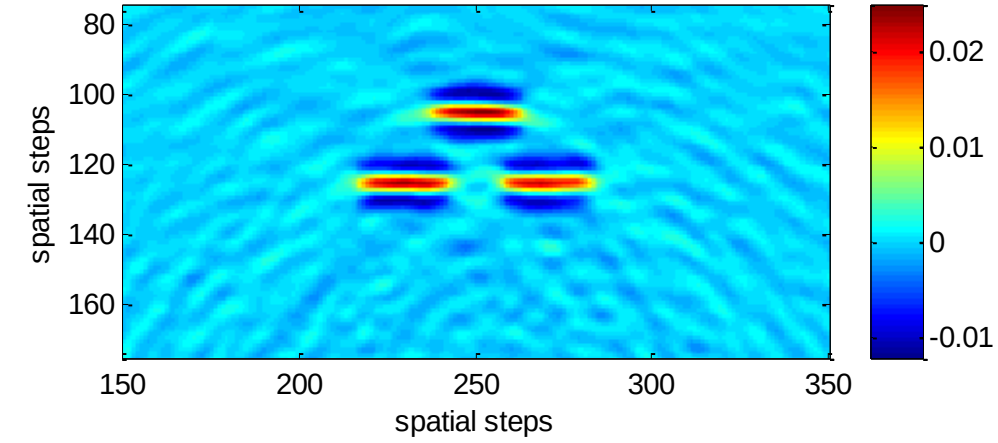

c)

Figure 2.38 Merged foci: a) one wide focus; b) three wide foci; c) three merged foci in different planes

For a distance between sources bigger than the longitudinal width of a focal spot, focusing on separate positions is achieved. The ability to focus on different positions of a target at once or to focus on a wide area is of considerably importance when considering to focus on an extended object which has dimensions bigger than the focal spot or to focus only on its scattering centers.

Using multiple sources in separate locations, the wave can be focused on different multiple positions at the same time. In addition to focusing on one position, by reducing the distance between sources, a wide focus can be achieved from merged one position foci.

2.5 Conclusion

This chapter presents a short introduction on time reversal method from its beginning on acoustics to electromagnetics, followed by simulations results in FDTD showing the properties of a random medium used in a time reversal process which yields a focus quality that is not dependent on the aperture of the TRM.

Starting from the invariance of the wave equation under a time reversal operation, the concept of time reversal cavity is developed. Time reversal process using time reversal cavity consists of two steps. In the first step, a source placed inside the cavity emits a short pulse and the transducers forming the cavity record the signal they receive. During the second step, the recorded signals are reversed in time and each transducer on the cavity surface becomes a source which emits the time-reversed signals. The backward propagating field retraces all its paths and converges on the location of the source in a focal spot.

Due to the difficult practical realization of such cavity, a time reversal mirror proves to be more accessible. A mirror is an array of transducers with a limited aperture which leads to a loss of information. Only a part of the emitted wave by the source and recorded in the first step will be time-reversed and sent back from the mirror in order to focus on the position of the source, generating a degradation of the focal spot.

Nevertheless, the limited aperture of the TRM can be virtually increased by using random media or waveguides. When using a random medium, the mirror receives scattered waves coming from the entire length of the medium, resulting in an increased aperture which gives a better focusing quality. By using a waveguide, due to the multiple reflections on the walls, the apparent aperture of the mirror increases significantly, compared with the use of complex media. Chaotic cavities with reflecting walls are also used to perform time reversal

experiments, proving that using a single time reversal channel, a good reversal quality can be obtained without the limitations provided from using a limited aperture TRM.

As well, the reverberation chambers are exploited for time reversal experiments with good results on antenna efficiency measurement, for example. The temporal and spatial focus improves the accuracy of results when using a TR process.

Following this introductory theoretical aspects, the following section presents simulation results on the focusing properties of a time reversal process.

Using a FDTD method with a PML function to treat the boundaries, 2D simulations are carried out in order to show the properties of a time reversal process. The simulation comprises the two steps of a time reversal process. In the first step, a point-like source emits a short pulse, which propagates through the random medium, towards the TRM where the scattered signals are recorded. During the second step, the TRM emits the time reversed signals, which retrace their path backwards in order to focus on the position of the source.

By decreasing the number of elements of the TRM, the quality of focus is studied and compared with simulations carried in free space. The presence of the random medium between the source and the mirror assures multiple scattering inside the medium, causing a lens effect in order to focus the signal on the source position, due to spatial frequencies that are redirected towards the TRM, during the first step of the process.

Moreover, using multiple sources in a TR process, multiple foci can be obtained on different positions at the same time, or by controlling the distance between the point-like sources a wide focus can be achieved.

Following the simulation results on the focusing properties of a time reversal process, the next chapter presents simulations and measurement results on computational imaging using a method based on time reversal technique.

CHAPTER 3 ***Modeling of a microwave imaging system using a random medium***

3.1 Introduction

Detection and localization of an unknown target can be achieved by placing it in an investigation domain surrounded by measurement probes able to acquire samples of the scattered field. This chapter presents a microwave imaging method that takes advantage of the spectral degrees of freedom provided by the propagation through a random medium.

3.2 Microwave imaging

Microwave imaging has considerably evolved in latest years, receiving an increased attention in the literature. As opposed to older techniques, microwave imaging techniques use electromagnetic waves for detection or location of objects hidden or embedded in a structure. There are two main categories to classify these imaging techniques. Firstly, quantitative imaging techniques give the electrical and geometrical parameters of an imaged object by solving a nonlinear inverse problem. Secondly, qualitative microwave methods which give a qualitative profile called a reflectivity function to represent a hidden object using approximations to simplify the imaging problem and back-propagation algorithms to reconstruct the unknown image profile.

A microwave imaging system mainly comprises two parts, hardware and software. The hardware part represents the apparatus used to collect data from the object under test, such as antennas, measurement instruments or recording tools. Figure 3.1 shows a simple hardware system representation. In the case of imaging of a passive object, the antenna connected to the measurement instrument transmits an electromagnetic wave towards the object under test. The contrast between the electrical properties of the object and the surrounding medium causes the radiation of the reflected waves. A part of the scattered wave is collected and measured by the same antenna in the monostatic case, or a different receiver antenna in a bistatic case. The software part represents the post-processing of the collected data during measurements by applying imaging algorithms in order to determine the electrical and geometrical parameters or an estimate reflectivity function.

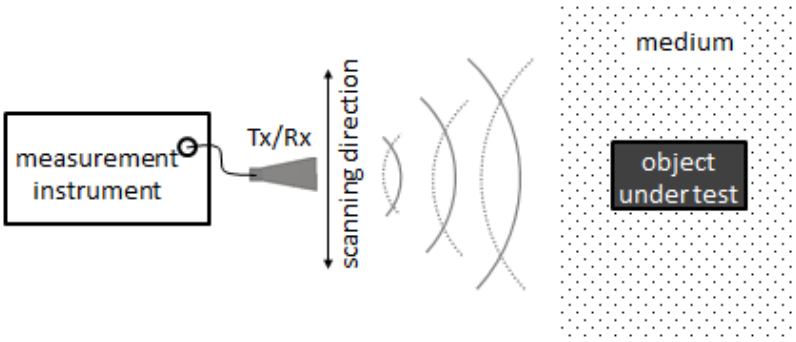

Figure 3.1 Microwave imaging hardware system schematic

Collected data consisting of reflected field data from an object can be migrated or back-propagated by adding appropriate time shifts in the time domain, or phase shifts in the frequency domain. Ground penetrating radar (GPR), range-Doppler algorithm, synthetic aperture radar, matched-filter migration and frequency-wave number migration algorithm belong to the qualitative imaging class [70]. The electrical and geometrical properties of an imaged object can be obtained with inverse scattering methods or quantitative imaging techniques. Image reconstruction procedure use Green‟s function in quantitative imaging methods [71]. Since modern computers are capable of solving inverse problems with an increasing complexity, computational imaging techniques allow a simplification of the hardware architecture on account of post-processing algorithms.

There are a variety of applications of microwave imaging, ranging from medical imaging or nondestructive testing and evaluation, structural health monitoring and through-the-wall imaging to concealed weapon detection [72], [73], [74], [75], [76]. For instance, microwave imaging for medical applications has an increasing interest. The difference between the dielectric properties of malignant tissue and normal tissue translates into a contrast detectable by microwave imaging methods. Also, infrastructure ageing has its benefits in microwave imaging, as well as structural health monitoring due to the fact that lower frequency microwaves can penetrate through concrete detecting anomalies such as cracks or air voids.

Any reflection-based imaging method involves some form of back-propagation of the scattered signals into the medium which is analog to time reversal process. The back-propagated fields indeed tend to focus on sharp reflectors in the medium. In physical time reversal, the back propagating fields are emitted by the TRM into the real medium, which is unknown. In synthetic time reversal, the back-propagation is done numerically assuming the knowledge of the medium [77]. Though time reversal has been mainly used for focusing on targets, multipath propagation through scattering medium can be exploited to obtain images.

3.3 Conception and design of the medium

Considering a classic configuration of a time reversal process, the design of the disordered medium is important due to the dependence of the directivity of time-reversed beam on the ratio of the coherent (ballistic wave) to the incoherent (coda) parts of the signal. If the coherent waves dominate, no focusing will be possible using a one element TRM. On the contrary, when the ballistic wave front vanishes and the coda dominates, the resolution will be finer, but the transmitted intensity becomes small. Those contributions can be estimated using diffusion theory.

The Fourier transform of the impulse response from the source to one element of the TRM can be written as:

$$H(\omega) = \langle H(\omega) \rangle + N(\omega) \tag{3.1}$$

where $\langle H(\omega) \rangle$ corresponds to the coherent impulse response and $N(\omega)$ is referred as the incoherent contribution. In average, the contributions of those terms depend on the length of the medium, L, and the mean free path, ℓ, [78] as:

$$|\langle H(\omega) \rangle|^2 = e^{-\frac{L}{\ell}} \tag{3.2}$$

$$\langle |N(\omega)|^2 \rangle \cong \frac{\ell}{L} \tag{3.3}$$

The mean free path is defined as the average distance traveled by the wave through the medium before it becomes diffuse. The focused intensity is the sum of the direct and diffuse intensity and decays with the distance traveled through the scattering medium [79].

To determine the proper distance between the rods and their appropriate diameter, three cases are studied. For a set diameter, the rods are placed at different distances of 0.2 λ_c, 0.5 λ_c, 1 λ_c, 2 λ_c, 2.5 λ_c and 3 λ_c, where λ_c is the wavelength for the central frequency, in order to check the transmitted electric field, using a plane wave to illuminate the line of rods.

3.3.1 First trial - rod diameter: 10 mm

Considering $\lambda_c = 50\ mm$ for the central frequency of 6 GHz, the proposed distances and the number of rods fitted in a 1000 mm line are shown in Table 3.1:

a) 0.2 λ_c	b) 0.5 λ_c	c) 1 λ_c	d) 2 λ_c	e) 2.5 λ_c	f) 3 λ_c
[10 mm]	[10 mm]	[10 mm]	[10 mm]	[10 mm]	[10 mm]
50 rods	29 rods	17 rods	9 rods	8 rods	7 rods

Table 3.1 First trial - The number of rods and the distances between them

The configuration for each case is similar to the one shown in the figure bellow. The simulation is performed in 2D.

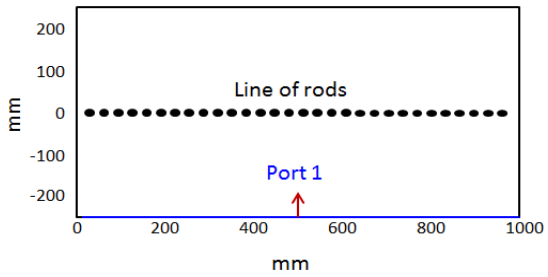

Figure 3.2 Test configuration

The rods are metallic discks placed on a centered line in front of a very large port, which replaces the bottom boundary. The direction of incidence is represented by the red arrow with a vertical polarization. Figure 3.3 shows the electric field transmitted through the rods for each of the proposed cases for the central frequency of 6 GHz.

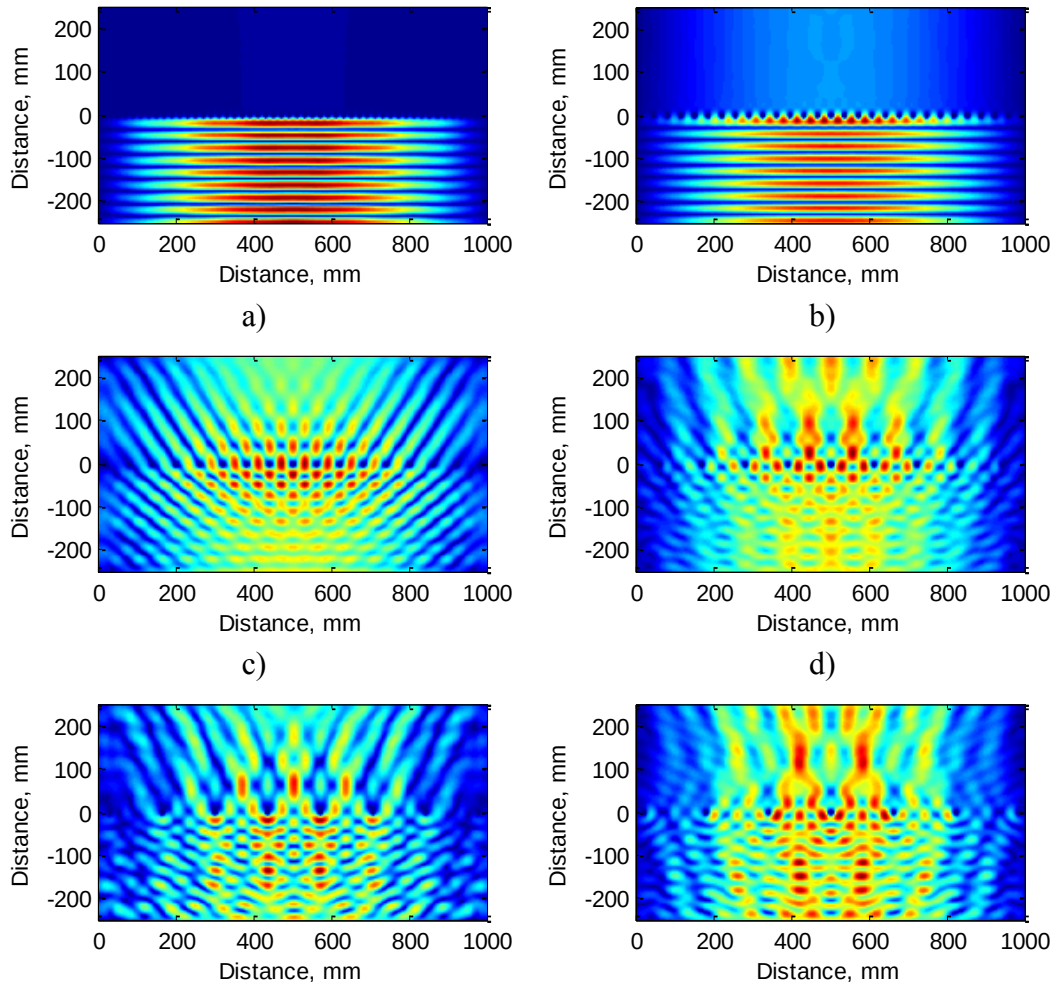

Figure 3.3 First trial - Electric field surface for distances: a) 10 mm; b) 25 mm; c) 50 mm; d) 100 mm; e) 125 mm; f) 150 mm;

Figure 3.4 shows the transmitted field (T) through the line of rods plotted in solid blue line and the backscattered field (B) from the rods, plotted in dashed black line, for the central frequency of 6 GHz.

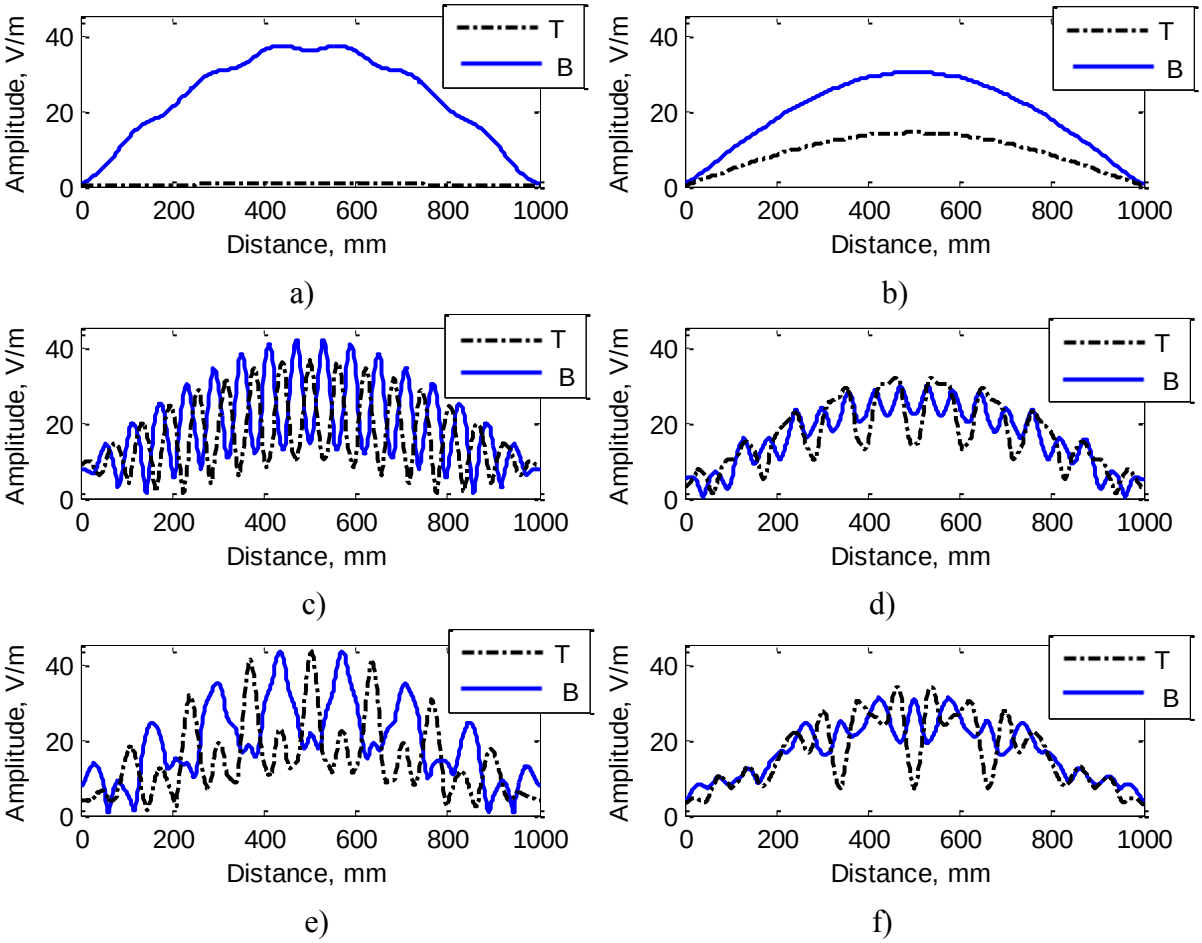

Figure 3.4 First trial - Electric field transmitted and backscattered for distances:
a) 10 mm; b) 25 mm; c) 50 mm; d) 100 mm; e) 125 mm; f) 150 mm;

3.3.2 Second trial - rod diameter: 15 mm

Table 3.2 shows the proposed distances and the number of rods fitted in a 1000 mm distance for rods with a diameter of 15 mm :

a) 0.2 λ_c	b) 0.5 λ_c	c) 1 λ_c	d) 2 λ_c	e) 2.5 λ_c	f) 3 λ_c
[10 mm]	[10 mm]	[10 mm]	[10 mm]	[10 mm]	[10 mm]
40 rods	25 rods	16 rods	9 rods	8 rods	6 rods

Table 3.2 Second trial - The number of rods and the distances between them

Figure 3.5 shows the electric field transmitted through the rods for each of the proposed cases for the central frequency of 6 GHz.

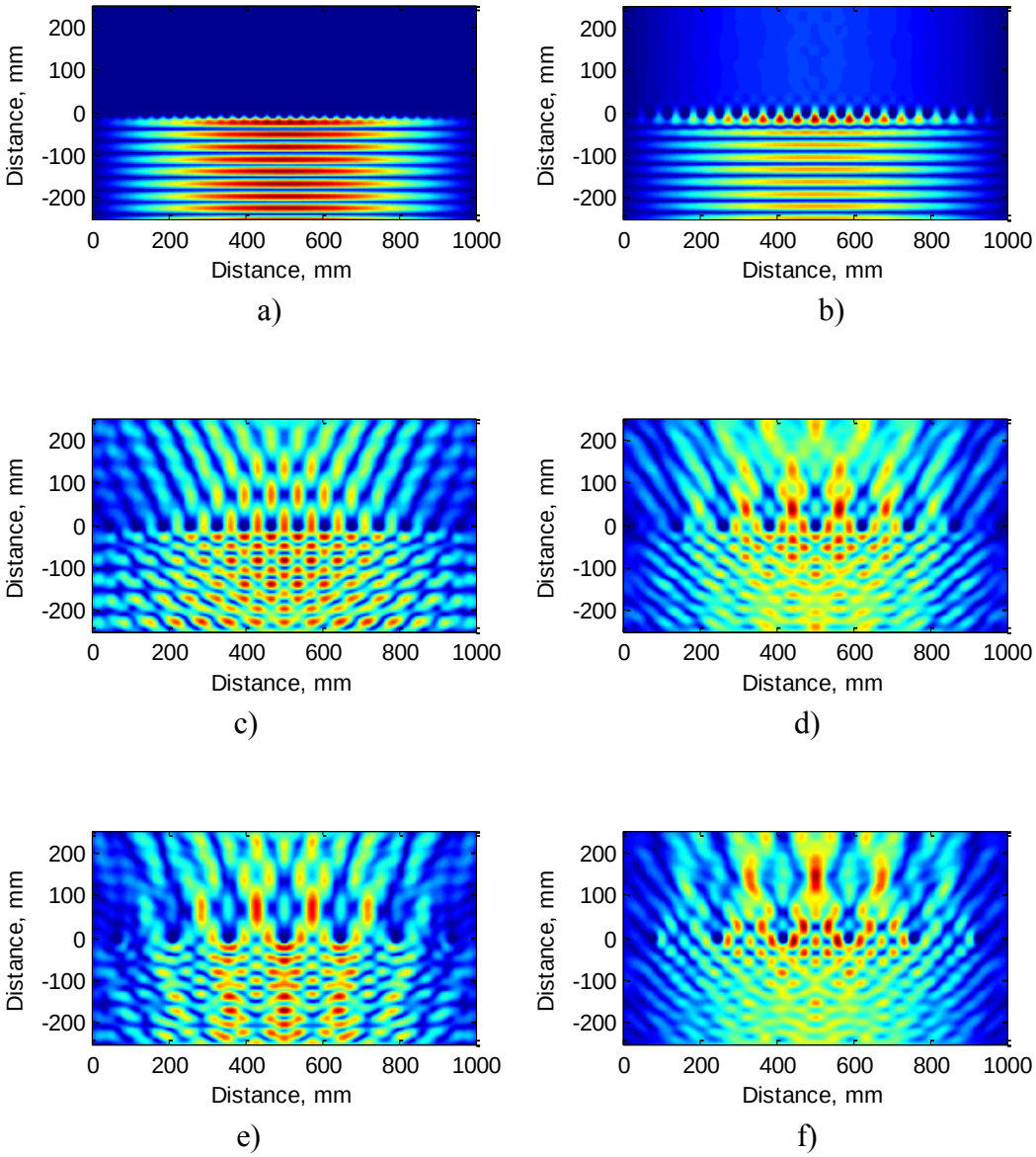

Figure 3.5 Second trial - Electric field surface for distances: a) 10 mm; b) 25 mm; c) 50 mm; d) 100 mm; e) 125 mm; f) 150 mm;

Figure 3.6 shows the transmitted field (T) through the line of rods plotted in dashed black line and the backscattered field (B) from the rods, plotted in solid blue line, for the central frequency of 6 GHz.

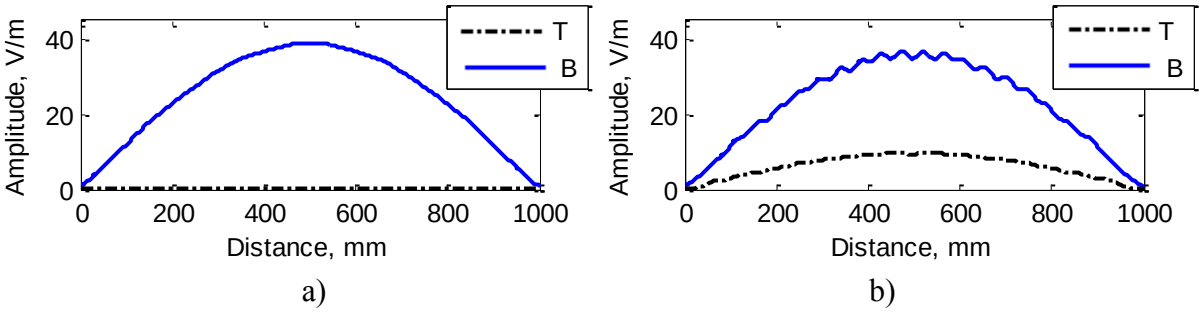

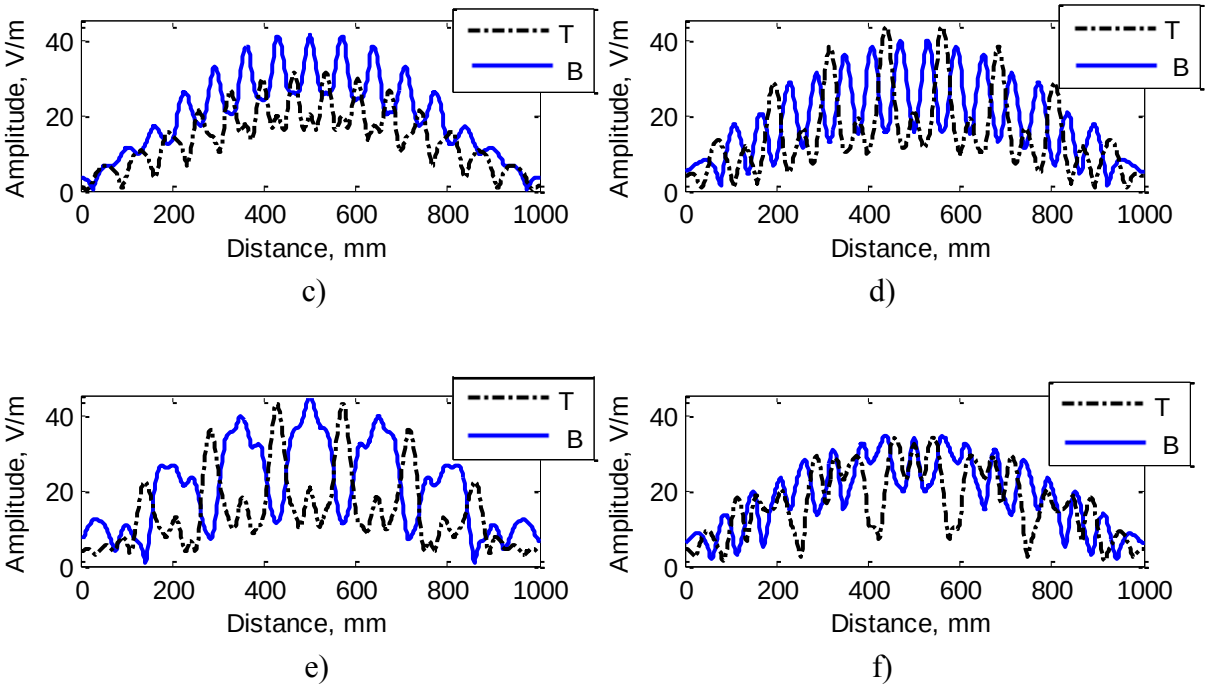

Figure 3.6 Second trial - Electric field transmitted and backscattered for distances: a) 10 mm; b) 25 mm; c) 50 mm; d) 100 mm; e) 125 mm; f) 150 mm;

3.3.3 Third trial - rod diameter: 20 mm

Table 3.3 shows the proposed distances and the number of rods fitted in a 1000 mm distance for rods with a diameter of 20 mm :

a) 0.2 λ_c	b) 0.5 λ_c	c) 1 λ_c	d) 2 λ_c	e) 2.5 λ_c	f) 3 λ_c
[10 mm]	[10 mm]	[10 mm]	[10 mm]	[10 mm]	[10 mm]
33 rods	22 rods	14 rods	9 rods	7 rods	6 rods

Table 3.3 Third trial - The number of rods and the distances between them

Figure 3.7 shows the electric field transmitted through the rods for each of the proposed cases for the central frequency of 6 GHz.

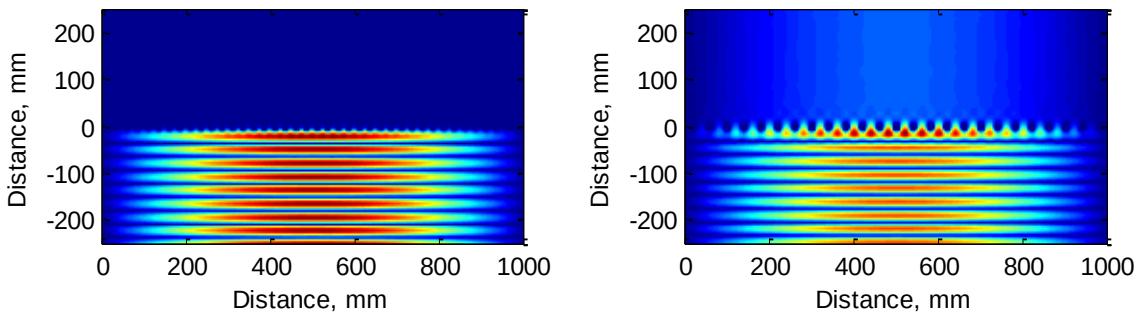

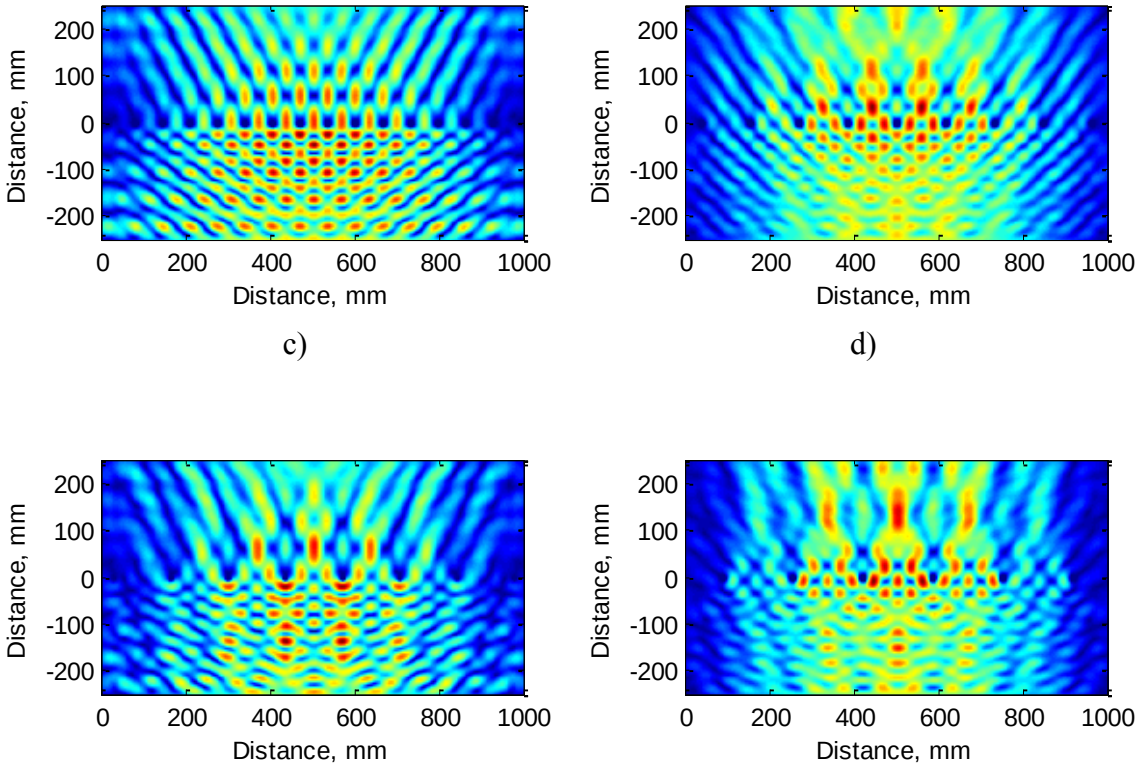

Figure 3.7 Third trial - Electric field surface for distances: a) 10 mm; b) 25 mm; c) 50 mm; d) 100 mm; e) 125 mm; f) 150 mm;

Figure 3.8 shows the transmitted field (T) through the line of rods plotted in dashed black line and the backscattered field (B) from the rods, plotted in solid blue line, for the central frequency of 6 GHz.

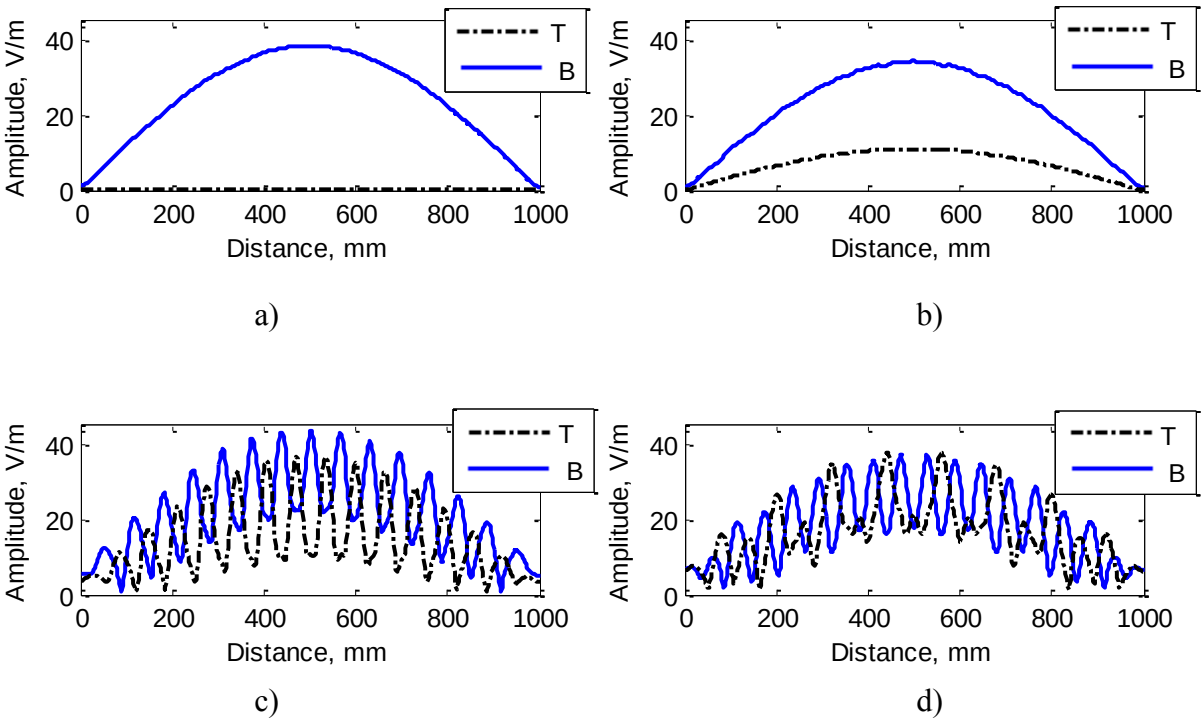

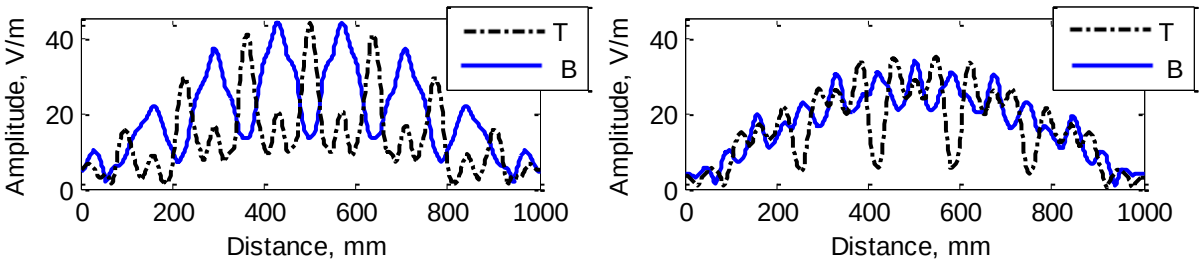

Figure 3.8 Third trial - Electric field transmitted and backscattered for distances: a) 10 mm; b) 25 mm; c) 50 mm; d) 100 mm; e) 125 mm; f) 150 mm;

Based on the obtained results in all three cases, the first proposed distance of 0.2 λ_c is too small to allow the electric field to pass through the line of rods. The electric field is almost entirely backscattered as shown in Figure 3.4.a), Figure 3.6.a) and Figure 3.8.a). The second proposed distance of 0.5 λ_c is sufficient to transmit some of the electric field through the line of rods, while the backscattered field is greater as shown in Figure 3.4.b), Figure 3.6.b) and Figure 3.8.b). For distances greater than half of wavelength for the central frequency, the transmitted electric field through the line of rods is comparable to the backscattered field, as shown in Figure 3.4.c) - f), Figure 3.6. c) - f) and Figure 3.8. c) - f).

Considering manufacturing reasons, the diameter of the rods was chosen to be $d = 10mm$. In order to obtain a good transmission through the medium, the distance between the rods should not be smaller than half of wavelength. Therefore, the medium was designed using a random distribution of the positions of the rods on the surface of the medium with a minimum et distance of 25 mm, half of wavelength for the central frequency of 6 GHz .

3.4 Target detection through a random medium 2D simulations

By means of simulation setups, it is further shown an approach of using a random medium to exploit the conversion between spatial and temporal degrees of freedom in order to image a target placed behind the medium.

3.4.1 Random medium characteristics

Figure 3.9 shows a 2D time reversal configuration in which the medium is placed between one emitting port and the time reversal mirror.

The proposed scattering medium consists of a random collection of 268 metallic rods of diameter 10 mm. The material used in the simulation software for the rods is steel. The minimum distance between the rods is 25 mm, half of wavelength for the central frequency

of 6 GHz. The height of the rods is considered to be infinite and the simulations are carried in 2D using COMSOL Metaphysics Modeling Software.

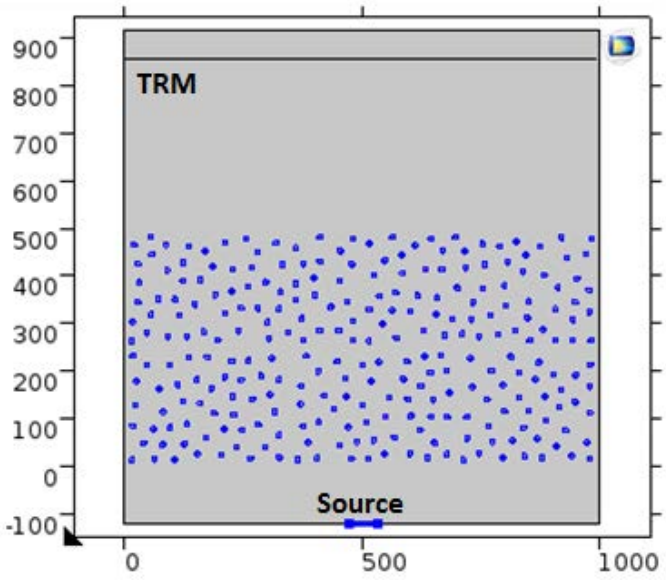

Figure 3.9 2D Time reversal configuration

The proposed scattering medium consists of a random collection of 268 metallic rods of diameter 10 mm. The material used in the simulation software for the rods is steel. The minimum distance between the rods is 25 mm, half of wavelength for the central frequency of 6 GHz. The height of the rods is considered to be infinite and the simulations are carried in 2D using COMSOL Metaphysics Modeling Software. The width of the medium is $W = 1000\ mm$ $(20\lambda_c)$ and the length is half of the width, $L = 500\ mm$, $10\lambda_c$.

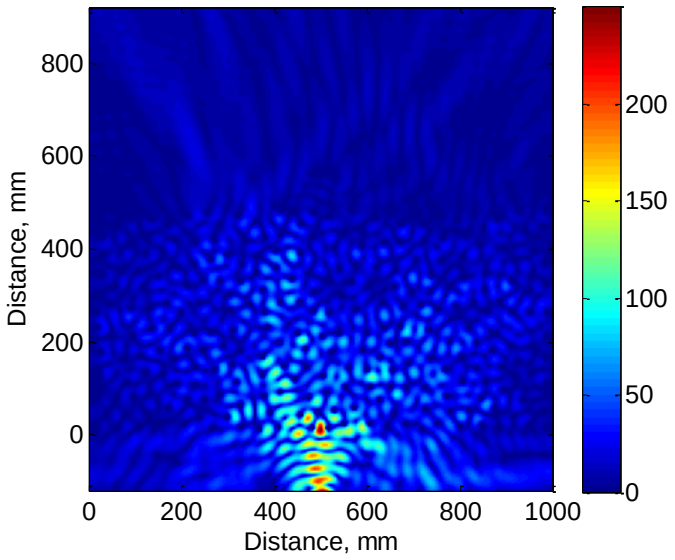

Figure 3.10 Surface electric field plot

The following spectra are simulated on $N_f = 401$ frequency points in the $5 - 7\ GHz$ frequency range. Figure 3.10 shows the spatial distribution of the field amplitude for the central frequency of 6 GHz.

The filed transmitted through the medium is recorded on a line of probes, the TRM, which has an aperture equal with the width of the medium and is placed parallel with the medium at position $y = 860\ mm$. The spectrum of the amplitude of the electric field registered at a central position on the TRM is shown in Figure 3.11.

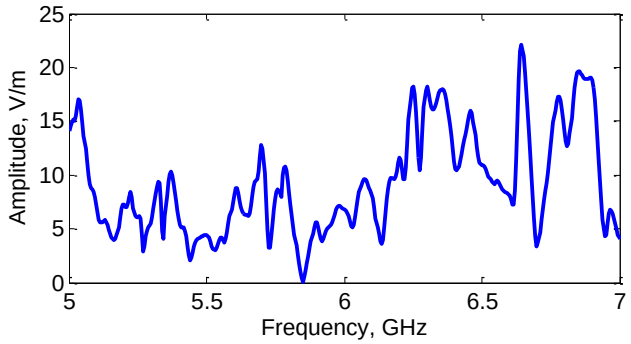

Figure 3.11 Electric field amplitude versus frequency

The spectrum is seen to strongly fluctuate as a signature of the scattering within the medium. Figure 3.12 shows the time signal registered on the line of probes at a central position.

The more heterogeneous the medium is, the longer the coda. While the coda seems completely random, the wave does not entirely lose its coherence [80], which means that the coda carries information about the medium, allowing a better focusing which does not depend on the TRM aperture.

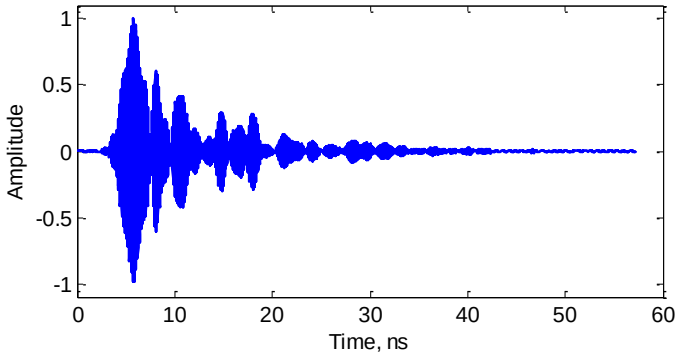

Figure 3.12 Time signal on TRM

The focusing performance of TR through a complex medium can be characterized by the ratio between the amplitude of the focused signal and the amplitude of the residual spatial and temporal sidelobes. This ratio is equal to the number of spatiotemporal degrees of

freedom which is the product of the number of spatial and temporal degrees of freedom, N_x and N_ω, respectively.

$$N = N_x \times N_\omega \tag{3.4}$$

Those contributions are detailed in the following:

a) Spatial degrees of freedom

For a coherence length, δx smaller than the distance between two elements of the array, the fields are decorrelated. Therefore, the number of spatial degrees of freedom is the ratio of the TRM array aperture, Δx, to the coherence length of the scattered field:

$$N_x = \frac{\Delta x}{\delta x} \tag{3.5}$$

As a wave penetrates a multiply scattering medium, spatial coherence is rapidly lost since the wave at any point is the sum of randomly scattered partial waves [81]. The scale of the speckle spots is set by the intensity correlation length. The resolution that can be achieved with time reversal methods is related to the field correlation length given by the following spatial field correlation function:

$$C(\delta x) = \frac{\langle E^*(x)E(x+\delta x)\rangle}{\sqrt{\langle |E(x)|^2\rangle\langle |E(x+\delta x)|^2\rangle}} \tag{3.6}$$

Figure 3.13 shows the computed spectral correlation function. The angle brackets denote an averaging over an ensemble of random configurations of the medium. Since a single configuration has been simulated over a large bandwidth, the averaging is performed over different intervals of $300\,mm$ along the total width of $1000\,mm$ of the medium. The length of spatial field correlation function is $\delta x \cong 25\,mm$, corresponding to $0.5\,\lambda_0$, where λ_0 is the central wavelength over the frequency range $5-7\,GHz$. Therefore, the number of spatial degrees of freedom is: $N_x \sim 40$. For diffusive waves, $\delta x \sim \lambda/2$ is been expected. This indicates that the propagation regime is in the diffusion regime.

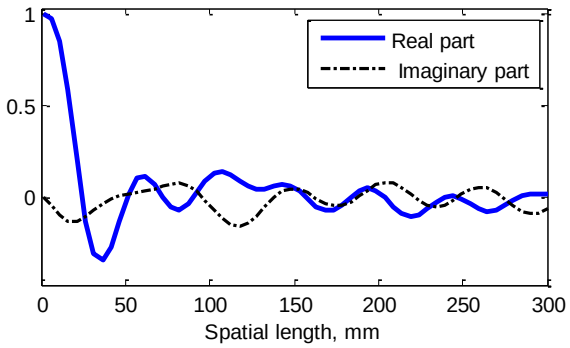

Figure 3.13 Spatial correlation function

b) Spectral degrees of freedom

The number of temporal degrees of freedom, N_ω is linked to the number of statistically independent frequency ranges within the bandwidth and can be expressed as:

$$N_\omega = \frac{\Delta\omega}{\delta\omega} \tag{3.7}$$

where $\Delta\omega$ is the bandwidth and $\delta\omega$ is the width of the spectral field-correlation function. The number of spectral degrees of freedom is given by the number of uncorrelated pieces of information within the bandwidth.

The correlation frequency signifies the inverse of the spread in transit time between the source and the reception [82]. For transmission through a random medium, $\delta\omega$ is inversely proportional to the typical time a photon spends traversing the medium, $\delta\omega = 1/\tau_d$.

The Thouless time [83], τ_d can be approximated as:

$$\tau_d \approx \frac{L^2}{c_0 \ell} \tag{3.8}$$

Therefore, from estimating the Thouless time by the inverse of the decay rate of the signal"s intensity through the medium, the mean free path can be approximated as:

$$\ell \approx \frac{L^2}{c_0 \tau_d} \tag{3.9}$$

Multiply scattering media, are characterized by the mean free path, found to be $\ell = 660\ mm$ and the diffusion constant D, defined as the rate at which the waves spread over the medium [84].

A broadband field with $\Delta\omega \gg \delta\omega$ couples to a large number of quasi-modes of average linewidth $\Gamma = {\tau_d}^{-1}$ so that the intensity at the focus is greatly enhanced due to constructive interference of the modes. On the other hand, the background intensity results from the destructive interferences of those modes. Those considerations highlight the influence of the bandwidth and show that spatial and temporal information are inextricably linked for a TR experiment.

The estimate of this number and therefore the performances that can be achieved, are given by the spectral correlation function:

$$C(\delta\omega) = \frac{\langle E^*(\omega) E(\omega + \delta\omega) \rangle}{\sqrt{\langle |E(\omega)|^2 \rangle \langle |E(\omega + \delta\omega)|^2 \rangle}} \tag{3.10}$$

In this case, the averaging is performed over different frequency ranges of 300 MHz within the $[5-7]$ GHz range for different positions in the scanned area in front the medium. Figure 3.14 shows the computed spectral corelation function.

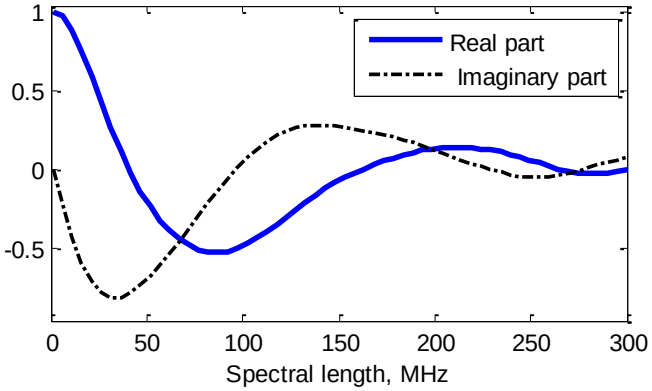

Figure 3.14 Spectral correlation function

The width of the spectral field correlation is seen to be equal to $\delta\omega = 40\ MHz$. This gives a number of $N_\omega \sim 50$ degrees of freedom within the bandwidth. Nevertheless, it is obtained a large number of spectral degrees of freedom within the bandwidth and in the same time a decent transmission. This is important to consider for applications requiring a good signal to noise ratio which can be expressed as:

$$SNR = \sqrt{\frac{\Delta\omega}{\delta\omega}} \tag{3.11}$$

Therefore, a higher number of degrees of freedom with the bandwidth provides a lower background intensity and assures a better SNR.

3.4.2 First simulation setup: Setup A

The setup for an imaging method in the microwave range using a random medium is inspired by the time reversal technique for focusing waves that allows spatial and temporal focusing of an electromagnetic signal. When used through a complex disordered medium, it takes advantage of multipath propagation to generate a focal spot of width given only by the multiple scattering medium.

In the context of RCS imaging, setup A presents a configuration for monostatic RCS using two ports close enough to be in a monostatic situation.

Figure 3.15 presents a first setup used to image the location of a device under test (DUT) by taking advantage of multipath propagation through a random medium.

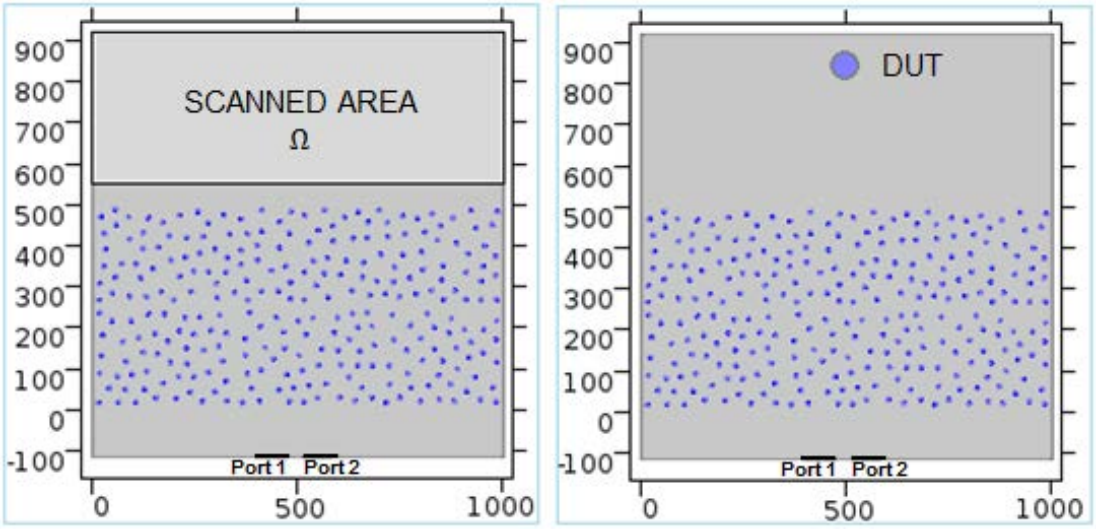

a) b)

Figure 3.15 First 2D simulation setup:
a) Scanning configuration; b) DUT configuration

There are two configurations used: Figure 3.15.a) presents the first - scanning configuration, in which the electric fields are registered over the scanned area and Figure 3.15.b) presents the second - DUT configuration in which the device under test is added in the scanned area. Due to the large dimensions of the setup, the simulation is performed in 2D software.

In order to perform the detection of the DUT and to estimate its position, three steps of simulation are required. During the first two steps, the information is acquired using the scanning configuration. The electric fields emitted by the two ports and transmitted through the medium are scanned for each frequency on $N_f = 401$ frequency points in the $5 - 7\ GHz$ frequency range. The scanned surface is the area located in front of the medium with the sizes of $1000\ mm$ by $370\ mm$. The electric fields denoted by $E_1(r, \omega)$ and $E_2(r, \omega)$, respectively, are recorded on a grid of $M = 15075$ points over an area of $0.37\ m^2$. Data are recorded with a spatial step of $5\ mm$ on each axis.

The transmission between ports, $S_{21}^{wo}(\omega)$ parameter that includes the back-scattered field from the medium and gives the coupling between the two ports, is also recorded. In the third step, the DUT configuration is used and the device under test consisting of a metallic sphere is added inside the scanned area at the position $x = 500\ mm, y = 830\ mm$. The new $S_{21}^{w}(\omega)$ parameter between the ports in the presence of the DUT is recorded. The material used for the sphere is steel. The diameter is $50\ mm$.

The parameter that includes not only the scattering from the DUT, but also the

propagation within the medium is given by the difference between the two S_{21} parameters recorded with and without de DUT added to the setup:

$$S_{21}(\omega) = S_{21}^{w}(\omega) - S_{21}^{wo}(\omega) \tag{3.12}$$

Assuming the first Born approximation [85] and that the scattering coefficient of the DUT is independent of frequency, $\sigma(\omega, r) = \sigma(r)$, the $S_{21}(\omega)$ parameter can be written as :

$$S_{21}(\omega) = \int_{\Omega} E_1(r,\omega)\, E_2(r,\omega)\sigma(r)\, d^2r \tag{3.13}$$

where $E_1(r,\omega)$, $E_2(r,\omega)$ are the electric fields recorded on the scanned area when port 1, respectively port 2 is emitting and $\sigma(r)$ is the spatial distribution of the scattering coefficient.

In order to retrieve the scattering coefficient, two methods are applied: one based on time reversal technique and one based on matrix inversion (MI).

3.4.2.1 Time reversal method

Using a method based on time reversal technique, the signal focused on the position of the DUT is obtained through the convolution of the time reversed signals recorded on the TRM and the signal scattered by the target. In the frequency domain, the convolution becomes a multiplication of the conjugated $S_{21}(\omega)$ parameter defined in equation (3.12) and the product of the two electric fields recorded on the scanned area from each port. For each position in front of the medium that has been scanned in the first two steps, an image is computed by:

$$I(r) = \left| \int S_{21}^{*}(\omega) E_1(r,\omega) E_2(r,\omega) d\omega \right|^2 \tag{3.14}$$

Figure 3.16 shows the reconstruction of the scanned area for the second configuration where the target constituted by a metallic sphere is added to the setup.

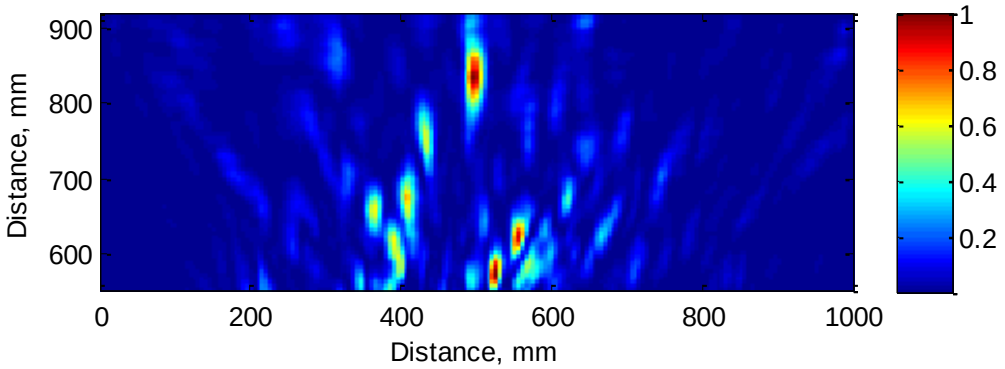

Figure 3.16 Reconstruction of scanned area using TR method – Setup A

For a small DUT located at position r_0, it is expected an enhanced intensity at this point due to the constructive interferences of the frequencies within the bandwidth. In contrast, for $r \neq r_0$, the interferences should be destructive. Figure 3.17 shows the amplitude of the reconstructed image is shown along x axis with $y = 830\ mm$.

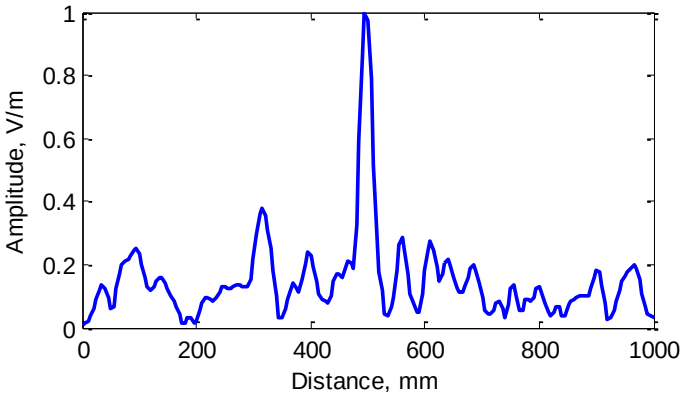

Figure 3.17 Sidelobes amplitude using TR method – Setup A

The DUT location is accurately imaged at its position ($x = 500\ mm, y = 830\ mm$). However, strong sidelobes are observed in this configuration when focusing the signal on the position of the target.

Because sidelobes are inherent to TR methods, being related to the mean distance between the rods [78], giving an increased amplitude of the secondary lobes when the most scattering paths cross each other in a wide medium, the next section presents a method based on a matrix inversion that provides much lower sidelobes.

3.4.2.2 Matrix inversion method

Making the assumption that the scattering coefficient of the DUT barely depends on the frequency over the frequency range of signals, makes it possible to write equation (3.13) in its discretized form as the multiplication of two matrices such as:

$$S_{21} = H\sigma \tag{3.15}$$

where, S_{21} is a vector of N_f frequencies, H is a $N_f \times M$ matrix and σ is a vector of dimension M. The dimension M is given by the spatial step of $5\ mm$ on each axis for the data recorded on a grid over the scanned area.

Matrix H is expressed as the product of the fields recorded on the scanned area from each port:

$$H_{ij} = E_1(r_j, \omega_i)E_2(r_j, \omega_i) \tag{3.16}$$

By inversing the matrix H, the spatial distribution of the scattering coefficient, $\sigma(r)$ can be written as:

$$\sigma = H^{-1}S_{21} \tag{3.17}$$

One possible method to estimate the inverse matrix H is to first perform a Singular Value Decomposition (SVD) of H:

$$H = USV^{\dagger} \tag{3.18}$$

where, U and $V^{\dagger}$ are complex unitary matrices whose columns contain the left-singular vectors and right-singular vectors of H, respectively and S is a rectangular diagonal matrix whose diagonal entries are the singular values of H. Therefore, the inverse of matrix H is expressed as:

$$H^{-1} = VS^{-1}U^{\dagger} \tag{3.19}$$

However, a significant weight is given to small singular values and this procedure may be very unstable in presence of noise. Figure 3.18 shows the distribution of singular values.

In order to avoid a significant impact of noise, a regularization method needs to be applied. By using the truncated SVD (TSVD) method [86], the inversed matrix can be expressed as:

$$H^{-1} = \sum_{n=1}^{p} v_n \frac{1}{s_n} u_n^{\dagger} \tag{3.20}$$

where, p is the index of the singular value which corresponds to the regularization parameter μ. The index p is therefore the number of singular values for which $s_n \geq \mu$. When using TSVD as a regularization method, the smallest singular values associated with noise are hence discarded as they would become a great noisy influence.

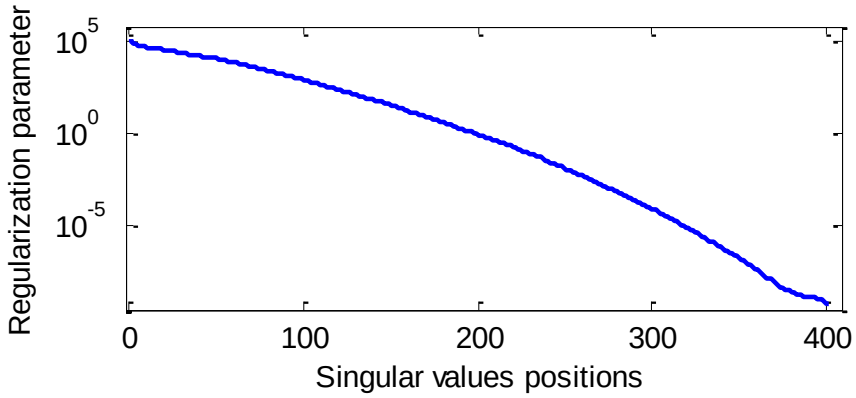

Figure 3.18 Distribution of singular values of matrix H

Another commonly used method of regularization, is Tikhonov regularization of ill-posed problems, which gives the following expression for the inverse matrix:

$$H^{-1} = \sum v_n \frac{s_n}{s_n^2 + \mu s_n} u_n^{\dagger} \tag{3.21}$$

The SNR is plotted in Figure 3.19 with respect to the regularization parameter μ. It is observed that the best regularization method is provided by the Tikhonov regularization.

Using Tikhonov regularization, the estimated vector of scattering coefficient $\tilde{\sigma}$ is expressed as:

$$\tilde{\sigma} = (H^{\dagger}H + \mu I)^{-1} H^{\dagger} S_{21} \tag{3.22}$$

where $\mu \geq 0$ is a regularized parameter that determines the amount of regularization and I is the identity operator [87].

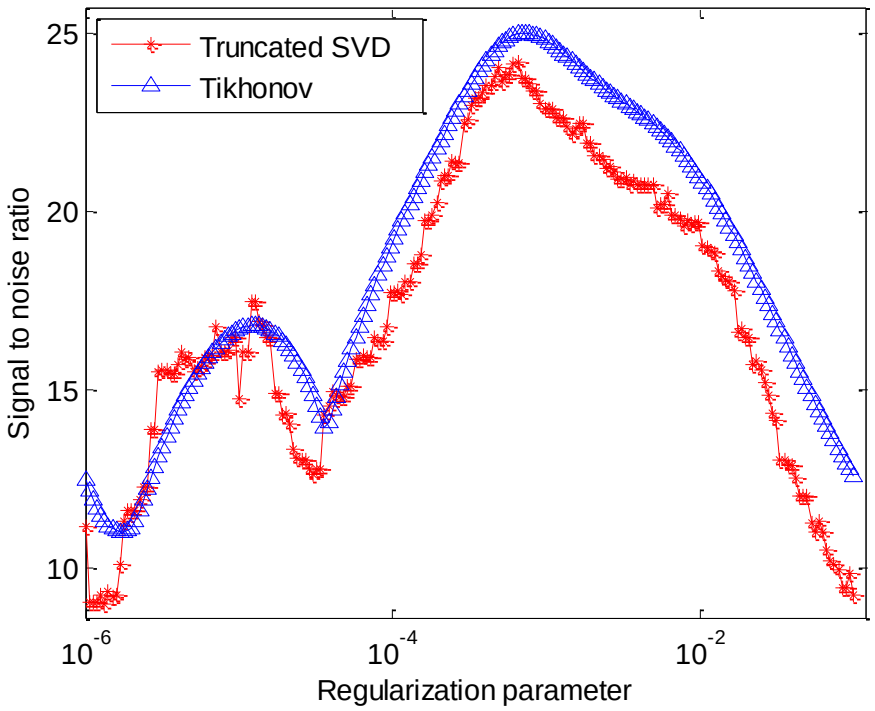

Figure 3.19 SNR

For each position in front of the medium using the matrix inversion method, an image is computed from:

$$I(r) = \left|(H^{\dagger}H + \mu I)^{-1} H^{\dagger} S_{21}\right|^2 \tag{3.23}$$

Figure 3.20 shows the reconstruction of the scanned area for the DUT configuration where the target is added to the setup.

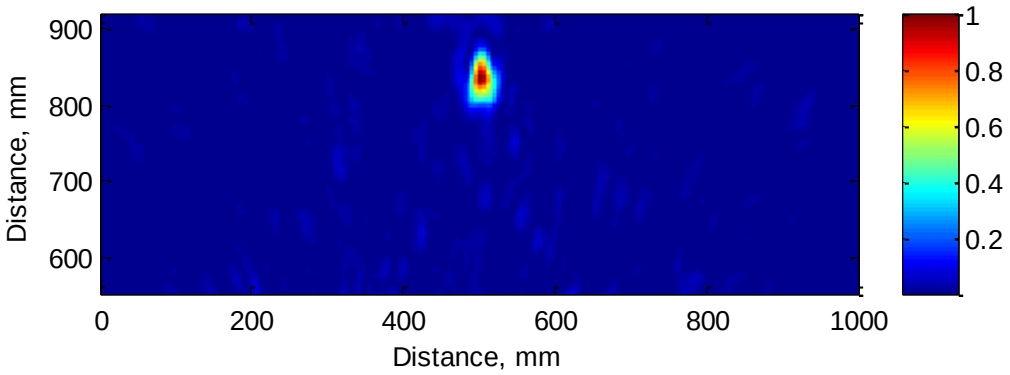

Figure 3.20 Reconstruction of scanned area using MI method – Setup A

The sidelobes have been strongly attenuated in comparison with the TR-like method. Using the matrix inversion method, the regularization process provides a better SNR as the small singular values associated with noise are filtered out.

The reconstruction of the scanned area in the DUT configuration shows the position of the target being placed in the right position ($x = 500\ mm,\ y = 830\ mm$).

Figure 3.21 shows the amplitude of the reconstructed image along x axis with $y = 830\ mm$.

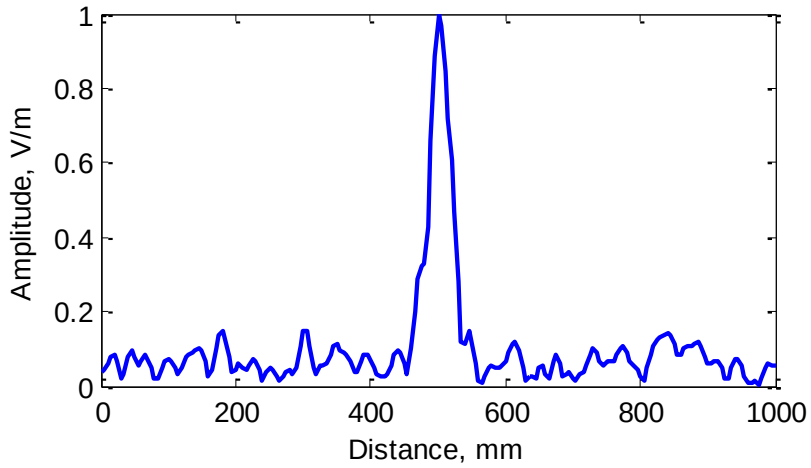

Figure 3.21 Sidelobes amplitude using MI method – Setup A

The detection of the DUT is clearly seen on the position $x = 500\ mm$. Compared with the time reversal method, a lower level of the sidelobes can be observed.

Although, the results of simulations using setup A are satisfying, the experimental validation of the method encounters difficulties. The detection and localization of the target is not performed. The retrieved image is noisy, due to the coupling between the two antennas placed behind the medium in the monostatic configuration.

3.4.3 Second simulation setup: Setup B

A second setup for an imaging method using a random medium is shown in Figure 3.22. In this case, the two used ports are in bistatic RCS configuration.

There are also two configurations used: Figure 3.22.a) presents the scanning configuration in which the medium is placed between two ports: port 1 behind the medium and port 2 in front of the medium. The ports are emitting and the electric field is registered over the scanned area. Figure 3.22.b) presents the DUT configuration in which the device under test is added in the scanned area. Since the second port is aligned with the first one on the x axis, the DUT is not centered, as in the previous setup. The center of the sphere is on the position $x = 600\,mm$. As well, the simulation is performed in 2D software, due to the large dimensions of the setup.

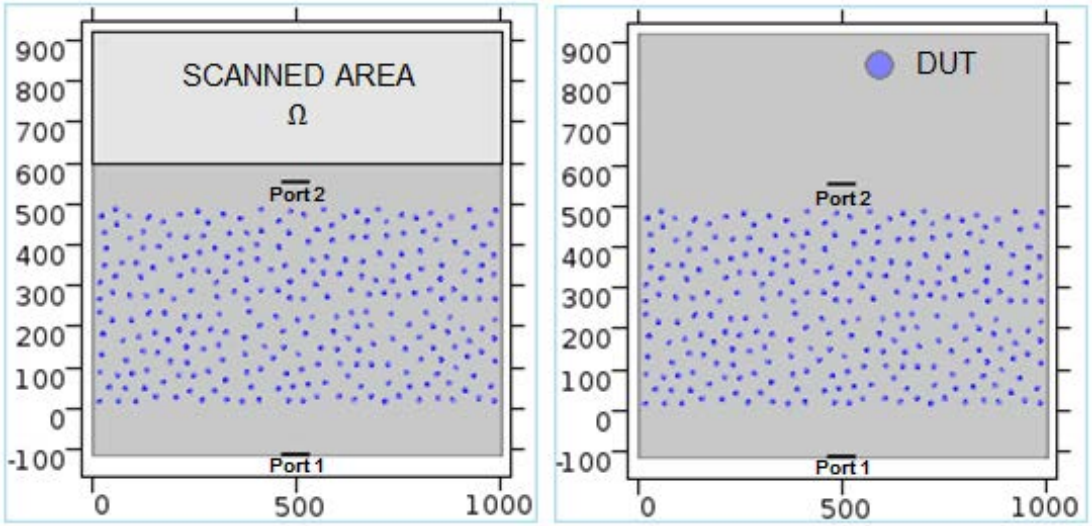

a) b)

Figure 3.22 Second 2D simulation setup:
a) Scanning configuration; b) DUT configuration

The two configurations of the setup are simulated in three steps. During the first two steps, using the scanning configuration, the electric field emitted by port 1 which is transmitted through the medium and the electric field emitted by port 2, are scanned for each frequency on $N_f = 401$ frequency points in the $5 - 7\,GHz$ frequency range. The scanned surface has the sizes of $1000\,mm$ by $320\,mm$. The electric fields denoted by $E_1(r, \omega)$ and $E_2(r, \omega)$, respectively, are recorded on a grid of $M = 13065$ points over an area of $0.32\,m^2$. Data are recorded with a spatial step of $5\,mm$ on each axis. In the same manner, the transmission between ports, $S_{21}^{wo}(\omega)$ parameter that includes the back-scattered field from the medium is also recorded. The third step of simulation is used to register the new $S_{21}^{w}(\omega)$

parameter between the ports in the presence of the DUT, a metallic sphere of 50 mm diameter placed inside the scanned area at the position $x = 600\ mm, y = 830\ mm$.

Similarly, by using equations (3.12) and (3.13), retrieving the scattering coefficient and imaging the position of the DUT is achieved by applying a method based on time reversal technique, as well as a matrix inversion method.

3.4.3.1 Time reversal method

The signal focused on the position of the DUT using a method based on time reversal technique is the multiplication of the conjugated $S_{21}(\omega)$ parameter defined in equation (3.12) and the product of the two electric fields recorded on the time reversal mirror from each port. Using equation (3.14), an image is computed for each position in front of the medium that has been scanned in the first two steps. Figure 3.23 shows the reconstruction of the scanned area with the target added, in the DUT configuration.

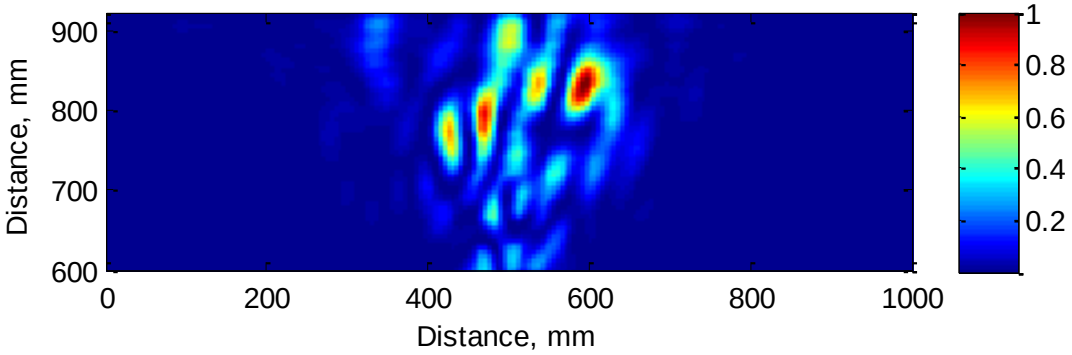

Figure 3.23 Reconstruction of scanned area using TR method – Setup B

At position $x = 600\ mm, y = 830\ mm$, the target is imaged, while strong sidelobes can be observed. Figure 3.24 shows the amplitude of the reconstructed image along x axis.

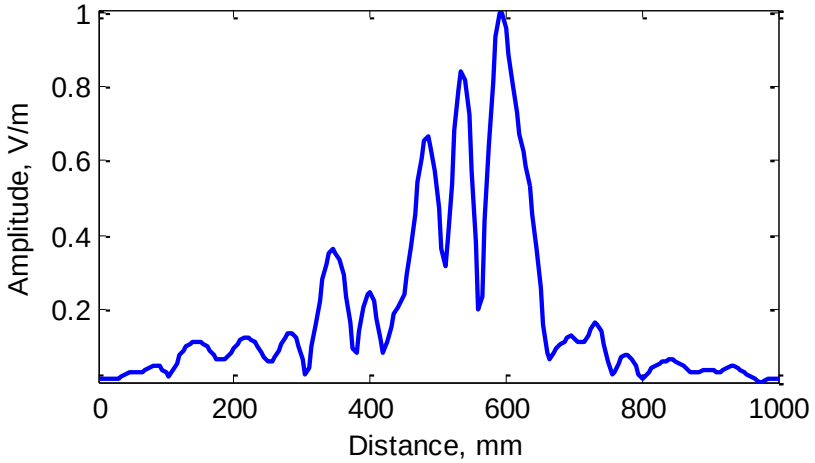

Figure 3.24 Sidelobes amplitude using TR method – Setup B

Clearly the target is detected at position $x = 600\ mm$ and definite secondary lobes are present on adjacent positions along the x axis.

Compared with setup A, the bistatic position of the two used ports presents higher sidelobes, as the second port is placed in front of the medium emitting in free space.

3.4.3.2 Matrix inversion method

Considering the previous expressed equations (3.15), (3.16), (3.17) and (3.22), an image is computed using equation (3.23) for each position in front of the medium using the matrix inversion method.

Figure 3.25 shows the reconstruction of the scanned area in the DUT configuration where the target is added to the setup.

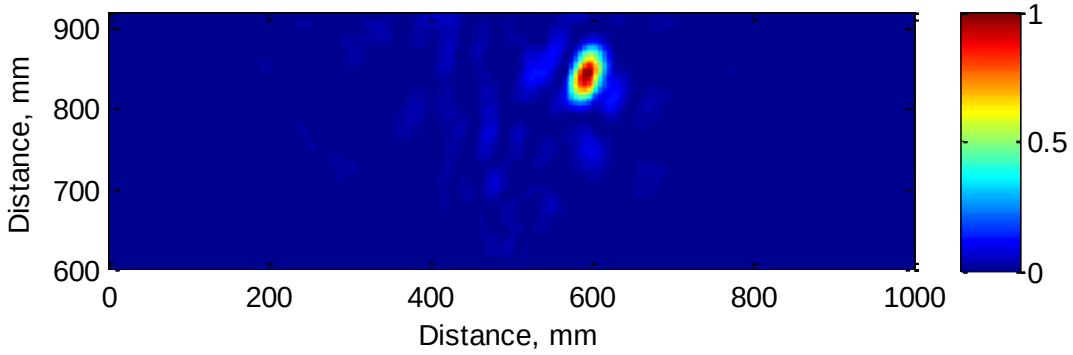

Figure 3.25 Reconstruction of scanned area using MI method – Setup B

Figure 3.26 shows the amplitude of the reconstructed image along x axis with $y = 830\ mm$. The target is clearly detected on the position $x = 600\ mm$.

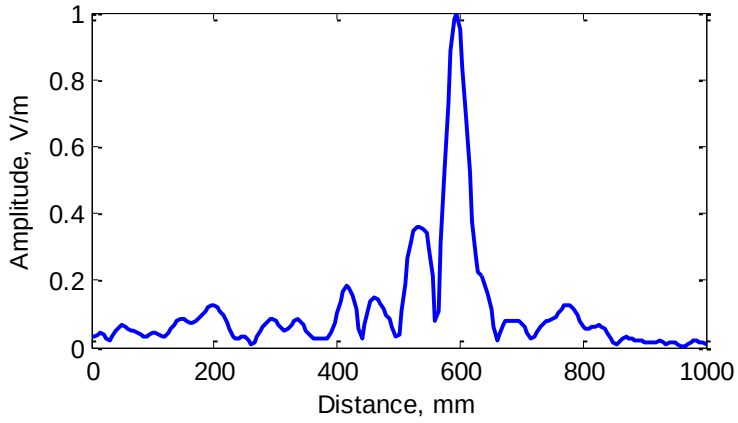

Figure 3.26 Sidelobes amplitude using MI method – Setup B

Compared with the TR method, the sidelobes have clearly been attenuated. The reconstruction of the scanned area in the DUT configuration shows the position of the target being placed in the right position.

3.4.4 Comparison of different metallic boundaries on simulation setup A

Thanks to the time compression of TR, an opened high quality factor medium such as a leaky chaotic cavity provides a way to obtain high amplitude pulses outside the medium. Such a medium can also be used to reconstruct the 3D image of a scene with a small number of emitting antennas [88]. For microwave imaging, such cavity can offer several advantages since waveguides cavities exhibit low losses and achieve high Q-factors. As well, in the ultrasound regime, resonant cavities have been used to perform 3D imaging [89] [90].

Inspired from the use of a cavity for microwave imaging, three versions of the simulated setup A with different PEC boundaries will be compared in order to determine the best results for an imaging method that takes advantage of the spectral degrees of freedom provided by the propagation through a random medium. Figure 3.27 shows the three version of the scanning configuration of the setup and Figure 3.28 shows the three version of the DUT configuration of the setup.

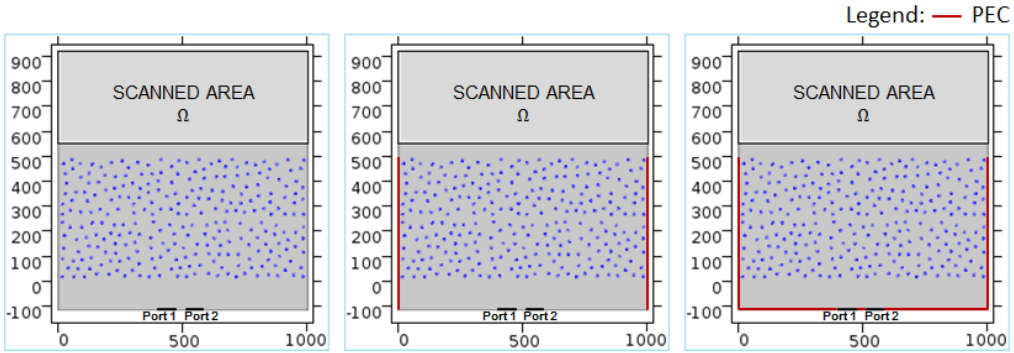

a) b) c)

Figure 3.27 Scanning configuration: a) version 1; b) version 2; c) version 3

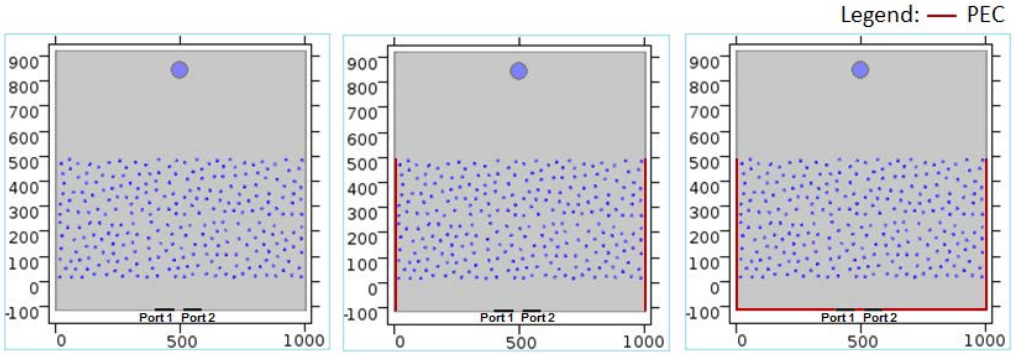

a) b) c)

Figure 3.28 DUT configuration: a) version 1; b) version 2; c) version 3

First version, V1, presents the whole setup with absorbing boundaries. In this version, the number of independent frequencies within the bandwidth is limited to the result of diffusion within the random medium. In the second and third versions, V2 and V3, the proposed medium is then surrounded by metallic walls in order to increase the Q-factor of the medium and hence the reverberation time. In the second version, the metallic walls are only on the sides of the medium from the line of ports until the end of the medium‟s length. The third version, presents metallic boundaries also on the line of ports.

Figure 3.29 shows a spectrum of the amplitude of the field at a given position in the scanned area for each version of the scanning configuration. Due to the diffusion within the medium the intensity fluctuates randomly.

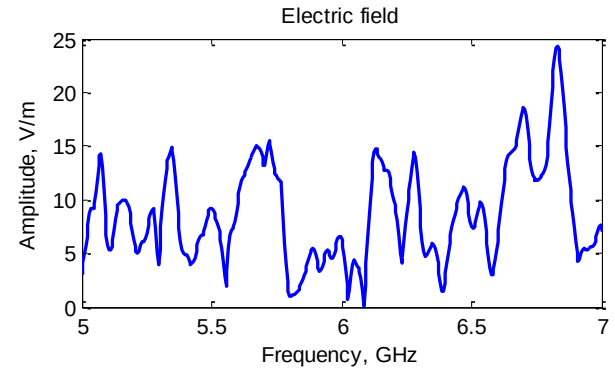

a)

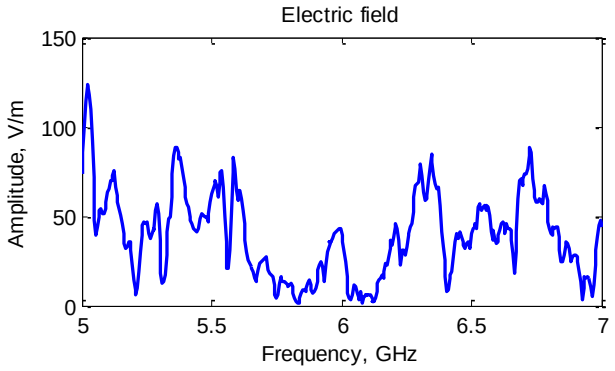

b)

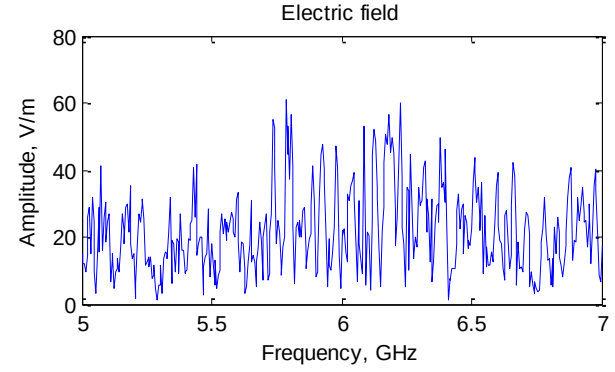

c)

Figure 3.29 Electric field amplitude versus frequency: a) version 1; b) version 2; c) version 3

Figure 3.30 shows the spectral correlation function expressed in equation (3.10), where the averaging is performed over different frequency ranges of $500\,MHz$ within the $[5-7]\,GHz$ range for different positions taken from 10 to 10 points along the x axis at $0.5\,\lambda$ in front of the medium in the scanned area.

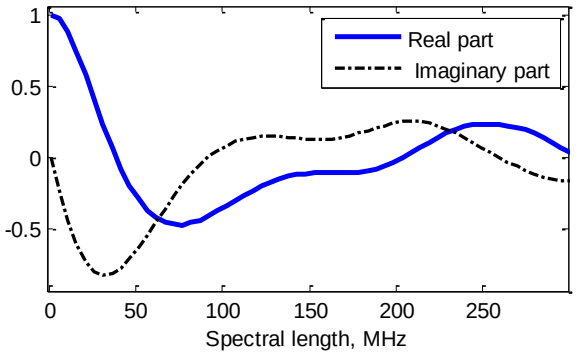

a)

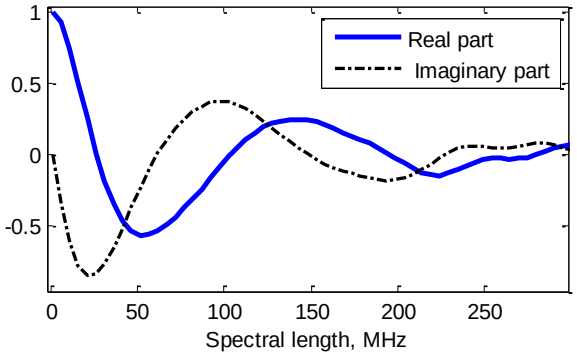

b)

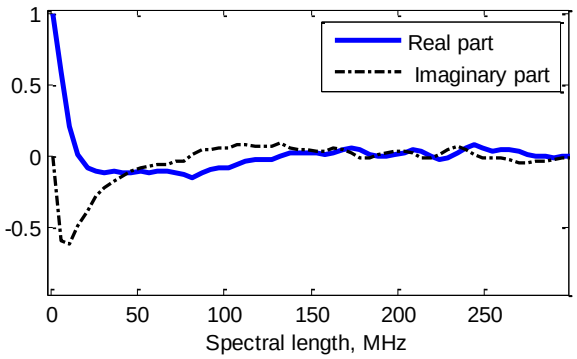

c)

Figure 3.30 Spectral correlation function: a) version 1; b) version 2; c) version 3

The spectrum is seen to strongly fluctuate as a signature of the scattering within the medium. The scale of those fluctuations decreases from the first version to the last one due to this higher reverberation times obtained by increasing the size of the metallic boundaries.

The width of the spectral field correlation is seen to be equal to: $\delta\omega_{V1} = 39\,MHz$, $\delta\omega_{V2} = 27\,MHz$ and $\delta\omega_{V3} = 16\,MHz$ for versions 1, 2 and 3, respectively. Applying

equation (3.7), the number of temporal degrees of freedom within the bandwith is $N_{\omega_{V1}} \sim 51$ for version 1, $N_{\omega_{V2}} \sim 74$ for version 2 and $N_{\omega_{V3}} \sim 125$ for version 3.

The reverberation time is inversely proportional to spectral correlation length: $Tr_{V1} = 25.64\,ns$, $Tr_{V2} = 37\,ns$ and $Tr_{V3} = 62.5\,ns$ for versions 1, 2 and 3, respectively. The number of uncorrelated pieces of information within the bandwidth gives the number of spectral degrees of freedom.

Retrieving the scattering coefficient and imaging the position of the DUT is achieved using equations (3.12) and (3.13) while applying a method based on time reversal technique, and a matrix inversion method.

3.4.4.1 Time reversal method

To focus the signal on the position of the DUT using a method based on time reversal technique, the multiplication of the conjugated $S_{21}(\omega)$ parameter defined in equation (3.12) and the product of the two electric fields recorded on the time reversal mirror from each port, is required. For each position in front of the medium that has been scanned in the first two steps, an image is computed using equation (3.14). Figure 3.31 shows the reconstruction of the scanned area in the DUT configuration, foe each of the three versions.

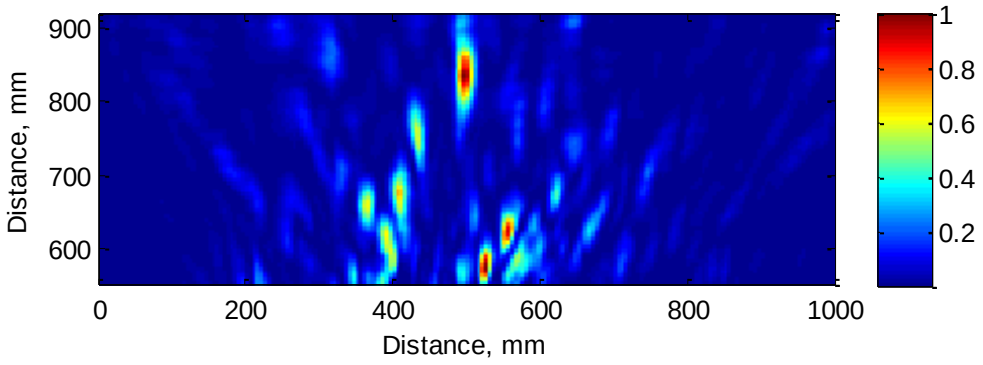

a)

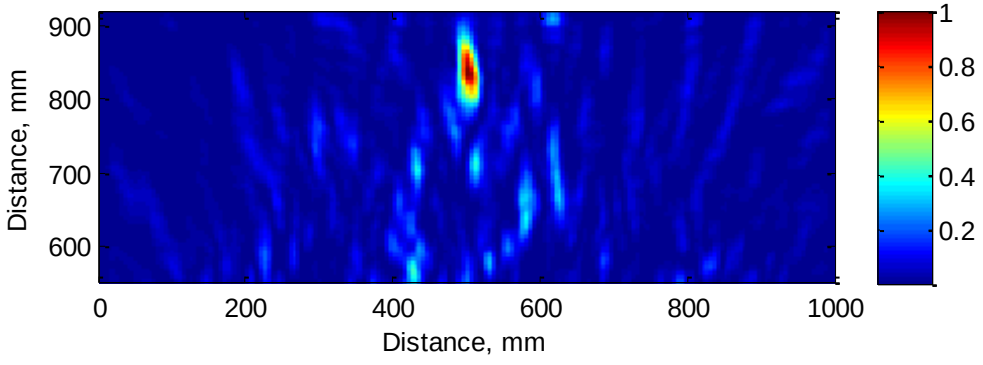

b)

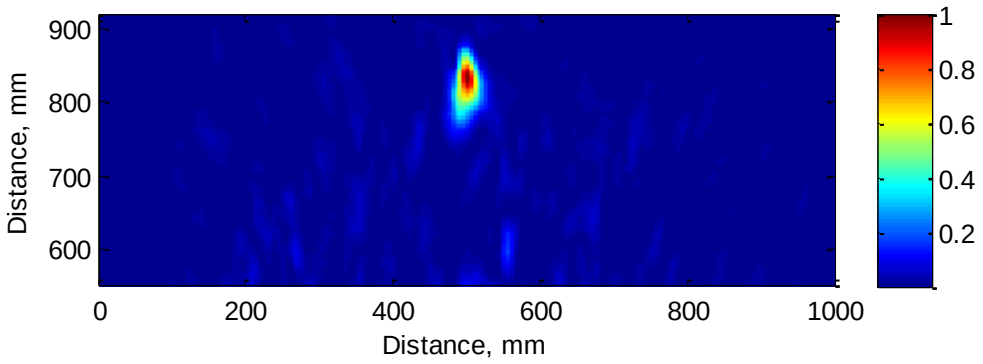

c)

Figure 3.31 Reconstruction of scanned area using TR method:

a) version 1; b) version 2; c) version 3

The target is accurately located for the three versions. However, strong sidelobes are observed for the first version. Those sidelobes are obviously decreasing as the metallic boundaries increase for the next two versions, as the number of temporal degrees of freedom within the bandwith is increasing. The best results are seen for the third version.

Figure 3.32 presents the amplitude of the sidelobes along the x axis with $y = 830\ mm$, presenting the same decrease for the waveguide configuration.

The presence of the DUT is detected at the central position ($x = 500\ mm$). The intensity is enhanced at the location of the DUT $r = r_0$, due to constructive interferences of the frequencies within the bandwidth and for any other of the positions $r \neq r_0$ the interferences should be destructive.

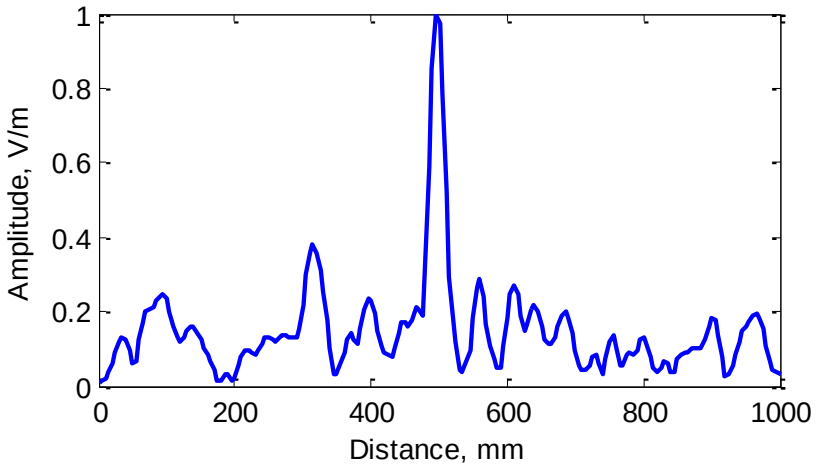

a)

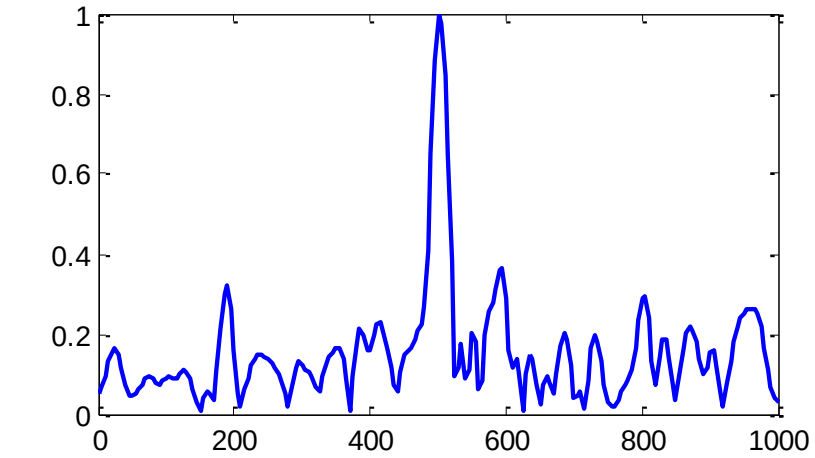

b)

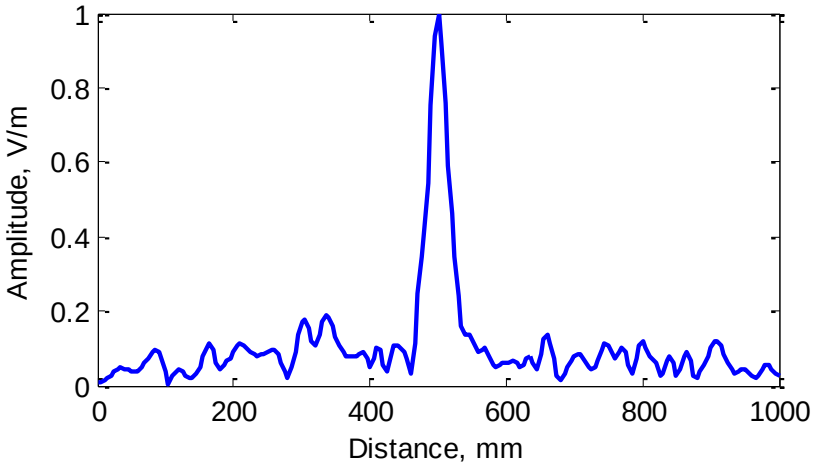

c)

Figure 3.32 Sidelobes amplitude using TR method:
a) version 1; b) version 2; c) version 3

The SNR defined in equation (3.11) is for each version: $SNR_{V1} = 7$, $SNR_{V2} = 9$ and $SNR_{V3} = 11$. From the first version to the last one, the amplitude of the secondary lobes is seen to decrease. The third version presents more than 50% decrease in the maximum amplitude of the secondary lobes compared with the first one, as the number of degrees of freedom is more than double for V3 compared to V1.

3.4.4.2 Matrix inversion method

Making the assumption that the scattering coefficient of the DUT barely depends on the frequency and by using the previous expressed equations (3.15), (3.16), (3.17), and (3.22), the matrix inversion method provides much lower sidelobes. For each position in front of the medium, an image is computed using equation (3.23).

Figure 3.33 shows the distribution of singular values for each of the three versions. As the number of degrees of freedom increases from first to last version, the smaller singular values are higher, providing less noise associations when performing the inversion of the matrix. For each version, the value of the regularization parameter, μ, is set to be the smallest singular value of matrix H which can still provide a stable inversion process. The values of the regularization parameter are $\mu_{V1} = 526.5$ for the first version, $\mu_{V2} = 906.8$ for the second version and $\mu_{V3} = 3934$ for the third one.

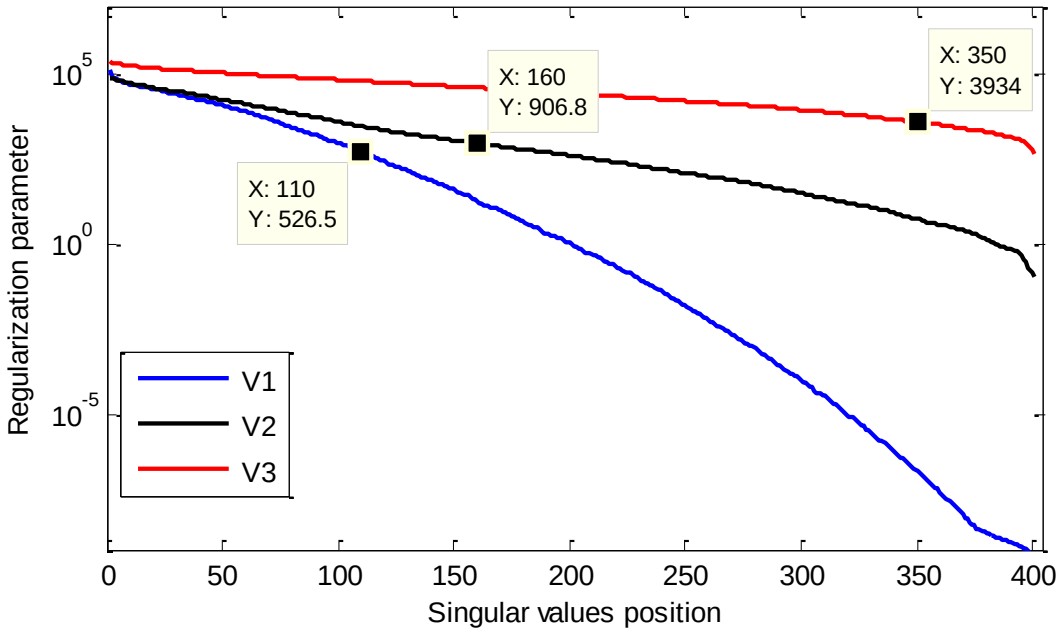

Figure 3.33 Distribution of singular values of matrix H

Figure 3.34 shows the reconstruction of the scanned area in the DUT configuration where the target is added to the setup.

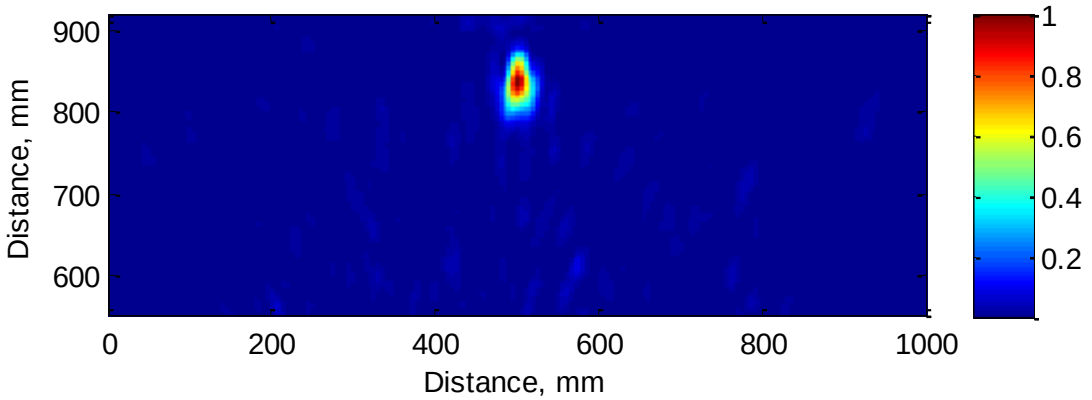

a)

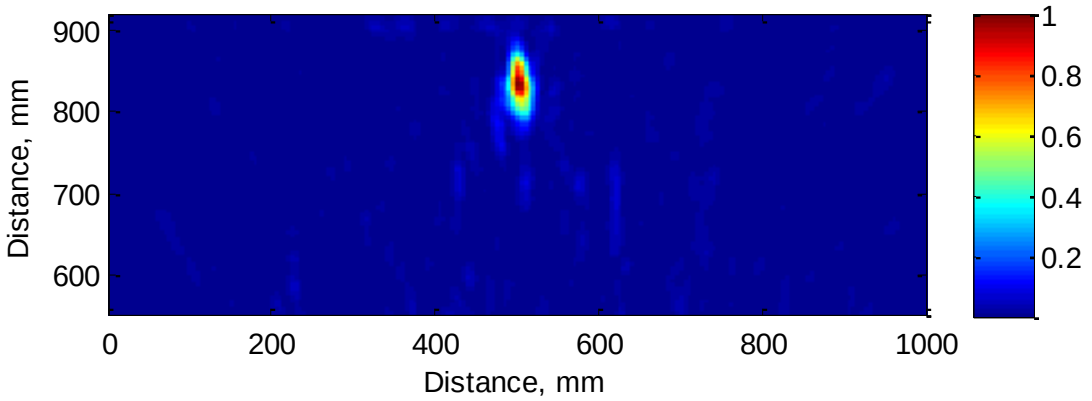

b)

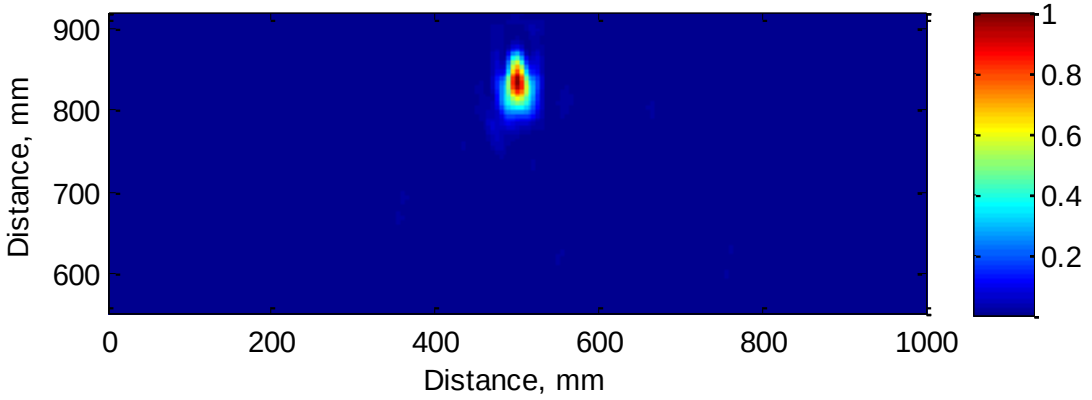

c)

Figure 3.34 Reconstruction of scanned area using MI method:
a) version 1; b) version 2; c) version 3

Figure 3.35 shows the amplitude of the reconstructed image along x axis with $y = 830\ mm$, for each of the versions.

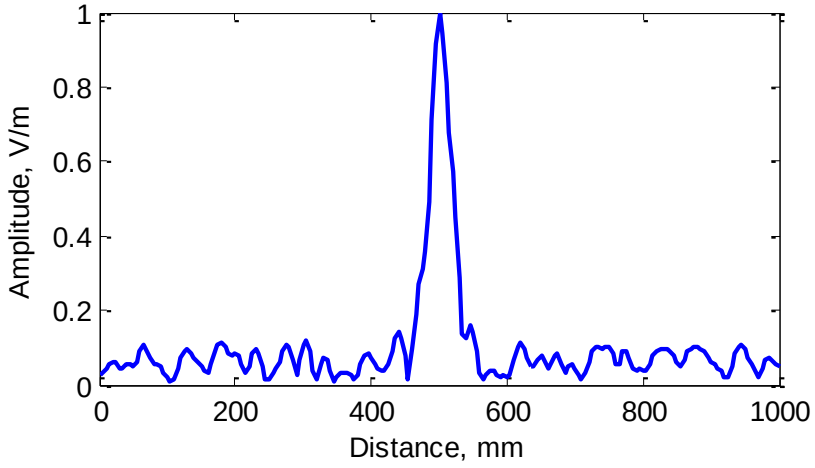

a)

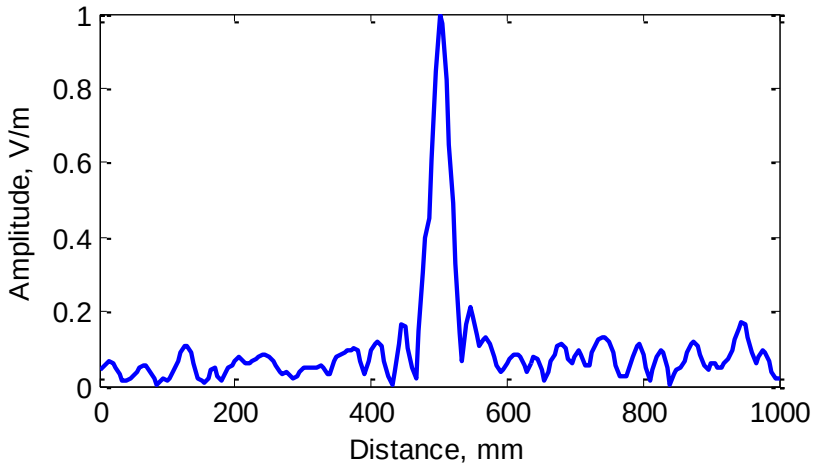

b)

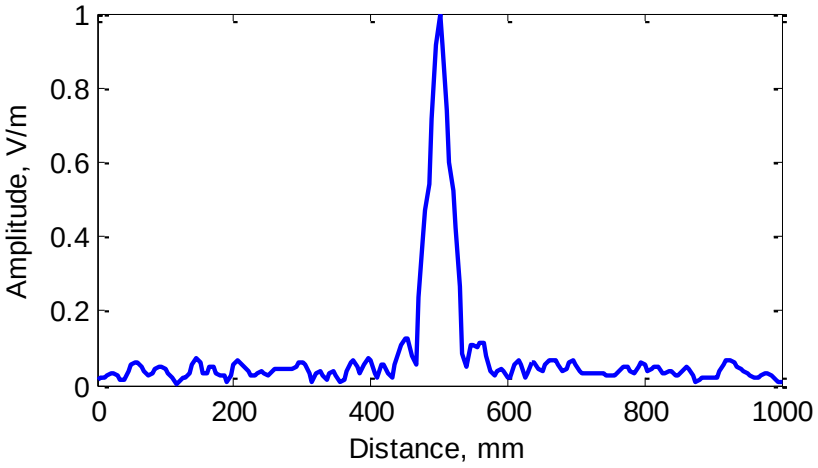

c)

Figure 3.35 Sidelobes amplitude using MI method:
a) version 1; b) version 2; c) version 3

For each version, the target is imaged in the right position ($x = 500\,mm,\ y = 830\,mm$) and secondary lobes are observed in the first to versions. Compared with the TR method, the sidelobes have been certainly attenuated. For the first version, a strong attenuation of the secondary lobes is achieved using the regularized matrix inversion method.

As for the amplitude of the secondary lobes, a lower level of the sidelobes is observed compared with the level of sidelobes shown on time reversal method.

The metallic boundaries added to the setup cause multiple scattering within the medium, increasing the reverberation time and the number of temporal degrees of freedom which gives a better signal to noise ratio. Therefore, the imaging quality is increased.

3.5 Conclusion

This chapter presents a short introduction on microwave imaging, followed by details regarding the conception of the medium and a few theoretical aspects regarding the characteristics of a random medium used for target detection. Simulations results for different setups used for target imaging with the aid of multipath propagation within the medium are presented, as well as experimental results.

Microwave imaging techniques allows the detection of objects hidden in a structure. Two main categories are used to classify the imaging techniques: quantitative imaging techniques and qualitative microwave methods, giving the electrical and geometrical parameters or a qualitative profile of an imaged object. The system is mainly comprised of two parts: the hardware part representing the apparatus used to collect data and the software part which represents the post-processing of the collected data. As for the applications of microwave imaging, there is a wide range from medical imaging or nondestructive testing and evaluation to through-the-wall imaging or concealed weapon detection.

Though time reversal has been mainly used for focusing on targets, multipath propagation through scattering medium can be exploited to obtain images and the characteristics of the medium are important due to the dependence of the directivity of time-reversed beam on the ratio of the coherent to the incoherent parts of the signal. If the coherent waves dominate, no focusing will be possible using a one element TRM. The focused intensity is the sum of the direct and diffuse intensity and decays with the distance traveled through the scattering medium.

The focusing performance of TR through a complex medium can be characterized by the ratio between the amplitude of the focused signal and the amplitude of the residual spatial and temporal sidelobes. This ratio is equal to the number of spatiotemporal degrees of freedom N which is the product of the number of spatial and temporal degrees of freedom, N_a and N_ω, respectively. Therefore, a higher number of degrees of freedom with the bandwidth provides lower background intensity and assures a better signal to noise ratio.

Simulation setups for an imaging method in the microwave range using a random medium is inspired by the time reversal technique for focusing waves that allows spatial and temporal focusing of an electromagnetic signal. When used through a complex disordered medium, it takes advantage of multipath propagation to generate a focal spot of width given only by the multiple scattering medium. The results are presented for two methods: one based

on time reversal technique and because sidelobes are inherent to TR methods, another method based on matrix inversion which provides lower sidelobes.

As well, the results of a comparison between simulation setups, is presented. Inspired from the use of a cavity for microwave imaging, three versions of a chosen simulated setup with different PEC boundaries are compared in order to determine the best results for an imaging method that takes advantage of the spectral degrees of freedom provided by the propagation through a random medium. As the PEC boundaries increase, the Q-factor of the medium increases, as well as the number of degrees of freedom, lowering the sidelobes level and increasing the quality of image.

In the context of the currently used methods for RCS measurements in anechoic chambers which can be perturbed at low frequencies, due to multi-path propagation from the scattering on the boundaries, by introducing a strongly disordered medium within the chamber, it is not necessary to make the walls fully absorbing. As well, merging the complex medium with a waveguide cavity shows an improvement in the desired results. Following the simulation results the next chapter presents measurement results on computational imaging using a method based on time reversal technique.

CHAPTER 4 Imaging through a random medium using two antennas

4.1 Introduction

Following the simulation results on a microwave imaging method that takes advantage of the spectral degrees of freedom provided by the propagation through a random medium, this chapter presents an experimental validation of the technique.

The location of a scatterer can be extracted with a high resolution even though only two antennas are used. The ability to image the target is shown using a synthetic time reversal technique and a matrix inversion method.

4.2 Random medium fabrication

The proposed design for the random medium used in the previous presented 2D simulations is applied to fabricate the experimental medium. A total number of 268 steel rods of 10 mm diameter is inserted on PVC substrates. Due to manufacturing reasons, the medium is divided in five parts. The minimum distance between the rods is $25\,mm$, half of wavelength and the height of the rods is $H = 400\,mm$, the equivalent of 8 wavelengths for the central frequency of 6 GHz. Figure 4.1 shows a schematic of the divided medium.

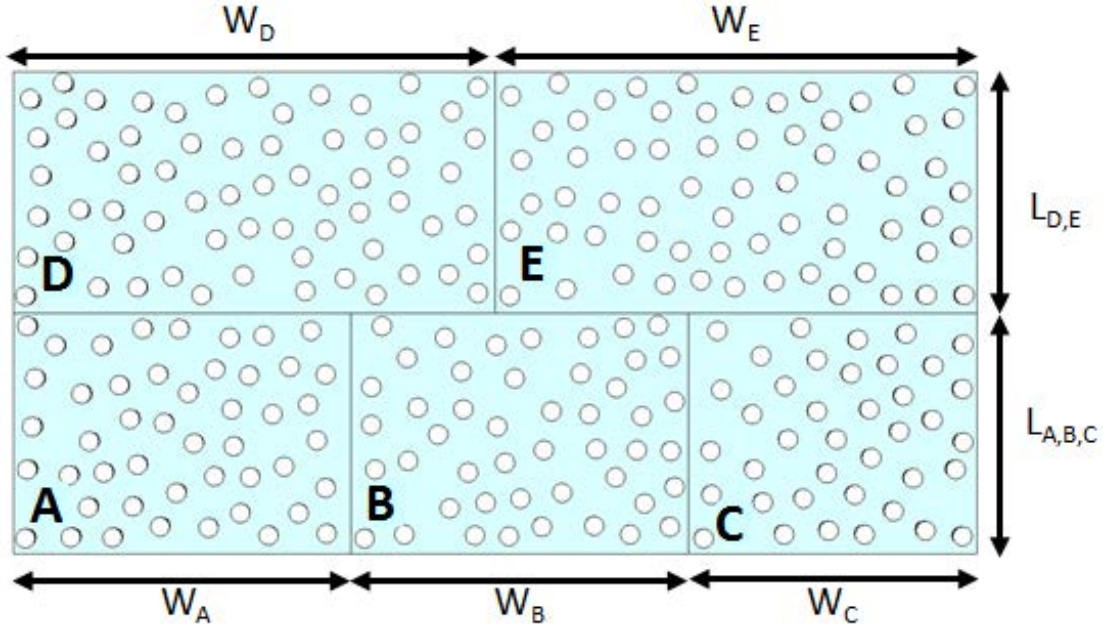

Figure 4.1 Fabricated medium parts schematic

The dimensions of the composing parts of the medium are: $L_{A,B,C} = L_{D,E} = 250\,mm$, $W_A = W_B = 350\,mm$, $W_C = 300\,mm$ and $W_D = W_E = 500\,mm$.

Figure 4.2 shows a schematic all parts of the medium assembled together as a unit.

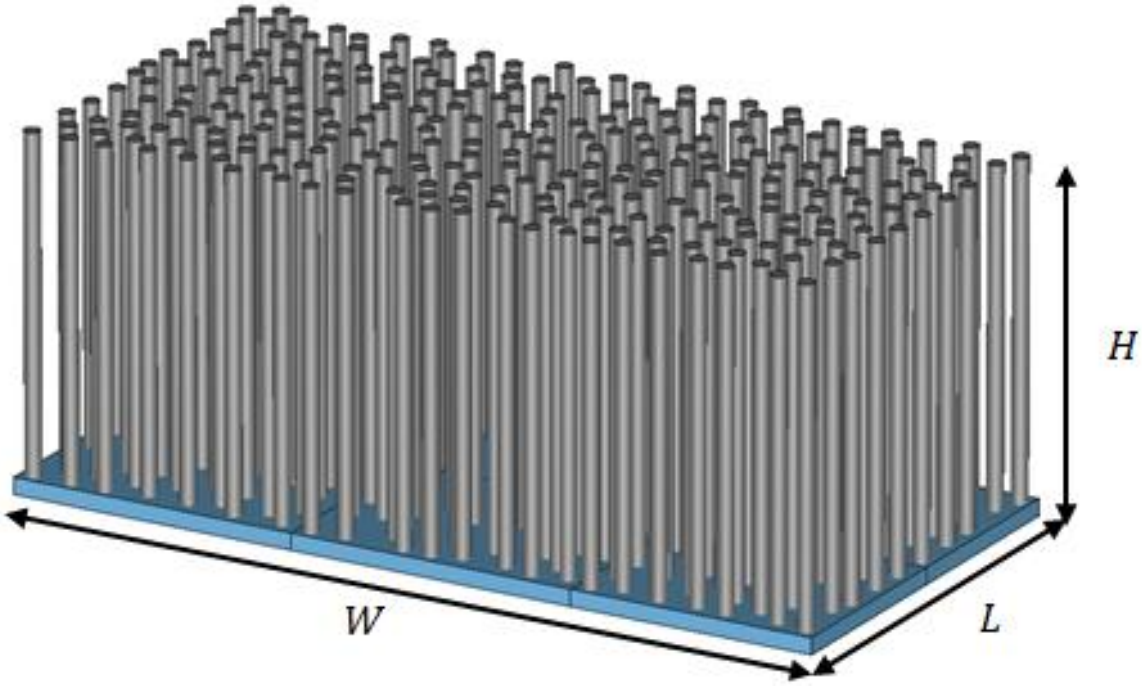

Figure 4.2 Fabricated random medium schematic

The total width of the medium is $W = 1000\,mm$, the equivalent of 20 wavelengths and the total length is half of the width, $L = 500\,mm$, the equivalent of 10 wavelengths.

Figure 4.3 shows a photograph of the medium.

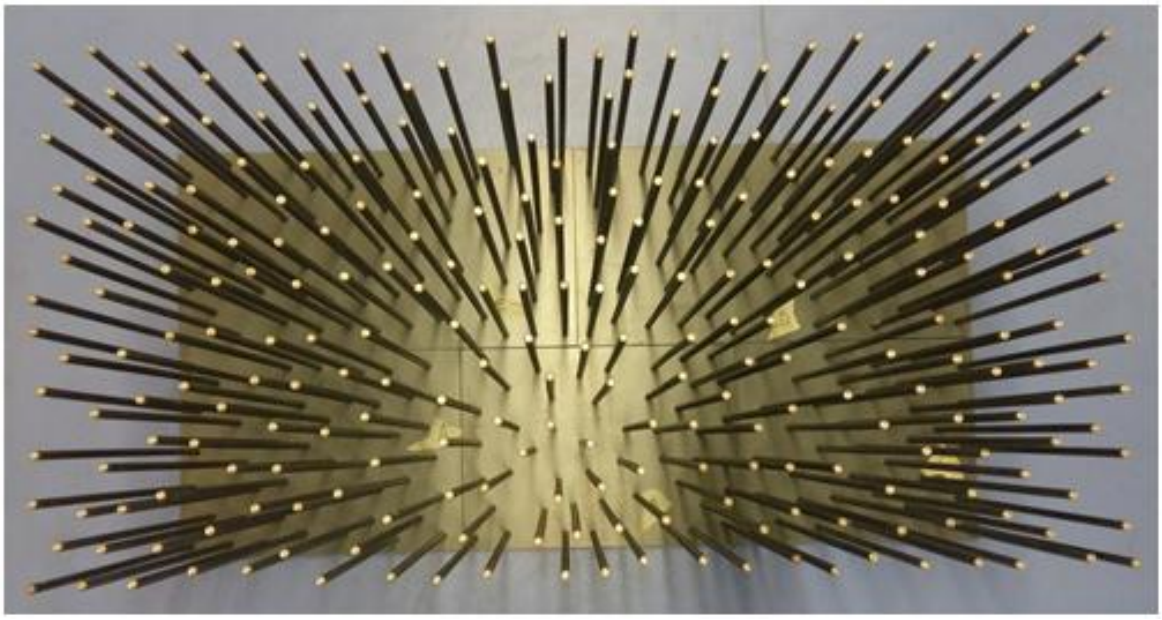

a)

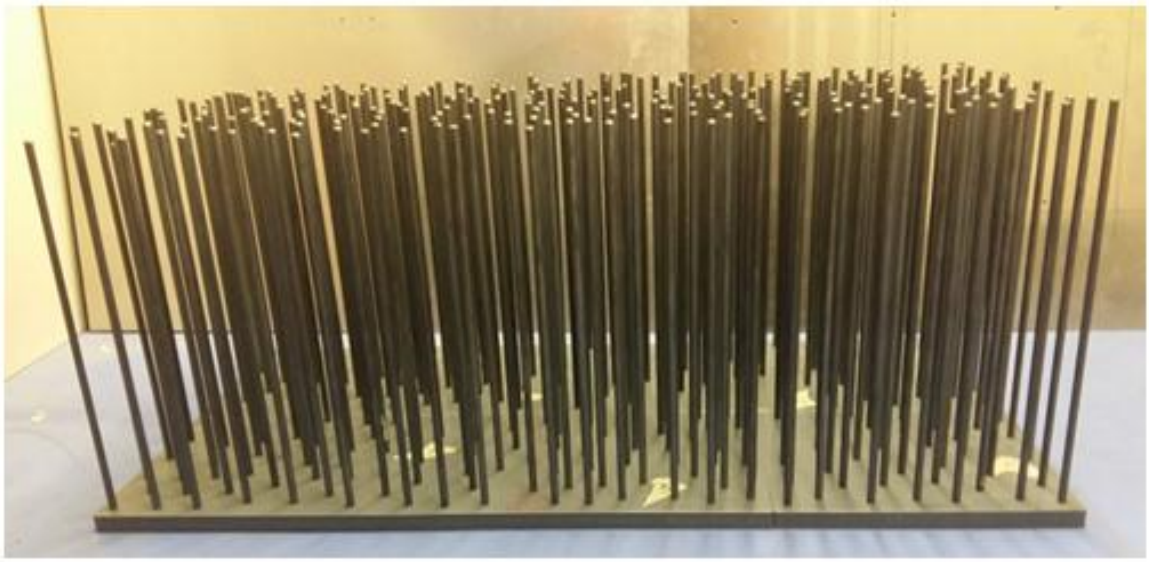

b)

Figure 4.3 Fabricated random medium: a) top view; b) side view

4.3 Experimental results

4.3.1 Measurement setup

The measurement setup is similar to simulation setup B. There are also two configurations used: scanning configuration and DUT configuration. The fabricated medium is placed between two horn antennas. Antenna A_1 is set behind the medium and antenna A_2 right in front of the medium.

In the first configuration, a third discone antenna A_3, is used to scan the field along the scanning line, which is placed approximately 1 meter away from the medium, in front of it. In the second configuration, the third antenna is replaced with a target, in this case, a corner reflector. Figure 4.4 shows the two configurations of the setup.

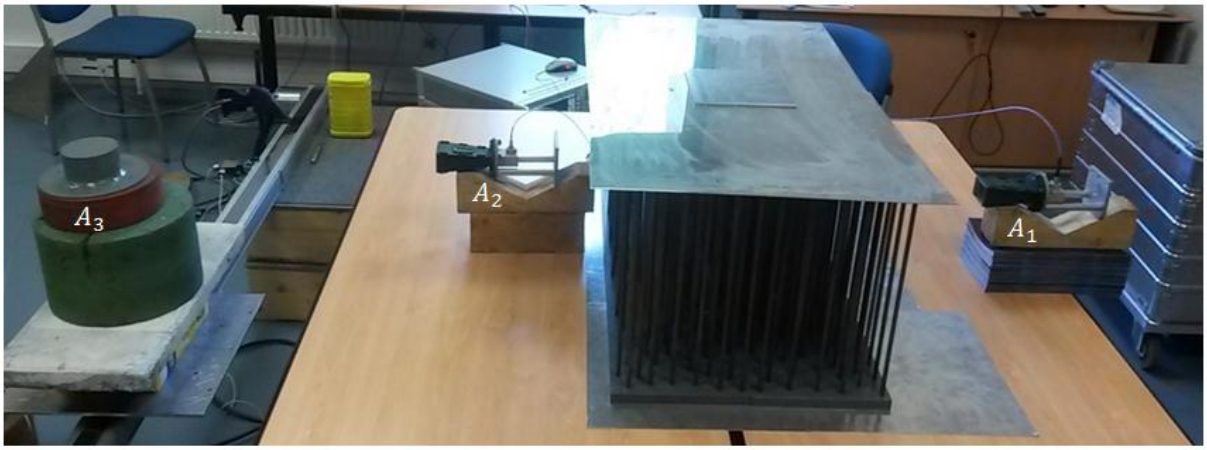

a)

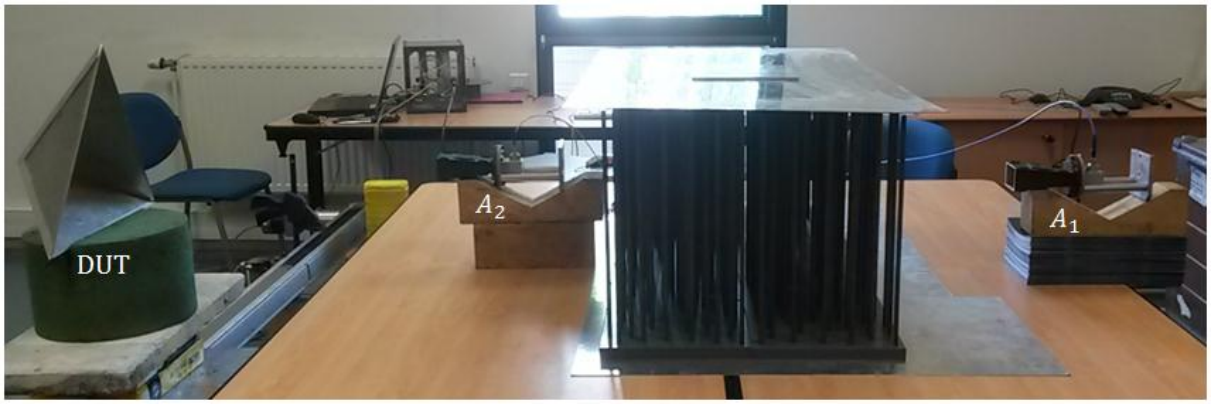

b)

Figure 4.4 Measurement setup:

a) Scanning configuration; b) DUT configuration

There are three steps in the measurement protocol. The first step requires a void measurement, in which are used only the antennas A_1 and A_2 placed behind and in front of the medium. The parameter S_{21}^{void} which gives the coupling between the two antennas in absence of the target is recorded.

During the second step of measurements, the scanning configuration is used. The antenna, A_3 is placed on a rail and moved parallel with the medium, in order to scan the field in front of medium on $N_f = 6001$ frequency points in the $4.64 - 7.05\ GHz$ frequency range, while antennas A_1 and A_2 are emitting. The length of the scanning line is $1000\ mm$ and parameters S_{31} and S_{32} are registered on 100 positions from 10 to 10 mm.

The registered parameters during the second step of measurements are shown in Figure 4.5 for the central frequency.

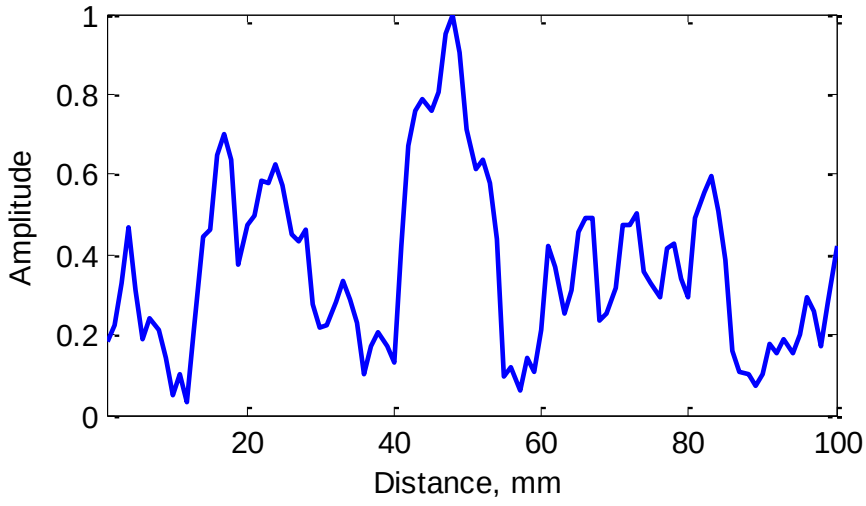

a)

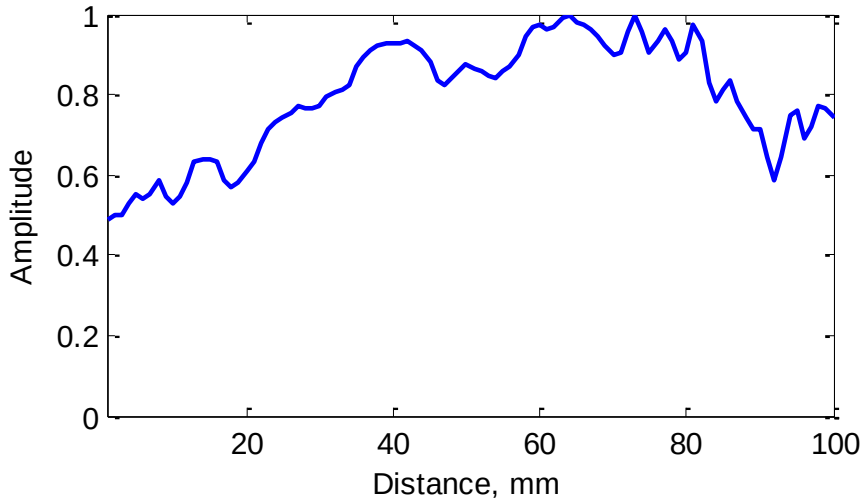

b)

Figure 4.5 S parameters at central frequency: a) $S_{31}(r)$; b) $S_{32}(r)$

The parameter S_{31} gives the transmission coefficient through the medium from antenna A_1 to scanning antenna A_3 and parameter S_{32}, gives the free space transmission coefficient from antenna A_2 to scanning antenna A_3.

Starting from the scanning line, in order to obain the filed in any position, the field emitted by the antennas A_1 and A_2 is reconstructed in front of the line, over an area with sizes of $1000\ mm$ by $500\ mm$, generic called in the followings, area F.

The third step of measurements uses the DUT configuration of the setup, where the target replaces the scanning antenna. The position on the rail is moved in front of the scanning line and the target is translated along a line which is parallel to the medium on 10 positions from 100 to 100 mm. In this step, the S_{21}^{w} parameter in the presence of the target is recorded for each position of the target.

The forward propagation is reconstructed using the 3D Green‟s functions [91]:

$$G_{3D}(r,r') = \frac{e^{-jk|r-r'|}}{4\pi|r-r'|} \tag{4.1}$$

Presuming Huygens‟ principle that every point on a wavefront could be regarded as a new source of waves [92], all the values of parameters $S_{31}(\omega,r)$ and $S_{32}(\omega,r)$ for each scanned position, are used to reconstruct the fields denoted by $G_1(r,\omega)$ and $G_2(r,\omega)$, respectively, taking into account the sum of all prior contributions. Figure 4.6 presents a schematic of the setup, showing the location of area F over which the reconstruction of the fields is performed.

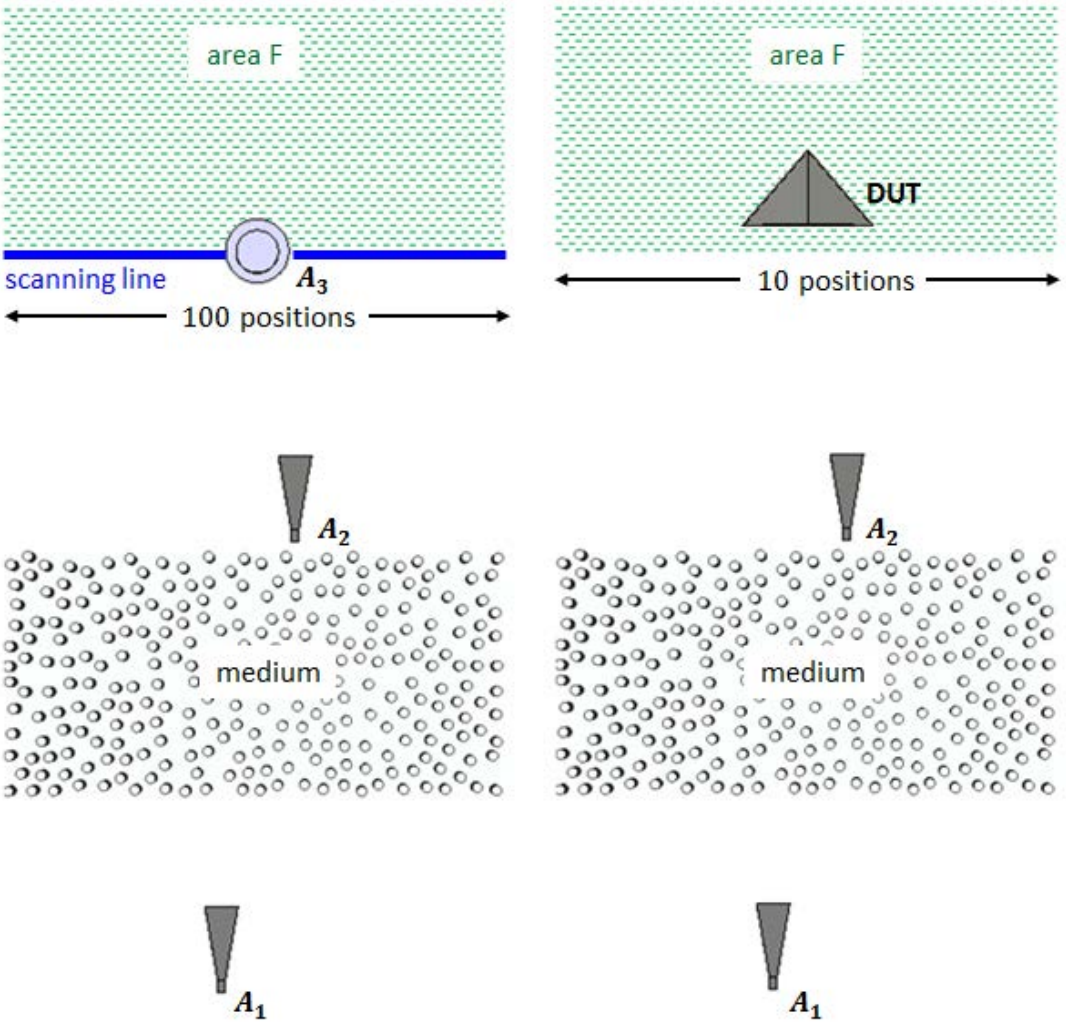

a) b)

Figure 4.6 Schematic setup:

a) Scanning configuration; b) DUT configuration

Figure 4.7 shows the propagation from antennas A_1 and A_2 on the area in front of the scanned line, for the central frequency.

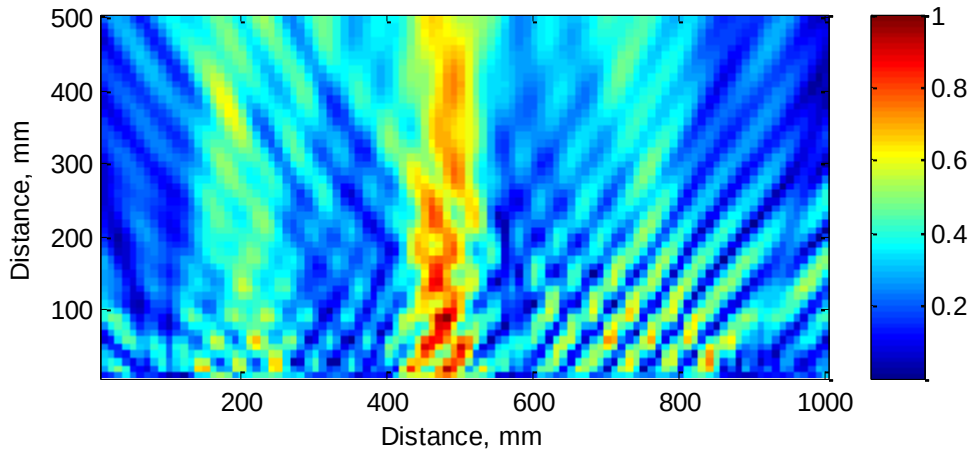

a)

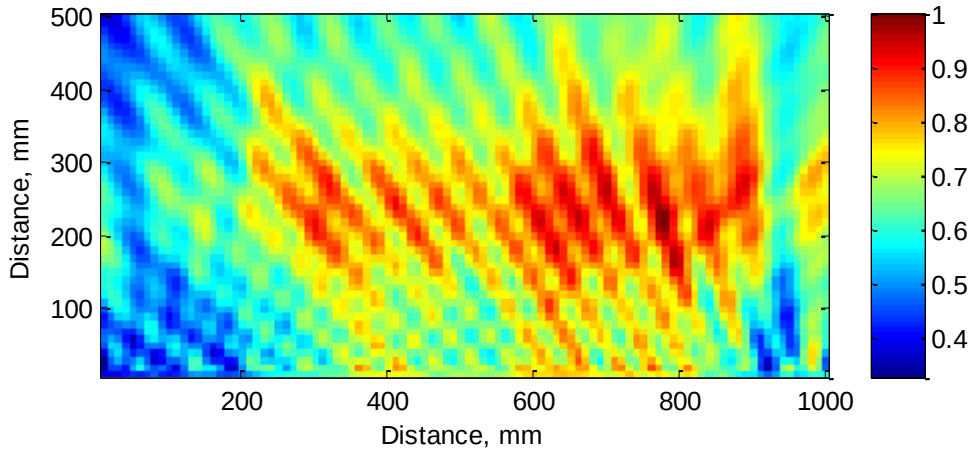

b)

Figure 4.7 Reconstructed area:

a) $G_1(r,\omega)$ – propagation through the medium; $G_2(r,\omega)$ – free space propagation

The coupling between the two antennas in absence of the DUT, parameter $S_{21}^{void}(\omega)$ is then subtracted to $S_{21}^{w}(\omega)$ and gives $S_{21}(\omega)$ which involves only the response of the DUT transmitted through the medium:

$$S_{21}(\omega) = S_{21}^{w}(\omega) - S_{21}^{void}(\omega) \tag{4.2}$$

Similarly to simulation approach, the $S_{21}(\omega)$ parameter can be written as :

$$S_{21}(\omega) = \int_{\mathrm{F}} G_1(r,\omega)\, G_2(r,\omega)\sigma(\omega,r)\, d^2r \tag{4.3}$$

where $G_1(r,\omega)$, $G_2(r,\omega)$ are the Green functions over area F when antenna A_1, respectively antenna A_2 are emitting and $\sigma(\omega,r)$ is the spatial distribution of the scattering coefficient.

We then assume that the scattering coefficient of the DUT is independent of frequency $\sigma(\omega,r) = \sigma(r)$. Therefore, equation (4.3) is expressed in its discretized form as the multiplication of two matrices: $S_{21} = H\sigma$.

The matrix H is expressed as the product of the Green functions reconstructed over area F from both antennas A_1 and A_2 :

$$H_{ij} = G_1(r_j,\omega_i)G_2(r_j,\omega_i) \tag{4.4}$$

Using Tikhonov regularization, the estimated vector of scattering coefficient $\tilde{\sigma}$ is expressed as:

$$\tilde{\sigma} = (H^{\dagger}H + \mu I)^{-1}H^{\dagger}S_{21} \tag{4.5}$$

For each position in front of the medium using the matrix inversion method, an image is computed from:

$$I(r) = \left|(H^{\dagger}H + \mu I)^{-1}H^{\dagger}S_{21}\right|^{2} \tag{4.6}$$

Figure 4.8 shows the reconstruction of area F for the DUT configuration where the target is added to the setup.

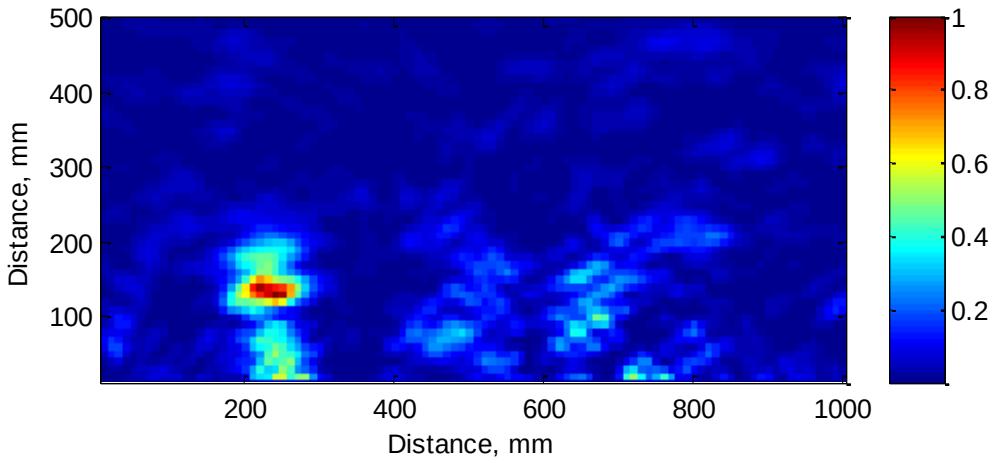

a)

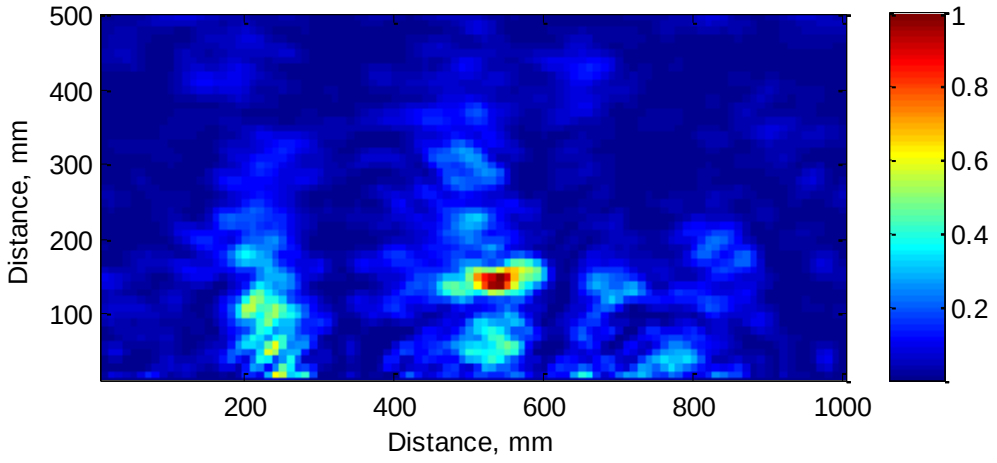

b)

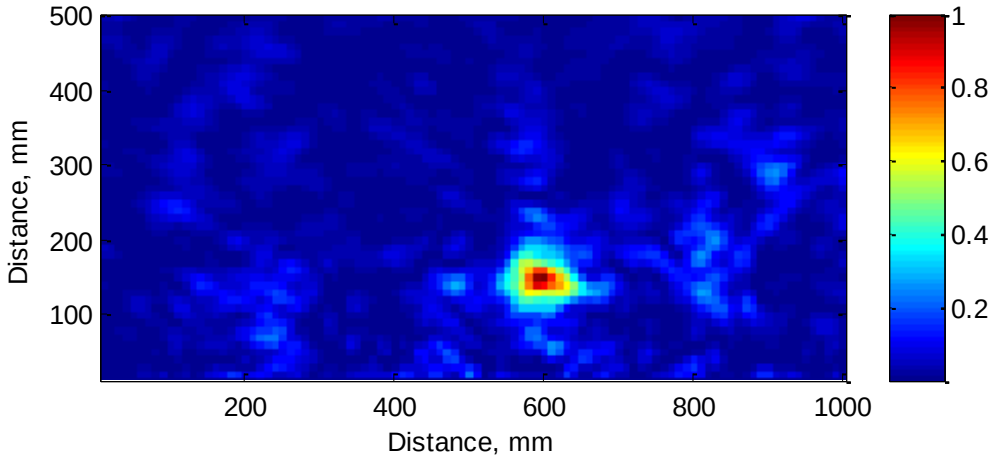

c)

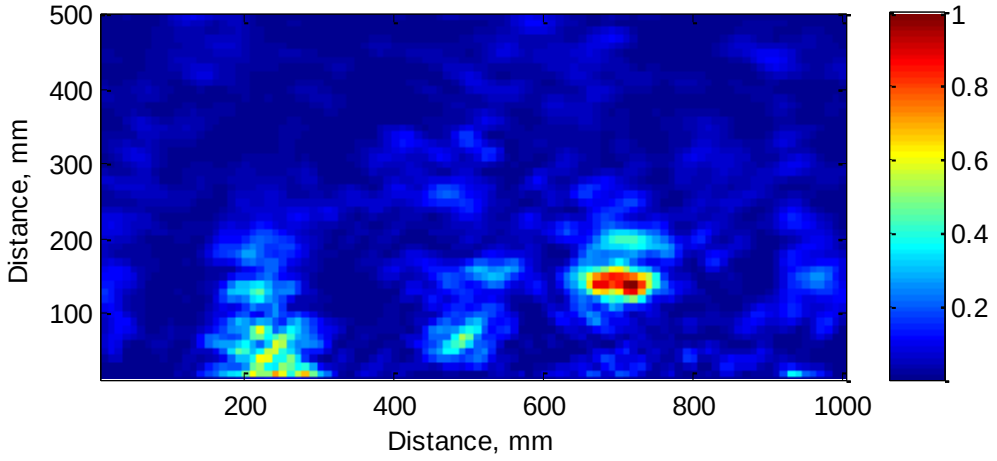

d)

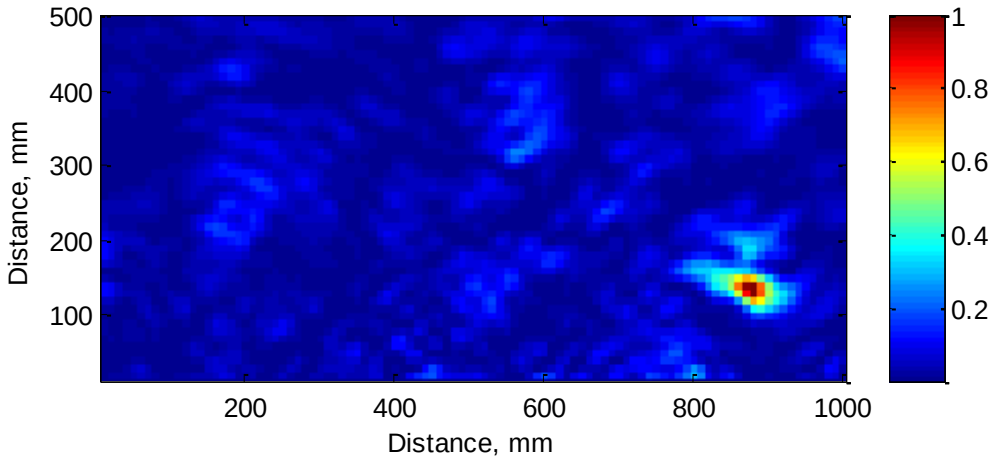

e)

Figure 4.8 Reconstruction of area F using MI method – Measurement setup: a) x_3~300 mm; b) x_5~500 mm; c) x_6~600 mm; d) x_7~700 mm; e) x_9~900 mm;

Figure 4.9 shows the amplitude of the reconstructed image along x axis for both MI and TR methods.

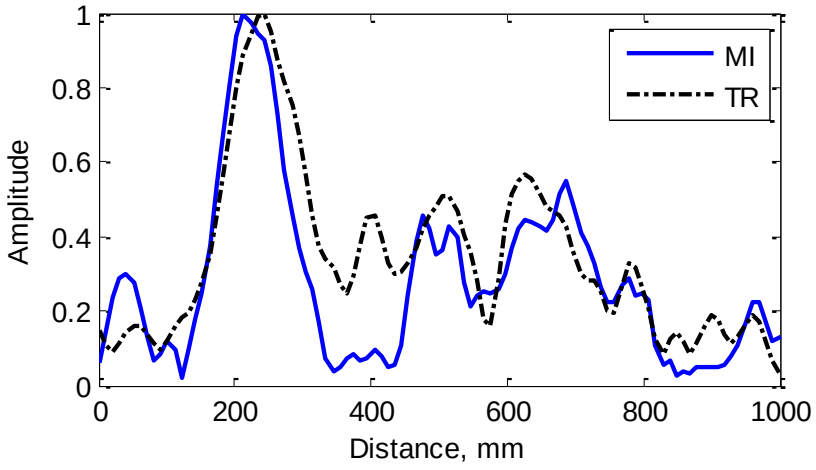

a)

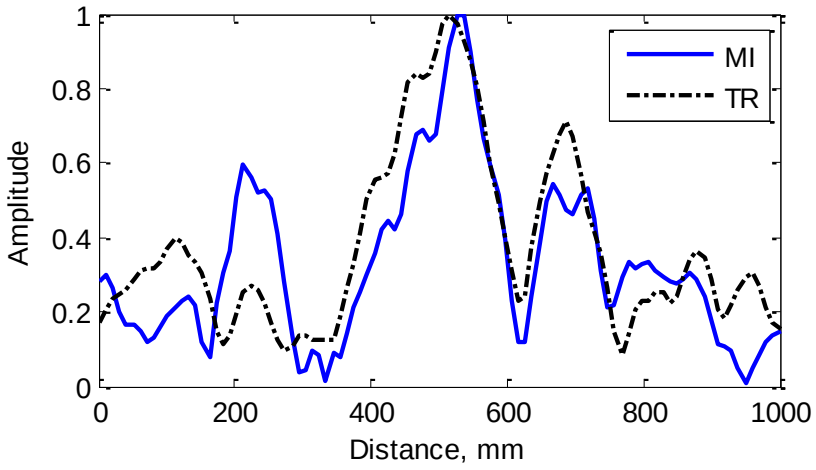
MI
TR
Amplitude
Distance, mm
0
0.2
0.4
0.6
0.8
1
0
200
400
600
800
1000

b)

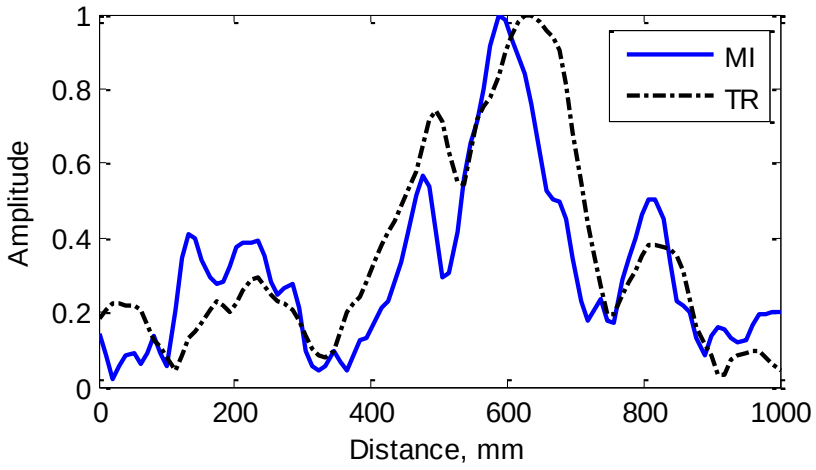
MI
TR
Amplitude
Distance, mm
0
0.2
0.4
0.6
0.8
1
0
200
400
600
800
1000

c)

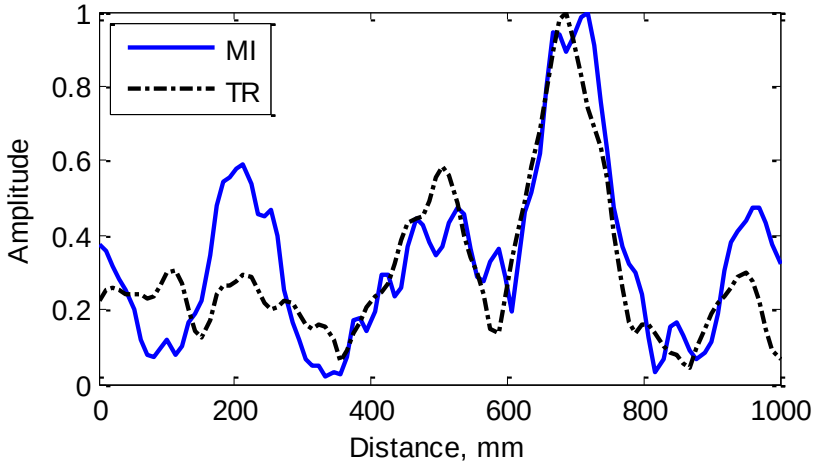
MI
TR
Amplitude
Distance, mm
0
0.2
0.4
0.6
0.8
1
0
200
400
600
800
1000

d)

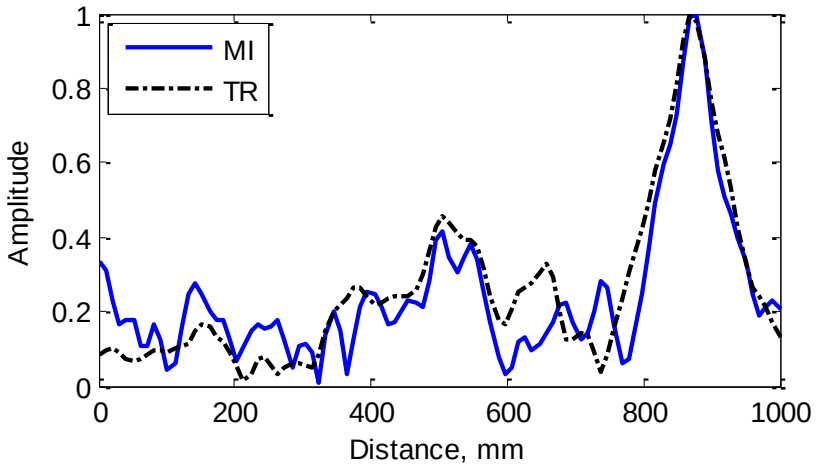

e)

Figure 4.9 Sidelobes amplitude MI vs TR method:

a) x_3~300 mm; b) x_5~500 mm; c) x_6~600 mm; d) x_7~700 mm; e) x_9~900 mm;

The target is seen to be located successively at positions $x_3 = 300\,mm$, $x_5 = 500\,mm$, $x_6 = 600\,mm$, $x_7 = 700\,mm$ and $x_9 = 300\,mm$. Due to the limited directivity of antenna A_2, the detection of the target is more precise for the right half of the area F.

The detection of the DUT is clearly seen on each of the presented figures. For the two methods, time reversal and matrix inversion, the level of the sidelobes is comparable when using only one emitting antenna through the medium.

4.3.2 Multiple antennas measurement setup

A multiple antenna setup in an anechoic environment is used to compare imaging abilities between different configurations. Similar to simulation setup B, there are two configurations used: the scanning configuration and the DUT configuration, while the fabricated medium is placed in font of three horn antennas A_1, A_2 and A_3, while a fourth antenna A_4 is placed on the right side of the medium. Antenna A_2 is centered with respect to the medium and the other two antennas A_1 and A_3 are placed 300 mm to the left and right, respectively.

In the same manner, during the first configuration, a fifth discone antenna A_5, is used to scan the field along the scanning line, which is placed approximately 1 meter away from the medium, in front of it. In the second configuration, the scanning antenna is replaced with a target, the corner reflector. Figure 4.10 shows the two configurations of the setup.

There are as well, three steps in the measurement protocol. During the first step, a void measurement, in which are used only the antennas A_1, A_2, A_3 and A_4 placed behind and on

the side of the medium. The parameters S_{41}^{void}, S_{42}^{void} and S_{43}^{void} which give the coupling between the antennas in absence of the target are registered.

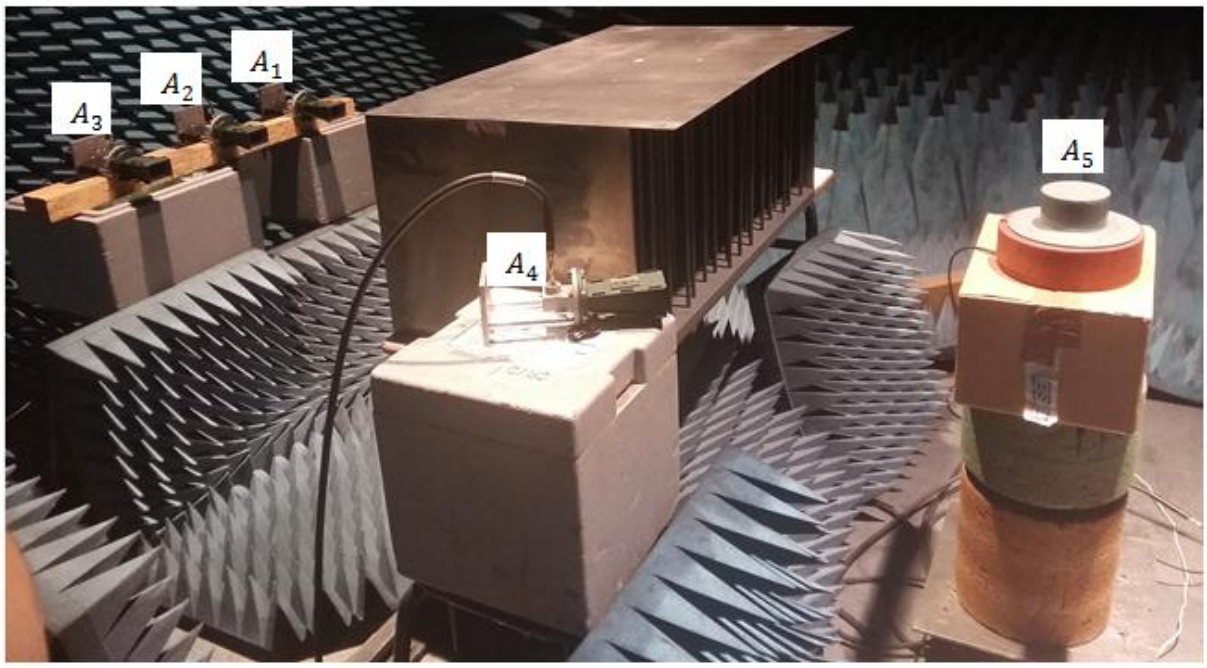

a)

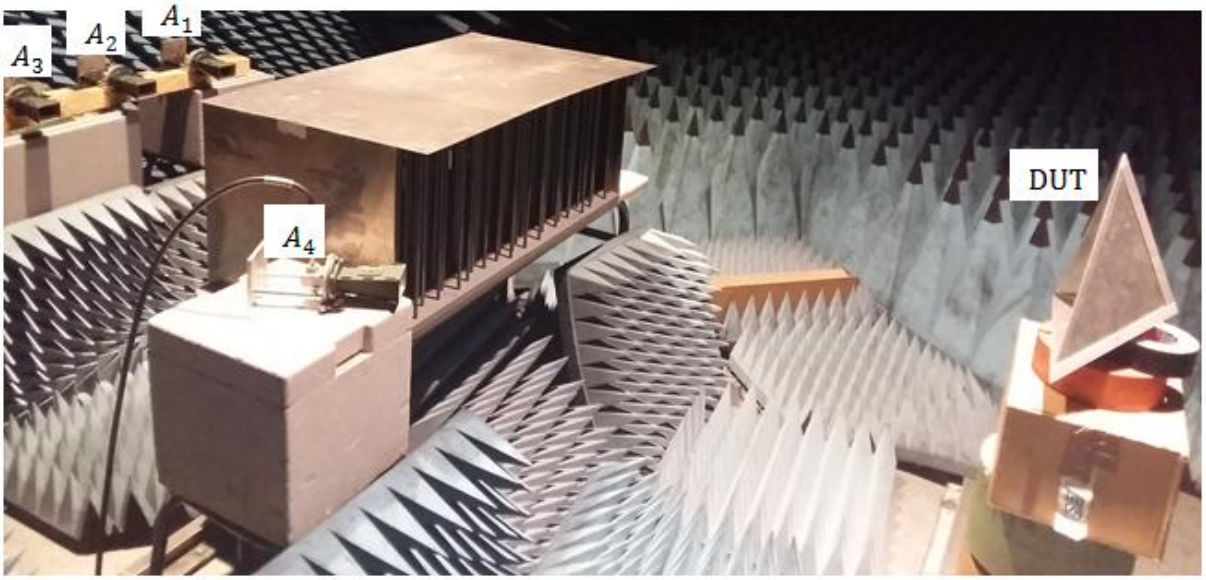

b)

Figure 4.10 Multiple antennas measurement setup:
a) Scanning configuration; b) DUT configuration

During the second step of measurements, the scanning configuration is used. The antenna, A_5 is placed on a rail and moved parallel with the medium, in order to scan the field in front of medium on $N_f = 4821$ frequency points in the $4.64 - 7.05\ GHz$ frequency range,

while antennas A_1, A_2, A_3 and A_4 are emitting. The length of the scanning line is 1100 mm and parameters S_{51}, S_{52}, S_{53} and S_{54} are registered on 111 positions from 10 to 10 mm.

The third step of measurements uses the DUT configuration of the setup, where the target is replacing the scanning antenna. The position of the rail is displaced in front of the scanning line and the target is placed on central position. In this step, the S_{41}^w, S_{42}^w and S_{43}^w parameters in the presence of the target are registered.

Figure 4.12 presents a schematic of the setup, showing the position of the antennas and the location of area F over which the reconstruction of the fields is performed.

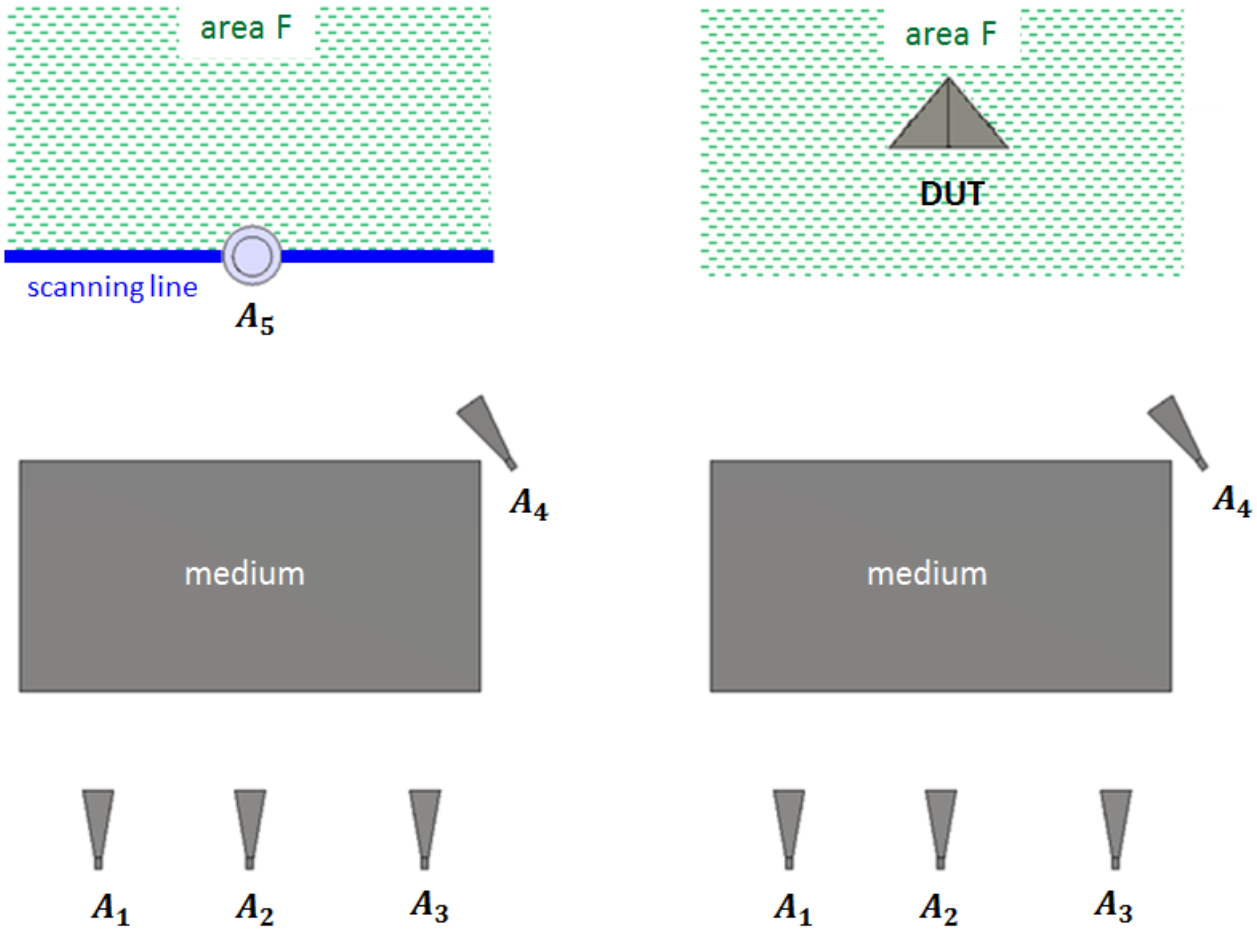

Figure 4.11 Multiple antennas schematic setup:
a) Scanning configuration; b) DUT configuration

Likewise, starting from the scanning line, the field emitted by antennas A_1, A_2, A_3 and A_4 is recostructed in front the line, over area F with the sizes of 1000 mm by 500 mm. The forward propagation is reconstructed using the 3D Green‟s functions from equation (4.1) and by presumming Huygens‟ Principle. All the values of parameters $S_{51}(\omega, r)$, $S_{52}(\omega, r)$, $S_{53}(\omega, r)$ and $S_{54}(\omega, r)$ for each scanned position, are used to reconstruct the fields denoted

by $G_1(r,\omega)$, $G_2(r,\omega)$, $G_3(r,\omega)$ and $G_4(r,\omega)$, respectively, taking into account the sum of all prior contributions.

Figure 4.12 shows the propagation from antennas A_1, A_2, A_3 and A_4 on area, for the central frequency.

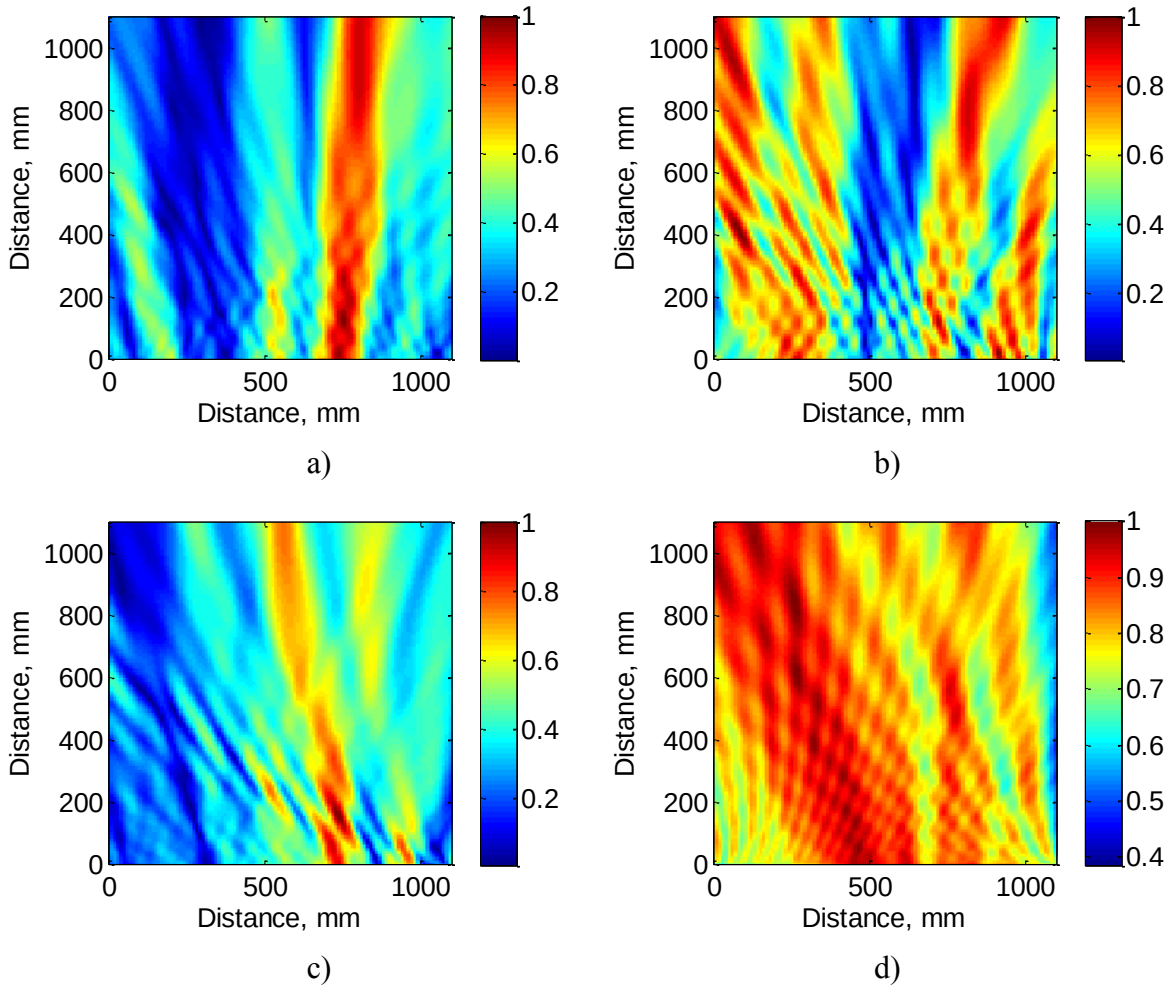

Figure 4.12 Reconstructed area:

a) $G_1(r,\omega)$ – propagation through the medium; a) $G_2(r,\omega)$ – propagation through the medium; a) $G_3(r,\omega)$ – propagation through the medium; $G_4(r,\omega)$ – free space propagation

Regarding the posibility of using two or more antennas to image the target, here are multiple situations compared in the followings.

4.3.2.1 Case 1 – one antenna emitting through the medium

Figure 4.13 presents a schematic of antennas A_1, A_2, A_3 and A_4 layouts in three situations where A_4 is always placed on the side of the medium. In case 1.1, 1.2 and 1.3 is used antenna A_1, A_2 and A_3, respectively. For simplicity, all parameters related to antennas A_1, $A_2$and A_3 include the index $n = \overline{1,3}$.

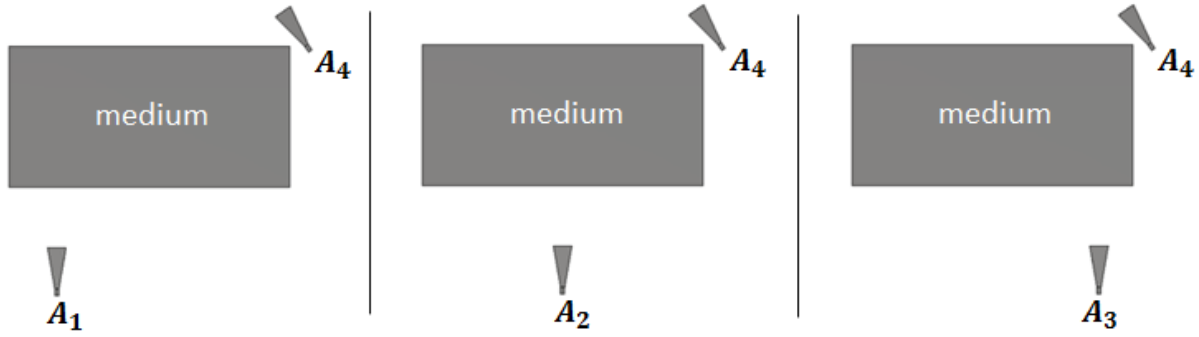

a) b) c)

Figure 4.13 Multiple antennas schematic - case 1:

a) case 1.1; a) case 1.2; a) case 1.3;

In these cases, the parameter that includes the scattering from the DUT, but also the propagation within the medium is given by the difference between the two S_{4n} parameters recorded with and without de DUT added to the setup:

$$S_{4n}(\omega) = S_{4n}^{w}(\omega) - S_{4n}^{void}(\omega) \tag{4.7}$$

By assuming that the scattering coefficient of the DUT is independent of frequency, $\sigma(\omega, r) = \sigma(r)$, the $S_{4n}(\omega)$ parameter for each case can be written as :

$$S_{4n}(\omega) = \int_{\mathrm{F}} G_n(r,\omega)\, G_4(r,\omega)\sigma(\omega,r)\, d^2r \tag{4.8}$$

where, $G_n(r,\omega)$ and $G_4(r,\omega)$ are the reconstructed Green function over area F when antenna A_n and antenna A_4 are emitting and $\sigma(\omega,r)$ is the spatial distribution of the scattering coefficient.

Using time reversal technique, the reconstructed images of area F for the DUT configuration is expressed in each case as:

$$Is_n(r) = \left| \iint S_{4n}^{*}(\omega) G_n(r,\omega) G_4(r,\omega) \right|^2 \tag{4.9}$$

The target is imaged at central position with strong sidelobes for case 1.1 and case 1.3, where the antennas behind the medium, A_1 and A_3 are located near the ends of the medium. For case 1.2, antenna A_2 in centered with respect to the medium‟s width, providing a better multipath propagation within the medium.

For the matrix inversion method, the matrices H_n are expressed as the reconstructed Green functions over area F when antennas A_n, and A_4 are emitting and $\sigma(\omega,r)$ is the spatial distribution of the scattering coefficient:

$$H_{n_{ij}} = G_n(r_j, \omega_i) G_4(r_j, \omega_i) \tag{4.10}$$

Using time reversal technique, Figure 4.14, show the reconstructed images of area F for the DUT configuration.

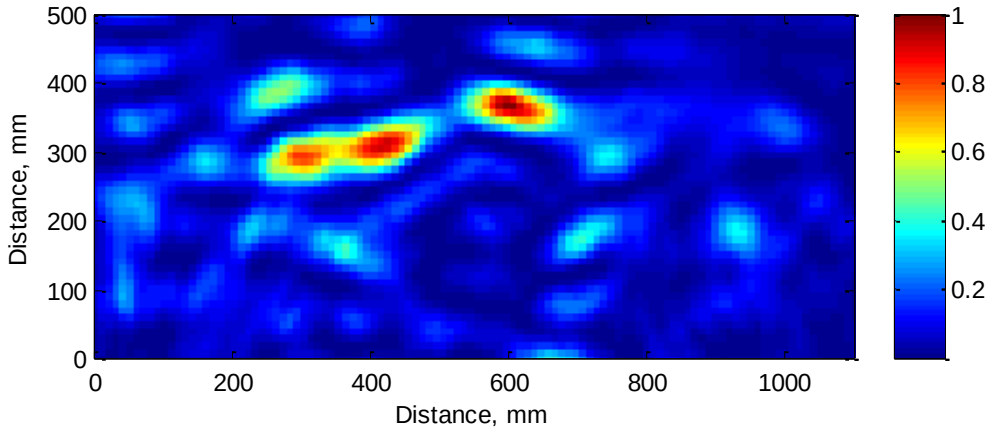

a)

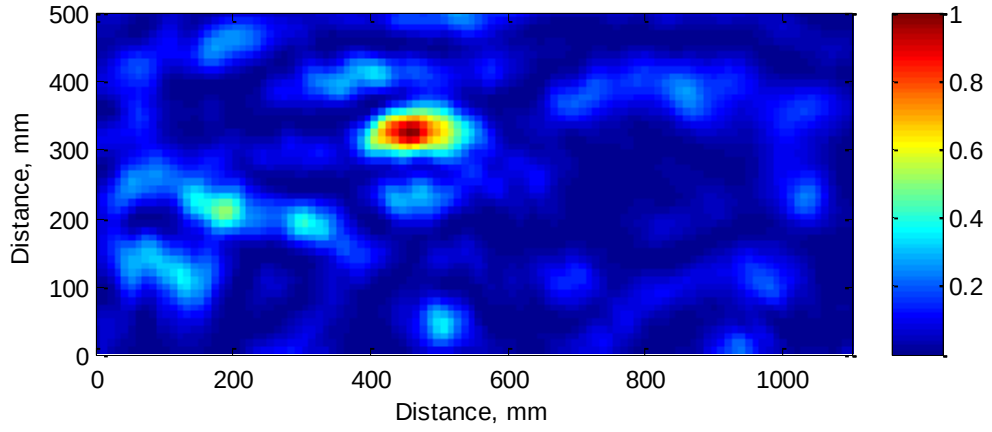

b)

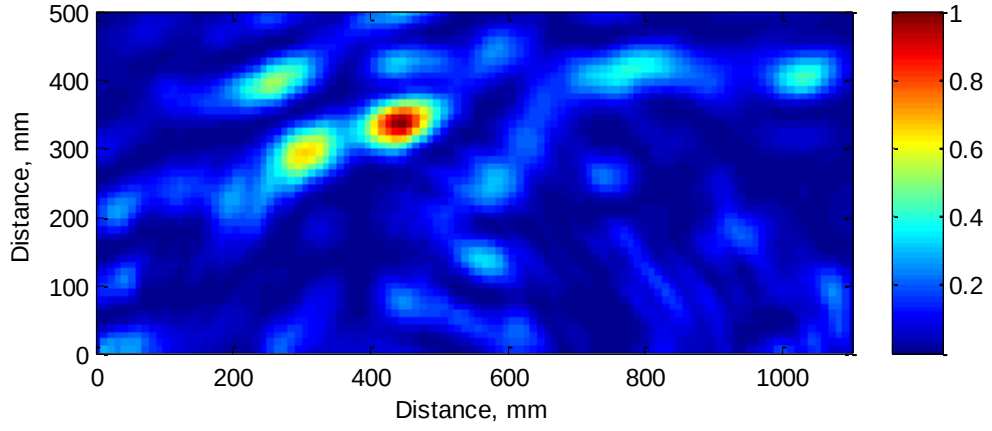

c)

Figure 4.14 Reconstruction of area F using TR method – Multiple antennas measurement setup: a) case 1.1; b) case 1.2; c) case 1.3

For each position of area F, following the approach previously formulated, an image is computed in each case, as:

$$Im_n(r) = \left| \left({H_n}^{\dagger} H_n + \mu I \right)^{-1} {H_n}^{\dagger} S_{4n} \right|^2 \tag{4.11}$$

Figure 4.15 shows the reconstruction of area F for the DUT.

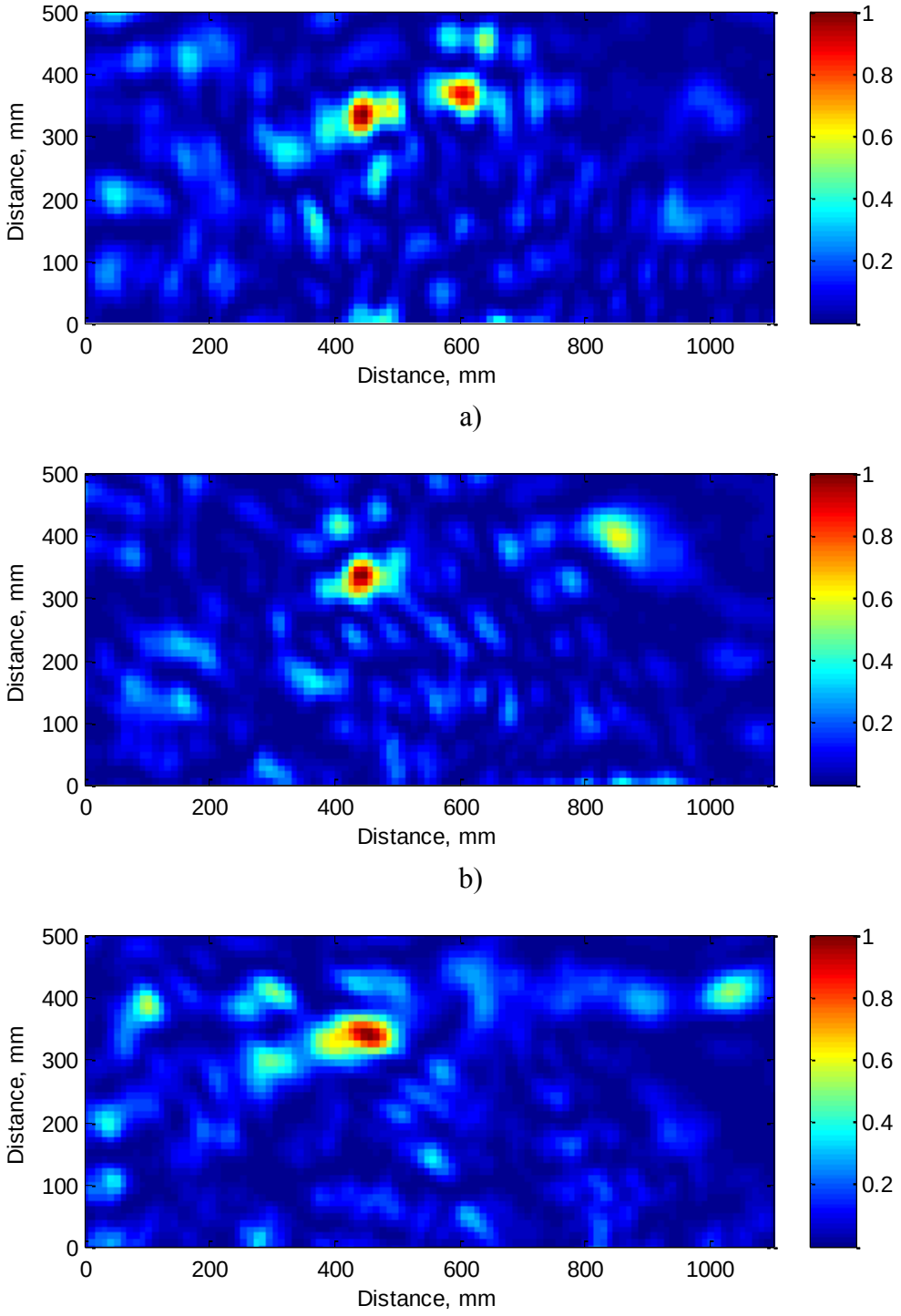

a)

b)

c)

Figure 4.15 Reconstruction of area F using MI method – Multiple antennas measurement setup: a) case 1.1; b) case 1.2; c) case 1.3

Similarly with time reversal method, the target is better imaged in the second case where the antenna behind the medium is placed on a central position along the medium.

Figure 4.16 shows the amplitude of the reconstructed image along x axis for both MI and TR methods. The detection of the DUT is clearly seen on each case. For both methods, the level of side lobes along the x axis is comparable.

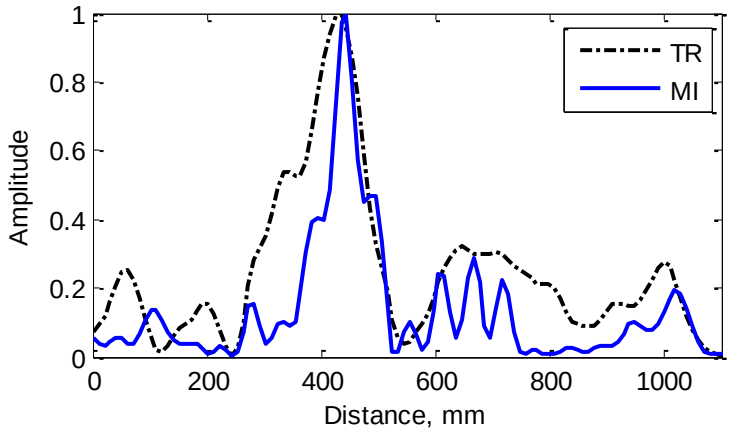

a)

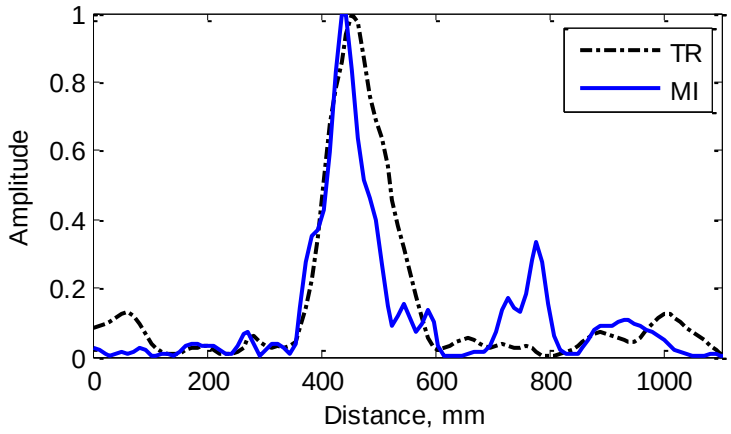

b)

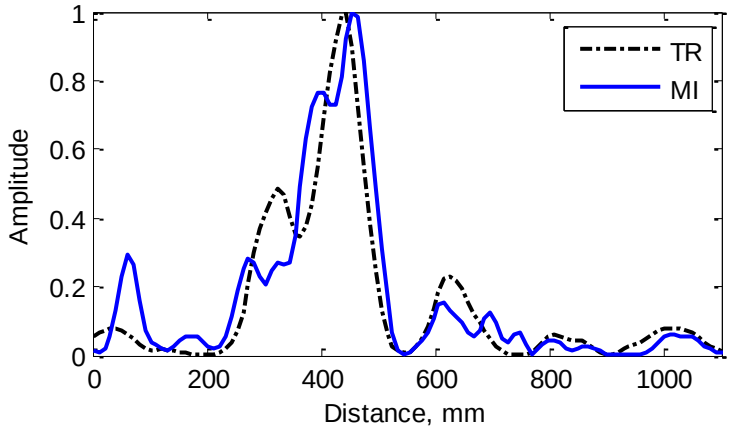

c)

Figure 4.16 Sidelobes amplitude MI vs TR method – Multiple antennas measurement setup: a) case 1.1; b) case 1.2; c) case 1.3

4.3.2.2 Case 2 – two antennas emitting through the medium

Figure 4.17 presents a schematic of antennas A_1, A_2, A_3 and A_4 layouts in three situations where A_4 is always placed on the side of the medium. In case 2.1, antennas A_1, A_2 are used, in case 1.2, antennas A_1, A_3 and in case 1.3, antennas A_2, A_3.

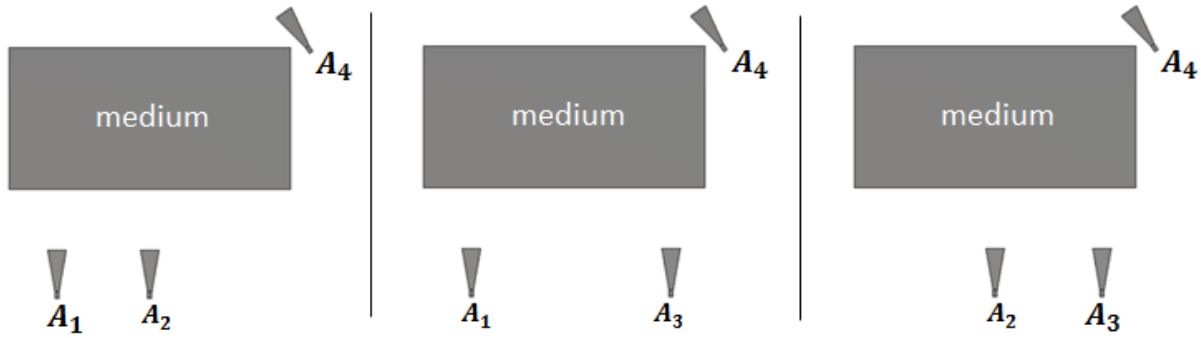

a) b) c)

Figure 4.17 Multiple antennas schematic - case 2:
a) case 2.1; a) case 2.2; a) case 2.3;

Using time reversal technique, the reconstructed images of area F for the DUT configuration is expressed in each case as:

$$Is_{12}(r) = \left| \int S_{41}^{*}(\omega) G_1(r,\omega) G_4(r,\omega) + S_{42}^{*}(\omega) G_2(r,\omega) G_4(r,\omega) \right|^2 \quad (4.12)$$

$$Is_{13}(r) = \left| \int S_{41}^{*}(\omega) G_1(r,\omega) G_4(r,\omega) + S_{43}^{*}(\omega) G_3(r,\omega) G_4(r,\omega) \right|^2 \quad (4.13)$$

$$Is_{23}(r) = \left| \int S_{42}^{*}(\omega) G_2(r,\omega) G_4(r,\omega) + S_{43}^{*}(\omega) G_3(r,\omega) G_4(r,\omega) \right|^2 \quad (4.14)$$

where, $Is_{12}(r)$, $Is_{13}(r)$ and $Is_{23}(r)$ corresponds to case 2.1 using antennas A_1, A_2, case 2.2 using antennas A_1, A_3, case 2.3 using antennas A_2, A_3, respectively.

While using two antennas behind the medium, the constructive interference of their individual contributions is meant to improve the quality of their field generation [93] compared with case 1 in which only one antenna is placed behind the medium.

When applying the matrix inversion method, the reconstructed images of area F for the DUT configuration is expressed in each case as:

$$Im_{12}(r) = \left| \left(H_1^{\dagger} H_1 + \mu I \right)^{-1} H_1^{\dagger} S_{41} + \left(H_2^{\dagger} H_2 + \mu I \right)^{-1} H_2^{\dagger} S_{42} \right|^2 \quad (4.15)$$

$$Im_{13}(r) = \left| \left(H_1^{\dagger} H_1 + \mu I \right)^{-1} H_1^{\dagger} S_{41} + \left(H_3^{\dagger} H_3 + \mu I \right)^{-1} H_3^{\dagger} S_{43} \right|^2 \quad (4.16)$$

$$Im_{23}(r) = \left| \left(H_2^{\dagger} H_2 + \mu I \right)^{-1} H_2^{\dagger} S_{42} + \left(H_3^{\dagger} H_3 + \mu I \right)^{-1} H_3^{\dagger} S_{43} \right|^2 \quad (4.17)$$

where, $Im_{12}(r)$, $Im_{13}(r)$ and $Im_{23}(r)$ corresponds to case 2.1 using antennas A_1, A_2, case 2.2 using antennas A_1, A_3, case 2.3 using antennas A_2, A_3, respectively.

Figure 4.18 shows the reconstruction of area F for the DUT for the time reversal based method.

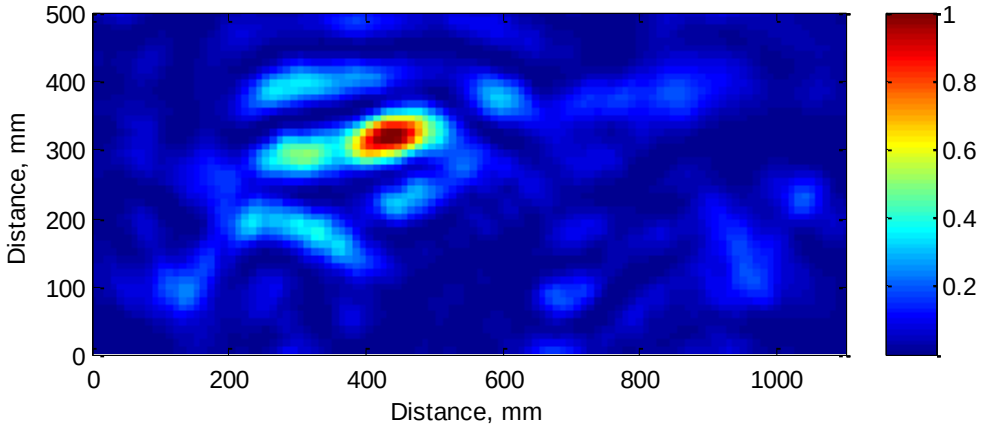

a)

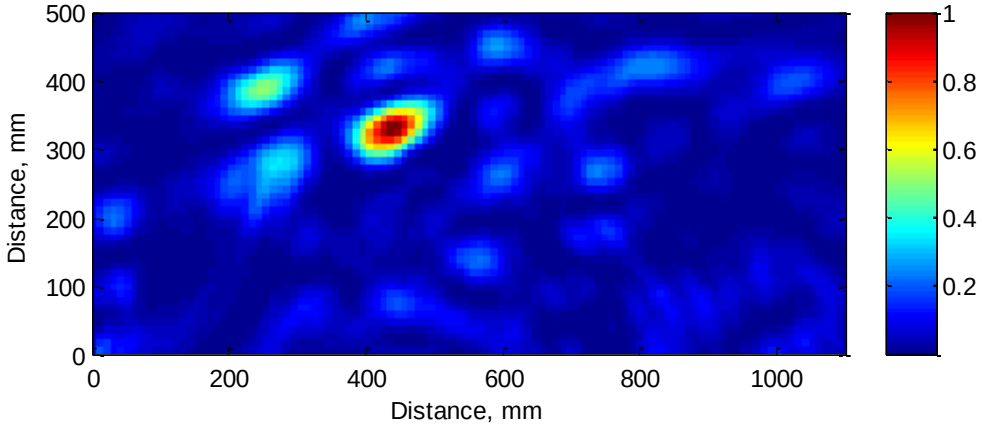

b)

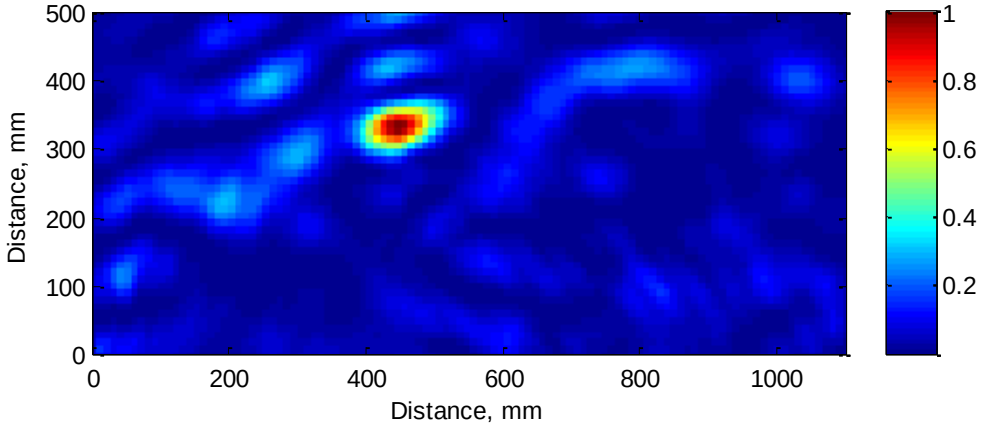

c)

Figure 4.18 Reconstruction of area F using TR method – Multiple antennas measurement setup: a) case 2.1; b) case 2.2; c) case 2.3

Figure 4.19 shows the reconstruction of area F for the DUT for the time reversal based method.

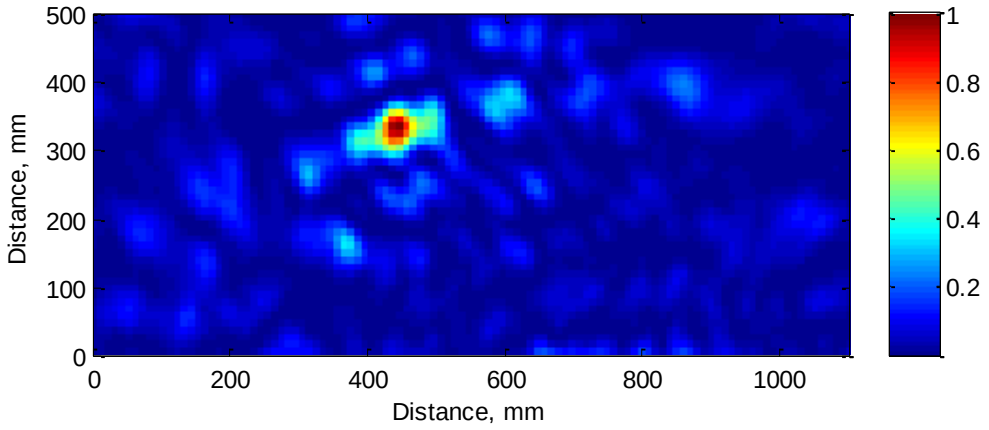

a)

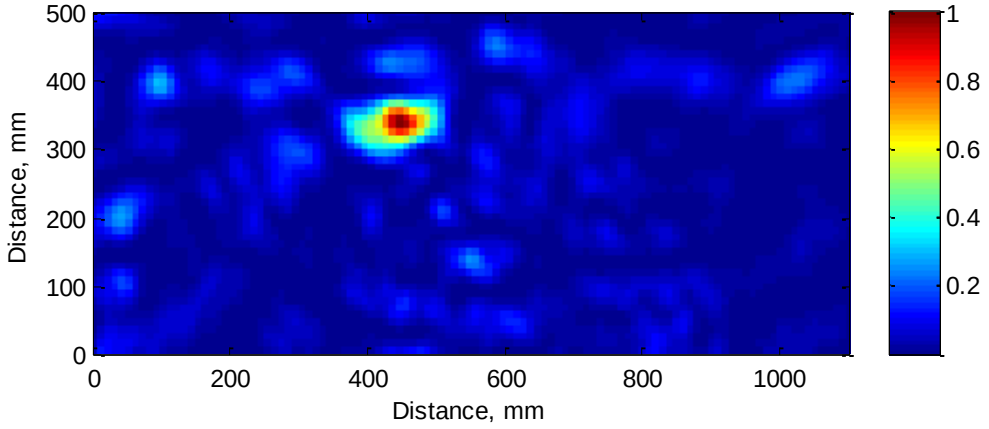

b)

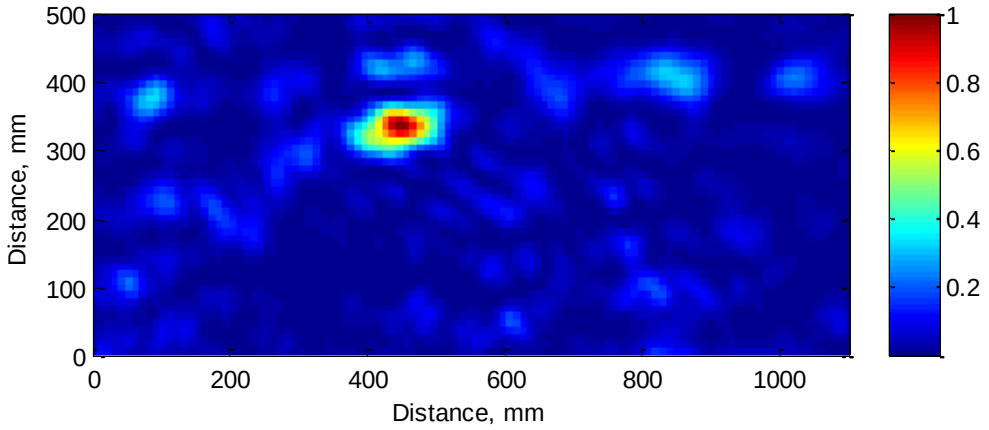

c)

Figure 4.19 Reconstruction of area F using MI method – Multiple antennas measurement setup: a) case 2.1; b) case 2.2; c) case 2.3

Similarly with time reversal method, for each case there is an improvement in the imaging quality, with lower sidelobes in comparison with the case where only one antenna is emitting through the medium.

Figure 4.20 shows the amplitude of the reconstructed image along x axis for both MI and TR methods.

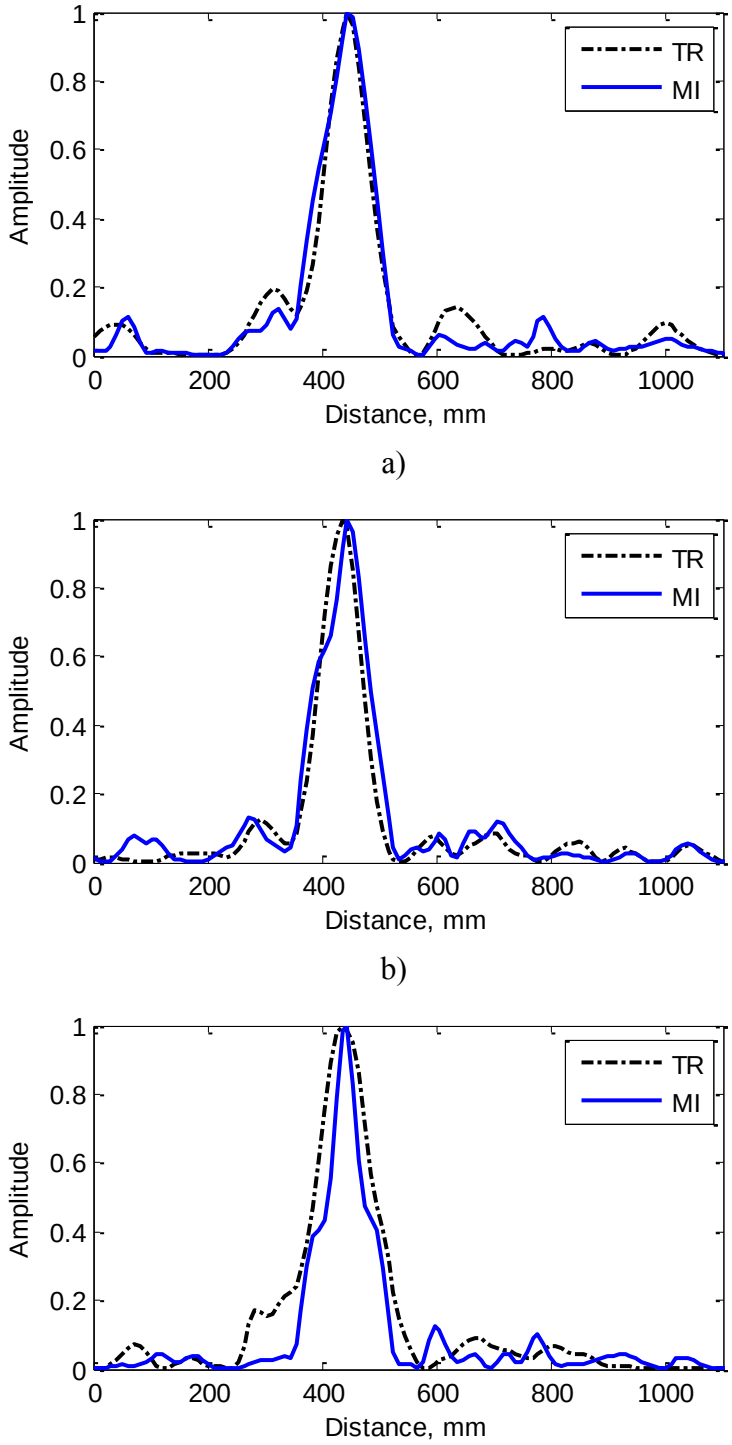

a)

b)

c)

Figure 4.20 Sidelobes amplitude MI vs. TR method – Multiple antennas measurement setup: a) case 2.1; b) case 2.2; c) case 2.3

The level of sidelobes for both methods is comparable, while the detection of the DUT is clearly seen.

4.3.2.3 Case 3 – three antennas emitting through the medium

Figure 4.21 presents a schematic of the layout with all antennas A_1, A_2, A_3 emitting through the medium and A_4 on the side, used in both scanning and DUT configurations.

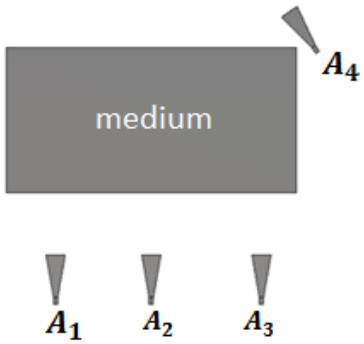

Figure 4.21 Multiple antennas schematic: Case 3

Using time reversal technique, the reconstructed image of area F for the DUT configuration shown in Figure 4.22, is expressed as:

$$Is_{123}(r) = \left| \int S_{41}^{*}(\omega) G_1(r,\omega) G_4(r,\omega) + S_{42}^{*}(\omega) G_2(r,\omega) G_4(r,\omega) + S_{43}^{*}(\omega) G_3(r,\omega) G_4(r,\omega) \right|^2 \quad (4.18)$$

The contributions of all antennas A_1, A_2 and A_3 placed behind the medium, give a better image than the precedent situations. The target is imaged at central position with lower background fluctuations.

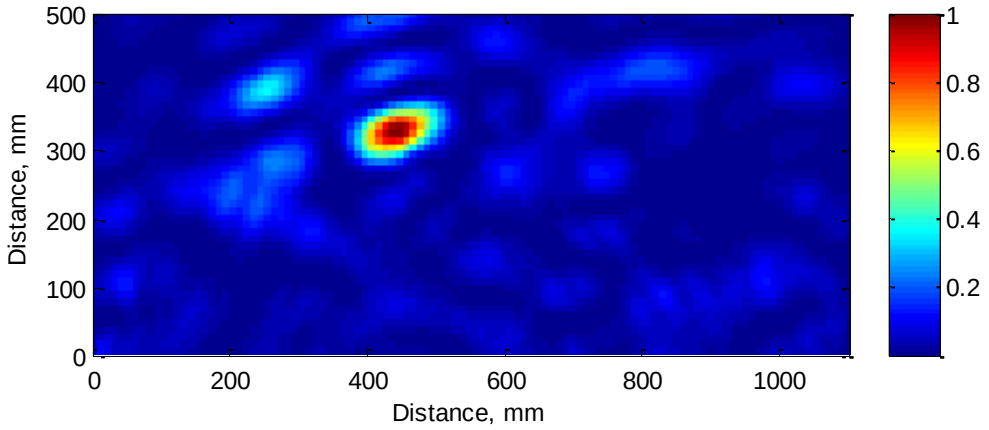

Figure 4.22 Reconstruction of area F using TR method – Multiple antennas measurement setup: Case 3

When applying the matrix inversion method, the reconstructed images of area F for the DUT configuration shown in Figure 4.23, is expressed as:

$$Im_{123}(r) = \left|\left(H_1{}^{\dagger}H_1 + \mu I\right)^{-1} H_1{}^{\dagger}S_{41} + \left(H_2{}^{\dagger}H_2 + \mu I\right)^{-1} H_2{}^{\dagger}S_{42} + \left(H_3{}^{\dagger}H_3 + \mu I\right)^{-1} H_3{}^{\dagger}S_{43}\right|^2 \tag{4.19}$$

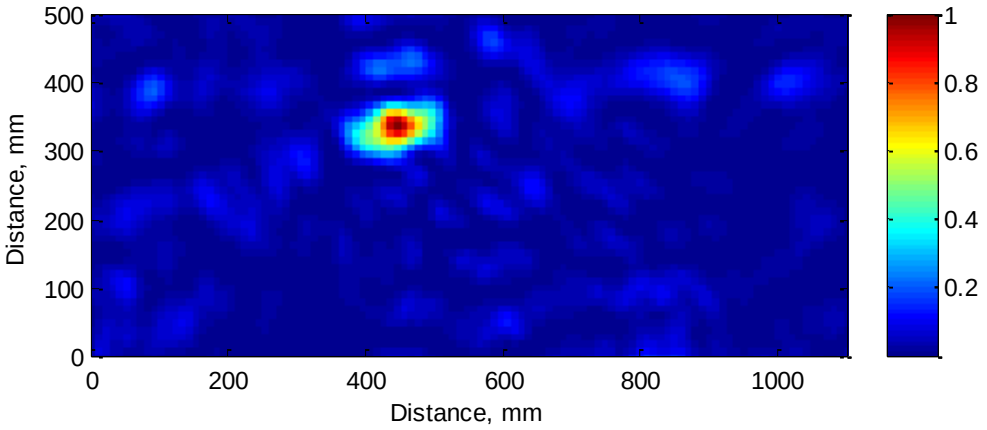

Figure 4.23 Reconstruction of area F using MI method – Multiple antennas measurement setup: Case 3

Similarly with time reversal method, the target is imaged in a central position, the image presenting lower background fluctuations compared with the cases with fewer antennas placed behind the medium.

Figure 4.24 shows the amplitude of the reconstructed image along x axis for both MI and TR methods.

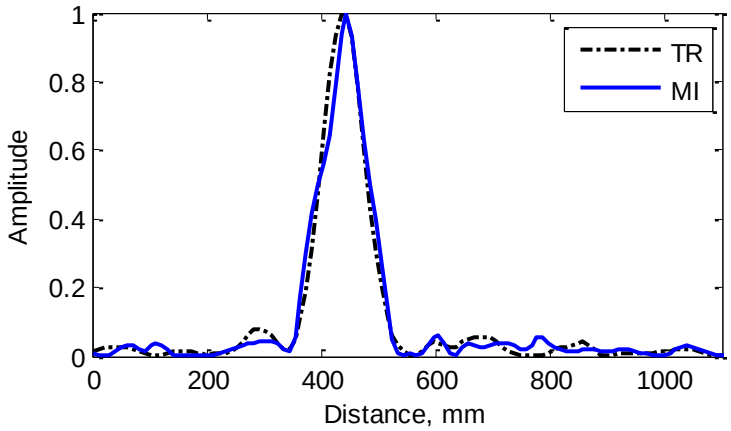

Figure 4.24 Sidelobes amplitude MI vs. TR method – Multiple antennas measurement setup: Case 3

Similarly with time reversal method, the target is imaged in a central position, the image presenting lower background fluctuations compared with the cases with fewer antennas placed behind the medium.

For the time reversal based method, Figure 4.25 shows the comparison between the amplitude at the focus in Figure 4.25.a) and between the sidelobes in Figure 4.25.b), for all three cases with one antenna A_2, two antennas A_1 and A_2 or three antennas, respectively.

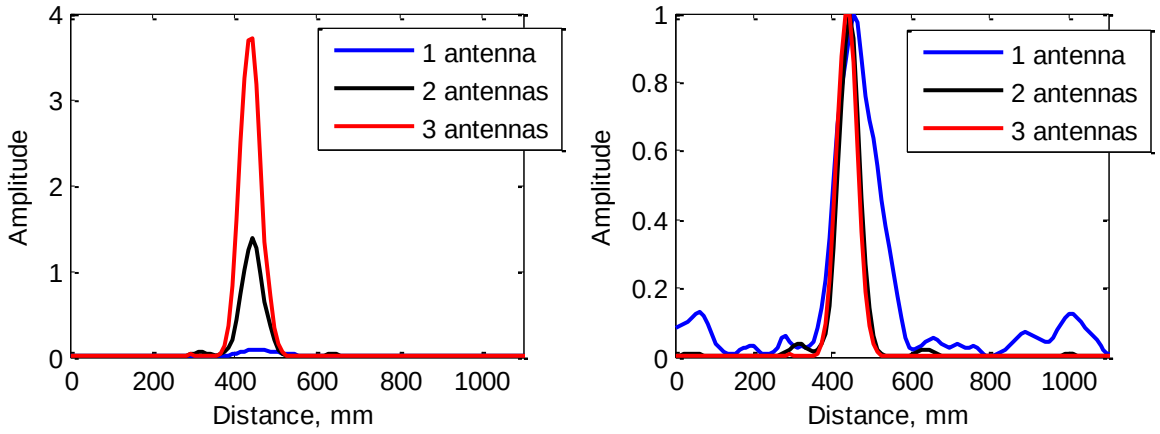

a) b)

Figure 4.25 Comparison for the three cases - TR method: a) amplitude; b) sidelobes

For the matrix inversion method, Figure 4.25 shows the comparison between the amplitude at the focus in Figure 4.26.a) and between the sidelobes in Figure 4.26.b), for all three cases with one antenna A_2, two antennas A_1 and A_2 or three antennas, respectively.

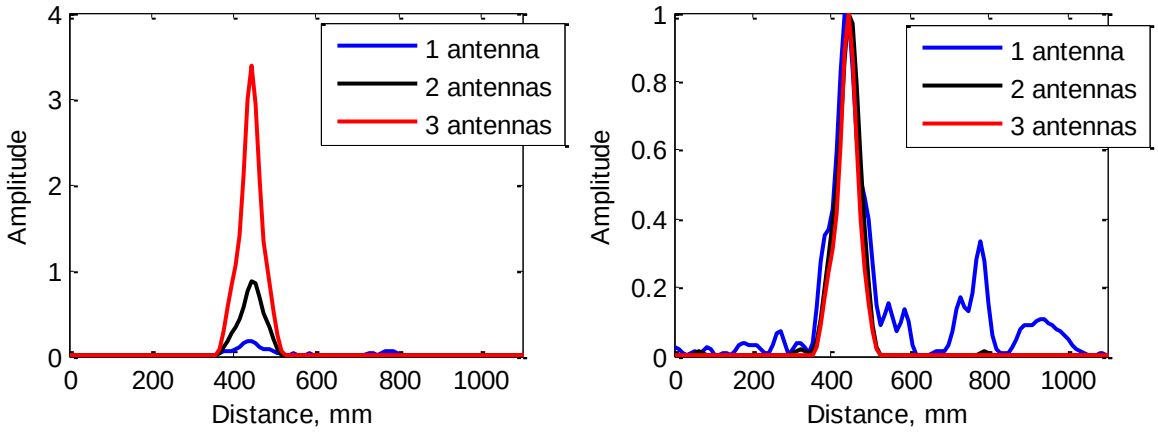

a) b)

Figure 4.26 Comparison for the three cases - MI method: a) amplitude; b) sidelobes

The coherent sum of the three images takes advantage of the individual contributions of each antenna increasing the amplitude at the focus. In comparison, by having the incoherent sum of the images expressed in equations (4.20) - (4.21) for the time reversal based method and in equations (4.22) - (4.23) for the matrix inversion method, it is seen in Figure 4.27 that the amplitude is much smaller.

$$Is_{23}(r) = Is_2(r) + Is_3(r) \tag{4.20}$$

$$Is_{123}(r) = Is_2(r) + Is_2(r) + Is_3(r) \tag{4.21}$$

$$Im_{23}(r) = Im_2(r) + Im_3(r) \tag{4.22}$$

$$Im_{123}(r) = Im_2(r) + Im_2(r) + Im_3(r) \tag{4.23}$$

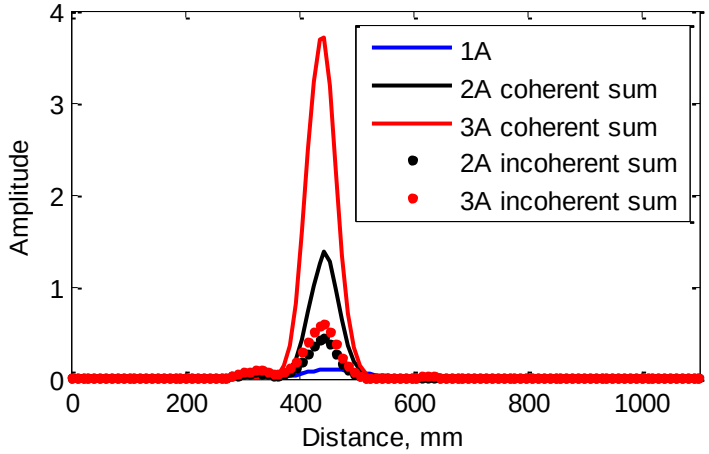

a)

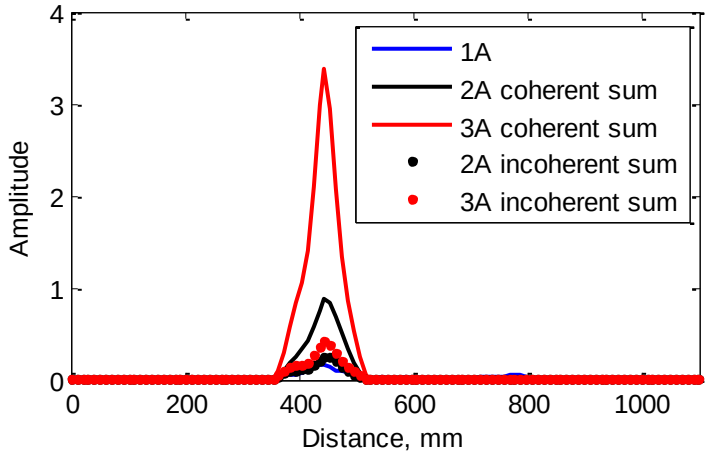

b)

Figure 4.27 Comparison between coherent and incoherent sum of images - TR method: a) TR method; b) MI method

For both methods, the solid line plot shows the coherent sum of the images of two and three antennas compared with the image obtained using one antenna and the dashed line plot shows the incoherent sum of the images. The incoherent sum presents lower amplitudes for the sum of two and three antennas, comparable with the amplitude of one antenna.

4.4 Conclusion

The experimental results validate our approach. We have used a setup similar to the one used in simulations, having the same design for the fabricated random medium. Following the

same post-processing approach on the collected data as in simulation, the target is detected for several positions.

Based on the measurement setup, there are presented layouts with an increased number of antennas used to improve the image quality. Comparing the results for the cases of one, two or three antennas used simultaneously, the constructive interferences of their individual contributions, give the best results for the last case. The background intensity of the image is reduced compared with previous cases. The amplitude of secondary lobes is seen to decrease significantly.

General conclusion and future work

General conclusion

This thesis presents an imaging method using a diffusive medium for RCS characterization in an anechoic chamber. Inspired by time reversal technique, this computational imaging method is a promising solution to overcome the measurement issues in anechoic chambers.

Regarding to the currently used methods for RCS measurements at low frequencies, there are several disturbing phenomena, such as the multipath propagation caused by reflections from the walls. While the wavelength becomes greater when descending in frequency, the thickness of absorbent materials is small compared with λ and they are no longer perfectly absorbent. Thus, the total incident field on the target becomes the sum of the incident wave and the reflected waves from the walls of the chamber.

Time reversal technique allows spatial and temporal focusing of an electromagnetic wave and greatly takes advantage of the reverberation within a scattering medium which provides a spatial diversity exploited in the second step. Using a multiple number of sources it was shown in simulations the ability to focus on different positions at the same time. This way, a wide focus can be created on an extended object with dimensions bigger than the focal spot by reducing the distance between the sources to half of lambda. By increasing the distance, multiple foci on different positions can be obtained in order to focus only on the scattering centers of the target.

The proposed imaging method uses a classic configuration of a time reversal process which benefits from the spectral degrees of freedom provided by the transmission through a random medium. The conception of the disordered medium which consists of a collection of randomly located metallic rods, takes into account the minimum allowed distance between them in order to guarantee a decent transmission.

Two setups, the monostatic and bistatic cases, are used to image a device under test, first in 2D simulations. Using a synthetic time reversal method, the target is shown to be accurately located. Nevertheless, strong sidelobes inherent to time reversal which maximizes

the amplitude at the focal point appear. Therefore, a second method based on a matrix inversion has been used. It is shown to provide much lower sidelobes.

Moreover, inspired by the use of a reverberating cavity for microwave imaging, a comparison between three versions with different boundary conditions is studied, using the monostatic case setup. While the target is detected and located at the right position, it is observed that the metallic boundaries added to the setup, increase the reverberation time within the scattering medium so that the number of temporal degrees of freedom is enhanced. A better signal to noise ratio is hence obtained on the image.

The experimental validation of the technique with a random medium presents the ability to image the target using a bistatic setup which is similar to the simulated one. By performing the reconstruction of the field over an area starting from a line of measurements, the device under test is imaged on a map for several positions, using both time reversal based and matrix inversion method.

From the proposed experimental setup, by increasing the number of antennas, three cases are studied. The results are compared for one, two or three antennas used simultaneously, showing that the best results given by the constructive interferences of their individual contributions are seen for the last case. Using three antennas to transmit through the medium decreases the amplitude of the secondary lobes. This demonstrates that spatial and spectral degrees of freedom can be combined to enhance the signal to noise ratio of the image. This is crucial to image extended targets.

Future work

Computational imaging systems based on time reversal method at microwave frequencies are developed for numerous applications among which radar cross section characterization at low frequencies in anechoic chamber represents the context of this thesis. An improved measurement protocol for RCS determination by introducing a scattering medium within the chamber to focus the field on the target is meant to benefit from the multipath propagation generated by the reflection of illuminated walls.

This work presents the concept of target detection and localization of a target through a random medium was studied at higher frequencies, in the range of $5-7\ GHz$. As future work, the following task is to determine the RCS of the DUT through this method.

As well, regarding the lower frequencies of a few MHz, the system should be adjusted with the proper sized medium. The medium may be optimized for a large bandwidth for both lower and higher working frequencies.

Another important aspect is represented by the monostatic configuration of the setup which suits better the anechoic rooms design. While simulations results are satisfying for this configuration, experimental validation failed to produce good results. It is required an improvement on the post processing procedure of data obtained through experimental measurements, in order to retrieve the scattering coefficient from a monostatic configuration of the imaging setup.

Communications and publications

1. International conferences

- ‹‹ Taking advantage of a diffuse medium for high resolution imaging using two antennas ››, Stefania Bucuci, Matthieu Davy, Ala Sharaiha and Philippe Pouliguen**,** Antenna Measurements & Applications (CAMA 2016), Syracuse, 23-27 October 2016. Oral presentation.

2. National conferences

- ‹‹ Imaging and radar cross section measurements using a random medium ››, Stefania Bucuci, Matthieu Davy, Ala Sharaiha and Philippe Pouliguen**,** 18th International Symposium on ElectroMagnetic Compatibility (CEM 2016), Rennes, 11-13 July 2016. Poster presentation.

2. Journée nationale

- ‹‹ Application of time reversal technique on RCS measurement in anechoic chamber ››, Stefania Bucuci, Matthieu Davy, Ala Sharaiha and Philippe Pouliguen**,** Assemblée générale "Interférences d'Ondes", Lyon, 19-21 October 2015. Poster presentation.

- ‹‹ Détection et localisation de cibles par imagerie électromagnétique utilisant un milieu diffusant ››, Stefania Bucuci, Matthieu Davy, Ala Sharaiha and Philippe Pouliguen**,** 20èmes Journées Nationales Micro-Ondes (JNM 2017), Saint-Malo, 16-19 May 2017. Oral presentation.

Bibliography

[1] Y. Blanchard, "Le centenaire de l‟˜invention du radar par Christian Hülsmeye, retour sur un anniversaire," *Le Radar : du centenaire aux évolutions les plus récentes*, no. 2, pp. 87-92, 2006.

[2] M. I. Skolnik. Encyclopædia Britannica. [Online]. https://www.britannica.com/technology/radar.

[3] National Communications System Technology and Standard Division, "Telecommunications: Glossary of telecommunications terms," General Services Administration Information Technology Service, 1996.

[4] M.I. Skolnik, *Introduction to radar systems*.: McGraw-Hill Book Co, 1981.

[5] S. R. German M.C. Budge Jr., *Basic radar analysis*.: Artech House, 2015.

[6] ICx Technologies Inc. https://www.copybook.com/companies/icx-technologies/articles/radar-operating-frequency.

[7] IEEE 100, *The Authoritative Dictionary of IEEE Standards Terms*.: Standards Information Network IEEE Press, 2000.

[8] J. F. Shaeffer M. T. Tuley E. F. Knott, *Radar cross section*.: SciTech Publishing, 2004.

[9] R. G. Driggers, *Encyclopedia of optical engineering*, 2nd ed.: Marcel Dekker Inc, 2003.

[10] P.W. Courteille, R. Kaiser, N. Piovella R. Bachelard, "Resonances in Mie scattering by an inhomogeneous atomic cloud," *EPL A Letters Journal Exploring the Frontiers of Physics*, vol. 97, no. 1, 2012.

[11] E. L. Nohara, I. M. Martin, G. G. Peixoto, M. C. Rezende M. A. S. Miacci, "Indoor radar cross section measurements of simple targets," *Jorunal of Aerospace Technology and Management*, vol. 4, no. 1, pp. 25-32, 2012.

[12] G. Brooker, *Sensors and signals*.: Australian Centre for Field Robotics, 2006.

[13] R. J. Niemeijer, J. S. van Sinttruyen, L. P. Ligthart C. M. H. Unal, "Calibration of a polarimetric radar using a rotatable dihedral corner reflector," *IEEE Transaction on Geoscience and Remote Sensing*, vol. 32, no. 4, pp. 837-845, 1994.

[14] X. Xu P. Wu, "A correction formulation for RCS measurements of dihedral reflector with quasi-monostatic geometry," in *International conference on electromagnetics in advanced applications (ICEAA)*, Cairns, Australia, 19-23 September 2016, pp. 381-384.

[15] E. F. Knott, *Radar cross section measurements*.: SciTech Publishing, 2006.

[16] Sandia National Laboratories, "Reflectors for SAR Performance Testing," Sandia Corporation, 2008.

[17] B. R. Mahafza, *Radar systems analysis and design using Matlab*.: CRC Press LLC, 2000.

[18] M.I. Skolnik, *Radar handbook*, 3rd ed.: McGraw-Hill Companies, 2008.

[19] http://asiangazette.blogspot.fr/2007_12_02_archive.html.

[20] K. Malaric, *EMI protection for communication systems*.: Artech House, 2000.

[21] V. Rodriguez, "Basic rules for anechoic chamber design, part one: RF absorber approximations," *Microwave Journal*, vol. 59, no. 1, pp. 72-78, 2016.

[22] J. Randa, "Low-frequency model for radio-frequency absorbers," *Journal of Research of the National Institute of Standards and Technology*, vol. 100, no. 3, pp. 257-267, 1995.

[23] D. Morgan, *A handbook for EMC testing and measurements*.: The Institution of Engineering and Technology, 2007.

[24] C. Ozdemir, *Inverse synthetic aperture radar imaging with MATLAB algorithms*.: John Wiley & Sons, 2012.

[25] M. Martorella V. C. Chen, *Inverse synthetic aperture radar imaging: principles, algorithms and applications*.: SciTech Publishing, 2014.

[26] B. P. Bogert, "Demonstration of delay distortion correction by time-reversal techniques," *IRE Transactions on Communications Systems*, vol. 5, no. 3, pp. 2-7, 1957.

[27] A. V. Oppenheim D. J. Harasty, "Television signal deghosting by noncausal recursive filtering," in *International Conference on Acoustics, Speech, and Signal processing,* New York, USA, 11-14 April,1988, pp. 1778-1781.

[28] V. K. Jain J. J. Kormylo, "Two-pass recursive digital filter with zero phase shift," *IEEE Transactions on Acoustics, Speech, and Signal Processing*, vol. 22, no. 5, pp. 384-387, 1974.

[29] C. S. Clay A. Parvulescu, "Reproducibility of signal transmissions in the ocean," *Radio and Electronic Engineer*, vol. 29, no. 4, pp. 223-228, 1965.

[30] M. Fink, "Time reversal of ultrasonic fields – part I: Basic principles," *IEEE Transactions on Ultrasonics, Ferroelectrics, and Frequency Control*, vol. 39, no. 5, pp. 555-566, 1992.

[31] J. Thomas, M. Fink F. Wu, "Time reversal of ultrasonic fields – part II: : Experimental results," *IEEE Transactions on Ultrasonics, Ferroelectrics, and Frequency Control*, vol. 39, no. 5, pp. 567-578, 1992.

[32] M. Fink D. Cassereau, "Time reversal of ultrasonic fields – part III: Theory of the closed time-reversal cavity," *IEEE Transactions on Ultrasonics, Ferroelectrics, and Frequency Control*, vol. 39, no. 5, pp. 579-592, 1992.

[33] J. de Rosny, A. Tourin, A. Derode, G. Montaldo, M. Fink G. Lerosey, "Time reversal of electromagnetic waves and telecommunication," *Radio Science*, vol. 40, no. 6, 2005.

[34] I.Z. Kovcs, P. C. F. Eggers H. T. Nguyen, "A time reversal transmission approach for multiuser UWB communications," *IEEE Transactions on Antennas and Propagation*, vol. 54, no. 11, 2006.

[35] G. Montaldo, M. Tanter M. Fink, "Time-reversal acoustics in biomedical engineering," *Annual Review of Biomedical Engineering*, vol. 5, 465-47 2003.

[36] W. Cai, M. Alrubaiee, M. Xu, S.K. Gayen B. Wu, "Time reversal optical tomography: locating targets in a highly scattering turbid medium," *Optics Express*, vol. 19, no. 22, pp. 21956-21976, 2011.

[37] J.-P. Montagner, M. Fink, Y. Capdeville, A. Tourin, E. Clévédé C. Larmat, "Time-reversal imaging of seismic sources and application to the great Sumatra earthquake'," *Geophysical Research Letters*, vol. 33, no. 19, 2006.

[38] M. Rubinsein F. Rachidi, "Time-reversal of electromagnetic fields and its application to lightning location," in *International Symposium on Lightning Protection (XII SIPDA)*, Belo Horizonte, Brazil, 7-11 October, 2013, pp. 378-383.

[39] M. Fink, F. Wu N. Chakroun, "Time reversal processing in ultrasonic nondestructive testing," *IEEE Transactions on Ultrasonics, Ferroelectrics, and Frequency Control*, vol. 42, no. 6, pp. 1087-1098, 1995.

[40] J.T. Rose, F-K. Chang C. H. Wang, "A synthetic time-reversal imaging method for structural health monitoring," *Smart Materials and Structures*, vol. 13, no. 2, pp. 415-423, 2004.

[41] D. Cassereau, A. Derode, C. prada, P. Roux, M. Tanter, J-L. Thomas, F. Wu M. Fink, "Time reversed acoustics," *Reports on Progress in Physics*, vol. 63, no. 12, pp. 1933-1995, 1999.

[42] M. Fink, "Time-reversal waves and super resolution," *Journal of Physics: Conference Series,* vol. 124, no. 1, 2008.

[43] G. Lerosey, A. Tourin, M.Fink J. de Rosny, "Time reversal of electromagnetic waves," in *Lecture Notes in Computational Science and Engineering*., ch. 7, pp. 187-202.

[44] P. Roux, M. Fink A. Derode, "Robust acoustic time reversal with high-order multiple scattering'," *Physical Review Letters*, vol. 75, no. 23, pp. 4206-4209, 1995.

[45] B. Roman, M. Fink P. Roux, "Time-reversal in an ultrasonic waveguide," *Applied Physics Letters*, vol. 70, no. 14, pp. 1811-1813, 1997.

[46] M. Fink C. Draeger, "One-channel time reversal of elastic waves in a chaotic 2D-silicon cavity," *Physical Review Letters*, vol. 79, no. 3, pp. 407-410, 1997.

[47] M. Fink C. Draeger, "One-channel time reversal in chaotic cavities: theoretical limits," *The Journal of the Acoustical Society of America*, vol. 105, pp. 611-617, 1999.

[48] J.-C. Aime, M. Fink C. Draeger, "One-channel time reversal in chaotic cavities: experimental results," *The Journal of the Acoustical Society of America*, vol. 105, pp. 618-625, 1999.

[49] M. Fink, "Acoustic time-reversal mirrors," *Imaging of Complex Media with Acoustic and Seismic Waves*, pp. 17-43, 2002.

[50] P. Denti, R. Saija, C.Cecchi-Pestellini F. Borghese, "On the polarization and depolarization of the electromagnetic waves," *Journal of Physics: Conference Series*, vol. 6, pp. 59-72, 2005.

[51] K. C. Yeh B. Dong, "Three-dimensional electromagnetic wave polarizations in a plasma," *Radio Science*, vol. 37, no. 6, 2002.

[52] E. Amador, P. Besnier C. Lemoine, "On the K-factor estimation for rician channel simulated in reverberation chamber," *IEEE Transactions on Antennas and Propagation*, vol. 59, no. 3, pp. 1003-1012, 2011.

[53] G. H. Koepke M. L. Crawford, *Design, evaluation and use of a reverberation chamber for performing electromagnetic susceptibility/vulnerability measurements*.: National Bureau of Standards Technical Note 1092, 1986.

[54] A. Cozza F. Monsef, "Average number of significant modes excited in a mode-stirred reverberation chamber," *IEEE Transactions on Electromagnetic Compatibility*, vol. 56, no. 2, pp. 259-265, 2014.

[55] P. Besnier, A. Sharaiha G. Le Fur, "Time reversal efficiency measurement in reverberant chamber," *IEEE Transactions on Antenas and Propagation*, vol. 60, no. 6, pp. 2921-2128, 2012.

[56] C. (J.) Zhou, N. Guo, J. Q. Zhang R. C. Qiu, "Time Reversal With MISO for Ultrawideband Communications: Experimental Results," *IEEE ANTENNAS AND WIRELESS PROPAGATION LETTERS*, vol. 5, pp. 269-273, 2006.

[57] C. Decroze, D. Carsenat T. Fromenteze, "Waveform coding for passive multiplexing: Application to microwave imaging," *IEEE TRANSACTIONS ON ANTENNAS AND PROPAGATION*, vol. 63, no. 2, pp. 593-600, 2015.

[58] G. Kang, L. Li, Y. Chen, S. Vasudevan, W. Joines, Q. H. Liu, J. Krolik, L. Carin D. Liu, "Electromagnetic time-reversal imaging of a target in a cluttered environment," *IEEE TRANSACTIONS ON ANTENNAS AND PROPAGATION*, vol. 53, no. 9, pp. 3058-3066, 2005.

[59] Y. Jiang, J. M.F. Moura Y. Jin, "Time reversal beamforming for microwave breast cancer detection," in *IEEE International Conference on Image Processing* , San Antonio, TX, USA, 2007, pp. 13-16.

[60] D. Carsenat, C.l Decroze T. Fromenteze, "A precorrection method for passive UWB time-reversal beamformer," *IEEE ANTENNAS AND WIRELESS PROPAGATION LETTERS*, vol. 12, pp. 836-840, 2013.

[61] C. Decroze D. Carsenat, "UWB antennas beamforming using passive time-reversal device," *IEEE ANTENNAS AND WIRELESS PROPAGATION LETTERS,* vol. 11, pp. 779-782, 2012.

[62] X. Yang, Y.Liu, R. Mittra W. Yu, *Electromagnetic simulation techniques based on the FDTD method*.: John Wiley & Sons, 2009.

[63] B. Kakde D. K. Soni, "Review of three-dimensional finite difference time domain techniques," *International Journal for Research in Technological Studies*, vol. 3, no. 1, 2015.

[64] F. Nataf, "Absorbing boundary conditions ans perfectly matched layers in wave propagation problems," in *Direct and inverse problems in wave propagation and applications*.: De Gruyer, 2013, vol. 14, pp. 219-231, Radon series on computational and applied mathematics.

[65] S. D. Gedney, *Introduction to the finite-difference time-domain (FDTD) method for electromagnetics*.: Morgan & Claypool Publishers, 2011.

[66] J-P. Berenger, "A perfectly matched layer for the absorbtion of electromagnetic waves," *Journal of Computational Physics*, vol. 114, pp. 185-200, 1194.

[67] J.-P. Fouque, J. Garnier A. Nachbin, "Time Reversal for Dispersive Waves in Random Media," *SIAM Journal on Applied Mathematics*, vol. 64, no. 5, pp. 1810–1838, 2004.

[68] L. Ryzhik G. Bal, "Time Reversal and Refocusing in Random Media," *SIAM Journal on Applied Mathematics*, vol. 63, no. 5, pp. 1475-1498, 2003.

[69] Y. Yang, M. Fink, A. Tourin, X Jia M. Harazi, "Time reversal of ultrasound in granular media," *European Physical Journal: Special Topics*, vol. 226, pp. 1487-1497, 2017.

[70] W. Zhang, F. Li L. Li, "Derivation and discussion of the SAR migration algorithm within inverse scattering problem: Theoretical analysis," *IEEE Transactions on Geoscience and Remote Sensing*, vol. 48, no. 1, pp. 415-422, 2010.

[71] Q. H. Liu, L.-P. Song F. Li, "Three-dimensional reconstruction of objects buried in layered media using born and distorted born iterative methods," *IEEE Geoscience and Remote Sensing Letters*, vol. 1, no. 2, pp. 107-111, 2001.

[72] X. Zeng, A. Fhager M. Persson, "Microwave Imaging for Medical Applications," in *EuCAP*, 2011, pp. 3070-3072.

[73] R. Zoughi S. Kharkovsky, "Microwave and millimeter wave nondestructive testing and evaluation - Overview and recent advances," *IEEE Instrumentation & Measurements Magazine*, vol. 10, no. 2, pp. 26-38, april 2007.

[74] C. Soutis, A. Haigh, R. Sloan, A. Gibson Z. Li, "Microwave imaging for delamination detection in T-joints of wind turbine composite blades," in *Proceedings of the 46th European Microwave Conference*, London, 2016, pp. 1235-1238.

[75] M. Dehmollaian, "Refocusing through building walls using synthetic aperture radar," *IEEE Transactions on Geoscience and Remote Sensing*, vol. 46, no. 6, pp. 1589-1599, 2008.

[76] D. L. McMakin, T. E. Hall D. M. Sheen, "Three-dimensional millimeter-wave imaging for concealed weapon detection," *IEEE Transactions on Microwave Theory and Techniques*, vol. 49, no. 9, pp. 1581-1592, 2001.

[77] G. Papanicolaou, C. Tsogka, J. Berryman L. Borcea, "Imaging and time reversal in random media," *Inverse Problems*, vol. 15, no. 5, pp. 1247-1279, 2002.

[78] A. Tourin, M. Fink A. Derode, "Random multiple scattering of ultrasound. II. Is time reversal a self-averaging process?," *Physical Review E*, vol. 64, 2001.

[79] F. Sciortino, P. Ziherl C. Bechinger, *Physics of Complex Colloids*.: IOS Press, 2013.

[80] E. Larose, M. Tanter, J. de Rosny, A. Tourin, M. Campilo, M. Fink A. Derode, "Recovering the Green‟s function from field-field correlations in an open scattering medium," *Journal of the Acoustical Society of America*, vol. 113, pp. 2973-2976, 2003.

[81] A. A. Chabanov, P. Sebbah, B.A. van Tiggelen A.Z. Genack, "Wave scattering in complex media: From theory to applications," *NATO Science Series*, vol. 107, 2003.

[82] R. Pnini and A. Z. Genack P. Sebbah, "Field and intensity correlation in random media," *Physical Review E*, vol. 62, pp. 7348-7352, 2000.

[83] A. Lagendijk, G. Lerosey, M. Fink A. P. Mosk, "Controlling waves in space and time for imaging and focusing in complex media," *Nature Photonics*, vol. 6, pp. 283-292, 2012.

[84] P. Lodah, A. Lagendijk I. M. Vellekoop, "Determination of the diffusion constant using phase-sensitive measurements," *Physical Review E,* vol. 71, 2005.

[85] M. A. Fiddy, S. Leeman L. Zapalowski, "On inverse scattering in the first Born approximation," in *IEEE 1984 Ultrasonics Symposium*, 1984.

[86] P. Xu, "Truncated SVD methods for discrete linear ill-posed problems," *Geophysical Journal International*, vol. 135, no. 2, pp. 505-514, 1998.

[87] S. Morigi, L. Reichel, F.Sgallari D. Calvetti, "Tikhonov regularization and L-curve for large discrete ill-posed problems," *Journal of Computational and Applied Mathematics*, vol. 123, pp. 423-446, 2000.

[88] O. Yurduseven, M. F. Imani, J. Gollub, C. Decroze, D. Carsenat, D. R. Smith T. Fromenteze, "Computational imaging using a mode-mixing cavity at microwave frequencies," *Applied Physics Letters*, vol. 106, 2015.

[89] D. Palacio, M.l Tanter, M. Fink G.l Montaldo, "Building three-dimensional images using a time-reversal chaotic cavity," *IEEE Transactions on Ultrasonics, Ferroelectrics, and Frequency Control*, vol. 52, no. 9, pp. 1489-1497, 2005.

[90] M. Pernot, M. Fink, M. Tanter B. Arnal, "Tunable time-reversal cavity for high-pressure ultrasonic pulses generation: A tradeoff between transmission and time compression," *Applied Physics Letters*, vol. 101, 2012.

[91] L. Greengard, M. Ferrando F. Vico, "Fast convolution with free-space Green's functions," *Journal of Computational Physics*, vol. 323, pp. 191-203, 2016.

[92] J. C. Monzon, "On Surface Integral Representations: Validity of Huygens‟ Principle and the Equivalence Principle in Inhomogeneous Bianisotropic Media," *IEEE Transaction on Microwave Theory and Techniques*, vol. 41, no. 11, pp. 1995-2001, 1993.

[93] F. Monsef A. Cozza, "Multiple-source time-reversal transmission in random media," *IEEE Transactions on Antennas and Propagation*, vol. 62, no. 8, pp. 4269-4281, 2014.